

## Durham E-Theses

---

*Characterisation of electrode microarrays produced  
photolithographically and with thiol self-assembled  
monolayers on gold electrodes*

SANTANA-AGUIAR, FRANCISCO,AURELIO

### How to cite:

---

SANTANA-AGUIAR, FRANCISCO,AURELIO (2009) *Characterisation of electrode microarrays produced photolithographically and with thiol self-assembled monolayers on gold electrodes*, Durham theses, Durham University. Available at Durham E-Theses Online: <http://etheses.dur.ac.uk/45/>

### Use policy

---

The full-text may be used and/or reproduced, and given to third parties in any format or medium, without prior permission or charge, for personal research or study, educational, or not-for-profit purposes provided that:

- a full bibliographic reference is made to the original source
- a [link](#) is made to the metadata record in Durham E-Theses
- the full-text is not changed in any way

The full-text must not be sold in any format or medium without the formal permission of the copyright holders.

Please consult the [full Durham E-Theses policy](#) for further details.

---

Academic Support Office, Durham University, University Office, Old Elvet, Durham DH1 3HP  
e-mail: [e-theses.admin@dur.ac.uk](mailto:e-theses.admin@dur.ac.uk) Tel: +44 0191 334 6107  
<http://etheses.dur.ac.uk>

Characterisation of electrode microarrays  
produced photolithographically and with thiol  
self-assembled monolayers on gold electrodes

Francisco Aurélio Santana Aguiar

A thesis submitted in part fulfilment  
of the requirements for the degree of  
Doctor of Philosophy.



Department of Chemistry  
Durham University

June 2009

## ***I. ABSTRACT***

---

The macroscale electrochemical theory breaks down with microstructures smaller than the dimensions of the diffusion layer, showing that such electrodes have significant quantitative effects and qualitative advantages.

The great advantage of microelectrodes over macroelectrodes is the minimisation of interference, which gives rise to much lower detection limits. Microelectrodes have much reduced ohmic drops and capacitive effects and can be used in the absence of supporting electrolyte. These features have opened a growing interest in the fabrication and application of microelectrodes in various areas. There are different microelectrode geometries, but disc type is the most used.

Microelectrode arrays have been proposed as a way of increasing the magnitude of the current (produced for a single microelectrode), while maintaining the advantages of the single microelectrode. Although the inlaid microdisc microelectrode can be considered as one the most popular microelectrode geometry, there is also a need to consider conical recessed, recessed and protruding microdiscs as photolithographic microfabrication techniques often result in non-ideal geometries. It has been proved using surface imaging techniques such as scanning Kelvin nanoprobe (SKN), scanning electron microscopy (SEM) and white light interferometer microscopy that conical recessed electrodes with gradient potential along the recessed walls are formed during standard photolithographic methods for producing microelectrode arrays.

Microarrays are ubiquitously used for high-throughput measurements using various signal transduction techniques. Ideally each sensor in a microarray platform should perform optimally to ensure an error free response. In this thesis, a simple method for designing a microelectrode array platform (MEA) is described, allowing a 'defective' cluster of sensing arrays to be easily identified. It is possible to extend this concept for multiple analyses on a single chip. Molecular electronic is a promising technology which would be an alternative. The concept of molecular electronics is the use of single molecules or arrays, or layers of molecules for the fabrication of electronic components such as wires, switches, and storage elements. Indeed, functionalised thiol monolayer-based microelectrode array may provide unique possibilities, facilitating electrochemical measurements involving electron transfer via electron tunnelling. The conjugated structure of rigid, linear molecule increases greatly the rate of electron transfer across the monolayer.

Charge transfer and self-assembly characteristics of novel fully conjugated molecules molecular wires (synthesised at the Department of Chemistry and Centre for Molecular and Nanoscale Electronics, Durham University) assembled on flat gold electrodes are evaluated using Marcus model of electron-transfer and tunnelling theory. The behaviour of these wires is compared with heptanethiol and dodecanethiol SAMs.

A preliminary study for application of self-assembled monolayer of molecular wires in microelectrode arrays for multiple analyses on a single chip has been successfully reached.

*“The hole in my life left behind from the death of a parent can never be filled...”*

*... But shows us how much more we need to appreciate those of that generation that are left.”*

*In memory to my mother and grandmother*

---

## II. ACKNOWLEDGEMENTS

---

*“Thesis and books are final products. In their formal perfection they appeared to have been written in a moment of inspiration, which makes the writer to emerge almost as a mighty figure. The acknowledgments, however, allows going a little beyond this mask of perfection and erudition, and understand that although academic work is mainly an individual endeavor, the outcome of his work is dependent on cooperation with others.”*

*Dr. Vasco Fernandes*

Dr. Vasco Fernandes is a Portuguese friend who finishes the PhD last year in Anthropology in this University, and he gave permission to add this sentence, because, after all, the acknowledgements is also a very important part of the thesis.

After 3 years of research, I look to the past and I've see so many people that contribute for my work, whether by personal life, whether by professional life. In sum, a thesis without acknowledgments is like a human being without soul.

These years in Durham were the most important in my short life. From now on, my professional career will be very different, carrying the valuable title of Doctor of Philosophy of Durham. However, in my personal life, everything changes... I've got married and my dear mother and grandmother started a new journey, leaving me in this world suffering. As I mentioned before, the hole in my life left behind from the death of a parent can never be filled, but shows us how much more we need to appreciate those of that generation that are left.

First to all, I would like to express my deep gratitude to my supervisor, Dr. Ritu Katakya for her help and patience throughout my PhD studies. Your guidance and complete support made my working and learning experience, a very special one. You are more than supervisor. You are one of my best friends, and, I will never forget what you have done for me, even in my worst moments. I will keep in touch with you until my mother decide call me from heaven. THANK YOU

Father, this degree is also yours. I remember when you worked so hard to earn money for my degree in Portugal. I owe you this. I will always keep in my mind the values that you pass me, and I will educate your grandchildren in the same way. I cannot forget my sister Solange and my nephew Rodrigo.

Leandra, I thank you with all my heart, for always being present in the worst and the wonderful moments. You're my wife but, our friendship is the most important value that we have. Especially my absence, her love, sensibility and trust were essential to me. Once this stage finished, I'm looking for our future



with happiness and I hope this difficult period reinforced our love, and that from now on I can become a clearer and more objective presence in her life.

My grateful thanks to my friends that so strongly support me, especially, the “Lusitana Society of Durham”: João Pires, João Mendes, Paula, Rui, Sérgio and Vasco, my friends in Portugal: Marco, Sergio, Quinzé, Tojal, Barradas, Riscas, Nuno, etc etc... (I will need another thesis in order to mention everybody), and my best friend, Zé Luis. YOU’RE MY BROTHER!!

I would like to express my gratitude to Prof. Isabel and Prof. Ana from Universidade da Beira Interior, Portugal. They gave me the opportunity to come to UK to do PhD. They opened a door, which for a poor family seemed impossible to unlock. THANK YOU SO MUCH!!

Listening Pink Floyd while I’m writing the most important part of this thesis, I finish the acknowledgements crying like a baby, but after all... **I DID IT!!**



*Francisco*

### III. DECLARATION

---

The research described in this thesis was undertaken in the Department of Chemistry of Durham University between October 2005 and March 2009. All work is my own, other than where specifically stated otherwise. No part of this work has been submitted previously for a degree at this or any other University.

Aspects of chapters 3, 4 and 5 are based on the following published works:

- F. A. Aguiar, A.J. Gallant, M.C. Rosamond, A. Rhodes, D. Wood, R. Katakya, *Conical recessed gold microelectrode arrays produced during photolithographic methods: Characterisation and causes*, *Electrochemistry Communications*, 9 (2007) 879 – 885;
- Francisco A. Aguiar, M.C. Rosamond, D. Wood, R. Katakya, *Towards multifunctional microelectrode arrays*, *Analyst*, 133 (2008) 1060 – 1063;
- Francisco A. Aguiar, R. Katakya, *Self assembly of rigid rod molecular wire characterised by electrochemistry and impedance spectroscopy*, manuscript submitted for publication;

### IV. STATEMENT OF COPYRIGHT

---

The copyright of this thesis rests with the author. No quotation from it should be published in any format, including electronic and internet, without the author's prior written consent. All information derived from this thesis must be acknowledged appropriately.

## V. TABLE OF CONTENTS

---

|   |           |
|---|-----------|
| I. Abstract   | i         |
| II. Acknowledgements  | iv        |
| III. Declaration  | vii       |
| IV. Statement of copyright  | vii       |
| V. Table of Contents  | viii      |
| VI. List of Symbols and Abbreviations                                   | xiii      |
| VII. List of Illustrations  | xvi       |
| VIII. List of Tables  | xxiv      |
| <br>  |           |
| <b>1. Introduction</b>  | <b>1</b>  |
| <br>  |           |
| <b>2. Background of electrochemistry and surface imaging techniques</b> |           |
| <br>  |           |
| <b>2.1. Abstract</b>  | <b>4</b>  |
| <b>2.2. History of electrochemistry and basic definitions</b>           | <b>5</b>  |
| <b>2.3. Electrodes</b>  | <b>9</b>  |
| <b>2.3.1. Reference electrode</b>                                       | <b>10</b> |
| <b>2.3.2. Working electrode</b>   | <b>14</b> |
| <b>2.3.2.1. Mercury electrodes</b>                                      | <b>15</b> |
| <b>2.3.2.2. Solid electrodes</b>  | <b>15</b> |
| <b>2.4. Electrical double layer</b>                                     | <b>18</b> |
| <b>2.4.1. Helmholtz model (1879)</b>                                    | <b>18</b> |
| <b>2.4.2. Guoy-Chapman model (1910-1913)</b>                            | <b>19</b> |

---

|  |    |
|--|----|
| <b>2.4.3.</b> Stern model (1924)                           | 20 |
| <b>2.4.4.</b> Graham model (1947)                          | 21 |
| <b>2.4.5.</b> Bockris, Devanathan and Müller model (1963)  | 22 |
| <b>2.5.</b> Transport process                              | 23 |
| <b>2.5.1.</b> Diffusion at planar electrodes               | 30 |
| <b>2.5.2.</b> Diffusion at spherical electrodes            | 32 |
| <b>2.5.3.</b> Diffusion at microdisc electrodes            | 35 |
| <b>2.6.</b> Kinetics of electrode reactions                | 41 |
| <b>2.6.1.</b> Heterogenous electrochemical reactions       | 41 |
| <b>2.7.</b> Electrochemical techniques                     | 46 |
| <b>2.7.1.</b> Cyclic voltammetry (CV)                      | 46 |
| <b>2.7.2.</b> Chronoamperometry (CA)                       | 52 |
| <b>2.7.3.</b> Electrochemical Impedance Spectroscopy (EIS) | 53 |
| <b>2.8.</b> Microelectrodes                                | 59 |
| <b>2.8.1.</b> The influence of the capacitive current      | 62 |
| <b>2.8.2.</b> The influence of the Ohmic drop              | 64 |
| <b>2.9.</b> Microelectrode arrays (MEAs)                   | 65 |
| <b>2.9.1.</b> Electrochemical behaviour                    | 69 |
| <b>2.9.1.1.</b> Cyclic voltammetric behaviour              | 69 |
| <b>2.10.</b> Surface imaging techniques                    | 74 |
| <b>2.10.1.</b> Scanning Electron Microscopy (SEM)          | 74 |
| <b>2.10.2.</b> White Light Interferometer Microscopy       | 76 |
| <b>2.10.3.</b> Scanning Kelvin Nanoprobe Microscopy (SKN)  | 78 |
| <b>2.10.4.</b> Atomic Force Microscopy (AFM)               | 83 |
| <b>2.10.</b> Fourier Transform Infrared Spectroscopy       | 84 |
| <b>2.11.</b> References                                    | 85 |

### **3. Conical recessed gold microelectrode arrays produced during photolithographic methods: characterisation and causes**

|  |     |
|--|-----|
| <b>3.1. Abstract</b>                           | 91  |
| <b>3.2. Introduction</b>                       | 92  |
| <b>3.3. Experimental</b>                       |     |
| <b>3.3.1. Microfabrication</b>                 | 96  |
| <b>3.3.2. Electrochemical characterisation</b> | 99  |
| <b>3.3.3. Surface analysis</b>                 | 101 |
| <b>3.4. Results and discussions</b>            |     |
| <b>3.4.1. Surface analysis</b>                 | 102 |
| <b>3.4.2. Electrochemical characterisation</b> | 112 |
| <b>3.5. Conclusions</b>                        | 124 |
| <b>3.6. References</b>                         | 125 |

### **4. Towards multifunctional microelectrode arrays**

|                                     |     |
|-------------------------------------|-----|
| <b>4.1. Abstract</b>                | 128 |
| <b>4.2. Introduction</b>            | 129 |
| <b>4.3. Experimental</b>            |     |
| <b>4.3.1. Microfabrication</b>      | 132 |
| <b>4.3.2. Surface analysis</b>      | 137 |
| <b>4.4. Results and discussions</b> | 142 |
| <b>4.5. Conclusions</b>             | 148 |
| <b>4.6. References</b>              | 149 |

## **5. Characterisation of self-assembled monolayers of alkanethiols and molecular wires on gold using PEIS and electrochemical techniques**

|  |     |
|--|-----|
| <b>5.1. Abstract</b>                                 | 151 |
| <b>5.2. Introduction</b>                             | 153 |
| <b>5.3. Experimental</b>                             | 166 |
| <b>5.3.1. Reagents and chemicals</b>                 | 166 |
| <b>5.3.2. Instrumentation</b>                        | 166 |
| <b>5.3.3. Substrate preparation</b>                  | 168 |
| <b>5.4. Results and discussions</b>                  | 170 |
| <b>5.4.1. Cyclic voltammetry</b>                     | 170 |
| <b>5.4.2. Electrochemical impedance spectroscopy</b> | 177 |
| <b>5.5. Electron transfer kinetics</b>               | 182 |
| <b>5.6. Influence of applied potential</b>           | 188 |
| <b>5.7. Conclusions</b>                              | 194 |
| <b>5.8. References</b>                               | 196 |

## **6. The mystery of the sharp peaks – electron transfer or gold cyanisation?**

|  |     |
|--|-----|
| <b>6.1. Abstract</b>                           | 203 |
| <b>6.2. Introduction</b>                       | 204 |
| <b>6.2.1. Gold cyanisation</b>                 | 207 |
| <b>6.2.2. Deposition of Prussian Blue (PB)</b> | 211 |
| <b>6.3. Experimental</b>                       | 212 |

|   |     |
|---|-----|
| <b>6.3.1.</b> Reagents and chemicals                            | 212 |
| <b>6.3.2.</b> Instrumentation                                   | 212 |
| <b>6.4.</b> Results and discussions                             | 213 |
| <b>6.4.1.</b> Cyclic voltammetry                                | 213 |
| <b>6.4.2.</b> Formation of Prussian Blue layer                  | 219 |
| <b>6.4.3.</b> Electron transfer kinetics                        | 221 |
| <b>6.4.4.</b> Characterisation of the surface electrode by FTIR | 225 |
| <b>6.4.5.</b> Influence of applied potential                    | 227 |
| <b>6.5.</b> Conclusions   | 231 |
| <b>6.6.</b> References  | 232 |
| <br>  |     |
| <b>7. Conclusion and future work</b>                            | 235 |

## VI. LIST OF SYMBOLS AND ABBREVIATIONS

---

Below are listed some of the common symbols and abbreviations used throughout this work. It is not an exhaustive list – any other symbols or abbreviations will be defined as and when they occur in the text.

The usual unit is that commonly used in electrochemical measurements. If a different unit is used in a particular case this will also be indicated in the text.

| Symbol          | Meaning                                    | Usual Unit                      |
|-----------------|--|---------------------------------|
| A               | Area                                       | cm <sup>2</sup>                 |
| a               | Microelectrode radius                      | μm                              |
| C               | Capacitance                                | F                               |
| C <sub>dl</sub> | Double-layer capacitance                   | F                               |
| C <sub>∞</sub>  | Bulk concentration                         | mol cm <sup>-3</sup>            |
| C <sub>0</sub>  | concentration at null time                 | mol cm <sup>-3</sup>            |
| D               | Diffusion coefficient                      | cm <sup>2</sup> s <sup>-1</sup> |
| d               | Inter-electrode distance                   | μm                              |
|                 | Length of molecule that form the monolayer | Å                               |
| d <sub>a</sub>  | average film thickness of defects          | Å                               |
| d <sub>0</sub>  | film thickness of well-assembled monolayer | Å                               |
| E               | Electrode potential                        | V                               |
| E <sup>0</sup>  | Standard electrode potential               | V                               |
| E <sub>F</sub>  | Fermi level                                | eV                              |
| e               | Elementary charge                          | 1.6022 × 10 <sup>-19</sup> C    |
| e <sup>-</sup>  | Electron                                   |                                 |
| F               | Faraday constant                           | 96485.4 C mol <sup>-1</sup>     |
| f               | Frequency                                  | s <sup>-1</sup> or Hz           |
| i               | Current                                    | A                               |



|              |   |   |
|--------------|---|---|
| $i_0$        | Current measured at a bare electrode                          | A   |
| $J(x,t)$     | Flux at distance $x$ and time $t$                             | $\text{mol cm}^{-2} \text{s}^{-1}$                      |
| $K$          | Equilibrium constant  |   |
| $k_B$        | Boltzmann constant  | $1.38066 \times 10^{-23} \text{ J K}^{-1}$              |
| $k_f$        | Heterogeneous rate constant of forwards (oxidation) reaction  | $\text{cm s}^{-1}$                                      |
| $k_b$        | Heterogeneous rate constant of backwards (reduction) reaction | $\text{cm s}^{-1}$                                      |
| $K_0$        | Electron-transfer rate constant for bare electrode            | $\text{cm s}^{-1}$                                      |
| $K_{app}$    | Apparent electron transfer rate constant                      | $\text{cm s}^{-1}$                                      |
| $L$          | Depth of the recess electrode                                 | $\mu\text{m}$   |
| $n$          | Stoichiometric number of species                              |   |
| $O$          | Generic oxidised form of an electroactive species             |   |
| $Q$          | Charge  | C   |
| $q$          | Charge  | C   |
| $R$          | Generic reduced form of an electroactive species              |   |
|              | Molar gas constant  | $8.31451 \text{ J K}^{-1} \text{ mol}^{-1}$             |
|              | Resistance  | $\Omega$  |
| $R_{ct}$     | Charge-transfer resistance                                    | $\Omega$  |
| $T$          | Absolute temperature  | K   |
| $t$          | Time  | s   |
| $u$          | Scan rate   | $\text{V s}^{-1}$                                       |
| $x$          | Distance from working electrode surface                       | cm  |
| $Z'$         | Real contribution towards impedance                           | $\Omega$  |
| $Z''$        | Imaginary contribution towards impedance                      | $\Omega$  |
| $Z$          | Number of microelectrodes in an array                         |   |
| $\alpha$     | Transfer coefficient  |   |
| $\beta$      | electrode tunnelling coefficient                              | $\text{\AA}^{-1}$                                       |
| $\delta$     | Diffusion layer thickness                                     | cm  |
| $\epsilon$   | Permittivity  | $\text{C N}^{-1} \text{ m}^{-2}$                        |
| $\epsilon_0$ | Permittivity of a vacuum                                      | $8.854 \times 10^{-12} \text{ C N}^{-1} \text{ m}^{-2}$ |
| $\xi$        | Zeta potential  | V   |
| $\eta$       | Overpotential   | V   |
| $\mu$        | Chemical potential  | $\text{J mol}^{-1}$                                     |
| $\sigma$     | Surface charge density  | $\text{C cm}^{-2}$                                      |
| $\sigma_0$   | fractional coverage of the well-assembled monolayer           |   |
| $\sigma_i$   | fractional coverage for defects with film thickness $i$       |   |

|            |  |                     |
|------------|--|---------------------|
| $\sigma_a$ | average fractional coverage of defects   |                     |
| $\tau$     | Time period                              | s                   |
| $\phi$     | Work function                            | eV                  |
| $\Psi$     | Normalised current                       |                     |
| $\phi$     | Electrostatic potential                  | V                   |
|            | Phase angle                              | rad                 |
| $\omega$   | Angular frequency                        | rad s <sup>-1</sup> |
| $\gamma$   | growth or decay factor of the resistance | V <sup>-1</sup>     |

### Abbrev.

### Meaning

|        |  |
|--------|--|
| AFM    | Atomic force microscopy  |
| CA     | Chronoamperometry  |
| CE     | Counter electrode  |
| CSW564 | S-4-((4-(biphenyl-4-ylethynyl)-2,5-bis(hexyloxy)phenyl)ethynyl)phenylthiol |
| CV     | Cyclic voltammetry   |
| DDT    | Dodecanethiol  |
| EIS    | Electrochemical impedance spectroscopy                                     |
| FTIR   | Fourier Transform Infrared Spectroscopy                                    |
| HPT    | Heptanethiol   |
| IHP    | Inner Helmholtz plane  |
| ME     | Microelectrode   |
| MEA    | Microelectrode array   |
| OHP    | Outer Helmholtz plance   |
| PB     | Prussian Blue  |
| PEIS   | Potentiodynamic electrochemical impedance spectroscopy                     |
| RE     | Reference electrode  |
| RJ12   | 3-(4-((5-iodopyridin-2-yl)ethynyl)phenyl)thiol                             |
| SAM    | Self-assembled monolayer   |
| SEM    | Scanning electron microscopy   |
| SKN    | Scanning Kelvin Nanoprobe  |
| UV     | Ultraviolet  |
| WE     | Working electrode  |

## VII. LIST OF ILLUSTRATIONS

---

### 2. BACKGROUND OF ELECTROCHEMISTRY AND SURFACE IMAGING TECHNIQUES

---

|  |    |
|--|----|
| Figure 1 – Alessandro Volta and Volta’s artificial electrical organ.   | 5  |
| Figure 2 – Schematic diagram of (a) Galvanic and (b) electrolytic cells.   | 7  |
| Figure 3 – Electron transfer at an inert metallic electrode. The potential applied to the electrode alters the highest occupied electronic energy level, EF, facilitating (a) reduction or (b) oxidation   | 8  |
| Figure 4 – Apparatus for a three-electrode cell.   | 10 |
| Figure 5 – Standard hydrogen and silver-silver chloride electrode  | 14 |
| Figure 6 – The Helmholtz model of the electrical double layer  | 19 |
| Figure 7 – The Gouy-Chapman model of the electrical double layer   | 19 |
| Figure 8 – The Stern model of the electrical double layer  | 20 |
| Figure 9 – The Grahame model of the electrical double layer  | 21 |
| Figure 10 – The Bockris, Devanathan and Muller model of the electrical double layer  | 22 |
| Figure 11 – Scheme of electron transfer at the electrode surface   | 23 |
| Figure 12 – Diffusion field at a microdisc   | 29 |
| Figure 13 – Variation of current with time according to the Cottrell equation  | 32 |
| Figure 14 – Conc. profiles for several times after the start a Cottrell experiment   | 38 |
| Figure 15 – Definition of the diffusion layer $\delta$   | 39 |
| Figure 16 – Potential time excitation signal in cyclic voltammetric experiment   | 47 |
| Figure 17 – Typical cyclic voltammogram for a macroelectrode at a reversible reaction. (1mM $\text{Ru}(\text{NH}_3)_6^{3+}$ + 0.1M $\text{KNO}_3$ WE electrode - Gold (d=3mm), counter electrode - Pt electrode, Reference electrode – Ag/AgCl, 3.5M KCl, scan rate – $0.15 \text{ Vs}^{-1}$ ) | 48 |

|  |    |
|--|----|
| Figure 18 – Typical cyclic voltammogram for a microelectrode at a reversible reaction. (1mM $\text{Ru}(\text{NH}_3)_6^{3+}$ + 0.1M $\text{KNO}_3$ ; WE electrode – Gold MEA (a =12.5 $\mu\text{m}$ , Z=319 MEs ), counter electrode - Pt electrode, Reference electrode – Ag/AgCl, 3.5M KCl, scan rate – 0.10 $\text{Vs}^{-1}$ ) | 50 |
| Figure 19 – Three electrode arrangement  | 51 |
| Figure 20 – Potential step to obtain a diffusion-limited current of the electroactive species  | 52 |
| Figure 21 – Phasor diagram for voltage and current   | 54 |
| Figure 22 – impedance planar vector in rectangular   | 56 |
| Figure 23 – Illustration of the most common microelectrode geometries, and their diffusion fields  | 61 |
| Figure 24 – Evolution of current with time on applying a potential step at an electrode  | 63 |
| Figure 25 – Microelectrode arrays at a) hexagonal, b) square and c) random pattern   | 65 |
| Figure 26 – The typical "honeycomb" hexagonal arrangement made by bees   | 66 |
| Figure 27 – Illustration of a) inlaid and b) recessed microdisc  | 68 |
| Figure 28 – Diagram of the 4 categories of diffusion profile at microelectrode arrays  | 71 |
| Figure 29 – Dependence of the diffusion profile on experiment time   | 73 |
| Figure 30 – Scheme of the operation mode of Scanning Electron Microscope   | 74 |
| Figure 31 – Hitachi S2400 SEM in the clean room (Engineering Dept.)  | 75 |
| Figure 32 – Schematic diagram of an interferometer with Mirau objective  | 77 |
| Figure 33 - The famous Scottish scientist William Thompson, later to be given the title of Lord Kelvin.  | 78 |
| Figure 34 – Scanning Kelvin Nanoprobe in use at University of Durham   | 80 |

|  |    |
|--|----|
| Figure 35 – Systems level diagram of the scanning Kelvin nanoprobe | 81 |
| Figure 36 – Simple diagram of AFM operation                        | 83 |
| Figure 37 – Molecular vibrations modes induced by infrared beam    | 84 |

### **3. CONICAL RECESSED GOLD MICROELECTRODE ARRAYS PRODUCED DURING PHOTOLITHOGRAPHIC METHODS: CHARACTERISATION AND CAUSES**

---

|  |     |
|--|-----|
| Figure 1 – Distribution of microelectrodes in order to avoid diffusional overlap   | 93  |
| Figure 2 – Microelectrode arrays at hexagonal pattern  | 94  |
| Figure 3 – Scheme of the conical recessed microelectrode arrays microfabrication by photolithography   | 96  |
| Figure 4 – Structure of gold microelectrode array constructed by photolithography  | 98  |
| Figure 5 – Geometry of conical recessed microelectrode   | 99  |
| Figure 6 – SEM images of (a,b) a conical recessed microelectrode (CRME) of $a = 45\mu\text{m}$ and $\alpha = 160$ degrees and (c,d) an overview of the conical recessed microelectrode array (CRMEA) | 103 |
| Figure 7 – (a) Zygo White light interferometer image of a $45\mu\text{m}$ radius recessed microelectrode and (b) showing the measured angle and diameter   | 104 |
| Figure 8 – Difference of Volta energies ( $-e\psi$ ) of gold (Au) and the photoresist (Phr)  | 106 |
| Figure 9 – Scanning Kelvin nanoprobe images of a microelectrode with a radius of $45\mu\text{m}$ showing the gradient contact potential differences  | 109 |
| Figure 10 – General View of the glass mask and smooth transition between light and dark at the edges in the mask.  | 110 |

|  |     |
|--|-----|
| Figure 11 – Photoresist reflowing process at 110°C   | 111 |
| Figure 12 – Variation of the normalised current against the height of the side wall L  | 114 |
| Figure 13 – Cyclic voltammograms using MEA 3 ( $a = 12 \mu\text{m}$ ) at different scan rates (5–50 mVs <sup>-1</sup> ) in the presence of the probe molecule – K <sub>3</sub> Fe(CN) <sub>6</sub> at 0.01M in 0.1M KNO <sub>3</sub> | 115 |
| Figure 14 – Cyclic voltammograms using using all CRMEAs at 5 mVs <sup>-1</sup> in the presence of the probe molecule – K <sub>3</sub> Fe(CN) <sub>6</sub> at 0.01M in 0.1M KNO <sub>3</sub>  | 115 |
| Figure 15 – Chronoamperometric response for different CRMEAs in the presence of the probe molecule – K <sub>3</sub> Fe(CN) <sub>6</sub> at 0.01M in 0.1M KNO <sub>3</sub>  | 116 |
| Figure 16 – Variation of the normalised current for different equations with variation of microelectrode radius  | 117 |
| Figure 17 – Variation of the normalised current for different equations with variation of L/a ratio  | 117 |
| Figure 18 – Comparison of the chronoamperometric response of experimental and simulated current using CRMEA 1  | 120 |
| Figure 19 – Comparison of the chronoamperometric response of experimental and simulated current using CRMEA 2  | 121 |
| Figure 20 – Comparison of the chronoamperometric response of experimental and simulated current using CRMEA 2  | 121 |
| Figure 21 – Graph used from Amatore's paper to prove the experimental results  | 123 |

#### **4. TOWARDS MULTIFUNCTIONAL MICROELECTRODE ARRAYS**

---

|   |     |
|---|-----|
| Figure 1 – Pre-Oxidation Process  | 132 |
| Figure 2 – Develop Procedure  | 135 |
| Figure 3 – A Zygo White light interferometer images of a 12.5 $\mu\text{m}$ radius recessed microelectrode showing the measured angle “ $\alpha$ ”, depth “L” and diameter “d” with (a) 0.283 $\mu\text{m}$ and (b) 0.565 $\mu\text{m}$ of lateral resolution | 138 |

---

|   |     |
|---|-----|
| Figure 4 – Scheme of a ‘grouped’ microelectrode arrays. The microelectrodes are situated in the middle of each circle   | 139 |
| Figure 5 – AFM scan of gold substrate (RMS Roughness: 0.786nm)  | 141 |
| Figure 6 – Cyclic voltammograms obtained using MMEA at 5 mVs <sup>-1</sup> in the presence of the anodic probe molecule – Ru(NH <sub>3</sub> )Cl <sub>3</sub> at 1mM in 0.1M KNO <sub>3</sub> , showing the voltage window for ME behaviour | 143 |
| Figure 7 – Chronoamperograms obtained using MMEA at 5 mVs <sup>-1</sup> in the presence of the anodic probe molecule – Ru(NH <sub>3</sub> )Cl <sub>3</sub> at 1mM in 0.1M KNO <sub>3</sub> .  | 144 |
| Figure 8 – Plot of normalised current ( $\Psi$ ) against potential using MMEA at 5 mVs <sup>-1</sup> in the presence of the anodic probe molecule – Ru(NH <sub>3</sub> )Cl <sub>3</sub> at 1mM in 0.1M KNO <sub>3</sub>                     | 145 |
| Figure 9 – Plot of number of microelectrodes against normalised current ( $\Psi$ ) using MMEA at 5 mVs <sup>-1</sup> in the presence of the anodic probe molecule – Ru(NH <sub>3</sub> )Cl <sub>3</sub> at 1mM in 0.1M KNO <sub>3</sub>     | 146 |

## 5. CHARACTERISATION OF SELF-ASSEMBLED MONOLAYERS OF ALKANETHIOLS AND MOLECULAR WIRES ON GOLD USING PEIS AND ELECTROCHEMICAL TECHNIQUES

---

|   |     |
|---|-----|
| Figure 1 – A schematic view of the self-assembling surfactant molecule in SAMs  | 154 |
| Figure 2 – Miss Agnes Pockels and Lord Rayleigh   | 154 |
| Figure 3 – Some frequently used molecules for self-assembled monolayers. a) n-alkanethiols, b) alkanedithiols, c) mercaptoalkanol, d) mercaptoalkane carboxylic acids, e) Oligophenylthiols, f) dialkyl disulfides, g) dialkyl sulfides                     | 158 |
| Figure 4 – Top view of the Structure of SAMs of alkanethiols on Au (111), where the gray circles represent gold atoms and the orange circles represent alkanethiolate adsorbates (the red circles highlight the hexagonal (3 × 3) R30° overlayer structure) | 160 |
| Figure 5 – Side view of the structure of SAMs of alkanethiols on Au (111), where the adsorbates are packed 5 Å apart with their alkyl chains tilted 30 degrees from the surface normal in a trans-extended conformation                                     | 161 |

|  |     |
|--|-----|
| Figure 6 - Figure illustrating the different types of structures for a monolayer film that self-assembles on gold  | 163 |
| Figure 7 – Structure of the thiol molecules used in this work (HPT, DDT, CSW564, RJ12)   | 165 |
| Figure 8 - Potentiostat-Galvanostat Model 283 (Princeton Applied Research)   | 167 |
| Figure 9 - Polycrystalline gold disk electrodes (Au(111)) provided from Bioanalytical Systems (area 0.020 cm <sup>2</sup> ) used as working electrode  | 167 |
| Figure 10 – CVs obtained for scans from -0.2 to 0.6V in 1mM K <sub>3</sub> Fe(CN) <sub>6</sub> + 0.1M KNO <sub>3</sub> and 0.1M KNO <sub>3</sub> for heptanethiol SAM electrode                          | 170 |
| Figure 11 – CVs obtained for scans from -0.2 to 0.6V in 1mM K <sub>3</sub> Fe(CN) <sub>6</sub> + 0.1M KNO <sub>3</sub> and 0.1M KNO <sub>3</sub> for CSW564 SAM electrode                                | 171 |
| Figure 12 – CVs obtained for scans from -0.2 to 0.6V in 1mM K <sub>3</sub> Fe(CN) <sub>6</sub> + 0.1M KNO <sub>3</sub> and 0.1M KNO <sub>3</sub> for (CSW564+DDT) SAM electrode                          | 171 |
| Figure 13 – CVs obtained for scans from -0.2 to 0.6V in 1mM K <sub>3</sub> Fe(CN) <sub>6</sub> + 0.1M KNO <sub>3</sub> and 0.1M KNO <sub>3</sub> for DDT SAM electrode                                   | 172 |
| Figure 14 – CVs obtained for scans from -0.2 to 0.6V in 1mM K <sub>3</sub> Fe(CN) <sub>6</sub> + 0.1M KNO <sub>3</sub> and 0.1M KNO <sub>3</sub> for RJ12 SAM electrode                                  | 172 |
| Figure 15 - CVs obtained for scans from -0.2 to 0.6V in 1mM K <sub>3</sub> Fe(CN) <sub>6</sub> + 0.1M KNO <sub>3</sub> for CSW564 SAM electrode and the peak current dependence to the sqrt of scan rate | 174 |
| Figure 16 - CVs obtained for scans from -0.2 to 0.6V in 1mM K <sub>3</sub> Fe(CN) <sub>6</sub> + 0.1M KNO <sub>3</sub> for (CSW564+DDT) SAM electrode  | 175 |
| Figure 17 – Nyquist plot for 1mM Fe(CN) <sub>6</sub> <sup>3-/4-</sup> in 0.1M KNO <sub>3</sub> solution using HPT SAM electrode. Frequency range: 1Hz to 100KHz  | 177 |
| Figure 18 – Nyquist plot for 1mM Fe(CN) <sub>6</sub> <sup>3-/4-</sup> in 0.1M KNO <sub>3</sub> solution using CSW564 SAM electrode. Frequency range: 1Hz to 100KHz.                                      | 178 |
| Figure 19 – Nyquist plot for 1mM Fe(CN) <sub>6</sub> <sup>3-/4-</sup> in 0.1M KNO <sub>3</sub> solution using (CSW564+DDT) SAM electrode. Frequency range: 1Hz to 100KHz                                 | 178 |



|   |     |
|---|-----|
| Figure 20 – Nyquist plot for 1mM $\text{Fe}(\text{CN})_6^{3-/4-}$ in 0.1M $\text{KNO}_3$ solution using DDT SAM electrode. Frequency range: 1Hz to 100KHz                                   | 179 |
| Figure 21 – Nyquist plot for 1mM $\text{Fe}(\text{CN})_6^{3-/4-}$ in 0.1M $\text{KNO}_3$ solution using RJ12 SAM electrode. Frequency range: 1Hz to 100KHz                                  | 179 |
| Figure 22 – Nyquist plot for 1mM $\text{Fe}(\text{CN})_6^{3-/4-}$ in 0.1M $\text{KNO}_3$ solution using bare electrode. Frequency range: 1Hz to 100KHz.                                     | 180 |
| Figure 23 – Model used for the analysis of EIS data   | 184 |
| Figure 24 – Scheme of the SAM with various defects  | 186 |
| Figure 25 – Simplification of the defects in the SAM.   | 187 |
| Figure 26 – Simplification of the defects in the SAM  | 187 |
| Figure 27 – Nyquist plots for 1mM $\text{Fe}(\text{CN})_6^{3-/4-}$ in 0.1M $\text{KNO}_3$ solution using DDT SAM electrode. Frequency range: 1Hz to 100KHz at different applied potentials  | 189 |
| Figure 28 – Nyquist plots for 1mM $\text{Fe}(\text{CN})_6^{3-/4-}$ in 0.1M $\text{KNO}_3$ solution using RJ12 SAM electrode. Frequency range: 1Hz to 100KHz at different applied potentials | 189 |
| Figure 29 – Variation of Capacitance of the SAM electrodes over a potential range   | 191 |
| Figure 30 – Variation of Capacitance of the SAM electrodes over a potential range   | 192 |

## 6. THE MYSTERY OF THE SHARP PEAKS – ELECTRON TRANSFER OR GOLD CYANISATION?

---

|   |     |
|---|-----|
| Figure 1 – Explanation of the experimental procedure used in this work.   | 205 |
| Figure 2 – Structure of the aurocyanide or dicyanoaurate(I) complex.  | 207 |
| Figure 3 – Cyclic voltammograms of DDT SAM on gold in 0.1 M $\text{KNO}_3$ . Scan rate: 0.01 to 2.7 $\text{Vs}^{-1}$ .  | 213 |
| Figure 4 – Cyclic voltammograms of RJ12 SAM on gold in 0.1 M $\text{KNO}_3$ . Scan rate: 0.01 to 2.7 $\text{Vs}^{-1}$ . | 214 |

---

|   |     |
|---|-----|
| Figure 5 – Scan rate dependence of the anodic peak current in cyclic voltammetry for RJ12 SAM electrode in 0.1M KNO <sub>3</sub> solution.                              | 215 |
| Figure 6 – Scan rate dependence of the cathodic peak current in cyclic voltammetry for RJ12 SAM electrode in 0.1M KNO <sub>3</sub> solution.                            | 215 |
| Figure 7 – Scan rate dependence of the anodic peak current in cyclic voltammetry for DDT SAM electrode in 0.1M KNO <sub>3</sub> solution.                               | 216 |
| Figure 8 – Scan rate dependence of the cathodic peak current in cyclic voltammetry for RJ12 SAM electrode in 0.1M KNO <sub>3</sub> solution.                            | 216 |
| Figure 9 – Plot of overpotential vs. log v for DDT SAM on gold (in 0.1M KNO <sub>3</sub> ).   | 223 |
| Figure 10 – Plot of overpotential vs. log v for RJ12 SAM on gold (in 0.1M KNO <sub>3</sub> ).   | 223 |
| Figure 11 – FTIR spectra at bare gold electrode and DDT SAM on gold electrode after CA at 2V.   | 226 |
| Figure 12 – Nyquist plots in 0.1M KNO <sub>3</sub> solution using DDT SAM modified electrode. Frequency range: 1Hz to 100KHz at different applied potentials            | 227 |
| Figure 13 – Nyquist plots in 0.1M KNO <sub>3</sub> solution using RJ12 SAM modified electrode. Frequency range: 1Hz to 100KHz at different applied potentials           | 228 |
| Figure 14 – Mott-Schottky plots using pinhole free DDT and RJ12 SAM in 1mM Fe(CN) <sub>6</sub> <sup>3-/4-</sup> and 0.1M KNO <sub>3</sub> solution. Frequency: 100 KHz. | 229 |
| Figure 15 – Mott-Schottky plots using DDT and RJ12 SAM after CA at 2V in 0.1M KNO <sub>3</sub> solution. Frequency: 100 KHz.  | 230 |

## **VIII. LIST OF TABLES**

---

### **2. BACKGROUND OF ELECTROCHEMISTRY AND SURFACE IMAGING TECHNIQUES**

Table 1 – Electron standard electrode potential for Ag/AgCl electrode at different concentrations of Cl<sup>-</sup> 12

Table 2 – Electron standard electrode potential for SCE electrode at different concentrations of Cl<sup>-</sup> 13

Table 3 – cyclic voltammetric behaviour of a macroelectrode for a reversible reaction 49

### **3. CONICAL RECESSED GOLD MICROELECTRODE ARRAYS PRODUCED DURING PHOTOLITHOGRAPHIC METHODS: CHARACTERISATION AND CAUSES**

Table 1 – Characteristics of fabricated CRMEA 99

Table 2 – Comparison between experimental and theoretical results 118

### **4. TOWARDS MULTIFUNCTIONAL MICROELECTRODE ARRAYS**

Table 1 – Procedure for the oxidation furnace. 133

Table 2 – Characteristics of MMEA and comparison between experimental and theoretical current obtained for Ru(NH<sub>3</sub>)Cl<sub>3</sub> at 1mM in 0.1M KNO<sub>3</sub> using CV and CA 142

### **5. CHARACTERISATION OF SELF-ASSEMBLED MONOLAYERS OF ALKANETHIOLS AND MOLECULAR WIRES ON GOLD USING PEIS AND ELECTROCHEMICAL TECHNIQUES**

Table 1 – Experimental and theoretical rate constants 184

# 1. Introduction

---

*“An Open Door to the Future”*

The electrical properties of organic molecules have attracted much attention due to the continuous search for new approaches for further miniaturization of electronic devices.

Gordon Moore have postulated that complexity of integrated circuits has approximately doubled every year since their introduction, and since the formulation of this law (Moore's Law) <sup>1</sup>, the IT industry served as a goal for the investigation.

However, in 2005, Gordon Moore also stated in an interview that the law cannot be sustained indefinitely, because in the near future, the research will reach the physical limits of miniaturization at atomic or molecular levels. <sup>2</sup>

Molecular electronic is one of the promising technologies which would be an alternative. The concept of molecular electronics is the use of single molecules or arrays, or layers of molecules for the fabrication of electronic components such as wires, switches, and storage elements.

The molecules can be designed and tailor-made by chemical synthesis. Their physical properties are tuneable by their structure. In particular, a very small size of the molecules makes them ideal to fabricate a high-density electronic device.

The purpose of the research presented in this thesis was the characterisation of electrode microarrays and conventional electrodes modified with molecular wires as platforms for biosensors. This work provides solid basis for future studies in this field, showing valuable information about fabrication of microelectrode arrays patterning in different designs on silicon wafers by photolithography in order to promote multi-analyte sensing in a single microarray platform.

The formation and characterisation of thiol-based self-assembled monolayers on conventional-sized gold electrodes have been performed.

The charge transfer and self-assembly characteristics of novel molecular wires (fully conjugated molecules) which were synthesised at the Department of Chemistry were evaluated. This work will be very useful since it gives valuable information about the perfect conditions for deposition of thiol molecules on gold and its characterisation using electrochemistry. The electron transfer has also been studied in detail.

Although all experimental chapters contain an introduction, the second chapter gives an elucidation of the underlying electrochemical principles and techniques used, giving a good background of the concepts that were employed thorough the research, and can be a good source for future students who will continue this work.

The third chapter shows the fabrication process of gold microelectrode arrays. The devices characterisation is performed using electrochemistry and surface imaging techniques.

A new single microelectrode array platform divided into groups of microelectrodes that can be calibrated itself by comparison of normalised currents with the numbers of microelectrodes in the groups of arrays was fabricated and characterised successfully in the fourth chapter.

In the fifth chapter, the charge transfer and self-assembly characteristics of novel molecular wires assembled on flat gold electrodes are evaluated and the behaviour of these wires is compared with heptanethiol and dodecanethiol SAMs.

The sixth chapter gives the description of an intense investigation that has been carried out in order to identify the origin of the sharp peaks found by accident in the research of the fifth chapter. Intensively investigation has suggested that the formation of Prussian blue film and gold cyanisation may happen at the same time, competing for the gold vacancies created by the thiol desorption.

The seventh chapter states the conclusion of this research and the ongoing research is described.

## **1.1. REFERENCES**

---

---

1 – G. Moore, *Electronics Magazine*, 38 (1965) 114 – 117.

2 – [Http://www.techworld.com/opsys/news/index.cfm?newsid=3477](http://www.techworld.com/opsys/news/index.cfm?newsid=3477), accessed in 20/05/2009

## 2. BACKGROUND OF ELECTROCHEMISTRY AND SURFACE IMAGING TECHNIQUES

---

*“I am young enough to remember doing electrochemistry in my Chemistry degree at the University of London. I scrupulously avoided attempting the electrochemical questions in my final examination. I just could not work out what it was all about and the sign conventions quite defeated me.”*

Brynn Hibbert,

In “Introduction of electrochemistry”<sup>1</sup>

### 2.1. ABSTRACT

---

The sentence of Brynn Hibbert gives a perfect picture about working in electrochemistry. The definitions and the different conventions always struggle the apprentices of this area of chemistry. It takes time to learn properly the basic concepts, and sometimes, all the work done before is just useless.

The goal of this chapter is to explain the concepts and the techniques in detail that were employed thorough my research, and also to be a good source in order to help future students in my group.

## 2.2. HISTORY OF ELECTROCHEMISTRY AND BASIC DEFINITIONS

---

Electricity is a form of energy, and when it passes through matter it may be converted into other forms. The study of electrochemistry is mainly concerned with the interconnection between electrical and chemical forms of energy. <sup>1</sup>

Electrochemistry is a large and important area of physical chemistry, but, it is difficult to define precisely the limits of this area because has influence in so many areas in chemistry, biology and physics.



**Figure 1** – *Alessandro Volta and Volta's artificial electrical organ.*

The origins of electrochemistry are short and date back to the beginning of nineteenth century, when Alessandro Volta reported the results of his recent studies to the Royal Society of London, which described the “Voltaic piles”



(artificial electrical organ),<sup>2</sup> which was the first electrochemical cell, and Nicholson and Carlisle reported in Nicholson's Journal (The world's first independent scientific journal) their results that basically described the process to use electricity to decompose water to hydrogen and oxygen (the first step for fuel cells).

The first quantitative studies of electrolysis were carried out by Faraday in 1833, and it is he who first used the nomenclature which is still employed today.

In the first half of twentieth century, there were no significant advances, perhaps due the lack of good apparatus and instruments, but from the 1950's to now, the subject has been developing on several levels, such as experimental, theoretical and in applications, particularly on the electroanalysis, which have led to a substantial increase in its popularity. The main examples are development of microelectrodes, design of tailored interfaces and molecular monolayers, synthesis of ionophores and receptors containing cavities of molecular size, the development of ultratrace voltammetric techniques, high-resolution scanning probe microscopies, and the microfabrication of molecular devices.

An electrochemical reaction is a reaction involving the transfer of charge. The redox reaction is a type of this reaction and involves transfer of electrons from one chemical species to another. These can occur in solution (homogeneous reactions) or on the electrode surface (heterogeneous reactions). However, two or more charge transfers at opposite directions must happen in order to ensure electroneutrality.

This process is ruled by Faraday's law, which states that the amount of chemical change produced is proportional of the total amount of electrical

charge passed through the cell, and the current generated from that type of reactions is called Faradaic current.

There are two different types of redox reactions (half-reactions) which are distinguished by the changes of oxidation state of the element which occurs in them. The compound that loses electrons is said to be oxidized (oxidation reaction), the one that gain electrons is said to be reduced (reduction process).

When the redox reaction occurs spontaneously, the electrochemical cell is called galvanic cell (Figure 2.a). Otherwise, if it requires a supply of electrical energy in the external circuit in order to cause reactions to occur at the electrodes, the electrochemical cell is called electrolytic cell (Figure 2.b)

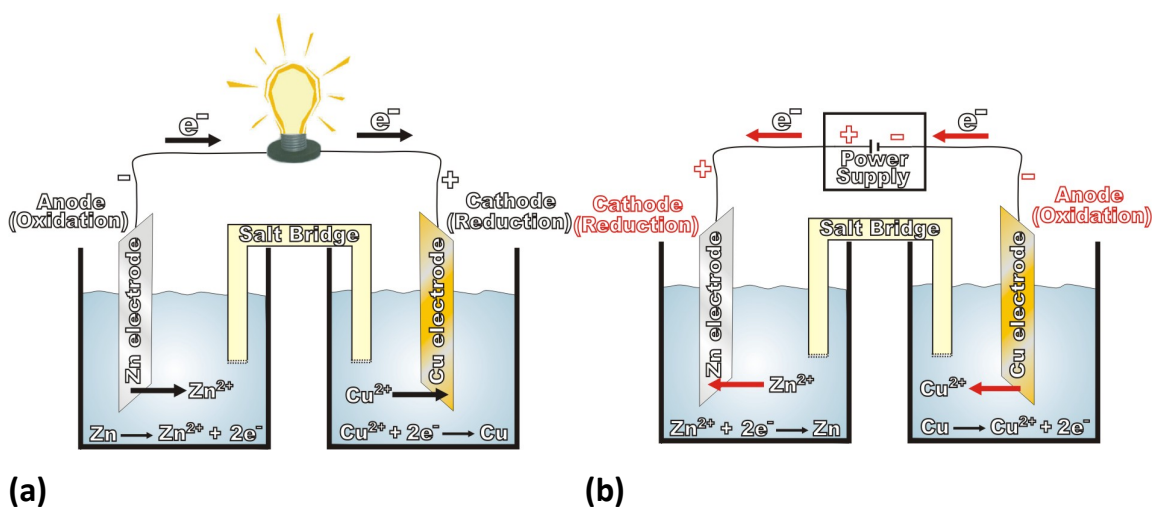


**Figure 2** – Schematic diagram of **(a)** Galvanic and **(b)** electrolytic cells.

In the case of homogeneous charge-transfer reaction, the reactants are in the same phase, whereas in the heterogeneous ones, the reactants are in two or more phases, and normally, the reactions take place on the solid electrode surface (electrode reactions), immersed in a conducting phase (electrolyte),

usually a solution, and are linked through the solution and through external wires to form an electrical circuit. If the electrolyte is different for each electrode, then the two compartments may be joined by a salt bridge (Figure 2).

Most of the charge-transfer processes can be represented in the simplest case of oxidized species, O, and reduced species, R, both soluble in solution, by



Where O receives n electrons in order to be transformed into R. The electrons in the electrode (a conductor) have a maximum energy which is distributed around the Fermi level.

For a reduction, the electrons in the electrode must have a minimum energy in order to be transferred from the electrode to the receptor orbital in O. For oxidation, the energy of the electrons in the donor orbital of R must be equal to or higher than the electrode's Fermi level in order to be transferred to the electrode.

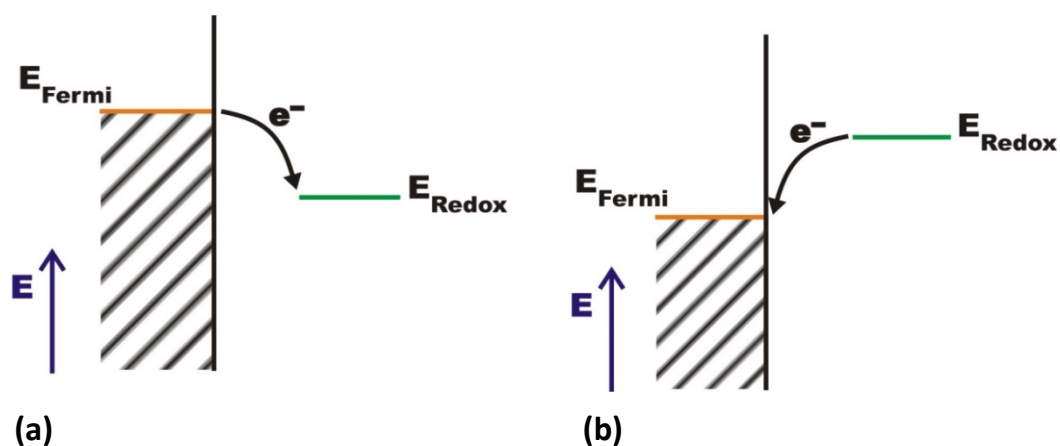


**Figure 3** – *Electron transfer at an inert metallic electrode. The potential applied to the electrode alters the highest occupied electronic energy level,  $E_F$ , facilitating (a) reduction or (b) oxidation.*

## 2.3. ELECTRODES

---

There are different types of electrodes which are widely encountered in electrochemistry and electroanalysis. The International Union of Pure and Applied Chemistry (IUPAC) established different classifications. The class 0 is referred to inert metals used in oxidation-reduction electrolytic cells. These materials exchange electrons reversibly with the electrolyte components and are not subject to oxidation or corrosion themselves, i.e., “ideally” polarisable electrodes.

Another type is class 1 that are reversible metal/metal ion (ion exchanging metals bathed in electrolytes containing their own ions), for example  $\text{Ag}/\text{Ag}^+$ .

Class 2 is for reversible metal/metal ion with saturated salt of the metal ion and excess anion  $\text{X}^-$ , for example  $\text{Ag}/\text{AgX}/\text{X}^-$ .

Finally, class 3 is for either reversible metal/metal salt or soluble complex/second metal salt or complex and excess second cation, for example  $\text{Pb}/\text{Pboxalate}/\text{Caoxalate}/\text{Ca}^{2+}$  or  $\text{Hg}/\text{HgEDTA}_2/\text{CaEDTA}^{2-}/\text{Ca}^{2+}$ .<sup>3</sup>

Generally, in electrochemical research, and in most electroanalytical experiments, it is the electrode process at one electrode, the working or indicator electrode, which is the prime electrode because it responds to the target analyte. Usually, the potential of this electrode is controlled with respect to a reference electrode (an ideal non-polarisable electrode) and the current passes between the working electrode and an auxiliary electrode (also called counter electrode).

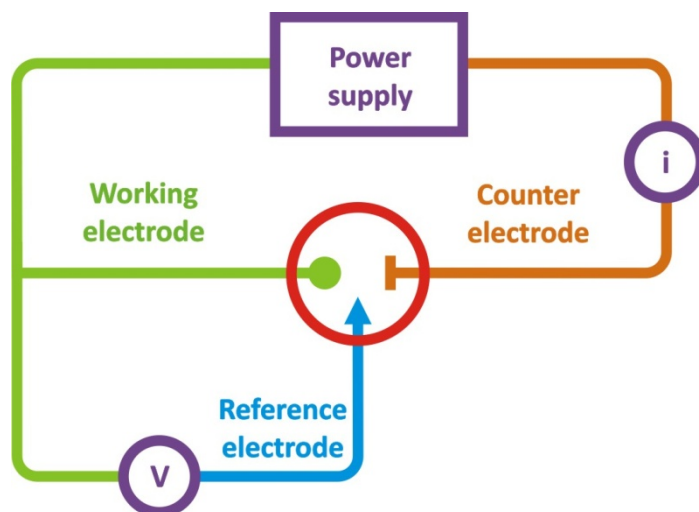


**Figure 4** – Apparatus for a three-electrode cell.

### 2.3.1. Reference electrode

The reference electrode is necessary to provide a stable and a reproducible potential against the working electrode, i.e., it is designed to produce the same potential whatever the solution. This type of electrode is composed by four distinct parts, an inert outer body, a reference element, an electrolyte(s) and a liquid junction(s). The body acts as a reservoir for the reference electrolyte and provides protection for the reference element.

A single electrode potential cannot be studied in isolation, and then it must be compared with another electrode. For this reason single electrode potentials are expressed on an arbitrary scale, and by an internationally accepted convention this is fixed by putting the standard electrode potential of the standard hydrogen electrode as equal to zero at all temperatures.

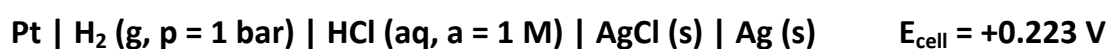
The standard hydrogen electrode (SHE) is an example of the reference electrode. It consists of an inert metal, platinized platinum electrode which is in contact with hydrogen gas (at 1 atm pressure) and it is immersed in a solution of hydrochloric acid (activity=1). Although it is extremely accurate, it is not convenient to use on a day-a-day basis, due to impracticality of maintaining platinum electrode activity, and also due to the dangers associated with hydrogen gas. Therefore substitutes have been developed.

The silver-silver chloride electrode (Ag/AgCl) is most commonly used due to its ease of manufacture and its superior temperature range, (usable even above 130°C).

The silver wire is oxidized in the presence of chloride ions, and a film of insoluble silver chloride is formed on the outside of the metal. When immersed in a solution of chloride ions, a potential is established with the half-cell reaction,



The standard electrode potential of the Ag/AgCl electrode is measured using the cell:



However, the standard electrode potential depends of the concentration of chloride ions in the filling solution. The Nernst equation is used to predict the potential at different concentrations:

$$E^{\text{Cl}^- / \text{AgCl} / \text{Ag}} = E^{0, \text{Cl}^- / \text{AgCl} / \text{Ag}} - \frac{RT}{F} \ln(a_{\text{Cl}^-}) \quad \text{Eq. (1)}$$

**Table 1** – Electron standard electrode potential for Ag/AgCl electrode at different concentrations of Cl<sup>-</sup>.

| <i>Half cell</i>                    | <i>Conditions</i>                | <i>E<sup>0</sup> vs. NHE (V)</i> |
|-------------------------------------|----------------------------------|----------------------------------|
| Cl <sup>-</sup>   AgCl (s)   Ag (s) | a <sub>Cl<sup>-</sup></sub> = 1M | + 0.223                          |
|                                     | KCl (0.1M)                       | + 0.289                          |
|                                     | KCl (1M)                         | + 0.237                          |
|                                     | KCl (3M)                         | + 0.209                          |
|                                     | KCl (3.5M)                       | + 0.205                          |
|                                     | KCl (sat.)                       | + 0.199                          |

Each vertical line in the above 'cell diagram' refers to a phase boundary. (If salt bridges were used, they would be represented by a double vertical line ||.) The convention is followed as introduced by IUPAC, in which the value reported relates to the potential (E) of the right hand electrode to that of the left hand electrode. Therefore, for the above cell

$$+0.223 \text{ V} = E_{\text{Ag}} - E_{\text{Pt}} \quad \text{Eq. (2)}$$

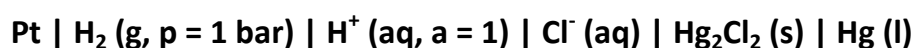
In this case, the potential of a Ag/AgCl (a<sub>Cl<sup>-</sup></sub> = 1) electrode relative to a standard hydrogen electrode is +0.223 V, so if measurements are made using

this electrode rather than a hydrogen electrode, this value must be subtracted to the measured voltage in order to get standard potential.

The calomel electrode (SCE) is also a reference electrode and is similar to silver-silver chloride one, with mercury (l) replacing silver. The half-reaction which leads to a potential is,



The standard electrode potential of the SCE electrode is measured using the cell:



The standard electrode potential also depends of the concentration of chloride ions in the filling solution.

**Table 2** – Electron standard electrode potential for SCE electrode at different concentrations of Cl<sup>-</sup>.

| <i>Half cell</i>  | <i>Conditions</i>                | <i>E<sup>0</sup> vs. NHE (V)</i> |
|---|----------------------------------|----------------------------------|
|   | a <sub>Cl<sup>-</sup></sub> = 1M | + 0.268                          |
|   | KCl (0.1M)                       | + 0.337                          |
| Cl <sup>-</sup> (aq)   Hg <sub>2</sub> Cl <sub>2</sub> (s)   Hg (l) | KCl (1M)                         | + 0.281                          |
|   | KCl (3.5M)                       | + 0.250                          |
|   | KCl (sat.)                       | + 0.244                          |



However, recently calomel has fallen into disfavor because of its toxicity.

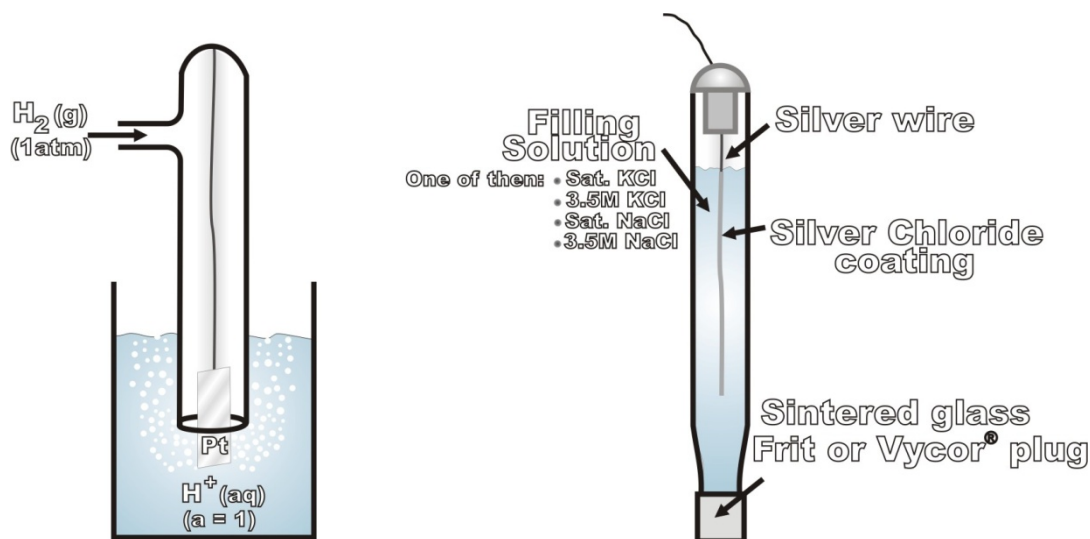


Figure 5 – Standard hydrogen and silver-silver chloride electrode.

### 2.3.2. Working electrode

The working electrode is where the electrode reactions under study take place. Thus, the electrode material that should be chosen depends of the redox behavior of the target analyte, the background current over the potential region required for the experiments, its potential window, solubility in the electrolyte, electrical conductivity, surface reproducibility, mechanical properties, cost, availability and toxicity.

A range of materials have found application as working electrodes for electroanalysis. The most popular are those involving mercury, carbon and noble metals (platinum, gold and Silver).<sup>4</sup>

### **2.3.2.1. Mercury electrodes**

Mercury is a very attractive choice of electrode materials because it has a high hydrogen overvoltage that greatly extends the cathodic potential window (compared to solid electrode materials). However, due to its toxicity, Mercury is slowly being replaced by “environmental-friendly” solid electrode materials.

### **2.3.2.2. Solid electrodes**

The anodic limit potential range of mercury electrodes has precluded their utility for monitoring oxidisable compounds. Accordingly, solid electrodes with extended anodic potential windows have attracted considerable analytical interest.<sup>4</sup>

#### ***a. Metals***

While a wide choice of noble metals is available, platinum and gold are the most widely used metallic electrodes. Such electrodes offer very favourable electron-transfer kinetics, high conductivity (low background currents) and a large anodic potential range. In contrast, the low hydrogen overvoltage at these electrodes limits the cathodic potential window.

## ***b. Carbon***

The electrochemical reactions are normally slower at carbon than at metallic electrodes. The electron-transfer kinetics is dependent on structure and surface preparation.

Carbon has a high surface activity. Bonds with hydrogen, hydroxyl and carboxyl groups can be formed at the carbon surface. The presence of these groups signifies that the behaviour of these electrodes can be very pH-sensitive.

Various types of carbon are used as electrodes. These include glassy carbons, carbon fibers, carbon black, various forms of graphite, carbon paste and recently boron doped diamond (BDD) and nanotubes.<sup>5</sup>

The boron-doped diamond (BDD) is found to be particularly attractive for electrolysis and electroanalytical applications due to its outstanding properties, which are significantly different from those of other conventional electrodes. In addition to innate properties of diamond, such as high thermal conductivity, hardness and chemical inertness, the attractive features of conductive BDD include a wide electrochemical potential window in aqueous and non-aqueous media, very low capacitance and extreme electrochemical stability.<sup>6</sup>

These properties make BDD electrodes particularly suited for electrochemical reactions with compounds that have highly positive standard potentials and which cannot be detected or produced using classical electrode materials.<sup>7</sup>

Carbon nanotubes (CNT's) are tube-shaped materials, made of carbon, which have a diameter measuring on the nanometer scale, and have high electrical conductivity, high chemical stability, and extremely high mechanical strength and modulus.<sup>8</sup>

Carbon nanotubes can have many structures, with differing lengths, thickness, types of spiral, and number of layers. Although they are formed from essentially the same graphite sheet, their electrical characteristics differ depending on these variations, acting either as metals or semiconductors.<sup>9</sup>

### *c. Chemically modified electrodes*

Chemically modified electrodes (CME's) have attracted considerable interest over the past three decades. There is a vast review literature available on this subject, discussing the preparation, characterisation and electrochemical behaviour of CME's.<sup>10,11,12,13</sup>

These electrodes are often prepared by the modification of a conductive substrate to produce an electrode suited to a particular function, whose properties are different from those of the unmodified substrate.<sup>14</sup> Such properties can be, for example, to improve sensitivity, selectivity and stability to electrochemical devices. One practical example, reported by A. J. Bard and Larry R. Faulkner<sup>14</sup>, is the adsorption of  $\text{CN}^-$  ions on Pt electrode increases the hydrogen overpotential and therefore, extends the range of the potential window to more negative potentials.

## 2.4. ELECTRICAL DOUBLE LAYER

---

The electrical double layer is the array of charged particles and/or oriented dipoles that exists at every material interface.<sup>4</sup>

The distribution of the array depends on the electrode materials, i.e., its crystalline structure and exposed crystallographic face.

Various models have been postulated over a period of time, and consequently, new concepts have been introduced. It is interesting see the historical evolution of these models in order to understand the newest one – The Brockris, Denavathan and Muller model.

### 2.4.1. Helmholtz model (1879)

This was the first and the simplest model of the electrical double layer. Helmholtz considered the ordering of positive and negative charges in a rigid fashion on the two sides of the interface, giving rise to the designation of *double layer*. This model is comparable to the classic problem of a parallel-plate capacitor. One plate is on the surface electrode and the other is on the centres of these ions. The latter has been called Helmholtz plane.<sup>5</sup>

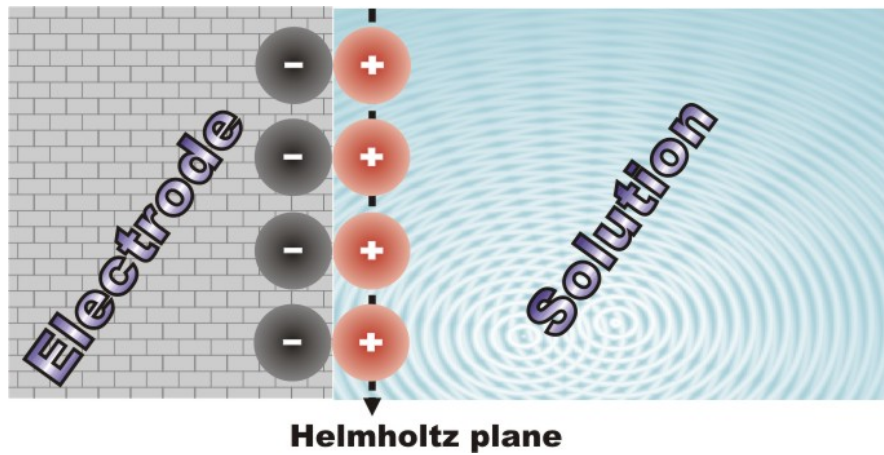


Figure 6 – The Helmholtz model of the electrical double layer.

### 2.4.2. Gouy - Chapman model (1910-1913)

At the beginning of the twentieth century, Gouy and Chapman independently developed a double layer model in which they considered that the applied potential and electrolyte concentration both influenced the value of the double layer capacity. Therefore, the double layer would not be compact as in Helmholtz's description but of variable thickness, the ions being free to move – *diffuse double layer*.<sup>5</sup> This model assumes that the ions are infinitely small and can get infinitely close to the surface of the electrode.

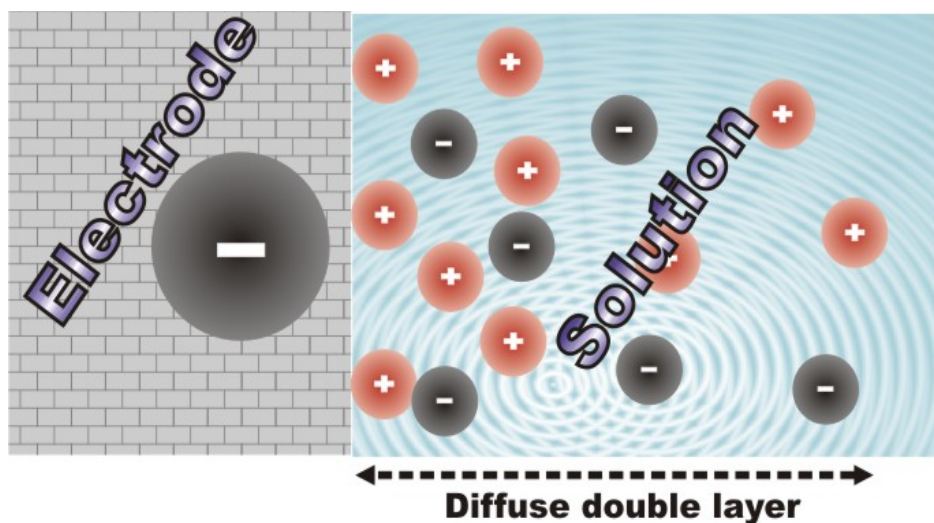


Figure 7 – The Gouy-Chapman model of the electrical double layer.

### 2.4.3. Stern model (1924)

Stern combined the Helmholtz model with the Gouy-Chapman model. Stern considered that the double layer was formed by a compact layer of ions next to the electrode followed by a diffuse layer extending into bulk solution. This zone is called *outer Helmholtz plane (OHP)*.

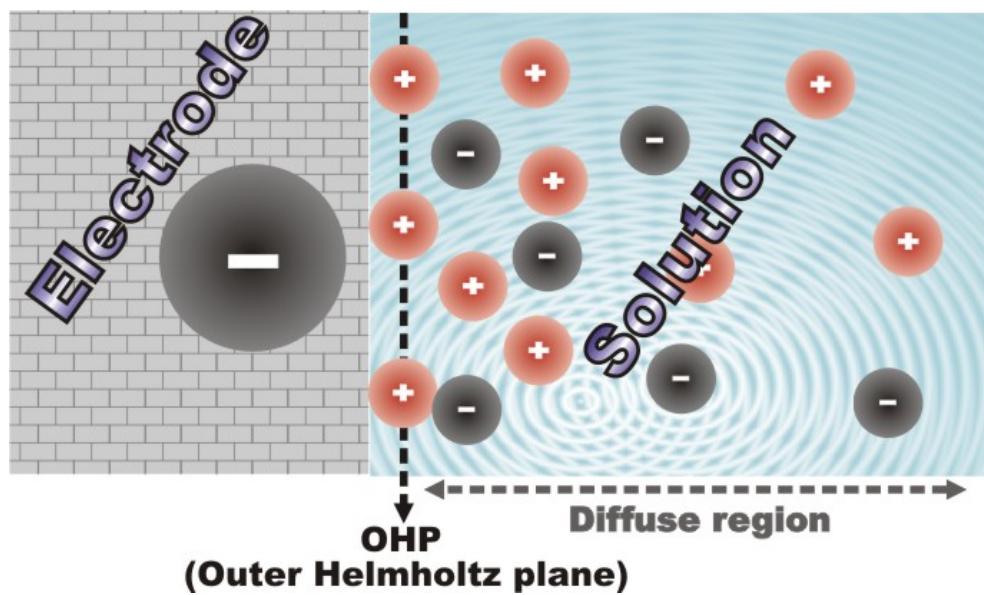


Figure 8 – The Stern model of the electrical double layer.

#### 2.4.4. Grahame model (1947)

Grahame developed the Stern model and the difference between them is the existence of specific adsorption. The ions lose their solvation, and approaching closer to the electrode surface.

The *inner Helmholtz plane (IHP)* passes through the centres of these ions, and the outer Helmholtz plane (OHP) passes through to the centres of the solvated and non-specifically adsorbed ions.

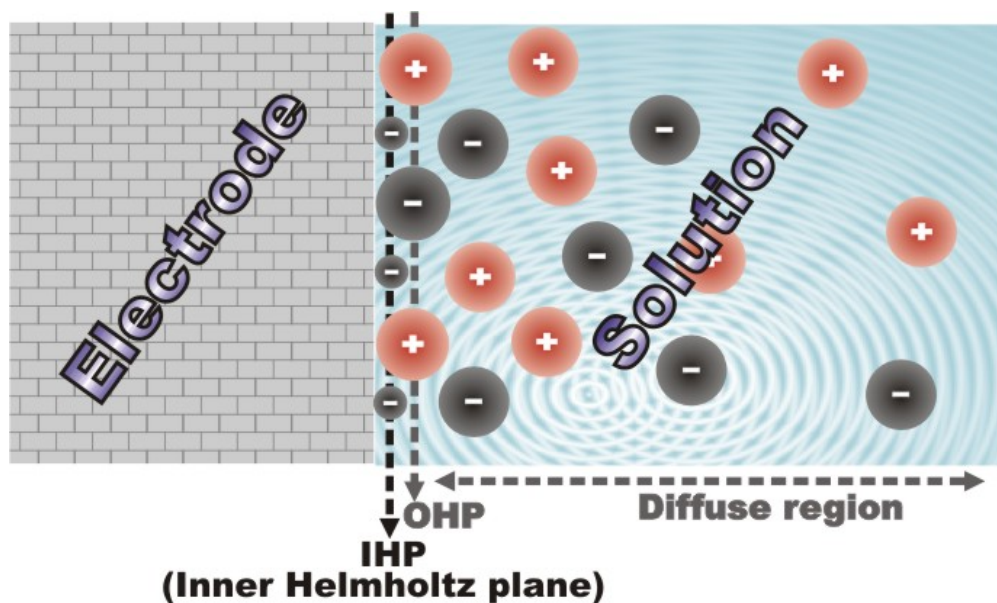


Figure 9 – The Grahame model of the electrical double layer.



### 2.4.5. Bockris, Devanathan and Muller model (1963)

This model has taken into account the physical nature of the interfacial region. Bockris, Devanathan and Muller proposed a model that included the influence of the solvent molecules near the interface.

The dipoles of these molecules would have a fixed alignment because of the charge in the electrode.

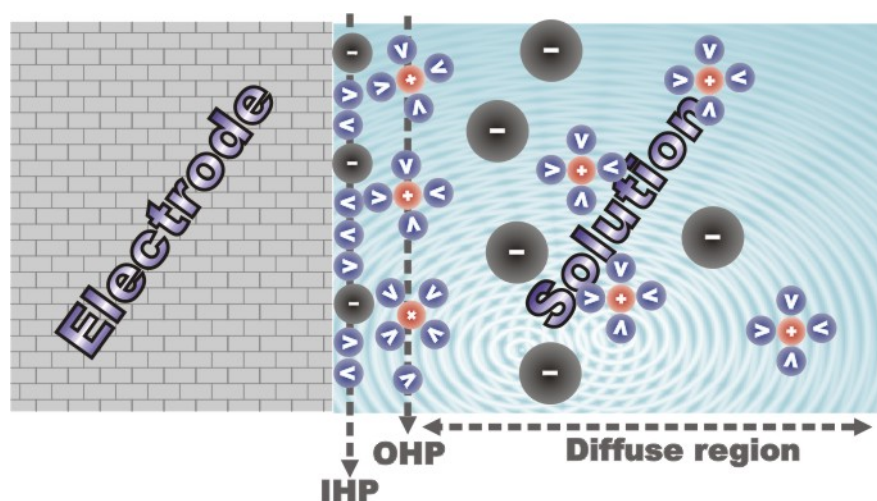


**Figure 10** – *The Bockris, Devanathan and Muller model of the electrical double layer.*

## 2.5. TRANSPORT PROCESSES

The pathway of the reaction electrode takes place in a sequence that involves several steps and its rate is determined by the slowest step in the sequence.

The rate of the reaction electrode is dependent either the transport of reactants to, or products from, the electrode surface (mass transport) or the rate of the heterogeneous electron transfer (electrode kinetics). The mechanism of the steps is shown on the following figure (Figure 11).

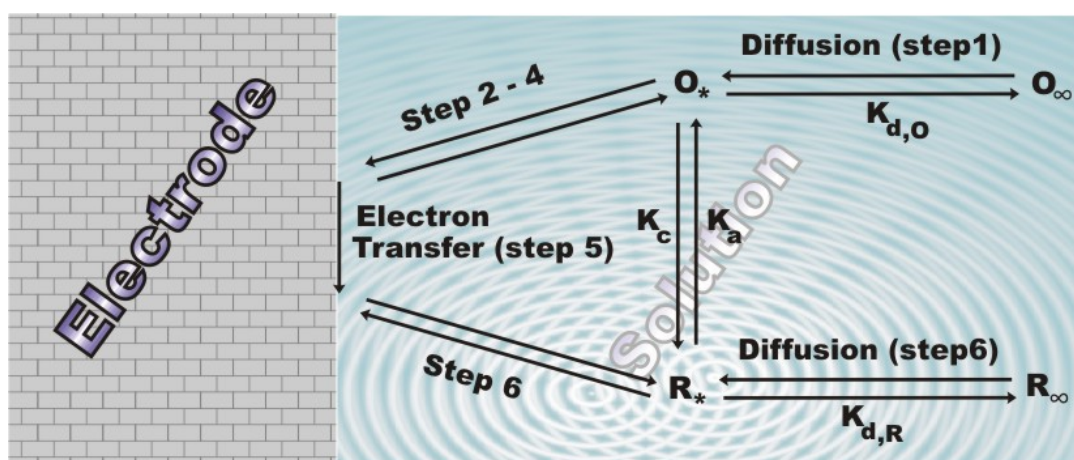


**Figure 11** – Scheme of electron transfer at the electrode surface.

First of all, the reactants have to reach the electrode surface (step 1). When the species reach the surface, several steps occur, such as rearrangement of the ionic atmosphere (step 2), reorientation of the solvent dipoles (step 3),

alteration in the distances between the central ion and the ligands (step 4). Such steps (2, 3 and 4) are as a type of pre-equilibrium before the electron transfer (step 5). After this step, there is relaxation in the inverse sense (step 6).<sup>5</sup>

Simple reactions involve only mass transport of the electroactive species to the electrode surface, the electron-transfer across the interface (electrical double layer), and the transport of the product back to the bulk solution.

When the overall reaction is controlled solely by the rate at which the electroactive species reach the surface, the mass transport is limited. Such reactions are called nernstian or reversible.

The net rate of the electrode reaction,  $v$ , is then governed totally by the flux ( $J$ ) at which the electroactive species is brought to the surface by mass transport (for oxidation),

$$J(x, t) = -\frac{i}{nFA} \quad \text{Eq. (3)}$$

Where:

$J(x, t)$  – Flux ( $\text{mol cm}^{-2} \text{s}^{-1}$ )

$i$  - Current (A)

$n$  – Number of electrons oxidized or reduced.

$F$  - Faraday constant (C/mol)

$A$  – Electrode area ( $\text{cm}^2$ )

The flux ( $J$ ) is a general for the rate of mass transport at a fixed point and is defined as the number of molecules penetrating a unit area of an imaginary plane in a unit of time.

This transport of the electroactive species from the bulk solution to the electrode surface can occur due to the influence of three different situations, such as diffusion, convection and migration.

Movement due to convection occurs when there is thermal and/or density gradients within the solution (natural convection), and under the effect of external forces, such as gas bubbling through solution, pumping or stirring.

Migration is a movement of charged particles along an electric field, and diffusion is the spontaneous movement under the influence of concentration gradient of electroactive species. Whilst diffusion occurs for all species, migration effects affect charged species, owing to existence of dipoles, or induced dipoles in neutral species.

This flux to the electrode is described mathematically by a differential equation (Nernst-Planck equation). Simplifying just for one dimension (along x-axis):

$$J(x, t) = -D \frac{\partial C(x, t)}{\partial x} - \frac{ZFDC_{\infty}}{RT} \frac{\partial E(x, t)}{\partial x} + C(x, t)V(x, t) \quad \text{Eq. (4)}$$

Where:

$J(x,t)$  – Flux ( $\text{mol cm}^{-2} \text{s}^{-1}$ )

$D$  - Diffusion coefficient ( $\text{cm}^2 \text{s}^{-1}$ )

$\frac{\partial C(x,t)}{\partial x}$  - Concentration gradient (at distance  $x$  and time  $t$ )

$Z$  – Charge of the electroactive specie

$F$  - Faraday constant (C/mol)

$C_\infty$  - Bulk concentration of the electroactive specie ( $\text{mol/cm}^3$ )

$R$  – Gas constant ( $8.314 \text{ J mol}^{-1} \text{ K}^{-1}$ )

$T$  - Temperature (K)

$\frac{\partial E(x,t)}{\partial x}$  - Potential gradient (at distance  $x$  and time  $t$ )

$V(x,t)$  – Hydrodynamic velocity.

This equation is the sum of the each effect on the total flux.

$$J(x,t) = -D \frac{\partial C(x,t)}{\partial x} - \frac{ZFDC_\infty}{RT} \frac{\partial E(x,t)}{\partial x} + C(x,t)V(x,t) \quad \text{Eq. (5)}$$

The diagram illustrates the three components of the flux equation. A blue dashed box encloses the diffusion term, with a blue arrow pointing to the label "Diffusion". A green dashed box encloses the migration term, with a green arrow pointing to the label "Migration". A red dashed box encloses the convection term, with a red arrow pointing to the label "Convection".

As indicated by previous equation, the situation is quite complex when the three modes of mass transport occur simultaneously. However, it can be greatly simplified by suppressing the migration (addition of supporting electrolyte) and convection (use of a quiescent solution). Under these conditions, the movement of the electroactive species is limited by diffusion. The reaction occurring at the electrode surface generates a concentration gradient adjacent to the surface (within the electrical double layer) – Fick's first law.

The Fick's first law is expressed by:

$$J(x,t) = -D \frac{\partial C(x,t)}{\partial x} \quad \text{Eq. (6)}$$

Combination of equations 1 and 3 yields a general expression for the current response (for oxidation):

$$i = nFAD \frac{\partial C(x,t)}{\partial x} \quad \text{Eq. (7)}$$

The diffusional flux is also time dependent. Such dependence is described by Fick's second law:

$$\frac{\partial C(x,t)}{\partial t} = D \frac{\partial^2 C(x,t)}{\partial x^2} \quad \text{Eq. (8)}$$

For any coordinate system, the Fick's second law has the general form:

$$\frac{\partial C}{\partial t} = D \nabla^2 C \quad \text{Eq. (9)}$$

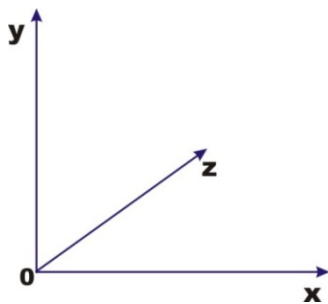
Where  $\nabla$  is called Laplace operator and vary for each coordinate system, as show next scheme:

**Coordinates**

**Laplace operator**

**Fick's 2<sup>nd</sup> law**

## Cartesian



**One direction**

( x-axis)

$$\nabla = \frac{\partial}{\partial x}$$

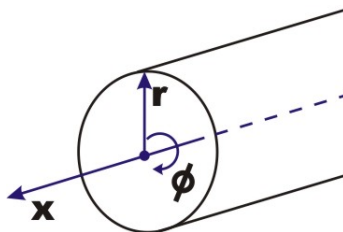
$$\frac{\partial C}{\partial t} = D \frac{\partial^2 C}{\partial x^2}$$

**Three directions**

$$\nabla = \frac{\partial}{\partial x} + \frac{\partial}{\partial y} + \frac{\partial}{\partial z}$$

$$\frac{\partial C}{\partial t} = D \left( \frac{\partial^2 C}{\partial x^2} + \frac{\partial^2 C}{\partial y^2} + \frac{\partial^2 C}{\partial z^2} \right)$$

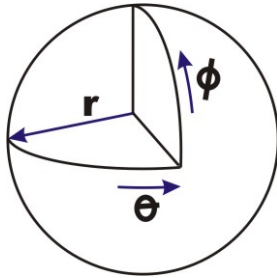
## Cylindrical



$$\nabla = \frac{\partial}{\partial r} + \frac{1}{r} \frac{\partial}{\partial \phi} + \frac{\partial}{\partial x}$$

$$\frac{\partial C}{\partial t} = D \left( \frac{\partial^2 C}{\partial r^2} + \frac{1}{r} \frac{\partial C}{\partial r} \right)$$

## Spherical



$$\nabla = \frac{\partial}{\partial r} + \frac{1}{r} \frac{\partial}{\partial \theta} + \frac{1}{r \sin \theta} \frac{\partial}{\partial \phi} \quad \frac{\partial C}{\partial t} = D \left( \frac{\partial^2 C}{\partial r^2} + \frac{2}{r} \frac{\partial C}{\partial r} \right)$$

For example, in three Cartesian directions ( $x,y,z$ ), the diffusional equation must be extended to describe transport in each direction (Figure 12),

$$\frac{\partial C}{\partial t} = D \frac{\partial^2 C(x,t)}{\partial x^2} + D \frac{\partial^2 C(y,t)}{\partial y^2} + D \frac{\partial^2 C(z,t)}{\partial z^2} \quad \text{Eq. (10)}$$

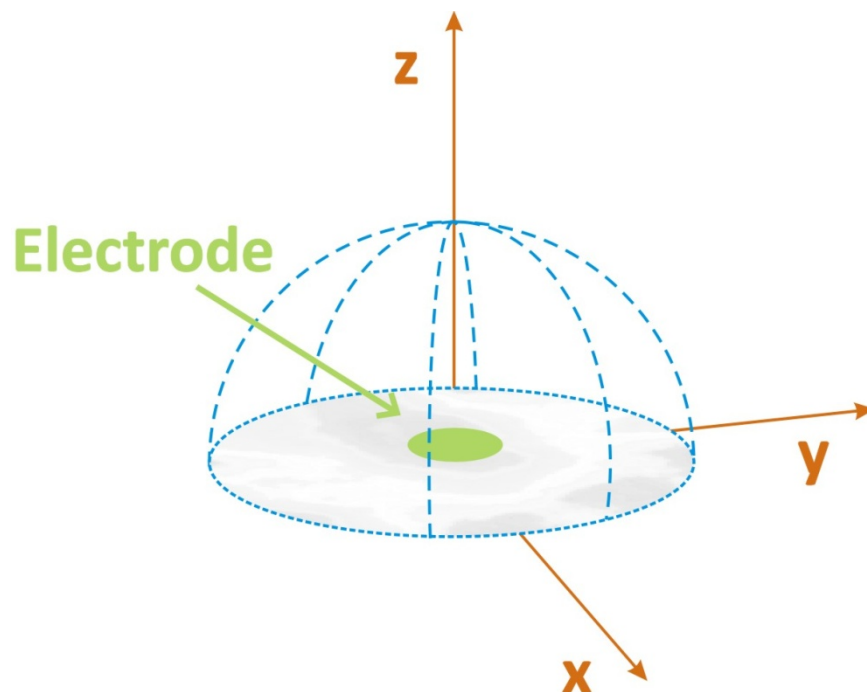


Figure 12 – Diffusion field at a microdisc.



In brief, Fick's laws describe the flux and the concentration of the electroactive species as functions of position and time.

The solution of this law gives the variation of flux, and consequently the diffusion-limited current, but it is necessary to define boundary conditions.

Chronoamperometry (CA) is the technique used in order to determine diffusion-limited current,  $I_d$ . The experiment consists in application of a potential step at  $t=0$  seconds to an electrode, in a solution containing either oxidized or reduced species, from a value where there is no electrode reaction to a value all electroactive species that reach the electrode surface react. The potential is controlled and the current response and its variation with time are registered.

### ***2.5.1. Diffusion at planar electrodes***

For planar electrode, the Fick's second law equation is Eq. (8). The boundary conditions that are necessary to solve this equation are:

$$t = 0 \text{ s} \quad \longrightarrow \quad C_0 = C_\infty$$

When there is no electrode reaction, there is no concentration gradient also.

$$t \geq 0 \text{ s} \quad \longrightarrow \quad \lim_{x \rightarrow \infty} C = C_\infty$$

There is no variation of concentration at large distance of the electrode surface.

$t > 0$  s  
 $x = 0$        $\longrightarrow$        $C_0 = 0$       There is no concentration of electroactive species in the electrode surface.

Using the Laplace transform and the boundary conditions, the diffusion-limited current equation is obtained:

$$I_d(t) = \frac{nFAD^{1/2} C_{\infty}}{(\pi t)^{1/2}} \quad \text{Eq. (11)}$$

Where:

$n$  - Number of electrons involved in ox/red.

$F$  - Faraday constant (C/mol)

$A$  - Electrode area (cm<sup>2</sup>)

$D$  - Diffusion coefficient (cm<sup>2</sup>/s)

$C_{\infty}$  - Bulk concentration (mol/cm<sup>3</sup>)

$t$  - Reaction time (s)

This equation is known as the Cottrell equation. As can see, the current decreases with  $t^{1/2}$ ,

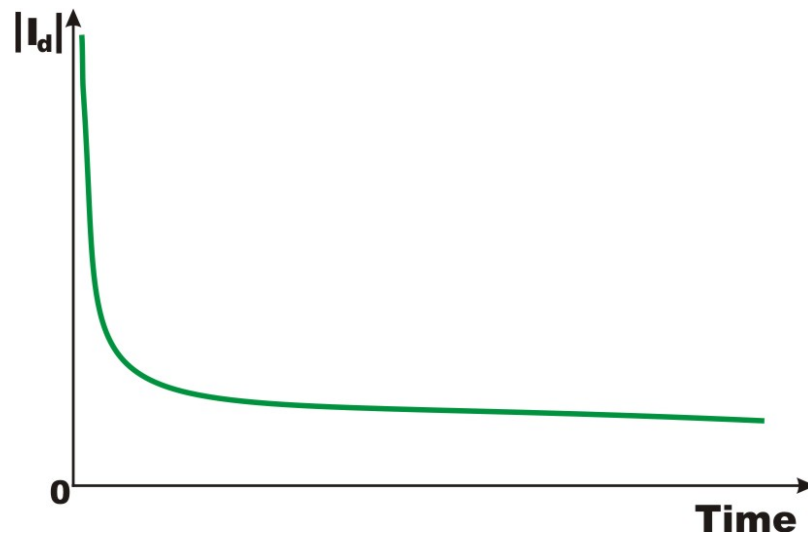


**Figure 13** – Variation of current with time according to the Cottrell equation.

For small values of  $t$ , there is a capacitive contribution to the current, due to double layer charging, that has to be subtracted.

### **2.5.2. Diffusion at spherical electrodes**

At a spherical electrode, the Fick's second law takes the following form:

$$\frac{\partial C}{\partial t} = D \left( \frac{\partial^2 C(r,t)}{\partial r^2} + \frac{2}{r} \frac{\partial C(r,t)}{\partial r} \right) \quad \text{Eq. (12)}$$

The boundary conditions are:

$t = 0s$   
 $r \geq r_0$ 
→
 $C_0 = C_\infty$ 
When there is no electrode reaction, there is no concentration gradient also.

$t \geq 0s$ 
→
 $\lim_{x \rightarrow \infty} C = C_\infty$ 
There is no variation of concentration at large distance of the electrode surface.


$t > 0s$   
 $r = r_0$ 
→
 $C_0 = 0$ 
There is no concentration of electroactive species in the electrode surface.

The equation for the variation of current with time is:


$$I_d(t) = nFADC_\infty \left[ \frac{1}{(\pi Dt)^{1/2}} + \frac{1}{r_0} \right] \quad \text{Eq. (13)}$$

This is the Cottrell equation plus a spherical term dependent on the reciprocal of the electrode radius,

$$I_d(t) = \frac{nFAD^{1/2} C_\infty}{(\pi t)^{1/2}} + \frac{nFADC_\infty}{r_0} \quad \text{Eq. (14)}$$



**Cottrell  
equation**



**Spherical  
correction**

For short times, diffusion at a sphere can be treated as linear diffusion (Cottrell's equation), because the second term is smaller enough than first term, which can be neglected.

$$I_d(t) = \frac{nFAD^{1/2} C_\infty}{(\pi t)^{1/2}} \quad \text{Eq. (15)}$$

For long times, the spherical term dominates, which represents a steady-state current. However, due to the effects of natural convection, this steady state is never reached at conventional-sized electrodes (macro-electrodes). It is possible to achieve a steady state at microelectrodes, because the smaller area is, the faster the steady state is achieved.

$$I_d(t) = \frac{nFADC_\infty}{r_0} \quad \text{Eq. (16)}$$

In the case of the times between the two limits, the full equation (Eq. (14)) has to be considered and the mass transport process is complicated.

### 2.5.3. Diffusion at microdisc electrodes

For microdisc electrodes, the current response is expressed using a modified equation of spherical electrodes, despite the non-uniform flux of electroactive species to the surface.

By the substitution of  $r_0 = \frac{\pi a}{4}$ , where  $a$  is the radius of the disc, the equation for the variation of current with time is:

$$I_d(t) = \frac{nFAD^{1/2} C_\infty}{(\pi t)^{1/2}} + \frac{4nFADC_\infty}{\pi a} \quad \text{Eq. (17)}$$

In the same way, at short times, diffusion at a microdisc can be treated as linear diffusion (Cottrell's equation (Eq. (8)), but in other way, at long time:

$$I_d(t) = \frac{4nFADC_\infty}{\pi a} \quad \text{Eq. (18)}$$

Replacing the microdisc area ( $A = \pi a^2$ ) on the Eq. (18):

$$I_d(t) = 4nFDC_\infty a \quad \text{Eq. (19)}$$

This equation is also defined as steady-state current equation.

As “short” and “long” times are relative terms, it is useful to determine the times over which transient and steady-state behaviours will predominate and how this time regime is affected by the electrode radius. This analysis gives a dimensionless parameter  $\chi$ :

$$\chi = \frac{\sqrt{\pi Dt}}{a} \quad \text{Eq. (20)}$$

This expression can be used to calculate a lower time limit at which the steady-state contribution will dominate the total current to a specified extent (10 times larger).

For a recessed microdisc, Bond et al. derived steady-state current equation for predicting the steady state limiting current of an isolated recessed microdisc electrode by a factor L.<sup>15</sup>

$$i_{lim} = 4nFDC_{\infty} a \left( \frac{\pi a}{\pi a + 4L} \right) \quad \text{Eq. (21)}$$

Where:

L – The depth of the cavity.

The distribution of the electroactive species near the electrode surface also can be obtained from the solution to the diffusion equation (Fick's 2<sup>nd</sup> law). In this case, chronopotentiometry is the technique used.

Starting at  $t = 0$  s, a constant current to the electrode is applied in order to causing oxidation or reduction of electroactive species, and the variation of the potential of the electrode with time is measured.

Using the Laplace transform and the same boundary conditions used previously, except the third condition, that is defined as:

**For planar electrode:**

$$\begin{array}{l} t > 0s \\ x = 0 \end{array} \longrightarrow i = n F A D \left( \frac{\partial C(x, t)}{\partial x} \right)_{x=0}$$

The concentration gradient is being imposed at the electrode surface

**For spherical electrode:**

$$\begin{array}{l} t > 0s \\ r = r_0 \end{array} \longrightarrow i = n F A D \left( \frac{\partial C(r, t)}{\partial r} \right)_{r=r_0}$$



An equation for variation of concentration with time is obtained, and is given by:

|   |  |          |
|---|--|----------|
| <b>For planar electrode:</b>  |  |          |
| $C_0 = C_\infty \operatorname{erf} \left[ \frac{x}{2(Dt)^{1/2}} \right]$                      |  | Eq. (22) |
| <b>For spherical electrode:</b>   |  |          |
| $C_0 = C_\infty - \frac{r_0}{r} \operatorname{erfc} \left[ \frac{r-r_0}{2(Dt)^{1/2}} \right]$ |  | Eq. (23) |

Next figure show the variation of concentration with distance for several times after the start of a Cottrell experiment.

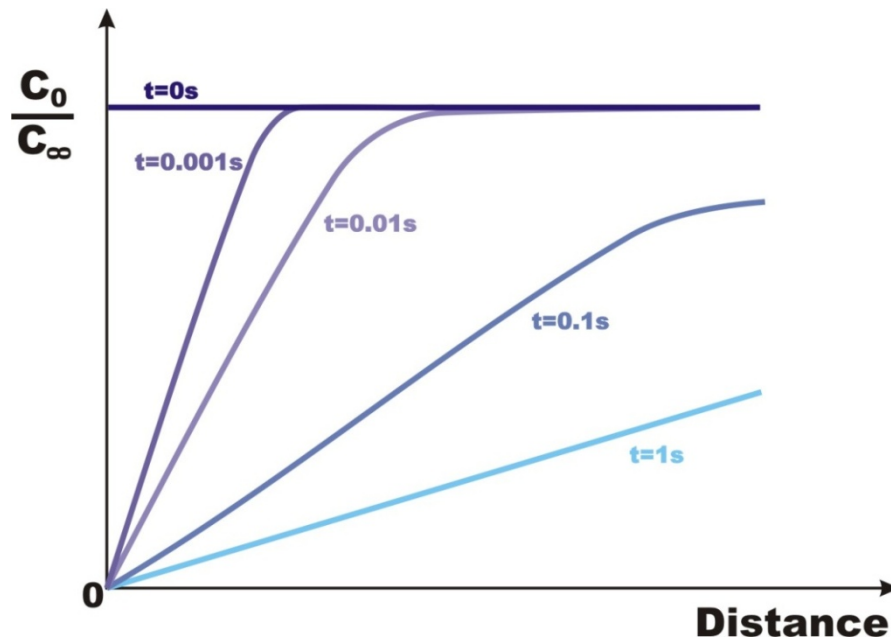


**Figure 14** – Concentration profiles for several times after the start a Cottrell experiment.<sup>14</sup>

The diffuse layer is defined as the zone when there is concentration gradient close to electrode surface. From the Figure 14, it's possible see that the diffusion layer thickness ( $\delta$ ) is time-dependent. For example, for  $t = 0.01s$ ,

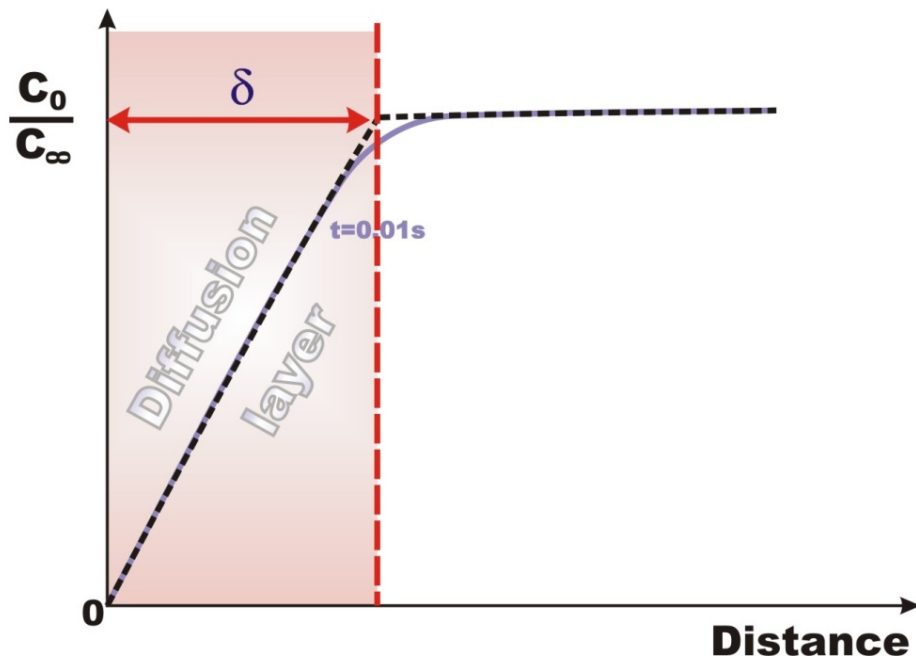


Figure 15 – Definition of the diffusion layer  $\delta$ .

An approximation for determination of the diffusion layer thickness was introduced by Nernst, which defined the diffusion layer as:

$$\frac{\partial C(x, t)}{\partial x} = D \frac{(C_{\infty} - C_0)}{\delta} \quad \text{Eq. (24)}$$

Applying this equation to the Cottrell equation (Eq. (8)), the diffusion layer thickness is given by:

$$\delta = (\pi D t)^{1/2} \quad \text{Eq. (25)}$$

The thickness increases with  $t^{1/2}$ . This fact proves that for large  $t$ , the steady-state is never reached at conventional-sized electrodes.

## 2.6. KINETICS OF ELECTRODE REACTIONS

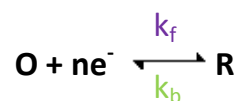
---

As it was mentioned before, an electrochemical reaction is a reaction involving the transfer of charge and these can occur in solution (homogeneous reactions) or on the electrode surface (heterogeneous reactions). We are going to focus to the heterogeneous reactions.

This type of reactions involves electron-transfer between two species in an electrochemical couple. The process usually occurs at the working electrode electrode surface, when electrons transfer between the solid-state electrode and solution-state electroactive species.

### 2.6.1. Heterogeneous electrochemical reactions

Consider the following simple one-electron reduction process with forward rate constant  $k_f$  and backward rate constant  $k_b$ :



Recall from section 2.4, that the general expression relating the current response to the reactant concentration gradient is given by:

$$i = nFAD \frac{\partial C(x, t)}{\partial x} \quad \text{Eq. (26)}$$

The reaction has a net reaction rate  $u$  of:

$$u = k_f C_O(0, t) - k_b C_R(0, t) \quad \text{Eq. (27)}$$

This equation can be incorporated into equation 8 to give the following analogy:

$$i = nFA[k_f C_O(0, t) - k_b C_R(0, t)] \quad \text{Eq. (28)}$$

Butler<sup>16</sup> and Volmer<sup>17</sup> have derived a pair of expressions that relate the rate constants,  $k_f$  and  $k_b$ , with the reversible formal potential,  $E_f^0$ , a standard rate constant,  $k_0$ , and a transfer coefficient,  $\alpha$ .

The transfer coefficient has a value between zero and unity and describes the slope of the transition-state energy profile. Usually, for metal electrodes and in case of reversible reaction, alpha is 0.5. It influences the shape, although not the position, of the voltammetric response.

The transfer coefficient has a typical value of 0.5. Note that the nomenclature  $E_f^0$  is used instead of  $E^0$  because the measurements are not usually performed under standard conditions of unit activity, temperature and pressure.

The potential of the electrochemical cell controls the rate of reaction, and therefore at a certain potential  $k_f$  and  $k_b$  are equal, and can be expressed

simple by one heterogeneous rate constant  $k_0$ . This means that rate constants at other potentials can be expressed in terms of  $k_0$  as follows:

$$k_b = k_0 \exp\left(\frac{(1-\alpha)nF(E-E_f^0)}{RT}\right) \quad \text{Eq. (29)}$$

$$k_f = k_0 \exp\left(\frac{-\alpha nF(E-E_f^0)}{RT}\right) \quad \text{Eq. (30)}$$

Where  $E$  is the equilibrium potential for the electrode system.

This can now be written in terms of current density as:

$$i = nFAk_0 \left[ C_O(0, t) \exp\left(\frac{-\alpha nF(E-E_f^0)}{RT}\right) - C_R(0, t) \exp\left(\frac{(1-\alpha)nF(E-E_f^0)}{RT}\right) \right] \quad \text{Eq. (31)}$$

At equilibrium, the cathode and anode would have equal currents, as the rate constants are identical for the forwards and backwards reactions. This can be reflected in the flowing equation:

$$nFAk_0 C_O(0, t) \exp\left(\frac{-\alpha nF(E-E_f^0)}{RT}\right) = nFAk_0 C_R(0, t) \exp\left(\frac{(1-\alpha)nF(E-E_f^0)}{RT}\right) \quad \text{Eq. (32)}$$

This is the Butler-Volmer equation, which is the fundamental relationship between the voltage applied and the current which flows inside an electrochemical cell.

In an equilibrium situation where  $C_O$  and  $C_R$  are identical, net current flow would therefore be zero. Even though this is the case, balanced Faradaic activity can still be envisaged as the exchange current,  $i_0$ . This is related to  $k_0$  by the simple relationship:

$$i_0 = nAFk_0C(0, t) \quad \text{Eq. (33)}$$

The Butler-Volmer equation therefore simplifies to:

$$i = i_0 \left[ \exp\left(\frac{-\alpha nF(E - E_f^0)}{RT}\right) - \exp\left(\frac{(1 - \alpha)nF(E - E_f^0)}{RT}\right) \right] \quad \text{Eq. (34)}$$

This equation is known as the current-overpotential equation. It is therefore possible to investigate the kinetics of reactions with different values of  $i_0$ , the larger the value of  $i_0$ , the larger the current change will be on the variation of  $E - E_0$ , and the quicker the kinetics of the reaction.

The limiting case of the Butler-Volmer equation is the Tafel equation, applied to high overpotential ( $\eta$ ) systems.

The Tafel equation is,

$$\eta = \frac{RT}{\alpha nF} \ln i_0 - \frac{RT}{\alpha nF} \ln i \quad \text{Eq. (35)}$$

Linearising this equation, gives:

$$\eta = a + b \log i \quad \text{Eq. (36)}$$

A plot of  $\log i$  vs  $\eta$  is known as a Tafel plot, with  $a$  being the intercept and  $b$  being the slope of the line.  $a$  provides information about the rate constant and the exchange current density of the reaction, and  $b$  is the 'Tafel slope', which provides information about the mechanism of the reaction. If the Tafel plot shows a straight line, then the reaction obeys the Tafel equation. In this way, Tafel plots can be used to investigate non-reversible reactions and non-equilibrium conditions in a way that Nernstian kinetics cannot.



## 2.7. ELECTROCHEMICAL TECHNIQUES

---

### 2.7.1. Cyclic Voltammetry (CV)

Cyclic Voltammetry is the most widely used technique for acquiring qualitative and quantitative information about electrochemical reactions. The power of CV results from its ability to provide considerable information on the thermodynamics of redox process, on the kinetics of heterogeneous electron-transfer reactions, and on coupled chemical reactions or adsorptions process.

CV is often the first experiment performed in electroanalytical studies due to its simplicity, speed, ease of use and ease of interpretation. A standard cyclic voltammetry experiment takes place in a three-electrode cell, using working, reference and counter electrodes.

Electrochemical cells usually contain the electroactive compound to be studied in solution, often along with a non-reactive electrolyte such as Potassium Nitrate or Potassium Chloride to facilitate ionic transport. A potential is applied to the working electrode, and the Faradaic current response at the working electrode is measured. The potential at the working electrode is then changed as a function of time, with scan rate  $\nu$ . This potential is generally swept from the starting potential to a fixed switching potential and then back in a triangular waveform (Figure 16).

More complicated cyclic voltammetry experiments will sweep the potential through three or more ending points and repeat the waveform for a number of cycles.

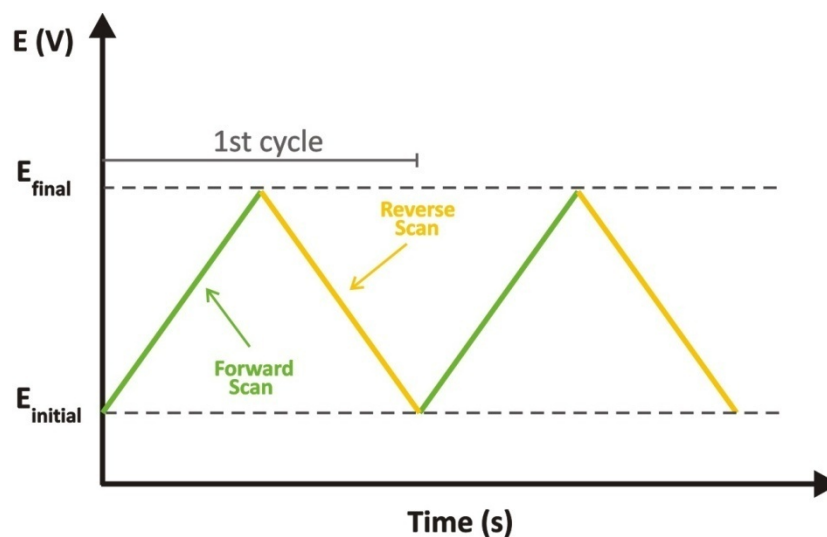


**Figure 16** – *Potential time excitation signal in cyclic voltammetric experiment.*

During the potential sweep, the potentiostat measures the current resulting from the applied potential, and this current is due to the occurrence of oxidation or reduction of electroactive species in solution (Faradaic current) and the double layer charging (Capacitive current).

As the working electrode is swept through the potential range, the potential applied to the electrode may prove sufficient to cause any electrochemical species present to undergo electron-transfer reactions.

Considering a redox couple, O and R:



Before the scan begins, the electrochemical cell will contain mostly the reduced form R. As the working electrode is swept through the redox potential, some of R is converted into O and a Faradaic current flows, increasing exponentially as the potential is neared. This is due to the surface concentration of R on the electrode – as the redox potential is neared, it drops, increasing the concentration gradient and thus the current flow. As the potential passes through the redox potential, mass transfer of R to the surface reaches a maximum rate, declining past this point due to depletion. A reversal current peak is seen when the potential is swept in the opposite direction, as the oxidised species O at the electrode surface gets converted back into R. The result is a curve as shown in Figure 17.

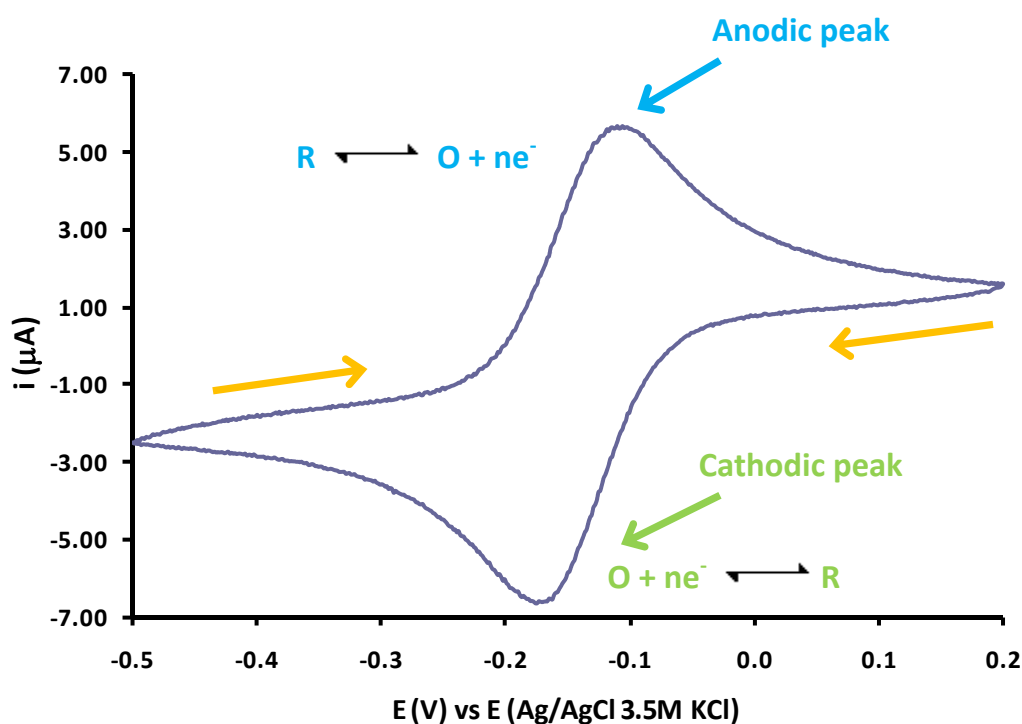


**Figure 17** – Typical cyclic voltammogram for a macroelectrode at a reversible reaction. (1mM  $Ru(NH_3)_6^{3+}$  + 0.1M  $KNO_3$  WE electrode - Gold (d=3mm), counter electrode - Pt electrode, Reference electrode – Ag/AgCl, 3.5M KCl, scan rate –  $0.15 \text{ Vs}^{-1}$ )

If a redox system remains in equilibrium throughout the CV, resulting in two peaks of equal height, then the reaction is known as reversible. This is an example of a standard reversible cyclic voltammogram shown above. There are a number of powerful analysis methods to obtain data relating to the kinetic and mechanistic features of the reaction.

For a reversible electron-transfer process, one with rapid heterogeneous kinetics, the following information can be obtained from a cyclic voltammogram (using macroelectrodes),

**Table 3** – *cyclic voltammetric behaviour of a macroelectrode for a reversible reaction*

|    |  |
|----|--|
| 1. | The Cathodic peak current ( $I_{pc}$ ) is equal to the anodic peak current ( $I_{pa}$ ), i.e.,<br>$I_{pc} = I_{pa}$              |
| 2. | The peak potentials ( $E_{pc}$ and $E_{pa}$ ), are independent of the scan rate ( $\nu$ )  |
| 3. | The formal potential of the redox couple ( $E_f^0$ ) is centred between $E_{pc}$ and $E_{pa}$ ,<br>$E_f^0 = (E_{pc} + E_{pa})/2$ |
| 4. | The peak current ( $I_p$ ) is proportional to the square root of scan rate ( $\nu^{1/2}$ )                                       |
| 5. | The separation between the peak potentials is 59 mV/n for an n-electron couple at room temperature                               |

The dependence of the peak current on the scan rate is given by the Randles-Sevcik equation,

$$i_p = 2.69E5 n^{3/2} D^{1/2} C u^{1/2} A \quad \text{Eq. (37)}$$

Where:

n - Number of electrons involved in ox/red)

D - Diffusion coefficient ( $\text{cm}^2 \text{s}^{-1}$ )

C - Bulk concentration ( $\text{mol cm}^{-3}$ )

u - Scan rate ( $\text{V s}^{-1}$ )

$i_{pa}$  - Anodic peak current (A)

A – Electrode area ( $\text{cm}^2$ )

For microelectrodes, a sigmoidal cyclic voltammogram (Figure 18) is observed at a certain timescale, because the mass transport is dominated by radial diffusion. In steady state, a constant current (steady-state current or limiting current) is yielded, as mentioned already.

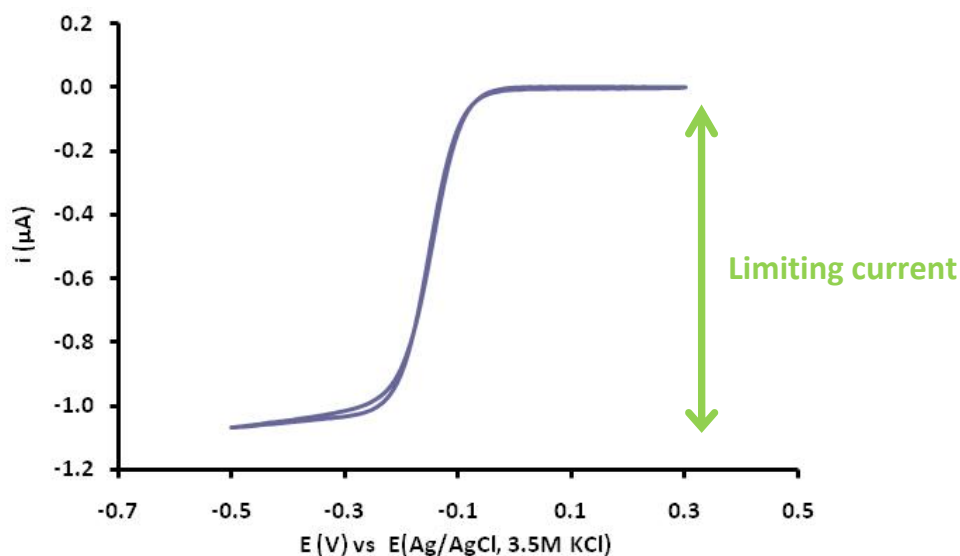


**Figure 18** – Typical cyclic voltammogram for a microelectrode at a reversible reaction. ( $1\text{mM Ru}(\text{NH}_3)_6^{3+} + 0.1\text{M KNO}_3$ ; WE electrode – Gold MEA ( $a = 12.5 \mu\text{m}$ ,  $Z=319 \text{ ME's}$ ), counter electrode - Pt electrode, Reference electrode – Ag/AgCl, 3.5M KCl, scan rate –  $0.10 \text{ Vs}^{-1}$ )

Three electrodes are usually necessary (Figure 19) in order to avoid passing current through the reference electrode and which would alter its potential via changes in the activities of the various species. The electrical circuit, through which the current passes, is between the working electrode and an auxiliary electrode. The reference electrode serves in a three electrode system to control the potential of the working electrode and thence the reaction which can occur there. There are a few exceptions where two-electrode systems may be able to be used, it is the case of microelectrodes, where the current are very small and so do not perturb the potential of the reference electrode.

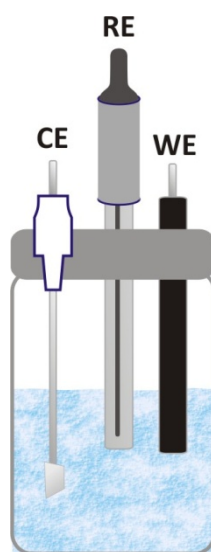


**Figure 19** – *Three electrode arrangement.*

## 2.7.2 – Chronoamperometry (CA)

Chronoamperometry is the variation of the current response with time under potentiostatic control. It involves application of a potential step at  $t=0$  to a working electrode, in a solution containing either oxidized or reduced species, from a value where there is no electrode reaction to the value where all electroactive species that reach the electrode react, as show in following figure,

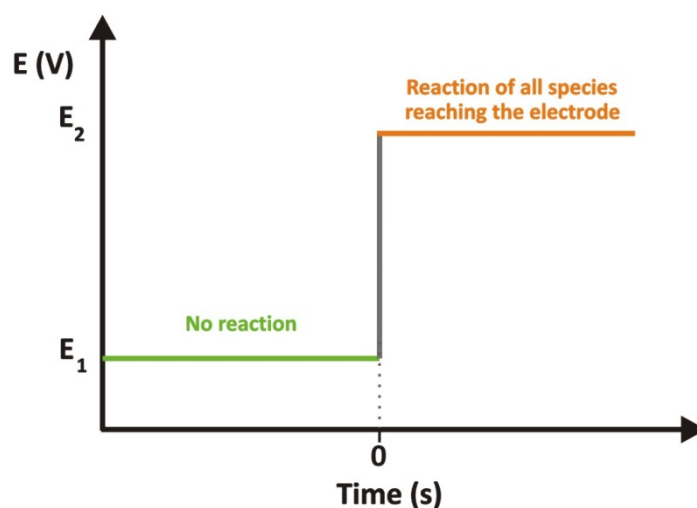


**Figure 20** – *Potential step to obtain a diffusion-limited current of the electroactive species.*

CA is often used for measuring the diffusion coefficient of electroactive species or the surface area of the working electrode, using microelectrodes as working electrode, and consequently, the steady state current equation.

### **2.7.3 - Electrochemical Impedance Spectroscopy (EIS)**

Electrochemical impedance spectroscopy (EIS) is a rapidly developing transduction technique for the characterisation of functionalised electrodes at the electrode surface. Impedance measurements provide detailed information on resistance / capacitance changes occurring at conductive or semiconductive surfaces. Since only small amplitude perturbing sinusoidal voltage signal is applied around an equilibrium point to the electrochemical cell.

EIS uses alternate current (a.c.) signals to determine impedance over a range of frequencies. Electrochemical impedance theory is a branch of ac theory that describes the response of a circuit to an alternating current or voltage as a function of frequency. The performance of an electrochemical cell can be represented by an equivalent circuit of resistors and capacitors. The Impedance is described by an analogous equation to the Ohm's law ( $E = I.R$ ), where E is dc potential (V), I is the current (A), and R is the resistance (Ohms) in direct current (dc). In the case of altern current, the resistance R is replaced by Impedance Z.

$$E = I . Z \qquad \text{Eq. (38)}$$

A typical plot of a potential sine wave (E) applied and the resultant ac current waveform (I) is shown in Figure 21.



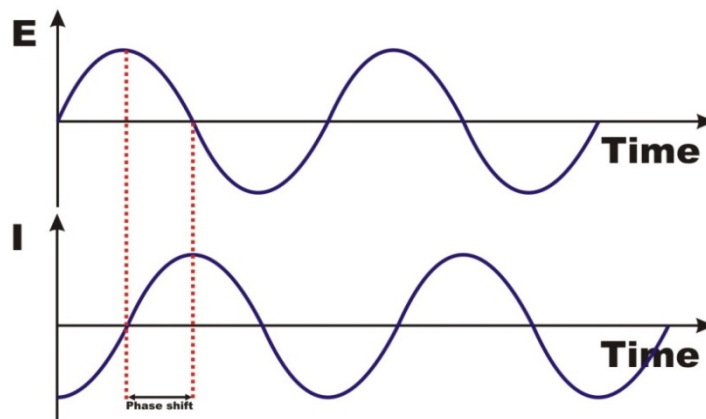


**Figure 21** – Phasor diagram for voltage and current.

The potential applied equation is:

$$E(t) = E_0 \sin(\omega t) \quad \text{Eq. (39)}$$

Where

$E(t)$  is the voltage as function of time (V)

$E_0$  is the voltage amplitude (V)

$\omega$  is the angular frequency ( $\text{rad s}^{-1} = 2\pi f$ )

$f$  is the frequency (Hz)

$t$  is the time (s).

The resulting current sine wave equation is:

$$i(t) = i_0 \sin(\omega t + \phi) \quad \text{Eq. (40)}$$

Where,

$I(t)$  is the current as function of time (A)

$I_0$  is the maximum current amplitude (A)

$\phi$  is the phase shift (rad).

Both sine waves are different in amplitude and are shifted in time implying that they are out of phase. In a purely resistive arrangement, the potential and the current sine waves would be exactly in phase, differing only in amplitude.

Using Ohm's law, the impedance as function of time can be expressed as,

$$Z(t) = \frac{E_0 \sin(\omega t)}{i_0 \sin(\omega t + \phi)} \quad \text{Eq. (41)}$$

In the EIS experiments the impedance is expressed as vector, where the raw data at each measured frequency consists of the real and imaginary components of the applied potential and the measured current. The magnitude and direction of a planar vector in the right-hand of orthogonal system of axes can be expressed by the sum of the vectors components. For instance, the case of impedance, the vector is,

$$Z(\omega) = Z' + jZ'' \quad \text{Eq. (42)}$$

Where,

$Z'$  and  $Z''$  are the real and the imaginary part of the impedance vector  $Z$  respectively.  $j$  is the imaginary number  $\sqrt{-1}$  (although Mathematicians use  $i$

to stand for  $\sqrt{-1}$ , but electrochemists use  $j$  in order to avoid confusion with  $i$ , symbol of current).

The impedance vector can be plotted in plane with rectangular or polar coordinates, as shown in Figure 22.

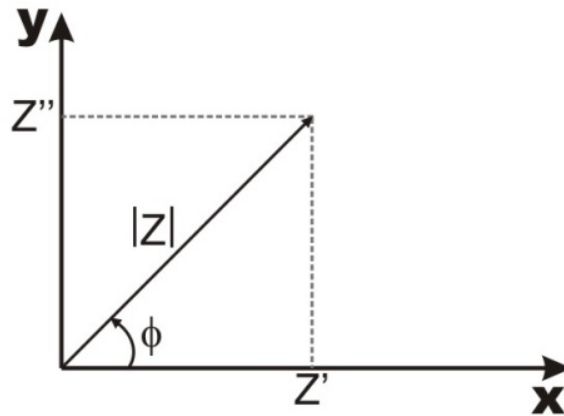


**Figure 22** – *impedance planar vector in rectangular.*

The two rectangular coordinates values are,

$$Z' = |Z| \cos \phi \quad \text{Eq. (43)}$$

$$Z'' = |Z| \sin \phi \quad \text{Eq. (44)}$$

The graph also has shown that the phase shift (Eq. (45)) and the total impedance (Eq. (46)) for each applied frequency are respectively:

$$\phi = \tan^{-1} \frac{Z'}{Z''} \quad \text{Eq. (45)}$$

$$|Z| = \sqrt{(Z')^2 + (Z'')^2} \quad \text{Eq. (46)}$$

The real part of the impedance complex number is pure resistance and the imaginary component is a combined capacitance and inductance. The total impedance in a circuit is the combined opposition of all its resistors, capacitors, and inductors to the flow of electrons.

The EIS data can be plotted in different formats. Each format has certain advantages for revealing particular characteristics of a chemical system. From the plots data it is possible to obtain an equivalent circuit for any electrochemical cell. However, difficulties in processing data using electrical components, such as resistances and capacitors, often arise because the non-linearity in the proposed equivalent circuit, thus, a constant-phase element (CPE) is used.

For instance, the double layer capacitance value of an electrochemical cell can be estimated from the impedance of the CPE, which is given by:

$$Z_{\text{CPE}} = \frac{1}{Q(j\omega)^\varphi} \quad \text{Eq. (47)}$$

Where Q is a constant,  $\omega$  is the angular frequency and  $\varphi$  is fractional with a value between 0.5 (for an ideally porous electrode) and 1 (for a perfectly smooth electrode). If  $\varphi = 1$  the CPE is an ideal capacitor and  $Q = C_{\text{dl}}$ .

A common way to present impedance data is the plot  $-Z''$  against  $Z'$ . This graph is called the Nyquist plot. Each point on this graph is characteristic of the complex impedance at a given frequency, however, this plot does not give indicate what the frequency is, that is the main disadvantage.

Another data presentation mode is the Bode plot. The impedance is plotted against the frequency logarithm and both the absolute value of the impedance and the phase shift are plotted on the y-axis.

Potentiodynamic electrochemical impedance spectroscopy (PEIS) derived from the typical EIS, following the theory and fundamentals. PEIS uses a small AC potential perturbation to characterise the small-signal response as a function of frequency for a potential scan.

In electrochemical experiments of modified electrodes, PEIS provides important information about the potential dependencies of the charge transfer resistance, capacitance and molecular conformations in the monolayer.

PEIS measurements are useful because it provides important information about the potential dependency of the electronic properties of semiconductor-organic interfaces, such as resistance and capacitance of the semiconductor space-charge region, the capacitance and electron-transfer resistance of the monolayer, and the capacitance of the electrochemical double layer.<sup>18</sup>

## 2.8. MICROELECTRODES

---

The first use of microelectrodes was reported in 1940 where Davies and Brink used a platinum microdisc to measure the oxygen in muscle tissue.<sup>19</sup> However, electrodes of micrometer dimensions were practically not used in electrochemical research prior to the end of the 1970s. Only in 1980, Fleischmann and co-workers at the University of Southampton establish that electrode of micrometer size has not only quantitative effects, but also qualitative effects.<sup>20</sup>

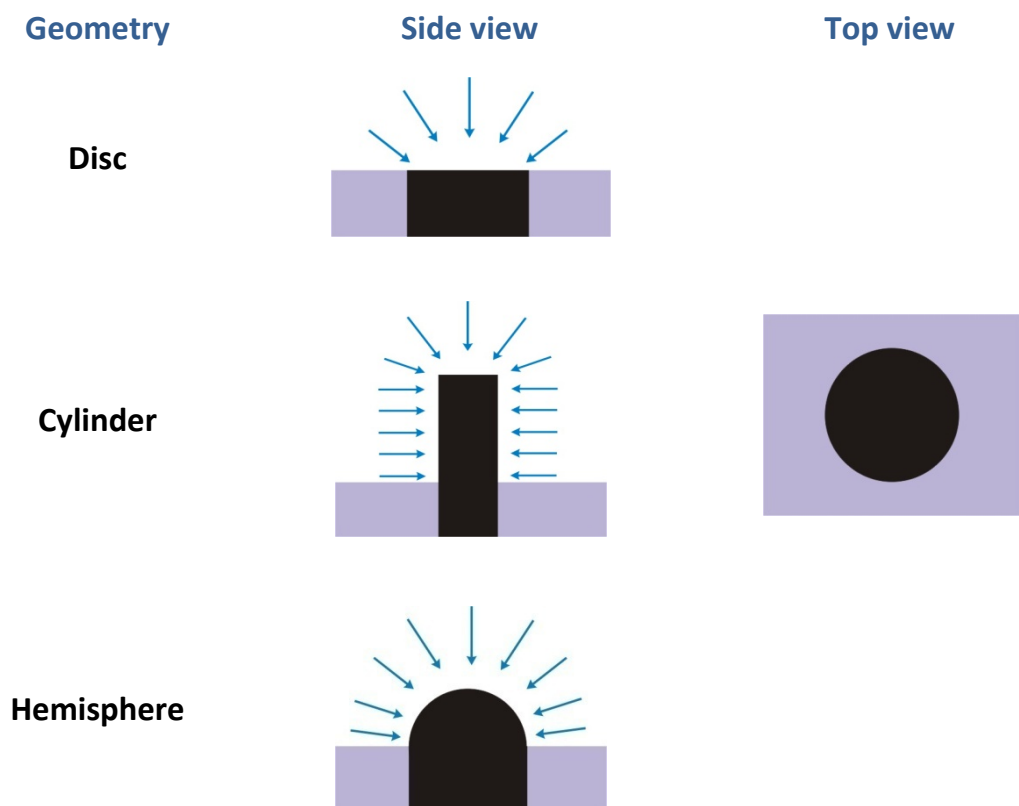
This discovery has encouraged numerous research groups to study the properties and applications of microelectrodes.

Since their introduction to electroanalytical chemistry about 25 years ago, microelectrodes have led to unprecedented advances in electrochemical science. Because many of the undesirable aspects of electrochemical techniques are reduced with microelectrodes and because are easily implemented and involve relatively low costs, and, the main reason is, applying microelectrode techniques to investigate a wide variety of problems, some of them not accessible with size-conventional electrodes.<sup>21</sup>

Nowadays, there is no consistent definition of a microelectrode, although there is a general agreement on the essential concept, which that the electrode is smaller than the scale of the diffusion layer.<sup>14,21,22</sup>

The main difference between authors was the size ranging of at least one dimension of the microelectrode. The question of how small the critical dimension of an electrode has to be in order to be considered microelectrode has been discussed but is not resolved. Different concepts are given here for reference: greater than  $50\ \mu\text{m}$ <sup>5</sup>,  $25\ \mu\text{m}$ <sup>4,23</sup>, between  $0.1$  and  $50\ \mu\text{m}$ <sup>22</sup>, between  $0.8$  and  $50\ \mu\text{m}$ <sup>24</sup>.

There are different microelectrode types, such as disc, cylinder, band, ring, sphere, and hemisphere (Figure 23). The critical dimension could be the radius of a disc, sphere, cylinder or hemisphere electrodes or the width of a band, cylinder or ring electrodes.



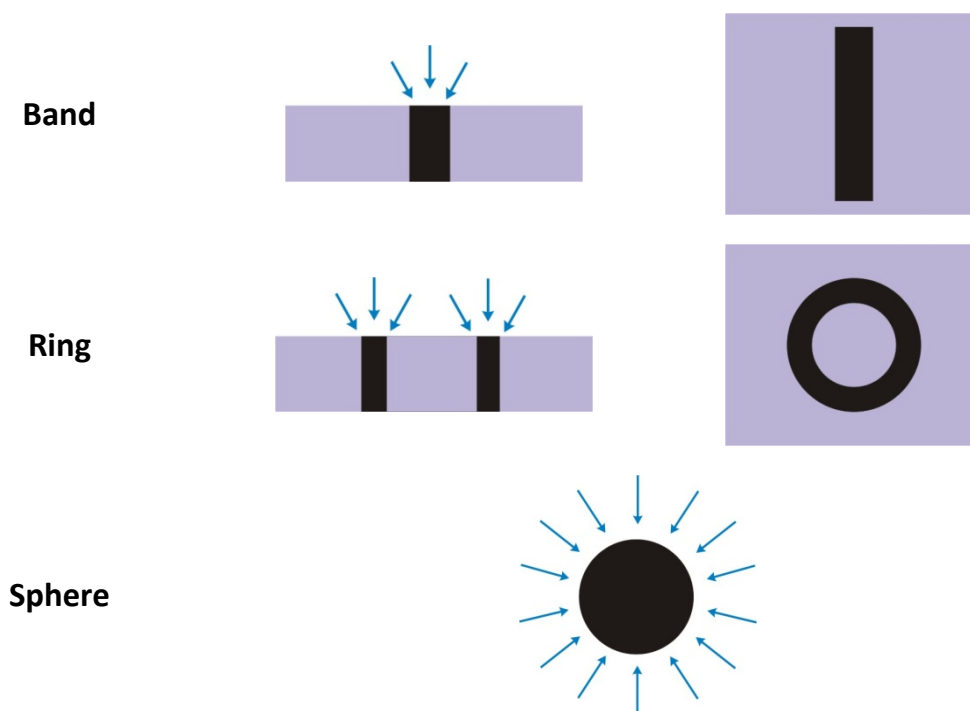


**Figure 23** – *Illustration of the most common microelectrode geometries, and their diffusion fields*

The most important type of microelectrode is the disc electrode, which is usually made of gold, platinum or carbon encapsulated in glass or plastic in order to isolate it completely from the electrolytic environment.<sup>20,25,26</sup>

The term “ultramicroelectrode” is also often used in the literature, but, to maintain the terminology consistent, it is preferable to stick to the more logical term, “microelectrode”.<sup>27</sup>

The theory and application of many microelectrode geometries has been discussed in the literature and relationships for diffusion limited currents obtained using a variety of classical mathematical approaches and digital simulations methods.<sup>28,29,30,31,32,33,34,35</sup>



The electrochemical responses at microelectrodes differ greatly from those seen at electrodes of conventional size. The great advantage of microelectrodes over macroelectrodes is the minimisation of interference, which gives rise to much lower detection limits. Microelectrodes have much reduced ohmic drops and capacitive effects and can be used in the absence of supporting electrolyte.<sup>14,4,5,22,21,27,23,24,30,20,25,34,9</sup>

### 2.8.1. The influence of the capacitive current

The current resulting due the electron transfer from redox reaction is named Faradaic current,  $I_F$ . For a planar electrode, it is expressed by the Cottrell equation, as mentioned already.

However, when the potential is changed, the double layer has to be charged, giving rise to a Capacitive current,  $I_C$ . The resulting plot current-time (Chronoamperogram) is shown schematically in Figure 24. As it can be seen, the Capacitive contribution for the total current dies away more quickly than Faradaic current, i.e.,  $I_C$  decays to zero (exponentially) in less than 50  $\mu\text{s}$ , and it can be neglected for longer times, as show the following equation,<sup>14,20</sup>

$$I_C(t) = \frac{\Delta E}{R_S} e^{\frac{-t}{RC}} \quad \text{Eq. (48)}$$

Where,

$\Delta E$  – Potential step applied;

$C$  – Double layer Capacity;

$t$  – Time;

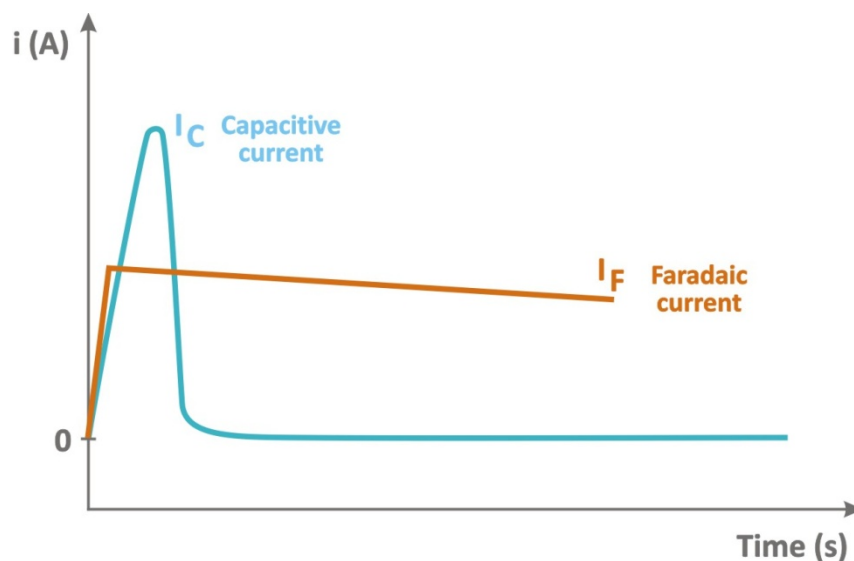


**Figure 24** – Evolution of current with time on applying a potential step at an electrode.<sup>4</sup>

The  $I_C$  is the same as that obtained when a potential step is applied to a series RC circuit.

When a rapid electrode process is being studied and 50  $\mu\text{s}$  is too long a timescale, the use of a microelectrode is recommended because the Capacitive current is proportional exponentially to the electrode area, and therefore, the  $I_C$  can be neglected in experiments using this type of electrodes. The smaller the characteristic dimension of the electrode and slower the scan rate, the better the current ratio  $\frac{I_F}{I_C}$ .

### ***2.8.2. The influence of the Ohmic drop***

When currents flow through solution, they generate a potential that acts to weaken the applied potential on the working electrode by an amount of  $iR$ , (where  $i$  is the total current and  $R$  is the cell resistance), leading to distortions of experimental responses (Ohmic drop). The lower the conductivity of the electrolyte (high resistance) and the larger total current (high total current), the larger this effect will be.<sup>20,26</sup>

Using microelectrodes, the Ohmic effect is significantly reduced, because the faradaic current becomes extremely small.

At short experimental timescales, where linear diffusion is dominant, the current is proportional to the electrode area (Cottrell equation). Therefore, the current response and consequently, the Ohmic drop decreases with decreasing the radius of microelectrode.

In steady-state conditions, at long experimental timescales, the current response depends only on the radius (Eq. (19)), making the Ohmic drop independent of the dimension of microelectrodes.

As result, electrochemical experiments could be performed in high resistive media using microelectrodes.

One obvious disadvantage associated with microelectrodes is that the current produced is very small. Consequently, the use of high sensitivity and expensive instruments is necessary. In order to minimise this problem, arrays of microelectrodes is an emerging area of interest in the field of microtechnology.

## 2.9. MICROELECTRODE ARRAYS (MEAs)

---

A theoretical analysis of microelectrode arrays has been originally initiated in order to explain the effect of the partial blocking at a large electrode, leading to a different result than expected.<sup>36</sup>

In recent years, microelectrode arrays have been shown to significantly enhance the sensitivity of electrochemically based analytical determination methods.

The theory of electrochemical behaviour of single microelectrodes (active sites) is now well established, with even precise analytical expressions. However, the theory of microelectrode arrays is still not developed due to its complexity.

Different geometries have been considered for the construction of MEAs. These include arrays of band, disc or irregularly shaped microelectrodes assembled in a number of possible ordered (Hexagonal or square) or disordered (random) patterns.<sup>31,37,38,39,40,41</sup> The most important geometry used in microelectrode arrays is the disc.

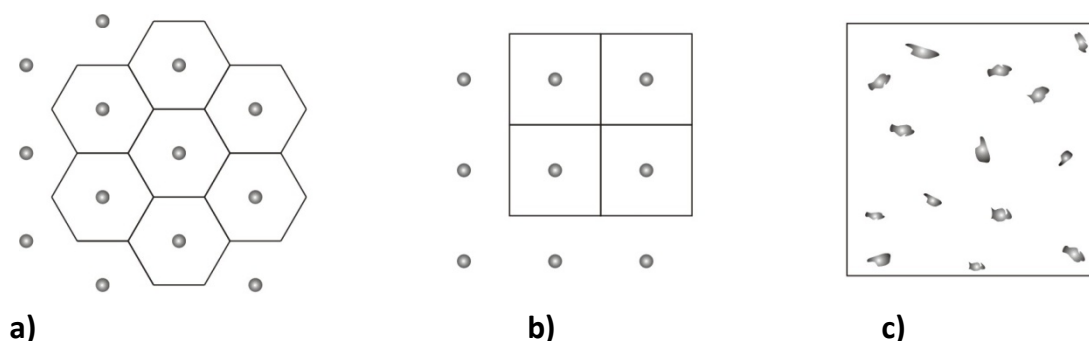


**Figure 25** – *Microelectrode arrays at a) hexagonal, b) square and c) random pattern.*

Hexagonal array is the best arrangement because is the most efficient way to pack as many cells as possible in a limited space. To confirm this idea, it is possible to resort an example from nature – the typical "honeycomb" hexagonal arrangement made by bees.



**Figure 26** – *The typical "honeycomb" hexagonal arrangement made by bees.*

Microelectrode arrays have been proposed as a way of increasing the magnitude of the current (produced for a single microelectrode), while maintaining the advantages of the single microelectrode with respect to diffusion and ohmic drop.<sup>42,37</sup>

However, the condition is that the microelectrode arrays have an adequate design and are of good quality, including an enough inter-electrode distance in order to avoid the shield effect due to overlapping of diffusion layers,

without residues on electrode surfaces and well isolated individual electrodes.<sup>31,15,37,38,41</sup>

If microelectrode arrays are not properly developed, they lose the advantageous properties, and will show the characteristic of macro or quasi-microelectrode. In order to check the quality of the devices, several simulations methods have been discussed in the literature, using different voltammetric techniques for electrochemical characterisation behaviour, such as cyclic Voltammetry<sup>38,43</sup>, chronoamperometry<sup>31</sup>, and scanning probe techniques for analysis surface, such as AFM (atomic force microscopy),<sup>15</sup> SEM (scanning electron microscopy)<sup>42</sup> and SCEM (scanning electrochemical microscopy)<sup>43</sup>. In the third chapter, two scanning probe techniques are used for this purpose – SKN (scanning Kelvin nanoprobe) and White Light Interferometer microscopy.

Depending on the inter-electrode distance, the response of an array is the sum of the individual response of each microelectrode.

The steady-state current for a microdisc array is given by:

$$i_{lim} = 4 Z n F D C_{\infty} a \quad \text{Eq. (49)}$$

Where

Z is the number of microelectrodes.

For a recessed microelectrode array (RMEAs), the steady-state current is given by:<sup>20</sup>

$$i_{lim} = 4 n Z F D C_{\infty} a \left( \frac{\pi a}{\pi a + 4L} \right) \quad \text{Eq. (50)}$$

However, the authors have assumed that the equation is not appropriate for shallow microelectrodes

Ferrigno et al <sup>44</sup> have proposed an expression that predicts the steady state current at the recessed microdisc based on curve fitting simulated data which is claimed to be an improvement on Eq. (50) for shallow recesses (in case of L/a ratio less than unity).

$$i_{lim} = 4 Z n F D C_{\infty} a e^{\frac{-0.96 L}{a}} \quad \text{Eq. (51)}$$

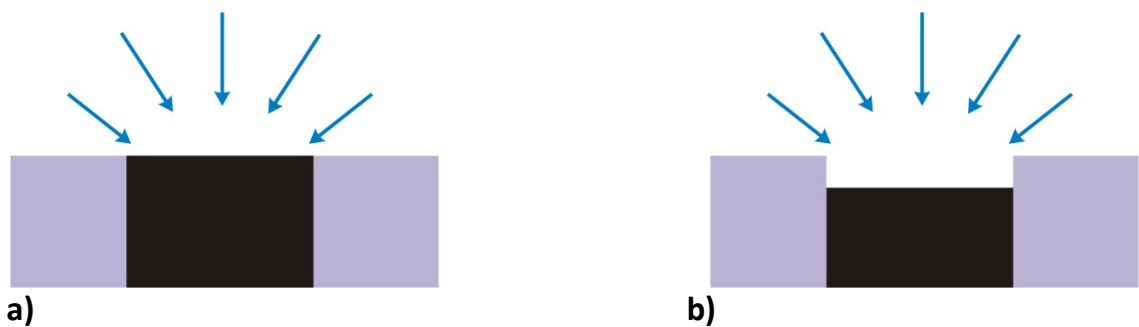


**Figure 27** – Illustration of a) inlaid and b) recessed microdisc.

## 2.9.1. Electrochemical behaviour

### 2.9.1.1. Cyclic voltammetric behaviour

The cyclic voltammetric behaviour of individual microelectrodes is well known, i.e, at low scan rates, the shape of the cyclic voltammogram is sigmoidal, indicating that the steady-state is attained due the radial diffusion and high mass transport rates. At high scan rates, a peak shaped cyclic voltammogram results.

The electrochemical behaviour of microelectrode arrays is more complicated. It depends on the geometry (in the case of microdiscs are the distance between active sites and radius of the active site) and the scan rate of experiments. The same array may exhibit the cyclic voltammetric behaviour of micro-, quasi micro-, or macroelectrodes.<sup>38,36</sup>

In a cyclic voltammetry experiment, as the redox reaction is driven by the applied potential, a depletion layer (or diffusion zone) will grow in the region of the electrode surface. In the case of an array of microdisc electrodes separated by insulating material, individual diffusion zones will develop, and continue to grow throughout the experiment.

It transpires that the voltammetry of the array is highly dependent on the size of the individual diffusion zones,  $\delta$ , vs. the size of the discs themselves ( $a$ ), and on the size of the diffusion zones vs. the centre-to-centre separation,  $d$ .



Based on these two factors, Figure 28 illustrates the four categories to which an array can be assigned and summarises the cyclic voltammetric characteristics associated with each category.<sup>38</sup>

### 1. Individual small diffusion layers : linear diffusion

$$\delta < a$$

$$\delta < d$$

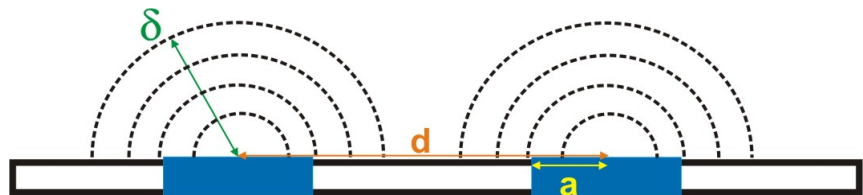


- Cyclic voltammetric behaviour of macroelectrode.

### 2. Individual diffusion layers : radial diffusion

$$\delta > a$$

$$\delta < d$$

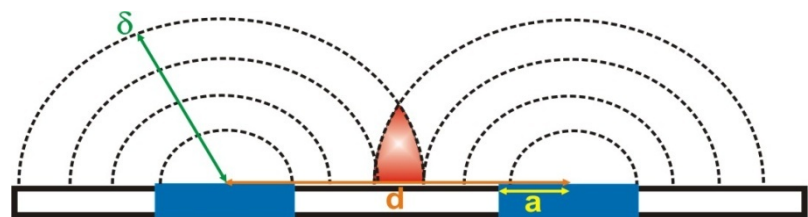


- Cyclic voltammetric behaviour of microelectrode.
- For certain scan rates, steady-state is reached, and can be used eqn.22.

### 3. Overlapping diffusion layers : mixed diffusion

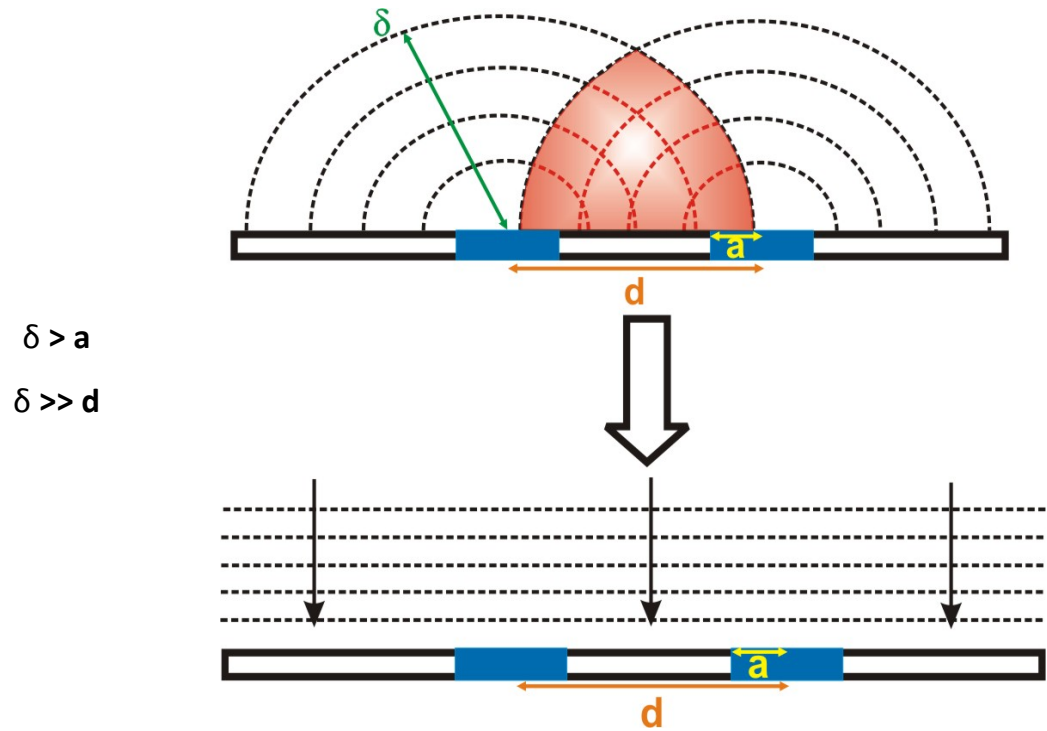
$$\delta > a$$

$$\delta > d$$



- ▶ Cyclic voltammetric behaviour of quasi-microelectrode.
- ▶ Difficult to analyse. Should be avoided.

#### 4. Heavy overlapping diffusion layers : linear diffusion



- ▶ Cyclic voltammetric behaviour of macroelectrode.

**Figure 28** – Diagram of the 4 categories of diffusion profile at microelectrode arrays.

Actually, the goal for research groups is find a critical factor in the design/fabrication of microelectrode arrays in order to obtain microelectrode behaviour (Category 2).

Most of the experiments involving microelectrode arrays reported in the literature have avoided overlap between diffusion layers.<sup>23,7,15,41</sup>

The scan rate of an experiment is also a very important factor for the electrochemical behaviour of microelectrode arrays. As mentioned already, as the redox reaction is driven by the applied potential, individual diffusion zones will develop, and continue to grow throughout the experiment. Generally, three cases can be distinguished.

At very short times (high scan rates), linear diffusion dominates within individual electrodes. This case corresponds to category 1, indicated on the previous page.

At very long times (very slow scan rates), similar effect is also observed, when linear diffusion is restored due to heavy overlap of the diffusion layers. This case corresponds to category 4.

As for intermediate times or scan rates, the linear diffusion dominant at short times transits to radial diffusion, and consequently, a steady-state will be reached, with a characteristic sigmoidal cyclic voltammogram.

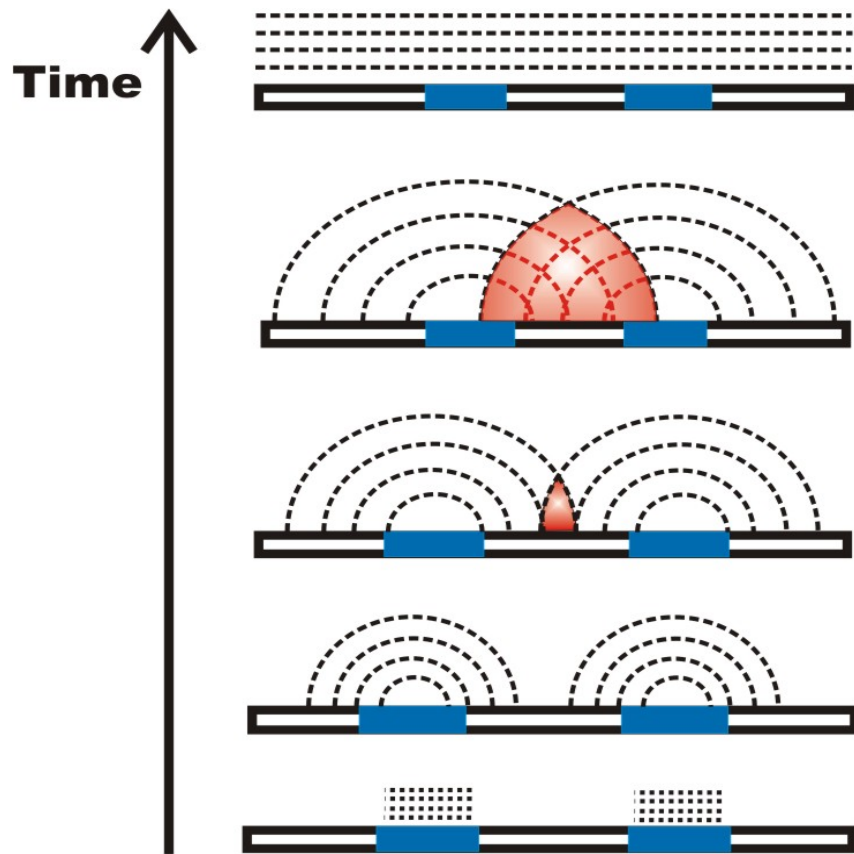


**Figure 29** – *Dependence of the diffusion profile on experiment time.*

## 2.10. SURFACE IMAGING TECHNIQUES

### 2.10.1. Scanning Electron Microscopy (SEM)

Scanning Electron Microscopy (SEM) is a microscope that uses electrons rather than light to form an image.

A beam of electrons, also referred primary electrons, is produced at the top of the microscope and follows a vertical path through the microscope, which is held within a vacuum. The beam travels through electromagnetic fields and lenses, which focus on a spot volume of the specimen, resulting in the transfer of energy to the spot. Consequently, this beam dislodges electrons (secondary electrons) from the specimen itself that are attracted and collected.

Detectors collect these X-rays, backscattered electrons, and secondary electrons and convert them into a signal that is sent to a screen similar to a television screen. This produces the final image.

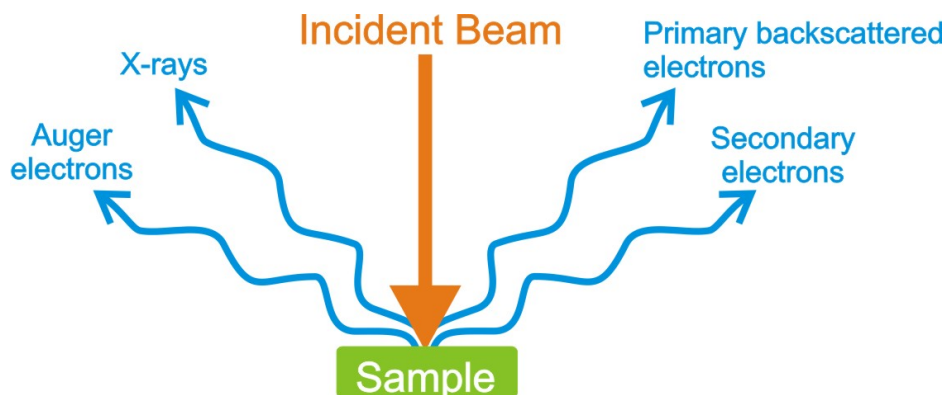


**Figure 30** – Scheme of the operation mode of Scanning Electron Microscope.

All non-metals need to be made conductive by covering the sample with a thin layer of conductive material, such as gold layer.

In this work, we have used a Hitachi S2400 SEM (Hitachi High-Technologies Europe GmbH, Berkshire, UK), which has 4 nm resolution and can achieve 300.000x of magnification.



**Figure 31** – *Hitachi S2400 SEM in the clean room (Engineering Dept.).*

### ***2.10.2. White Light Interferometer Microscopy***

White light interferometry is a fast and accurate 3D inspection method and has been widely used as a reliable non-contact profiling system for characterization of integrated circuits, semiconductor materials, microsystems step heights and discontinuities, biological tissues and rough surfaces.

The basic technique involves splitting an optical beam from the same source into two separate beams – one of the beams is passed through, or reflected from, the object to be measured whilst the other beam (the reference) follows a known and constant optical path.

The light source provides a beam which is passed through a filter and reflected by the upper beam splitter (acting essentially as a mirror at this stage) down to the objective lens. The lower beam splitter in the objective lens creates and combines the light beams reflected from the sample surface and the reference surface in a Mirau type interferometer arrangement as shown in Figure 32.

This creates an interference pattern of light and dark fringes (an interferogram) which is magnified by the microscope optics (i.e. at which the image is brightest). Once this is achieved, provided the vertical movement of the lens can be accurately tracked, it is possible to create a 3D map of the sample surface by measuring the position of the lens required to produce the brightest image at each point on the CCD array.

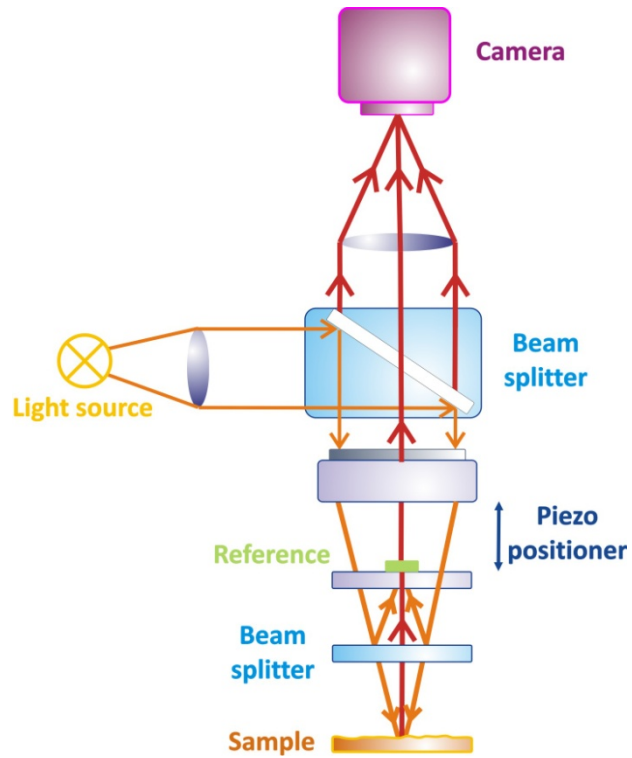


**Figure 32** – Schematic diagram of an interferometer with Mirau objective.

A Zygo New View 100 White Light Interferometer microscopy (Zygo Co-op., Middlefield, CT, US) was used to determine the characteristics of the microelectrodes. The images were obtained using a 40x Mirau objective with a vertical resolution of 0.1nm and maximum lateral resolution of 0.283  $\mu\text{m}$ .



### ***2.10.3. Scanning Kelvin Nanoprobe Microscopy (SKN)***

SKN microscopy is a refined development of the Kelvin probe, a device used in corrosion studies and studies of semi-conducting interfaces, as well as in the investigation of layer and surface processes <sup>45</sup>.

The Kelvin probe takes its name from the famous Scottish scientist William Thompson, later to be given the title of Lord Kelvin. In a British Institution lecture in 1884 <sup>46</sup> he demonstrated the “phenomenon of the contact electrification of metals”. This was demonstrated using two large plates, one made of copper and the other zinc. When brought into contact via a wire, the two plates developed surface charges and thus a potential difference between them when brought into close proximity to one another. The cause of this phenomenon was unknown at the time. Today, a century later, this effect becomes the core of relative work function measurement, and thus of the Scanning Kelvin Nanoprobe.

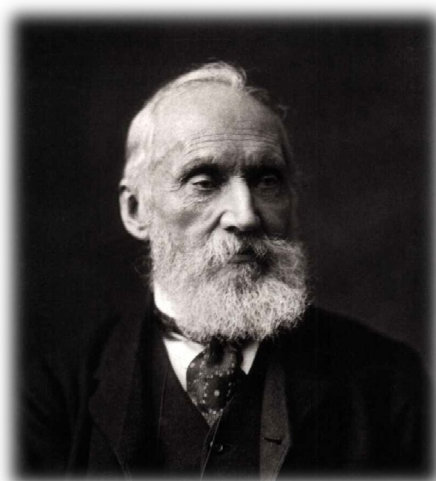


**Figure 33** - *The famous Scottish scientist William Thompson, later to be given the title of Lord Kelvin.*

The scanning Kelvin nanoprobe in use at Durham was developed by Professor Michael Thompson and his research group at the University of Toronto <sup>47</sup>. This probe utilises piezoelectrically vibrated tungsten microelectrode tips of a  $\sim 50\text{nm}$  radius, protected by a guard shield surrounding and electrically isolating the tip.

Tungsten is used as the tip material due to its extremely stable work function, which is highly resistant to changes in temperature and environmental conditions, and remains stable over a large period of time. Stray capacitance is minimised by this guard shield, as well as electrical shielding on all leads and surfaces.

The tungsten tip and an accompanying metallic piezoelectric table form a system of two metallic plates, which function as a capacitor. A sample placed on the piezoelectric table, and therefore between the two plates, has measurable properties based on the change of dielectric permittivity between the material and the free space between the plates (usually air). The CPD (contact potential difference) of the material compared to the tip is therefore measured by the local capacitor thus formed between the vibrating tip and the sample.

The theory of this technique is detailed in next chapter.

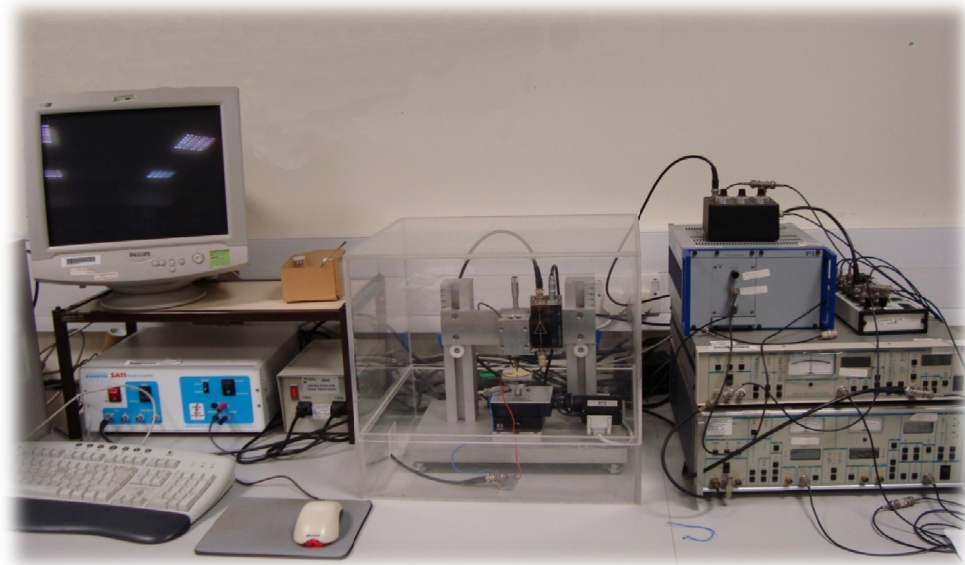


**Figure 34** – *Scanning Kelvin Nanoprobe in use at University of Durham.*

In the SKN in use at Durham, the tip vibrates at a frequency of between 1.7 and 2kHz, depending on the exact properties of the tip. As there are slight variations in size and length between tips, caused by natural variances in the manufacturing process, this frequency is set manually when a new tip is installed and is calibrated precisely to minimize background noise at the tip.

The tip is positioned close to the substrate surface firstly by manual approach, and then by automated computer control, which measures the Kelvin current obtained and positions the tip in an area bounded by preset CPD values. Once an operational distance is reached, the tip is scanned over the substrate surface in a preset pattern in the x and y axes. This is also fully automated, allowing for extremely small (up to 100nm) steps to be taken.

The collected Kelvin current signal arising from the vibrating capacitive field is extremely small, in the picoamp region, due to the small size of the tip. This signal is thusly boosted through an ultra-low noise amplifier and converted to a voltage, which is then inputted into a pair of lock-in amplifiers. One of these

amplifiers detects the CPD signal, the other the topographical signal. The tip is kept at a constant height by a z-axis piezopositioner, which maintains the distance via a feedback loop by ensuring the tip is kept within the CPD bounds previously specified. This mechanism also allows the simultaneous collection of topographical images.

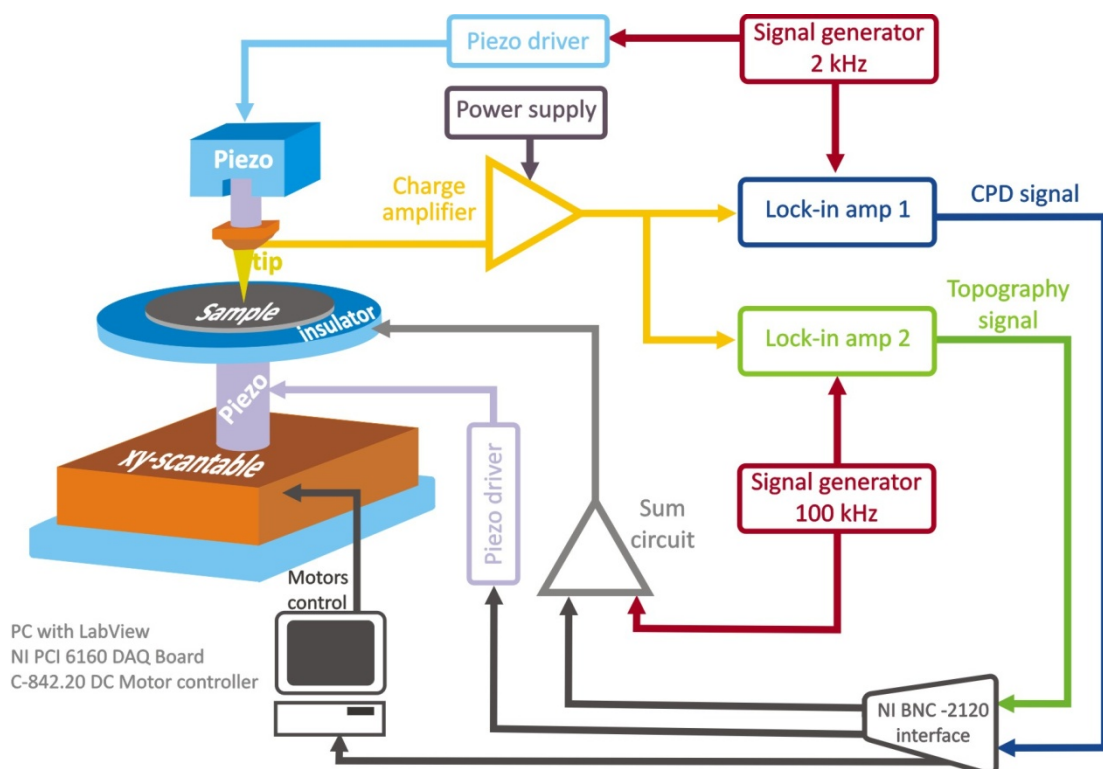


**Figure 35** – Systems level diagram of the scanning Kelvin nanoprobe.

The two signals are fed from the lock-in amplifiers via a data acquisition card (DAQ) into a personal computer. The computer contains the user interface and control mechanism for the SKN, which is implemented in National Instrument’s Labview software.

Labview is a powerful tool for controlling scientific instruments, as it allows the construction of virtual circuitry and thus instruments within the PC. This

allows precise tuning and testing of the SKN instrumentation without the need for complex and expensive physical hardware and is therefore an extremely important component of the developmental SKN. The Labview SKN control programs automate measurement and data collection, and return a pair of ASCII text files from a completed scan, which contain values at each point of the scan for the CPD and topography values respectively. These can be measured using any capable mathematical analysis program. In this thesis, OriginLab 7.5 has been used to analyse the measured SKN data.

#### 2.10.4. Atomic Force Microscopy (AFM)

Atomic force microscopy is an imaging tool used widely in fundamental research and it is one of the oldest and best known forms of probe microscopy. AFM has been used here to investigate the magnitude of the flatness of the gold surface produced by electron beam evaporation by operating in tapping mode.

Atomic Force Microscopy was developed in 1986 by Binnig, Quate and Gerber <sup>48</sup>. Like the Kelvin probe and other scanning-probe microscopes, it uses a fine tip which is scanned across the surface of a sample to form an image.

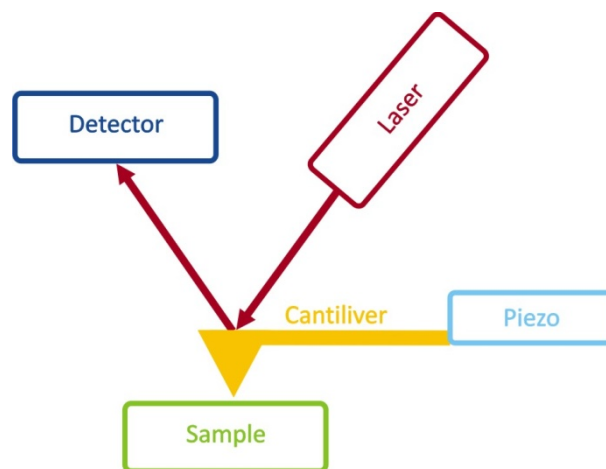


**Figure 36** – Simple diagram of AFM operation.

In a standard AFM, the probe tip is mounted on the end of a cantilever, which deflects according to the force on the tip. This force is measured, usually by focusing a laser on the cantilever and measuring the change in laser signal by a photodiode. This allows very small differences in topography to be imaged – the latest AFMs have a resolution measured in picometres <sup>49</sup>.

## 2.11. FOURIER TRANSFORM INFRARED SPECTROSCOPY

Infrared (IR) spectroscopy is one of the most common spectroscopic techniques used by organic and inorganic chemists. This technique consists in to promote the excitation of molecular vibrations by submitting a sample to an infrared beam. This technique measures the range of wavelengths in the infrared region that are absorbed by a material which correspond to the frequencies of vibrations between the bonds of the atoms making up the sample. Infrared light can be categorized as far infrared ( $4 - 400 \text{ cm}^{-1}$ ), mid infrared ( $400 - 4000 \text{ cm}^{-1}$ ) and near infrared ( $4000 - 14000 \text{ cm}^{-1}$ ).

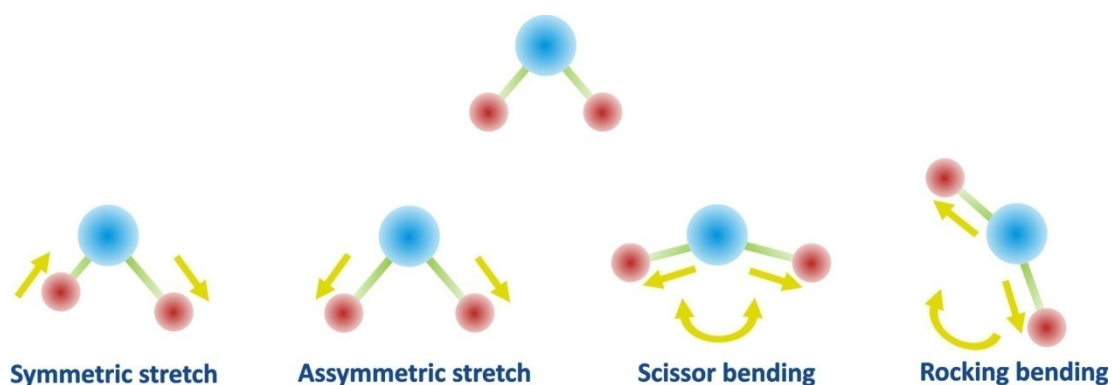


**Figure 37** – *Molecular vibrations modes induced by infrared beam.*

Molecules have specific frequencies at which they rotate or vibrate corresponding to vibrational modes. If there is variation in the permanent dipole of the molecule, these resonant frequencies are active, being detectable by IR.

These infrared absorption bands identify molecular components and structures, representing a molecular fingerprint of the sample, because there are no two compounds producing the exact same infrared spectrum.

Initially, the infrared instruments were of the dispersive type. And these instruments separated the individual frequencies of energy emitted from the infrared source, being a very slow scanning process. The FT-IR (Fourier transform infrared spectroscopy) instruments were developed in order to solve this problem.

Instead of viewing each component frequency sequentially, as in a dispersive IR spectrometer, all frequencies are examined simultaneously in Fourier transform infrared (FTIR) spectroscopy.

Basically, instead of using a monochromator that is a device used to disperse a broad spectrum of radiation and provide a continuous calibrated series of electromagnetic energy bands of determinable frequency range, the FTIR instruments use an interferometer, which divides radiant beams, generates an optical path difference between the beams, then recombines them in order to produce repetitive interference signals measured as a function of optical path difference by a detector, producing a interferogram, that is finally converted to the final IR spectrum by a mathematical operation known as Fourier transformation.



## 2.12. REFERENCES

---

- 
- 1 – Brynn Hibbert, *Introduction to Electrochemistry*, Macmillan Press Ltd., London, 1993.
  - 2 – S. Glasstone, *The Electrochemistry of solution*, Methuen, second edition, London, 1937.
  - 3 – J. Inczedy, T. Lengyel, A. M. Ure, *Compendium of Analytical Nomenclature. Definitive rules 1997, "The Orange Book"*, Blackwell Science, Oxford, 1998.
  - 4 – Joseph Wang, *Analytical Electrochemistry, Second Edition*, Wiley-VCH Publishers, New York, 2000.
  - 5 – Christopher M.A. Brett and Ana Maria Oliveira Brett, *Electrochemistry: principles, methods, and applications*, Oxford science publications, Oxford, 1993.
  - 6 – A. Lopes, S. Martins, A. Morão, M. Magrinho, I. Gonçalves, *Portugaliae Electrochimica Acta*, 22 (2004) 279 – 294.
  - 7 – C. Provent, W. Haenni, E. Santoli, P. Rychen, *Electrochimica Acta*, 49 (2004) 3737 – 3744.
  - 8 – P.M. Ajayan, *Chem. Rev.*, 99 (1999) 1787 – 1799.

---

9 – M. Daenen, R. D. Fouw, B. Hamers, P. G. A. Janssen, K. Schouteden, M. A. J. Veld, *The Wondrous World of Carbon Nanotubes: “a review of current carbon nanotube technologies”*, Eindhoven University of Technology, Eindhoven, 2003.

10 – W. Kutner, J. Wang, M. L'Her, R. P. Buck, *Pure and Appl. Chem.*, 70 (1998) 1301 – 1318.

11 – E. R. de Sousa, E. P. Marques, E. N. Fernandes, J. Zhang, A. L. B. Marques, *J. Braz. Chem. Soc.*, 17 (2006) 177 – 183.

12 – D. W. M. Arrigan, *Analyst*, 119 (1994) 1953 – 1966.

13 – K. O. Lupetti, I. C. Vieira, H. J. Vieira, O. F. Filho, *Analyst*, 127 (2002) 525 – 529.

14 – Allen J. Bard and Larry R. Faulkner, *Electrochemical Methods, Fundamentals and Applications*, second edition, John Wiley and Sons Inc, USA, 2001.

15 – G. Grancharov, E. Khosravi, D. Wood, A. Turton, R. Katakya, *Analyst*, 130 (2005) 1351 – 1357.

16 – J. A. V. Butler, *Faraday Soc.*, 19 (1924) 729 – 733.

17 – T. Erdey-Gruz, M. Volmer, *Z. Physik. Chem.*, 150A (1930) 203 – 213.

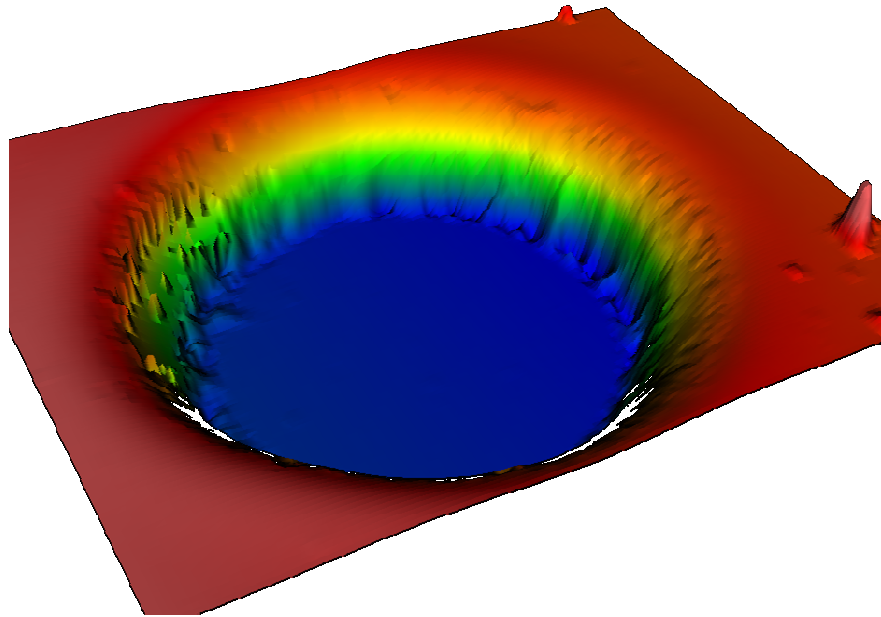
- 
- 18 – A. S. Bondarenko, G. A. Ragoisha, *J. Solid State Electrochem.*, 9 (2005) 845 – 849;
- 19 – O. Montgomery, H. Horwitz, *J. Clin. Invest.*, 29 (1950) 1120 – 1130.
- 20 – Jurgen Heinze, *Angew. Chem. Int. Ed. Eng.*, 32 (1993) 1268 – 1288.
- 21 – B. R. Scharifker. “*Microelectrode Technique in Electrochemistry*”, in *Modern Aspects of Electrochemistry*, J. O. M. Bockris, B. E. Conway, R. E. White , Vol. 22, pp. 467–519, Plenum Press, New York and London, 1992.
- 22 – M. I. Montenegro, M. A. Queirós, J. L. Daschbach, *Microelectrodes: Theory and Applications*, NATO ASI Series, Vol. 197, Kluwer, Dordrecht, 1991.
- 23 – Xudong Xie, Doris Stüben, Zsolt Berner, Jörg Albers, R. Hintsche , E. Jantzen, *Sensors and Actuators B*, 97 (2004) 168 – 173.
- 24 – A. N. Correia, L. H. Mascaro, S. A. S. Machado, L. H. Mazo e L. A. Avaca, *Química Nova*, 18 (1995) 475 – 480.
- 25 – S. M. Silva, C. R. Alves, A. N. Correia, A. L. Nobre, S. A. Machado, L. H. Mazo, L. A. Avaca, *Química Nova*, 21 (1998) 78 – 85.
- 26 – Cynthia G. Zoski, *Electroanalysis*, 14 (2002) 1041 – 1051.
- 27 – K. Štulík, C. Amatore, K. Holub, V. Mareèek, W. Kutner, *Pure Appl. Chem.*, 72 (2000) 1483 – 1492.

- 
- 28 – R. Ferrigno, P.F. Brevet, H.H. Girault, *Electrochim. Acta*, 42 (1997) 1895 – 1903.
- 29 – R. Ferrigno, H.H. Girault, *J. Electroanal. Chem.*, 492 (2000) 1 – 6.
- 30 – Stanley Bruckenstein, Jolanta Janiszewska, *J. Electroanal. Chem.*, 538 – 539 (2002) 3 – 12.
- 31 – C. Beriet, R. Ferrigno, H.H. Girault, *J. Electroanal. Chem.*, 486 (2000) 56 – 64.
- 32 – F.L. Qiu, Adrian C. Fisher, *Electrochemistry Communications*, 5 (2003) 87 – 93.
- 33 – Cynthia G. Zoski, Michael V. Mirkin, *Anal. Chem.*, 74 (2002) 1986 – 1992.
- 34 – J. Galceran, S.L. Taylor, P.N. Bartlett, *J. Electroanal. Chem.*, 476 (1999) 132 – 147.
- 35 – C. Amatore, I. Svir, *J. Electroanal. Chem.*, 557 (2003) 75 – 90.
- 36 – H. J. Lee, C. Beriet, R. Ferrigno, H.H. Girault, *J. Electroanal. Chem.*, 502 (2001) 138 – 145.
- 37 – B. R. Scharifker, *J. Electroanal. Chem.*, 240 (1988) 61 – 76.
- 38 – T. J. Davies, S. Ward-Jones, C. E. Banks, J. Del Campo, R. Mas, F. X. Munoz, R. G. Compton, *J. Electroanal. Chem.*, 585 (2005) 51 – 62.

- 
- 39 – T. J. Davies, C. E. Banks, R. G. Compton, *J. Solid State Electrochem.*, 9 (2005) 797 – 808.
- 40 – C. Amatore, J. M. Savéant, D. Tessier, *J. Electroanal. Chem.*, 147 (1983) 39 – 51.
- 41 – M. Kudera, H.O. Hill, P. J. Dobson, P. A. Leigh, W. S. McIntire, *Sensors*, 1 (2001) 18 – 28.
- 42 – R. Feeney, S. P. Kounaves, *Electroanalysis*, 12 (2000) 677 – 684.
- 43 – O. Koster, W. Schuhmann, H. Vogt, W. Mokwa, *Sensors and Actuators B*, 76 (2001) 573 – 581.
- 44 – R. Ferrigno, P.F. Brevet, H.H. Girault, *Electrochim. Acta*, 42 (1997) 1895 – 1903.
- 45 – K. Besocke, S. Berger, *Rev. Sci. Instrum.*, 47 (1976) 840 – 842.
- 46 – Lord Kelvin, *Philos. Mag.*, 46 (1898) 82 – 120.
- 47 – L. Cheran, M. Thompson, *Analyst*, 124 (1999) 961 – 970.
- 48 – G. Binnig, C. F. Quate, C. Gerber, *Phys. Rev. Lett*, 56 (1986) 930 – 933 .
- 49 – N. G. Orjia, R. G. Dixonb, J. Fub and T. V. Vorburgerb, *Wear*, 257 (2004) 1264 – 1269.

### 3. Conical recessed gold microelectrode arrays produced during photolithographic methods: characterisation and causes

---



#### 3.1. ABSTRACT

---

In this work, surface imaging techniques such as scanning Kelvin nanoprobe (SKN), scanning electron microscopy (SEM) and white light interferometer microscopy show that conical recessed electrodes with gradient potential along the recessed walls are formed during standard photolithographic methods for producing microelectrode arrays. The experimental behaviour of these electrode arrays fits very well with the numerical solution using optimal quasi-conformal mappings proposed recently by Amatore and co-workers [C. Amatore, A. Oleinick, I. Svir, *J. Electroanal. Chem.* 597 (2006) 69; C. Amatore, A. Oleinick, I. Svir, *J. Electroanal. Chem.* 597 (2006) 77]. The possible reasons for the formation of conical recesses are discussed.

### 3.2. INTRODUCTION

---

The first use of microelectrodes was reported in 1940 when Davies and Brink used a platinum microdisc to measure oxygen in muscle tissue<sup>1</sup>. However, electrodes of micrometer dimensions were not used widely in electrochemical research until 1980 when Fleischmann et al.<sup>2</sup> showed that such electrodes have significant quantitative effects and qualitative advantages. Microelectrodes have been shown to have much reduced ohmic drops and capacitive effects making them usable in the absence of supporting electrolyte<sup>3,4,5,6,7,8</sup>. There has been a growing interest in the fabrication and application of microelectrodes as new technologies are being sought for improving the efficiency and sensitivity of microelectrodes. However, there appears to be no consistent definition of microelectrode dimensions, although there is a general agreement on the essential concept, which is that the electrode is smaller than the scale of the diffusion layer<sup>3,4,6,9,10,11</sup>.

In order to maximise sensitivity, microelectrodes are fabricated in arrays<sup>8,12,13,14,15</sup>.

When fabricating a microelectrode array (MEA), the most sought after geometry is the in-laid microdisc, as the theory of electrochemical behaviour of single microdisc electrodes is now well established, with precise analytical expressions. However, the theory of microelectrode arrays is still not fully developed due its complexity.

Unlike single microelectrodes, for arrays the geometry, i.e. the ratio ( $d/a$ ) of inter-electrode distance ( $d$ ) to the microelectrode radius ( $a$ ) have to be considered, in order to get a collective current response while maintaining the advantageous features of a single microelectrodes. The response of an

array can be simply the sum of the individual response of each microelectrode, when the inter-electrode distance is large compared to the individual diffusion layers. However, there is no consensus about the optimal ratio  $d/a$  above which the response of the microelectrode arrays will be the sum of the individual responses.

Thus, for electroanalytical purposes, by far the most important property of microelectrode arrays is that the centre-to-centre distance separation between two microelectrodes, “ $d$ ”, must be large enough to avoid diffusional overlap between adjacent microelectrodes (“shielding effect”), but not too large to result in inefficient use of space, as show Figure 1.

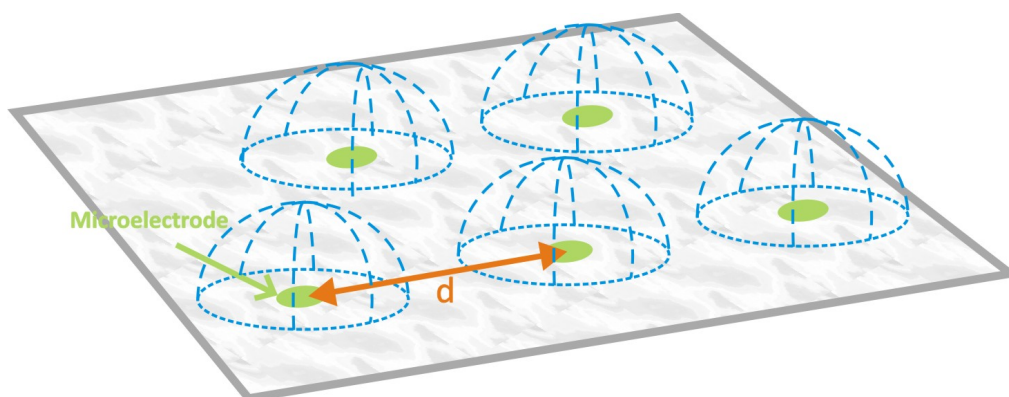


**Figure 1** – *Distribution of microelectrodes in order to avoid diffusional overlap*

Different geometries have been considered for the construction of MEAs. These include arrays of band, disc or irregularly shaped microelectrodes assembled in a number of possible patterns such as hexagonal, square or disordered (random) patterns<sup>12,13,14</sup>.



The hexagonal array (Figure 2) is deemed to be the geometry of choice as this is the most efficient arrangement for packing cells in a limited space.

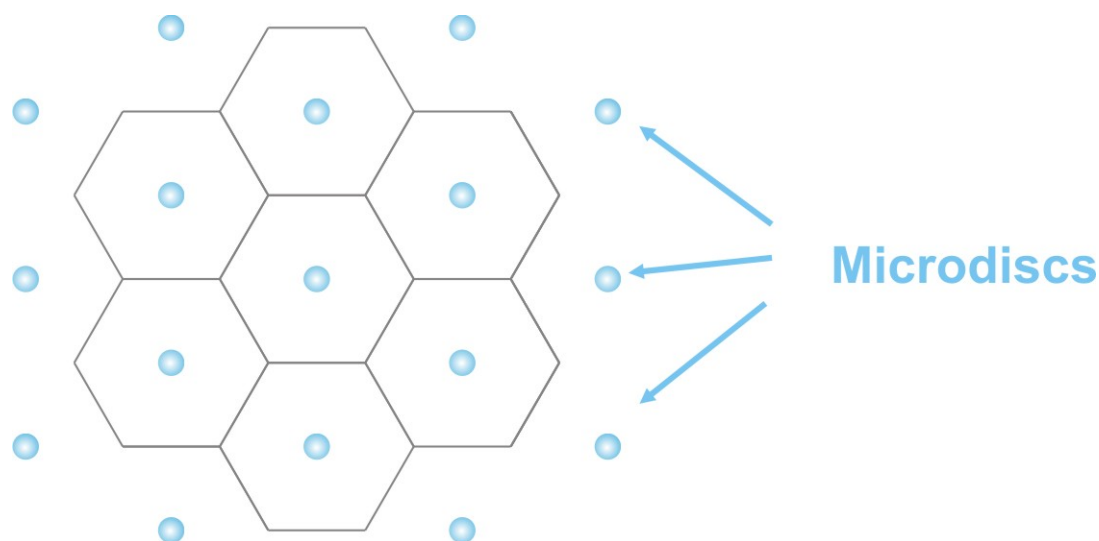


**Figure 2** – *Microelectrode arrays at hexagonal pattern.*

In order to check the quality of the devices, several simulation methods have been discussed in the literature, using different voltammetric techniques for electrochemical characterisation behaviour, such as cyclic voltammetry<sup>14,16</sup>, chronoamperometry<sup>12</sup>, and scanning probe techniques for analysis surface characteristics, such as AFM (atomic force microscopy)<sup>8</sup>, SEM (scanning electron microscopy)<sup>17</sup> and SECM (scanning electrochemical microscopy)<sup>16</sup>.

Several publications on the theoretical treatment of mass transport can be found in the literature. Compton et al.<sup>14</sup> proposed a 2D simulation method for cyclic voltammetry and linear sweep voltammetric response of regular and random microdisc, based on the diffusion domain approximation initially proposed by Amatore et al.<sup>18</sup>. They have shown that there are three parameters which can have an impact on the required "d". These parameters are the disk radius (a), the diffusion coefficient (D), and the scan rate to be

used ( $u$ ). The proposed simulation was a significant advance, however, a universal relationship which could be used to evaluate the required  $d$ , given  $a$ ,  $u$ , and  $D$ , was still lacking<sup>6,19,20</sup>.

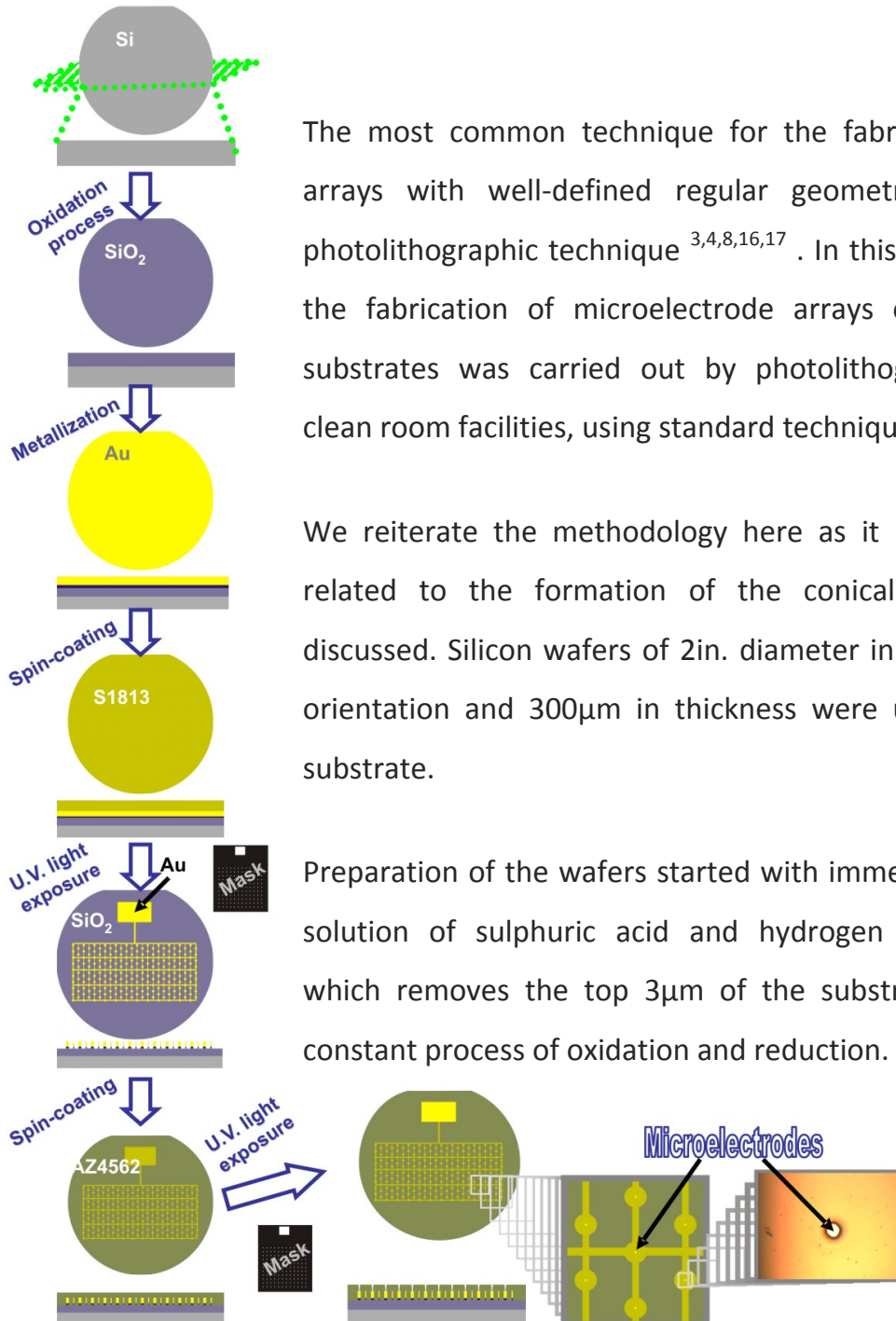
To add to the complexity of the theory, although the inlaid microdisc microelectrode can be considered as one the most popular microelectrode geometries, there is also a need to consider recessed and protruding microdiscs as photolithographic microfabrication techniques often result in non-ideal geometries. This gives rise to local concentration gradients proportional to the current densities resulting in singularities at the electrode-insulator surface, for example, which could not be accounted for by conventional numerical solutions.

This problem has been recently addressed by Amatore and co-workers<sup>21,22</sup>, who have proposed the application of the quasi-conformal mappings for precise numerical solution of 2D diffusion at inlaid microdisc and recessed or protruding microelectrodes with varying angles of inclination. The authors have presented a general approach for the simulation of recessed and protruding microelectrodes and their arrays using this approach.

In this chapter, analysis of microelectrode arrays produced using photolithographic techniques is presented and the possible reasons for formation of conical microdisc electrodes and analysis of their behaviour using SEM, Scanning Kelvin Nanoprobe (SKN) technology and traditional electrochemical methods.

### 3.3. EXPERIMENTAL

#### 3.3.1. Microfabrication



The most common technique for the fabrication of arrays with well-defined regular geometry is the photolithographic technique<sup>3,4,8,16,17</sup>. In this research, the fabrication of microelectrode arrays on silicon substrates was carried out by photolithography in clean room facilities, using standard techniques.

We reiterate the methodology here as it is directly related to the formation of the conical recesses discussed. Silicon wafers of 2in. diameter in the (100) orientation and 300 $\mu$ m in thickness were used as a substrate.

Preparation of the wafers started with immersion in a solution of sulphuric acid and hydrogen peroxide, which removes the top 3 $\mu$ m of the substrate via a constant process of oxidation and reduction.

**Figure 3** – Scheme of the conical recessed microelectrode arrays microfabrication by photolithography.

Immediately prior to oxidation, the silicon wafers were etched in 10% hydrofluoric acid (HF) solution in order to ensure removal of any native oxide. The wafers were then placed in a high temperature, steam atmosphere furnace for 1h, which produces a layer of silicon dioxide ( $\text{SiO}_2$ ) via consumption of the silicon surface.

The oxide thickness is dependent on growth time and furnace temperature, and typically 5000Å of oxide was produced. A metallization of 200 Å of chromium followed by 800Å of gold was then coated onto the oxide (the layer of chromium served to improve the adhesion between silicon and gold) using electron beam evaporation.

A wafer was then spin-coated with a positive photoresist (S1813 (Rohm and Haas UK Ltd., Dewsbury) and exposed to UV light for 5s through a mask containing the pattern for the electrodes and their interconnects.

With a positive photoresist, the areas exposed to UV light dissolve in the developer, AZ351, leaving photoresist on the wafer only in those places that were masked.

The wafer was then dipped in successive etching solutions to dissolve gold ( $4\text{KI}:\text{I}_2:8\text{H}_2\text{O}$  w/w) and chromium ( $2\text{K}_3\text{Fe}(\text{CN})_6:\text{NaOH}:8\text{H}_2\text{O}$  w/w) in the unprotected zones. After patterning, the S1813 photoresist was removed in acetone and a further 6  $\mu\text{m}$  thick layer of a different positive photoresist (AZ4562, (Clariant UK, Ltd., Northallerton) was spin-coated onto the device and exposed to UV light for 4 min through a mask containing the pattern for the microelectrodes and for the pad (external electronics) and cured at 110°C for 30 min. This step is crucial to the success of the reproduction of electrode fabrication.

It was done with the primary purposes of helping the resist to withstand chemical attack, and ensure a better adhesion to the metal to prevent seepage under the edge. As we will see later it also has an effect on the profile of the resist, and hence the associated recess. Development of the AZ4562 resist is carried out in AZ351 solution, as for the S1813 resist.

The structure of the devices is shown in Figure 4. The microelectrodes are located in the centre of each circle and they are connected to each other with tracks in order to minimise the possible existence of pinhole defects on the AZ4562 layer above the gold.

The microelectrode arrays are connected in a geometry that gives a minimal resultant capacitance in electrolyte solutions. Each microelectrode was found to have a conical recessed structure (Figure 5), resulting in conical recessed microelectrode arrays (CRMEAs).

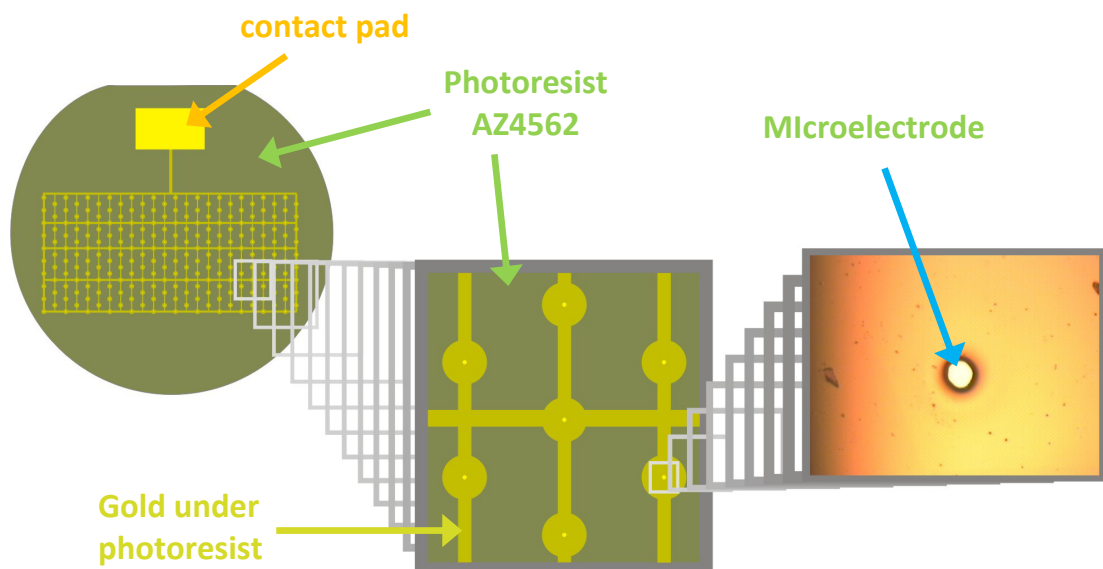


**Figure 4** – Structure of gold microelectrode array constructed by photolithography.

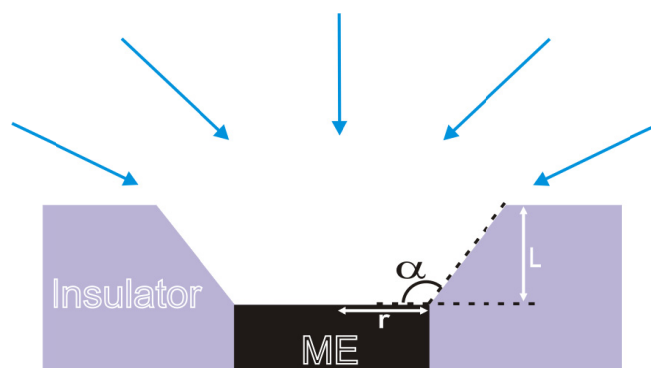


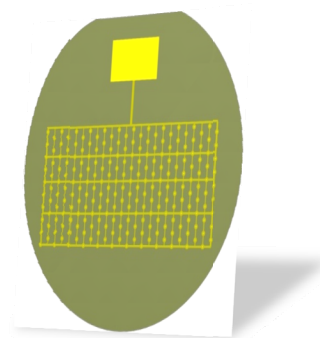
**Figure 5 – Geometry of conical recessed microelectrode.**

### 3.3.2. Electrochemical characterisation

The gold microelectrode arrays were made with  $d/a$  ratio (spacing between electrodes/radius of active site) large enough in order to avoid overlap between diffusion layers of each microelectrode, and consequently, independent responses of microelectrodes were expected. The main difference between the three devices characterised here (CRMEA 1, CRMEA 2 and CRMEA 3) was the radius of the active sites (Table 1).

**Table 1 – Characteristics of fabricated CRMEA**

| CRMEA | Z   | d<br>( $\mu\text{m}$ ) | L<br>( $\mu\text{m}$ ) | a<br>( $\mu\text{m}$ ) | d/r | L/r  |
|-------|-----|------------------------|------------------------|------------------------|-----|------|
| 1     | 228 | 1800                   | 6                      | 45                     | 40  | 0.13 |
| 2     | 228 | 1800                   | 6                      | 30                     | 60  | 0.20 |
| 3     | 228 | 1800                   | 6                      | 12                     | 150 | 0.50 |



Where:

Z is the number of microdiscs in the array.

d is the distance inter-electrode .

L is the depth of the cavity (cm).

a is the radius of microdisc.

The microelectrode arrays were characterised by cyclic voltammetry (CV) and chronoamperometry (CA).

Cyclic voltammetry (CV) in 1M sulphuric acid from -0.2 and 1.6 V (vs. Ag/AgCl/KCl 3.5M) was employed as a measure of the cleanliness of the gold surface. Stripping charges higher than  $1.4 \mu\text{C cm}^{-2}$  were obtained for the microelectrode arrays.

A multichannel potentiostat model VMP (Perkin–Elmer Instruments) was used for electrochemical measurements. A three electrode cell containing Ag/AgCl (3.5 M KCl), Pt foil ( $A = 1 \text{ cm}^2$ ) and the microelectrode array were employed as reference, auxiliary and working electrodes, respectively. The cell was placed in a Faraday cage to eliminate external interference. All potentials in this work are reported with respect to Ag/AgCl (3.5 M KCl). The measurements were made at 25 K.

Analysis for gold CRMEAs were performed at a scan rate of  $5 - 150 \text{ mV s}^{-1}$  (cyclic voltammetry) and from data acquired by stepping the potential from an initial potential 0.3 V to -0.4 V, at 20ms intervals (chronoamperometry), in solutions containing 0.01 M of probe molecule,  $\text{K}_3\text{Fe}(\text{CN})_6$  (Aldrich,  $D = 8.3 \times 10^{-6} \text{ cm}^2 \text{ s}^{-1}$ ) and 0.1 M  $\text{KNO}_3$  (BDH) as background electrolyte.

### **3.3.3. Surface analysis**

Scanning electron microscopy (Hitachi S2400 SEM - Hitachi High-Technologies Europe GmbH, Berkshire, UK), Zygo New View 100 White Light Interferometer microscopy (Zygo Co-op., Middlefield, CT, US) and scanning Kelvin nanoprobe microscopy (SKN) developed by Thompson et al.<sup>23</sup> was applied to measure the contact potential differences and thereby check the quality of the devices and their specifications such as microelectrode radius (a) and inclination angle  $\alpha$  (angle between the electrode surface and the recess walls).

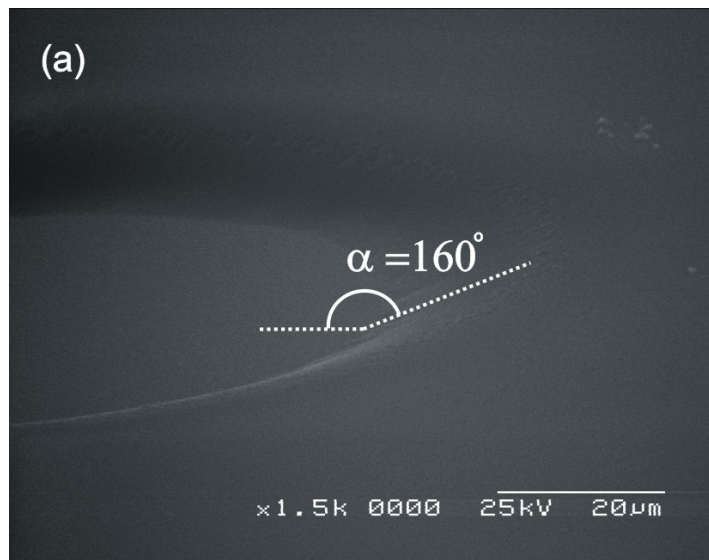


## 3.4. RESULTS AND DISCUSSIONS

---

### 3.4.1. Surface analysis

The SEM images (Figure 6) showed that the microelectrode arrays produced by the procedure described produced regular arrays with each microelectrode situated at the bottom of a conical recess with the walls inclined at 160 degrees from the electrode surface ( $\alpha = 0.9\pi$ ). The vertical depth of each microelectrode was 6  $\mu\text{m}$  and the distance “d” between each electrode was 1800  $\mu\text{m}$ .



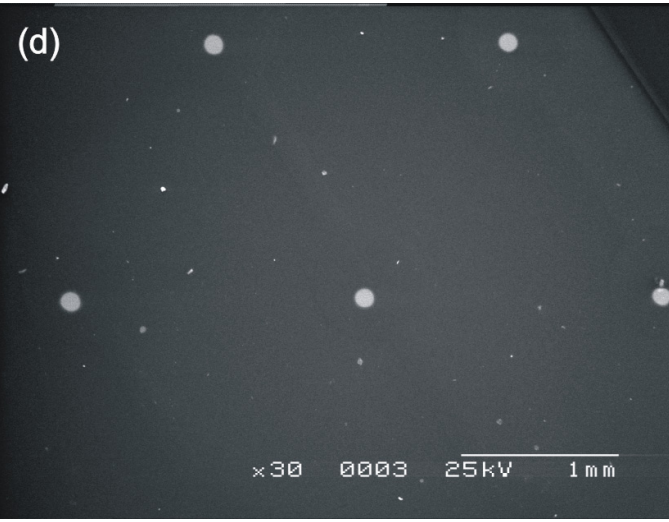
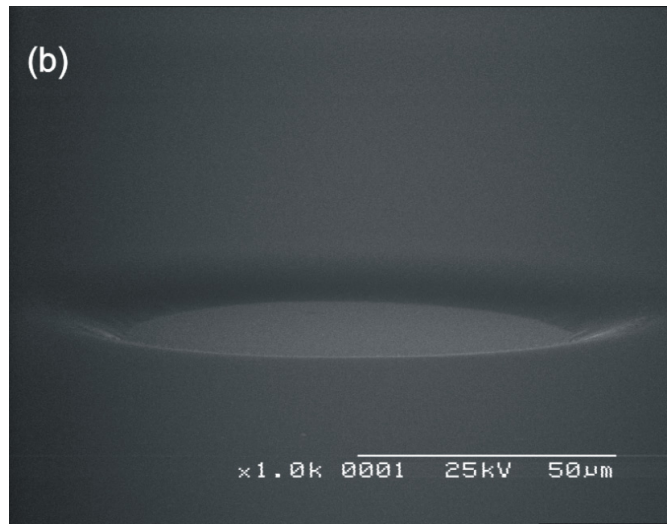


**Figure 6** – SEM images of (a,b) a conical recessed microelectrode (CRME) of  $a = 45\mu\text{m}$  and  $\alpha = 160$  degrees and (c,d) an overview of the conical recessed microelectrode array (CRMEA).

The radius of each microelectrode in the three devices used was 45, 30 and 12 $\mu\text{m}$  for device 1, 2 and 3 respectively (Table 1). The angle of inclination and microelectrode diameter was re-confirmed using a Zygo New View 100 White Light Interferometer microscope.

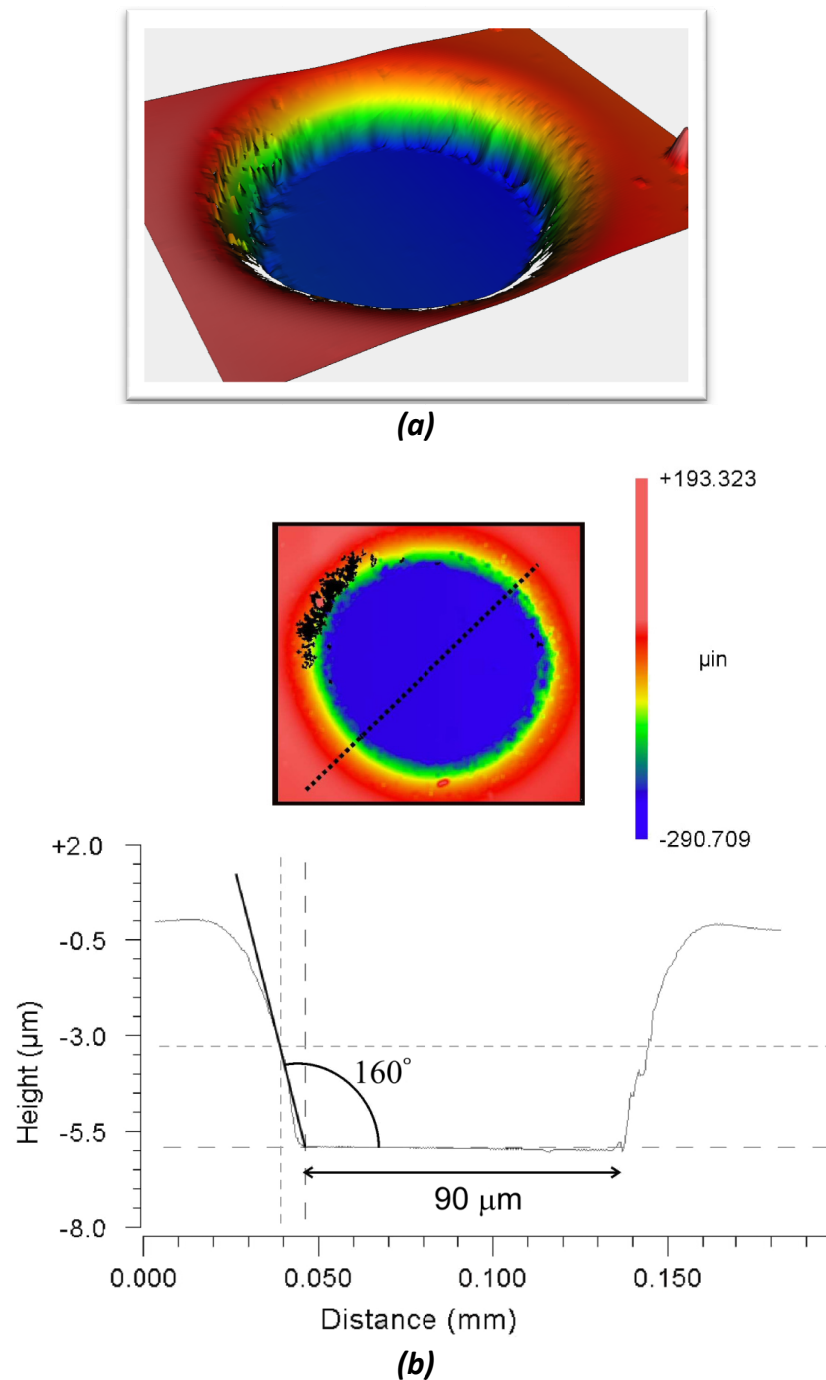


**Figure 7** – (a) Zygo White light interferometer image of a 45  $\mu\text{m}$  radius recessed microelectrode and (b) showing the measured angle and diameter.

A scanning Kelvin nanoprobe microscope with a tungsten nanotip probe of diameter 100 nm was also used for the first time to characterise individual microelectrodes. This method maps the contact potential differences between the tungsten nanotip and the microfabricated electrode thus enabling any variations in dielectric materials to be mapped. The principles underlying the measurement are briefly discussed.

The work function of an electronic conductor is defined as the difference between the Fermi energy and Volta Energy (Eq. (1)).

$$\phi = -e\Psi - E_F \quad \text{Eq. (1)}$$

Where,

$\phi$  is the work function.

$\Psi$  is the Volta potential.

$e$  is the unit charge.

$E_F$  is the Fermi level within the solid.

The Volta potential is the potential at ca. 10 nm from the surface where surface (image) forces do not affect the unit charge  $e$  (Figure 8). The Volta energy is unit charge  $\times$  the Volta potential ( $-e\Psi$ ). The electrical potential at infinity is assumed to be zero<sup>12</sup>. When two conductors with work functions  $\phi_1$  and  $\phi_2$  and Fermi levels  $E_{F1}$  and  $E_{F2}$  are contacted, the flow of charge

allows the Fermi levels to equalize giving rise to a potential difference called the contact potential difference, either  $V_C$  or CPD (Eq. (2)).

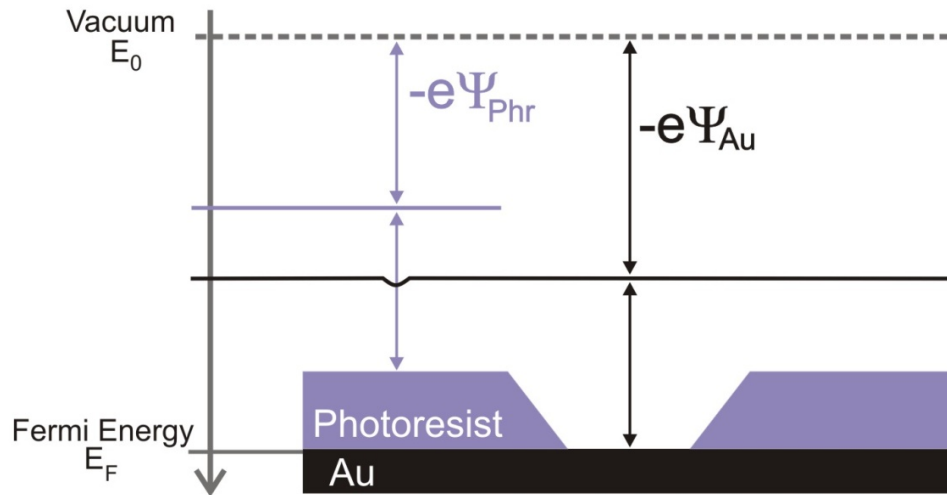


**Figure 8** – Difference of Volta energies ( $-e\Psi$ ) of gold (Au) and the photoresist (Phr).

$$V_C = \Delta\phi = (\phi_1 - \phi_2) \quad \text{Eq. (2)}$$

The application of a backing potential of equal and opposite sign to  $V_C$ , negates the surface charges and this potential is equal to the work function difference between the materials (Eq. (2)). To enable repeated measurements of  $V_C$ , a vibrating capacitance probe is used. Combining the equations for capacitance and the sinusoidal movement of the probe at equilibrium, an equation for the Kelvin current is derived as:

$$i_t = \frac{dQ}{dt} = (V + V_0) \frac{\epsilon\omega d_1 \sin(\omega t)}{(d_0 + d_1 \cos(\omega t))^2} \quad \text{Eq. (3)}$$

Where,

$d_0$  is the rest position.

$V_0$  is the voltage of the probe.

$d_1$  is the amplitude of vibration.

$V$  denotes the voltage at equilibrium between the probe and the sample.

$\epsilon$  the permittivity of the material.

$\omega$  is the angular frequency of vibration.

At equilibrium, when the contact potential is compensated by the backing potential, no current flows in the system and this null condition is detected in the SKN. In our work we used a scanning Kelvin nanoprobe (SKN) microscope with a tungsten nanotip probe of diameter 100 nm developed by Thompson et al.<sup>23,24,25</sup>.

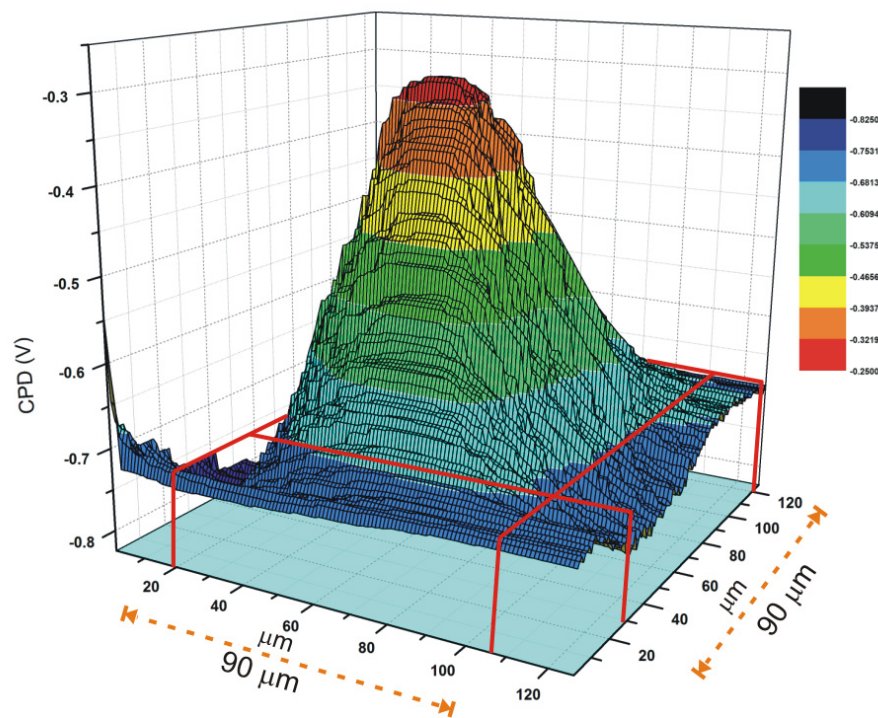
When a conical recess with a photoresist along the walls of the cavity is encountered by the SKN nanotip, the Volta potential and the corresponding work function of the sample and material change (Figure 8), giving the relationship<sup>26</sup>

$$\Delta\phi_{xs} = \phi_x - \phi_s = -e(\psi_x - \psi_s) \quad \text{Eq. (4)}$$

Where the subscript x refers to either the photoresist or the Au electrode and  $\phi_x$ ,  $\phi_s$  and  $\Delta\phi_{xs}$  are the work functions of the conical recess, the substrate and the difference, respectively.  $\psi_x$  and  $\psi_s$  are the Volta potentials of the

conical recess and the substrate, respectively. The difference in work function, therefore, arises from the change in the Volta potential when the vibrating tungsten tip which is at a fixed distance from the substrate encounters a recess.

The SKN scan of a single micro electrode from CRMEA 1 (Figure 9) shows an inlaid electrode radius of  $45\ \mu\text{m}$  in accordance with the SEM scans. The variation of the CPD values at increasing depth of the cone show a graded exposure of the underlying layer.



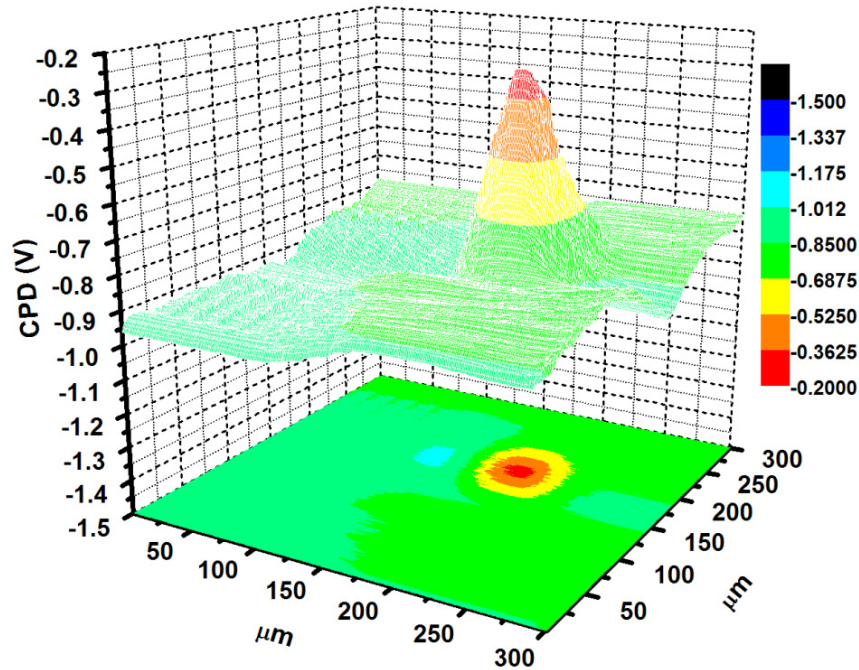


**Figure 9** – Scanning Kelvin nanoprobe images of a microelectrode with a radius of  $45\ \mu\text{m}$  showing the gradient contact potential differences.

Thus surface analysis techniques lead us to believe that the geometry of microelectrodes produced as standard with the photolithography protocol described above is conical recessed. This is clearly evident from the SKN scans which show a decrease in CPD values with increasing depth.

The explanation for the resist profile is most likely to lie in a combination of factors. First, the mask itself, which uses a photosensitive emulsion on glass, does not have a smooth transition between light and dark at the edges: it has been designed to have more of a gradation ('grey area') (Figure 10), which will give a corresponding effect on the amount of light passing through to the resist. Second, on exposure the intensity of the UV light decreases with depth: this is a significant issue for a  $6\ \mu\text{m}$  thick resist. Overexposure of the resist can also lead to an angled profile.



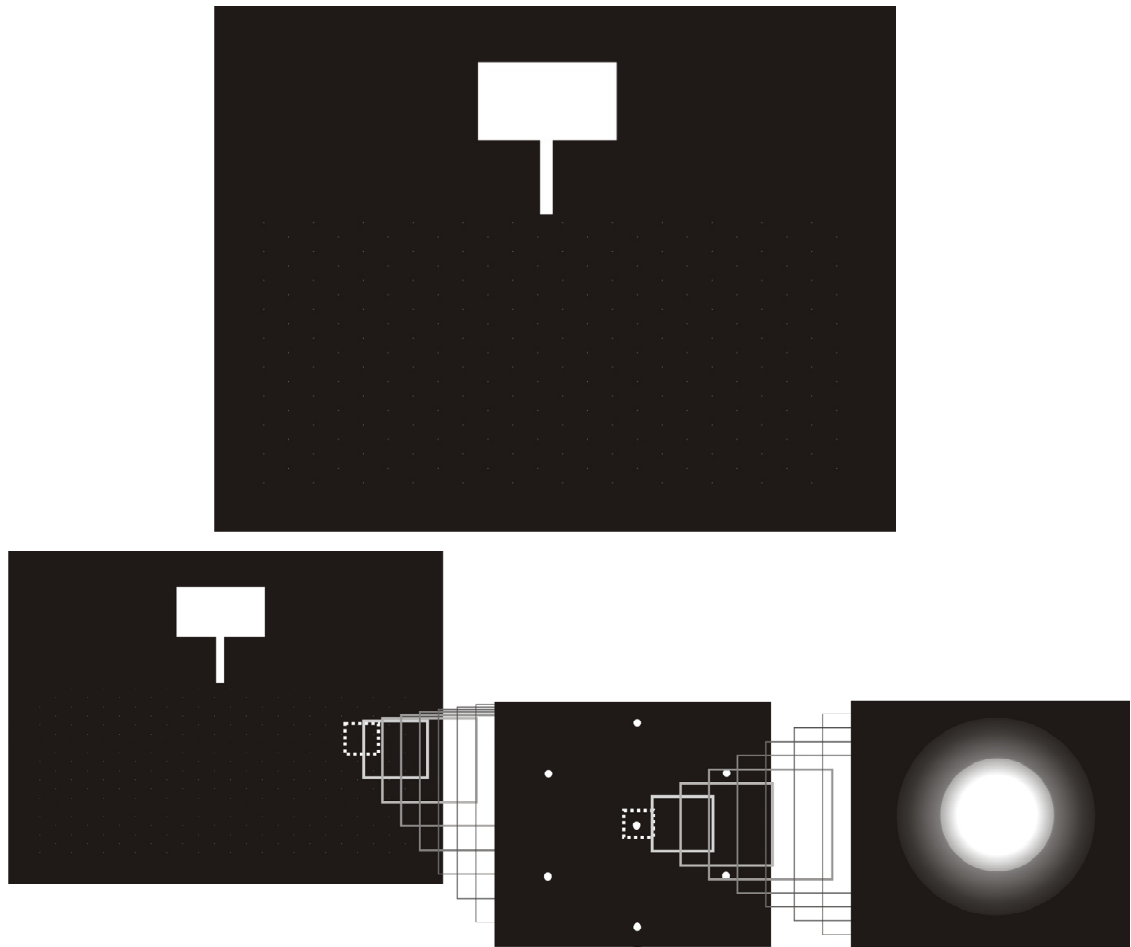


**Figure 10** – *General View of the glass mask and smooth transition between light and dark at the edges in the mask.*

Finally, for a thick resist the pre-exposure bake can rarely remove all the casting solvent. Excess solvent has the effect of lowering the resist's glass transition temperature, which in the post exposure bake at 110 °C will lead to the resist reflowing (Figure 11).

The control of the above factors to produce a reliable process angle is a complex process for thick resists, and is something we can overcome and make the sidewall vertical with additional processing techniques, but previous experience has shown us that a vertical profile is not advantageous when making microelectrodes. This is because the electrolyte tends to seep

under the edge of the resist where it touches the electrode surface, with subsequent unwanted effects on the measurements.

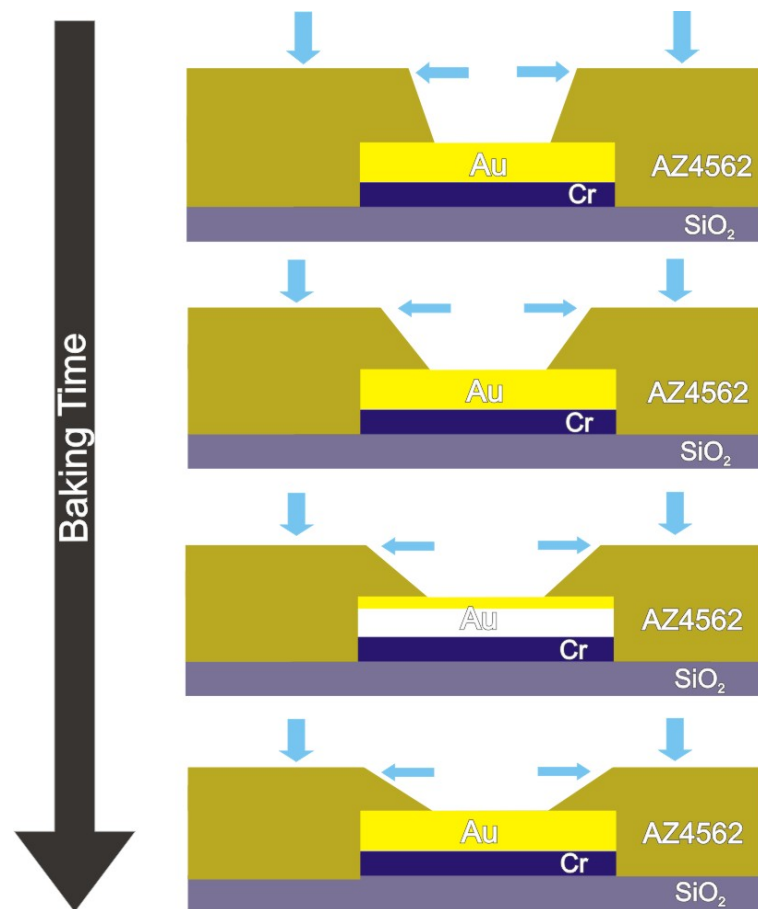


**Figure 11** – Photoresist reflowing process at 110°C.

Photoresists profiles used in the IC industry (Integrated Circuit) do not have a conical profile because they use chrome on glass masks (a definitive transition between dark and light areas), the photoresists used are much thinner ( $\sim 1\mu\text{m}$ ) and the post-exposure bake regimes are less extreme than used in this case.

### 3.4.2. Electrochemical characterisation

The microelectrodes were tested to assess their response as recessed, conical recessed and inlaid electrode.

For inlaid microdisc electrodes under steady-state conditions, the current response is given by:

$$i_{lim} = 4 Z n F D C_{\infty} a \quad \text{Eq. (5)}$$

Where:

$n$  is the number of electrons involved in ox/red.

$Z$  is the number of microdiscs in the array.

$F$  is the Faraday constant ( $96484.6 \text{ C mol}^{-1}$ ).

$D$  is the diffusion coefficient ( $\text{cm}^2 \text{ s}^{-1}$ ).

$C_{\infty}$  is the bulk concentration ( $\text{mol cm}^{-3}$ ).

$a$  is the radius of microdisc (cm).

For a recessed microdisc, Bond et al. derived steady-state current equation for predicting the steady state limiting current of an isolated recessed microdisc electrode by a factor  $L$ .<sup>27</sup>

$$i_{lim} = 4 Z n F D C_{\infty} a \left( \frac{\pi a}{\pi a + 4L} \right) \quad \text{Eq. (6)}$$

where  $L$  is the depth of the cavity (cm).

However, Bond et al <sup>27</sup> clearly pointed out that this equation is inappropriately to shallow recessed microdiscs, since there are significant discrepancies in the experimental responses predicted by the theoretical treatment.

Nevertheless several authors have applied this theory to microelectrode arrays with shallow recesses and to single recessed microdiscs <sup>28</sup>.

To fill this gap for Bond's equation, Ferrigno et al <sup>28</sup> have proposed an expression that predicts the steady state current at the recessed microdisc based on curve fitting simulated data which is claimed to be an improvement on Eq. (6) for shallow recesses (in case of L/a ratio less than unity).

$$i_{lim} = 4 Z n F D C_{\infty} a e^{\frac{-0.96 L}{a}} \quad \text{Eq. (7)}$$

The responses predicted using the equations give by Bond et al.<sup>27</sup> and Ferrigno et al <sup>28</sup> can be evaluating from the following graph:

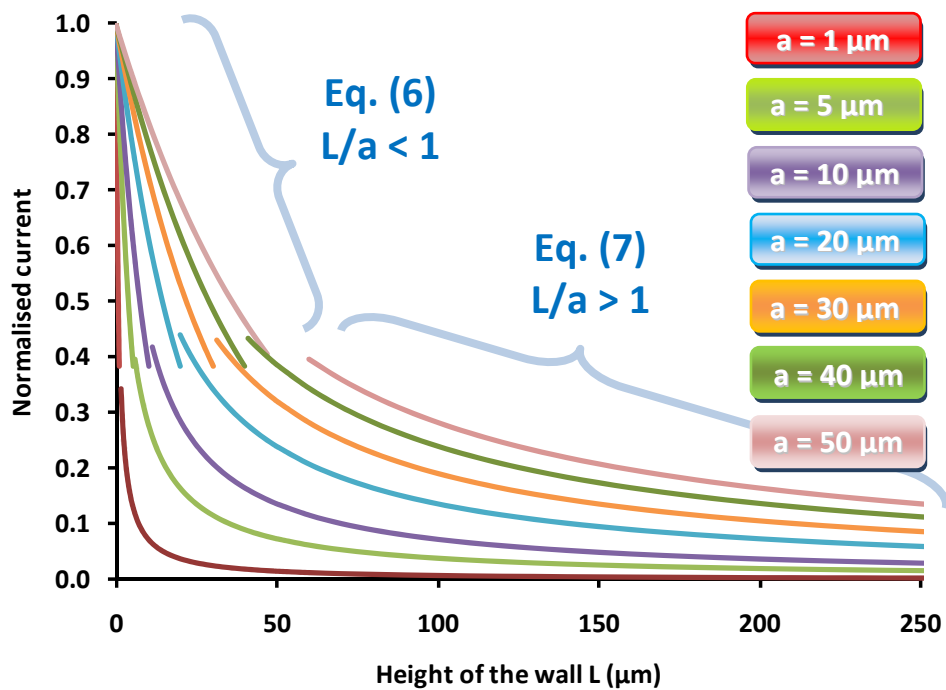


**Figure 12** – Variation of the normalised current against the height of the side wall  $L$ .

From this graph, one can see that the normalised current decrease in an exponentially order with the increase of the height of the side wall  $L$ , i.e., from shallow to deep holes. This fact is even more pronounced in case of small microelectrodes. In all situations, the  $L/a = 1$  limit region is around 0.4 and it is very difficult to predict the response for larger radius because the different currents give by Eq. (6) and Eq. (7).

The fabricated CRMEAs have  $L/a$  ratio less than the unity, means that they are situated in a narrow zone of the graph where the variation is higher implying that the response changes a lot even with slight alterations on the MEA characteristics.

Initially, the CRMEAs were electrochemically characterised and the experimental response was compared with the theoretical steady-state current obtained by Eq. (5) and Eq. (7).

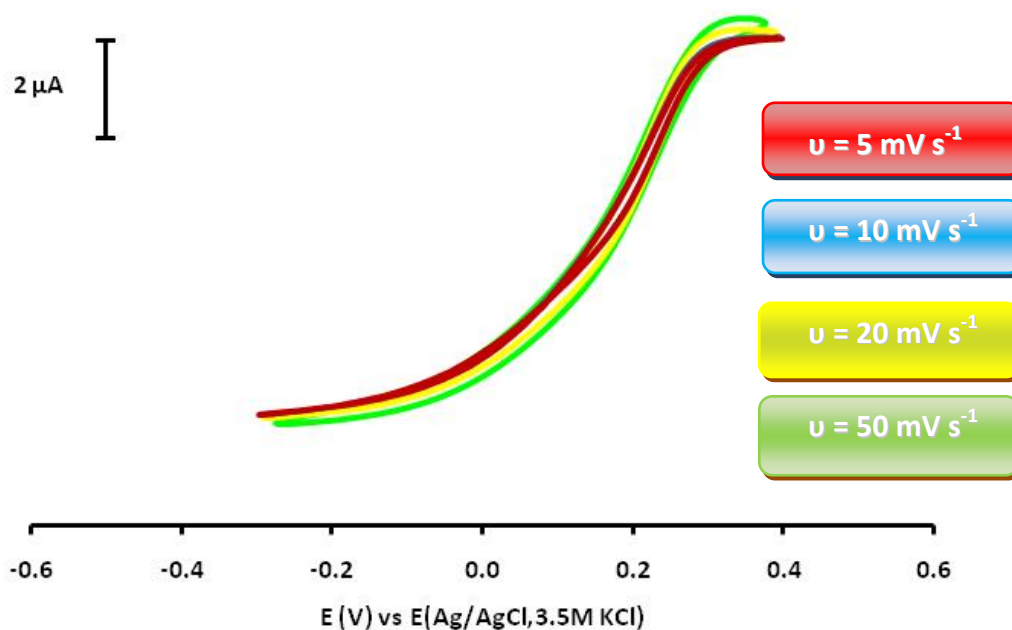


**Figure 13** – Cyclic voltammograms using MEA 3 ( $a = 12 \mu\text{m}$ ) at different scan rates ( $5\text{--}50 \text{ mVs}^{-1}$ ) in the presence of the probe molecule –  $\text{K}_3\text{Fe}(\text{CN})_6$  at  $0.01\text{M}$  in  $0.1\text{M KNO}_3$

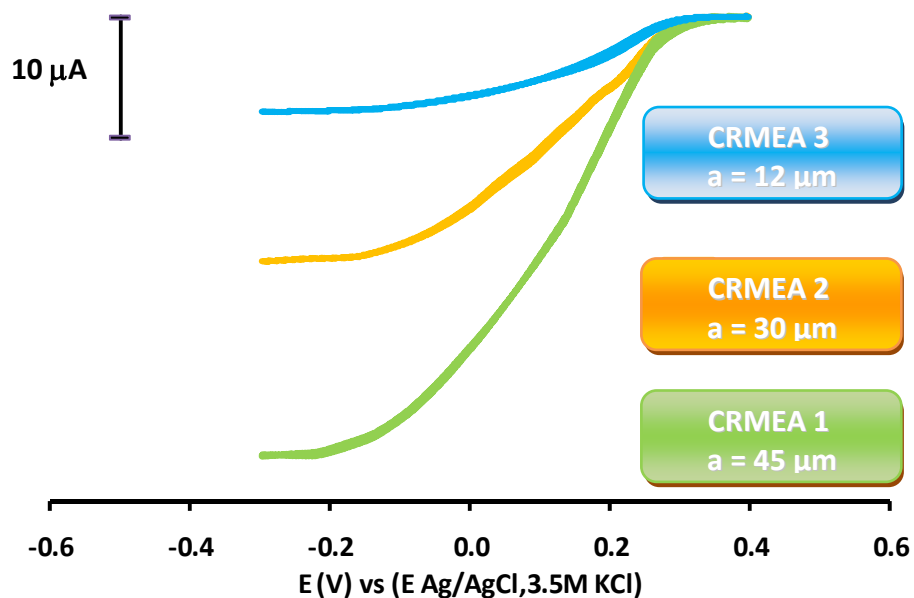


**Figure 14** – Cyclic voltammograms using using all CRMEAs at  $5 \text{ mVs}^{-1}$  in the presence of the probe molecule –  $\text{K}_3\text{Fe}(\text{CN})_6$  at  $0.01\text{M}$  in  $0.1\text{M KNO}_3$

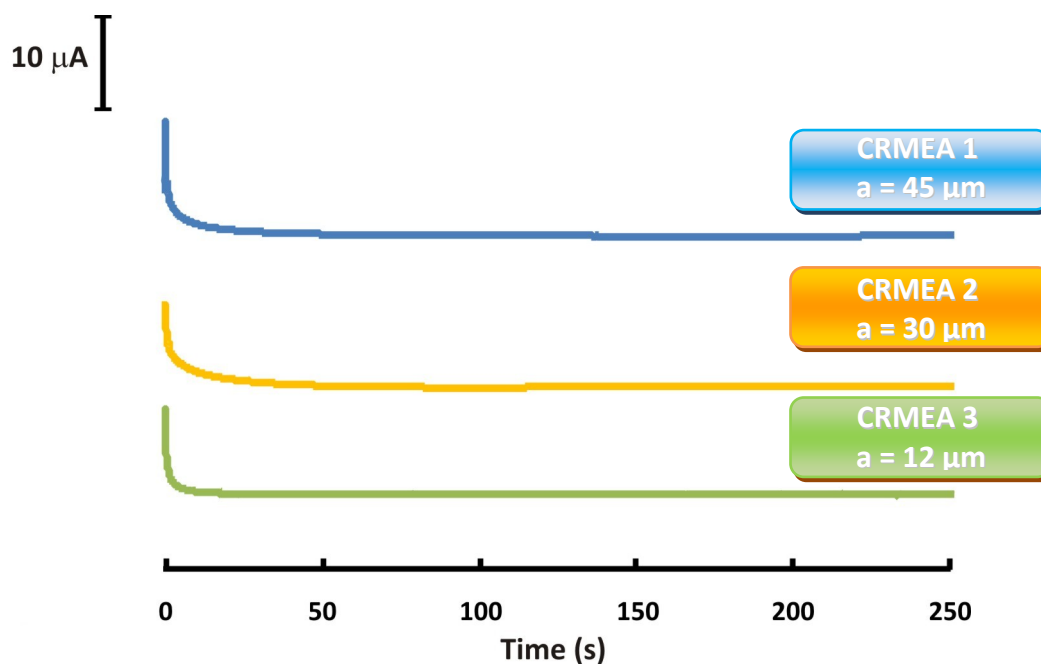


**Figure 15** – Chronoamperometric response for different CRMEAs in the presence of the probe molecule –  $K_3Fe(CN)_6$  at 0.01M in 0.1M  $KNO_3$ .

Figure 13 shows the CVs for CRMEA 3 ( $a = 12 \mu\text{m}$ ) at scan rates 50-5 mV/s. Sigmoidal voltammograms with negligible hysteresis were observed (Figure 14) at a scan rate of 5 mV/s for all three conical recessed microelectrode arrays, indicating that a steady-state is reached due to the radial diffusion at slower scan rates. The limiting current redox reaction was constant up to 200  $\text{mV s}^{-1}$ . Above this sweep rate, an increase in the limiting current was observed and the voltammogram began to acquire a peak-shape.

The  $d/a$  ratio in all devices are large enough in order to avoid overlap between diffusion layers ( $d/a > 40$ ). The steady-state currents from the electrochemical characterisation of the CRMEAs were compared with theoretical values calculated from Eq. (5) and Eq. (7).

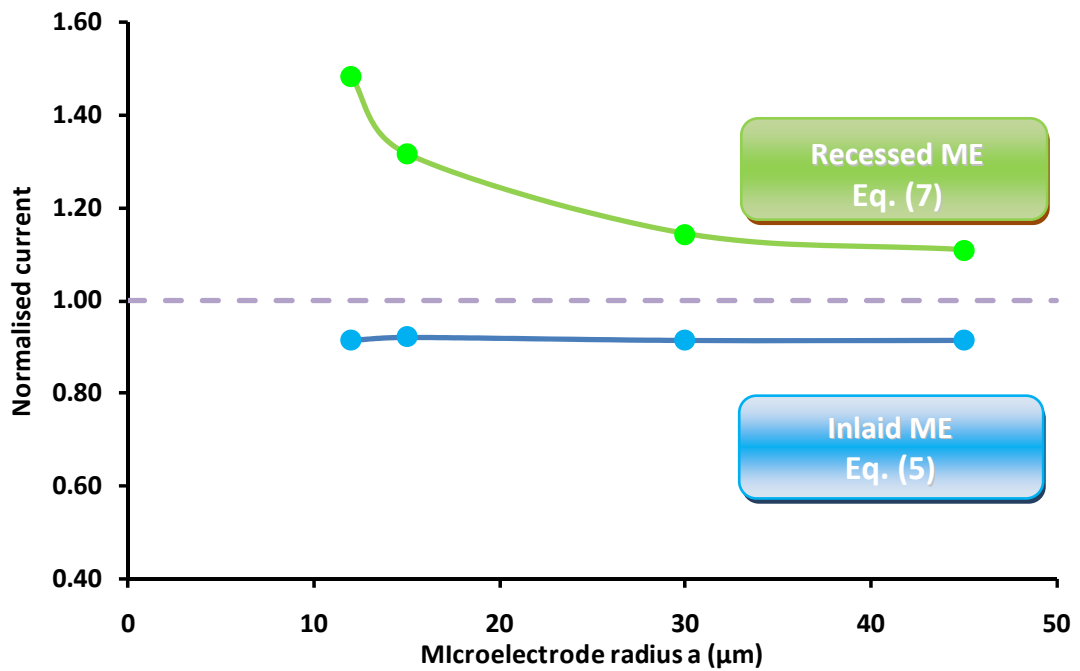


Figure 16 – Variation of the normalised current for different equations with variation of microelectrode radius.

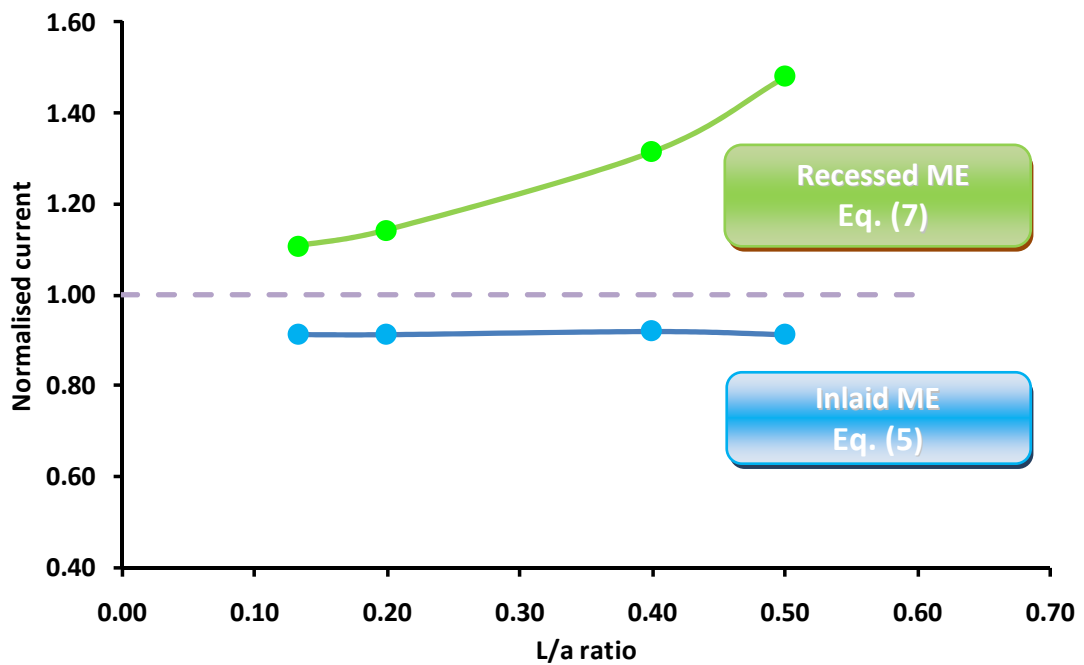


Figure 17 – Variation of the normalised current for different equations with variation of L/a ratio.



**Table 2** – Comparison between experimental and theoretical results.

| device | a           | Z   | d    | L           | d/a | L/a  | $i_{lim}$ ( $\mu A$ ) |                       | $i_{nor}$ |         |
|--------|-------------|-----|------|-------------|-----|------|-----------------------|-----------------------|-----------|---------|
|        | ( $\mu m$ ) |     |      | ( $\mu m$ ) |     |      | CV                    | CA                    | Eq. (5)   | Eq. (7) |
| 1      | 45          | 228 | 1800 | 6           | 40  | 0.13 | 35.5<br>( $\pm 0.2$ ) | 35.8<br>( $\pm 0.1$ ) | 1.1       | 0.9     |
| 2      | 30          | 228 | 1800 | 6           | 60  | 0.20 | 19.8<br>( $\pm 0.2$ ) | 19.6<br>( $\pm 0.1$ ) | 1.1       | 0.9     |
| 3      | 12          | 228 | 1800 | 6           | 150 | 0.50 | 8.1<br>( $\pm 0.2$ )  | 8.0<br>( $\pm 0.1$ )  | 1.5       | 0.9     |

In a previous paper, Grancharov et al. <sup>8</sup> have shown that for gold microelectrodes made using a similar process, with radii 15  $\mu m$  and depth 6  $\mu m$ , the normalised current was 0.92 and 1.32, for Eq. (5) and Eq. (7) respectively, similar to the trend observed in this works, and can be observed in the previous figures (Figure 16 and Figure 17) .

Note that the normalised current for the recess electrode is high than unity. The response for this type of electrode geometry is in between those two equations, but is close to the predicted response from inlaid equation, because with L/a ratio less than 0.5, the microelectrode has a shallow hole. As the L/a ratio increase, the close the response is compared to inlaid electrode.

The results show that for all three devices, the normalised current for Eq. (7) increases as L/a ratio increases (Table 2). In contrast, the normalised current for Eq. (5) remains constant ( $\sim 0.91$ ), independently of L/a value.

The microelectrode behaviour was further proved by the chronoamperometric response (Figure 15) of the devices.

For a microelectrode array, chronoamperometric responses are complex and depend on the time frame of the experiment. At short times, the array behaves as individual electrodes and the response to a potential step shows linear diffusion (Cottrellian behaviour) since no interference from overlapping diffusion occurs. At longer times, this behaviour changes to a mixed regime where hemispherical diffusion prevails and this regime is finally converted again to one of planar diffusion. In this last case, the diffusion layers fully overlap and the entire array behaves as a macroelectrode whose area is equal to the total geometric surface area.

Shoup and Szabo<sup>29</sup> have suggested a digital simulation for chronoamperometric response of a microelectrode array. According to this theory, the current response of a hexagonal arrangement of an infinite number of microdisc interfaces is:

$$i(\tau, \sigma) = i_{lim} \cdot f(\tau, \sigma) \quad \text{Eq. (8)}$$

Where  $f(\tau, \sigma)$  is the function of the experimental time and the geometry of the microelectrode array, and is:

$$f(\tau, \sigma) = \frac{\sqrt{\pi}}{2\sqrt{\tau}} + \frac{\pi}{4} + \left(1 - \frac{\pi}{4}\right) \exp\left[-\frac{0.7823\theta^2(3-2\theta)}{\sqrt{\tau}}\right] - \exp\left\{\frac{-\left[\frac{\theta\sqrt{\pi}}{2(1-\theta)} + 0.7823\theta^2(3-2\theta)\left(1 - \frac{\pi}{4}\right)\right]}{\sqrt{\tau}}\right\} \left(1 + \frac{3\theta^3\sqrt{\pi}}{2\tau(1-\theta)}\right)^{-1} \quad \text{Eq. (9)}$$

Where  $\tau$  is the dimensionless time and  $\sigma$  the coverage array:

$$\tau = \frac{4Dt}{a^2} \quad \text{Eq. (10)}$$

$$\theta = \left(\frac{2a}{d}\right)^2 \quad \text{Eq. (11)}$$

Where:

D - Diffusion coefficient ( $\text{cm}^2\text{s}^{-1}$ )

t – Reaction time (s)

a – Microelectrode radius (cm)

d – Distance inter-electrode (cm)

The comparison of the chronoamperometric results with the digital simulation indicates that the experimental response is close to the simulation performed using Eq. (5) corresponding to the cyclic voltammetry behaviour.

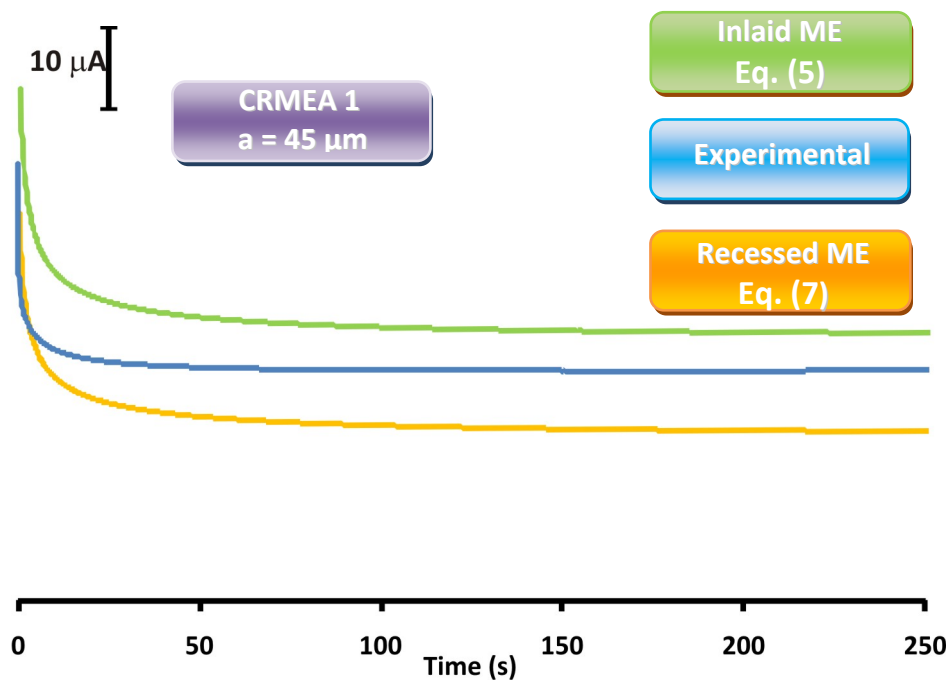


**Figure 18** – Comparison of the chronoamperometric response of experimental and simulated current using CRMEA 1.

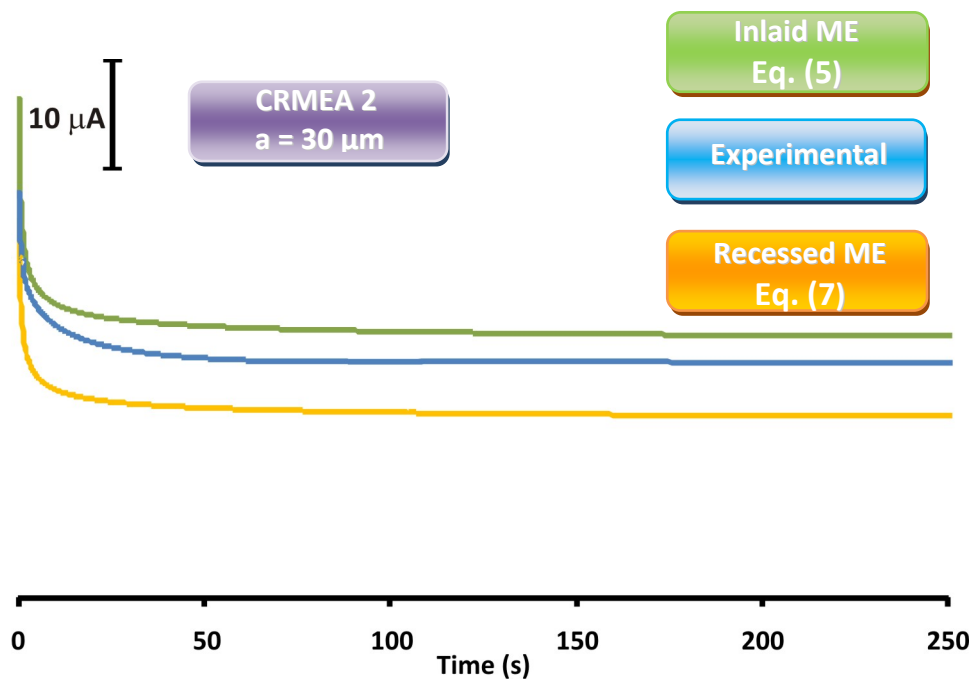


**Figure 19** – Comparison of the chronoamperometric response of experimental and simulated current using CRMEA 2.

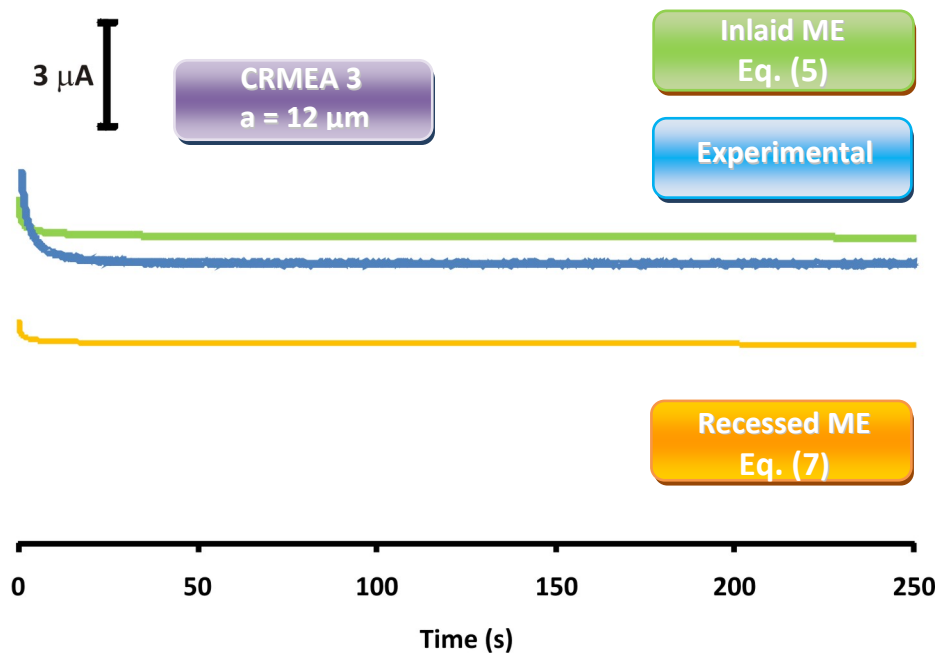


**Figure 20** – Comparison of the chronoamperometric response of experimental and simulated current using CRMEA 2.

Recently, Amatore et al.<sup>21</sup> proposed a generalized solution based on the application of the quasi-conformal mappings for efficient numerical solution of 2D diffusion at microelectrodes, which allowed for singularities which arise at electrode edges.

Using this mathematical model, the authors showed that concave, convex and protruding electrode geometries which are described by a common list of parameters: radius of microdisc electrode  $a$ , depth of the recess  $L$ , the conical recess angle  $\alpha$  in the insulator, the mean half distance between electrode centers  $r_c$  and an angle  $\beta$  (which is the angle between the perpendicular at  $r_c$  and the insulator and represents the outer boundary of the electrode diffusion compartment), can be solved by a uniform numerical solution.

With this simulation, the normalised dimensionless current  $\Psi$ , of a recessed or protruding electrode with respect to the steady-state current of an ideal inlaid microdisc electrode is related by the equation

$$\Psi = \frac{I(\tau)}{4 Z n F D C_{\infty} a} \quad \text{Eq. (12)}$$

Where  $I(\tau)$  is the steady-state current of a recessed or protruding microdisc electrodes which is dependent on inclination angles ( $\alpha$ ) and depth  $L$  of the electrodes<sup>21</sup>.

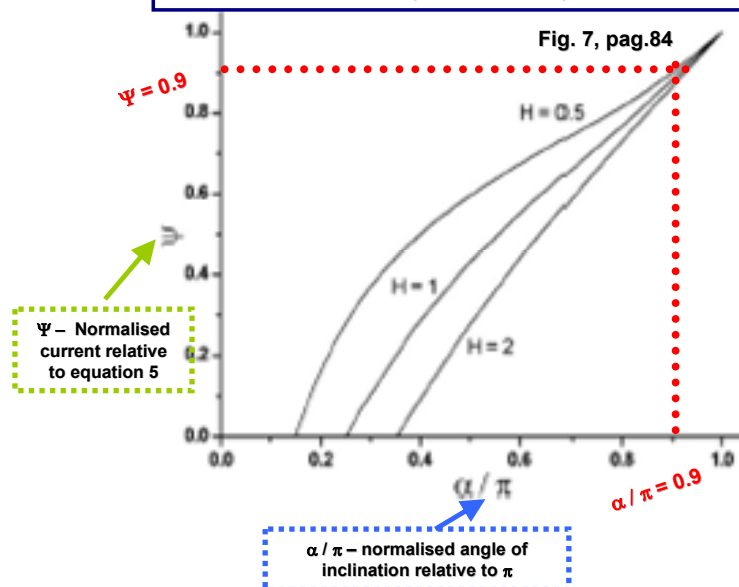


**Figure 21** – Graph used from Amatore's paper to prove the experimental results. Reproduced with permission from ref 21. Copyright © (2006) Journal of Electroanalytical Chemistry, Elsevier Publications.

For  $\alpha$  equal to 160 degrees ( $\alpha \sim 0.9\pi$ ) and  $L/a$  ratio  $\leq 0.5$  (shallow microelectrodes),  $\Psi$  is approximately 0.9. This observation is in accordance with our experimental results, since the normalised current which is the observed current divided by the current calculated using Eq. (5), is 0.9 for all devices (Figure 17).

### 3.5. CONCLUSIONS

---

The results reported in this work demonstrate that standard photolithographic techniques produce regular conically recessed microelectrodes whose behaviour are in accordance with the 2D numerical simulation of diffusion at microelectrodes proposed recently by Amatore et al<sup>21</sup>.

In this chapter, we have demonstrate experimentally that the equation that gives a better prediction for shallow microelectrodes is the inlaid structure equation.

Scanning Kelvin nanoprobe microscopy has shown itself to be a powerful non-contact scanning probe technique for characterising these electrodes without risk of damage to the surface. The SKN profiles clearly show the photoresist profile alongside the inclined walls of the conical recess. This resist profile is caused by a number of factors during the fabrication process.

### 3.6. REFERENCES

---

- 1 – H. Montgomery, O. Horwitz, *J. Clin. Invest.*, 29 (1950) 1120 – 1130.
- 2 – Jurgen Heinze, *Angew Chem. Int. Ed. Eng.*, 32 (1993) 1268.
- 3 – M. I. Montenegro, M. A. Queiros, J. L. Daschbach, *Microelectrodes: Theory and Applications*, NATO ASI Series, Vol. 197, Kluwer, Dordrecht, 1991.
- 4 – B. R. Scharifker, , *Modern Aspects of Electrochemistry*, J. O. M. Bockris, B. E. Conway, R. E. White , Vol. 22, pp. 467–519, Plenum Press, New York and London, 1992.
- 5 – Štulík, K., Amatore, C., Holub, K., Mareèek, V., W. Kutner, *Pure Appl. Chem.*, 72 (2000) 1483 – 1492.
- 6 – Xudong Xie, Doris Stüben, Zsolt Berner, Jörg Albers, R. Hintsche , E. Jantzen, *Sensors and Actuators B*, 97 (2004) 168 – 173.
- 7 – Stanley Bruckenstein, Jolanta Janiszewska, *J. Electroanal. Chem.*, 538 – 539 (2002) 3 – 12.
- 8 – G. Grancharov, E. Khosravi, D. Wood, A. Turton, R. Katakya, *Analyst*, 130 (2005) 1351 – 1357.



---

9 - Christopher M.A. Brett and Ana Maria Oliveira Brett, *Electrochemistry: principles, methods, and applications*, Oxford science publications, Oxford, 1993.

10 - Joseph Wang, *Analytical Electrochemistry, Second Edition*, Wiley-VCH Publishers, New York, 2000.

11 - A. N. Correia, L. H. Mascaro, S. A. S. Machado, L. H. Mazo, L. A. Avaca, *J. Electroanal. Chem.*, 407 (1996) 37 – 43.

12 - C. Beriet, R. Ferrigno, H.H. Girault, *J. Electroanal. Chem.*, 486 (2000) 56 – 64.

13 - B. R. Scharifker, *J. Electroanal. Chem.*, 240 (1988) 61 – 76.

14 – T. J. Davies, S. Ward-Jones, C. E. Banks, J. Del Campo, R. Mas, F. X. Munoz, R. G. Compton, *J. Electroanal. Chem.*, 585 (2005) 51 – 62.

15 – M. Kudera, H.O. Hill, P. J. Dobson, P. A. Leigh, W. S. McIntire, *Sensors*, 1 (2001) 18 – 28.

16 – O. Koster, W. Schuhmann, H. Vogt, W. Mokwa, *Sensors and Actuators B*, 76 (2001) 573 – 581.

17 – R. Feeney, S. P. Kounaves, *Electroanalysis*, 12 (2000) 677 – 684.

18 – C. Amatore, J. M. Savéant, D. Tessier, *J. Electroanal. Chem.*, 147 (1983) 39 – 51.

---

19 - C. Provent, W. Haenni, E. Santoli, P. Rychen, *Electrochimica Acta*, 49 (2004) 3737 – 3744.

20 – S. H. Tan, S. P. Kounaves, *Electroanalysis*, 10 (1998) 364.

21 – C. Amatore, A. Oleinick, I. Svir, *J. Electroanal. Chem.*, 597 (2006) 69 – 76.

22 – C. Amatore, A. Oleinick, I. Svir, *J. Electroanal. Chem.*, 597 (2006) 77 – 85.

23 – L. E. Cheran, S. Sadeghi, M. Thompson, *Analyst*, 130 (2005) 1569 – 1576.

24 – L. E. Cheran, M. Thompson and H. D. Liess, *Analyst*, 124 (1999) 961 – 970.

25 – M. Thompson, L. E. Cheran, M. Zhang, M. Chacko, H. Huo and S. Sadeghi, *Biosensors and Bioelectronics*, 20 (2005) 1471 – 1481.

26 – P. Bergveld, H. Hendrickse, W. Olthuis, *Meas. Sci. Technol.*, 9 (1998) 1801 – 1808.

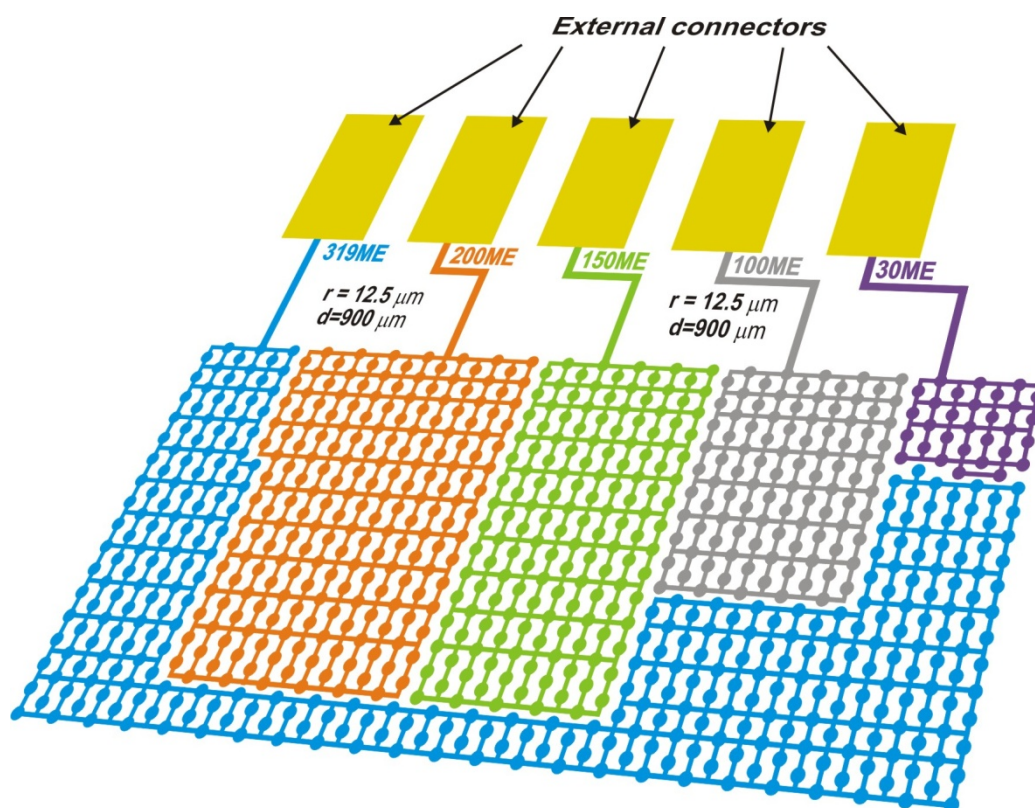
27 – A. M. Bond, D. Luscombe, K. B. Oldham, C. G. Zoski, *J. Electroanal. Chem.* 249 (1988) 1 – 14.

28 – R. Ferrigno, P.F. Brevet, H.H. Girault, *Electrochim. Acta*, 42 (1997) 1895 – 1903.

29 – D. Shoup, A. Szabo, *J. Electroanal. Chem.*, 160 (1984) 19 – 26.

## 4. Towards multifunctional microelectrode arrays

---



### 4.1. ABSTRACT

---

A single microelectrode array platform, divided into groups of microelectrodes with flexible multiplexing can enable a 'defective' cluster of microelectrodes to be readily identified, by comparing normalised currents with the numbers of microelectrodes in the groups of arrays. This generic design principle may be extended for integrating multiple analyte sensing in a single microarray platform. The calibration of the microelectrode arrays, using white light interferometry and electrochemistry is described. The application for multianalyte detection is discussed.

---

## 4.2. INTRODUCTION

---

Microarrays are ubiquitously used for high-throughput measurements using various signal transduction techniques. Ideally each sensor in a microarray platform should perform optimally to ensure an error free response. In this paper a simple method for designing a microelectrode array platform (MEA) is described. The design allows a 'defective' cluster of sensing arrays to be easily identified. It is possible to extend this concept for multiple analyses on a single chip.

There is a plethora of papers related to the theory and applications of microelectrode arrays<sup>1,2,3,4,5,6,7</sup>. Of particular relevance to this publication are the criteria for constructing MEAs which allow radial diffusion to predominate over planar diffusion resulting in the achievement of steady state behaviour<sup>8</sup>.

The parameters that require control to achieve steady state behaviour for microdisc electrode arrays are "d" the centre-to-centre inter-electrode distance, "a" the radius of the microdisc, "D" the diffusion coefficient of the electroactive species under investigation and "v" the scan-rate used in the experiment. Compton and co-workers have reported that the inter-electrode distance condition that best defines *d* to ensure independent radial diffusion domains is given by the relationship:

$$d > 2\sqrt{2D} \frac{\Delta E}{U} \quad \text{Eq. (1)}$$

where  $D$  is the diffusion coefficient of the electroactive species,  $\Delta E$  is the potential window for microelectrode behaviour (Figure 6) and  $v$  is the scan rate. This relationship is reasonably successful for microelectrodes with  $a > 5 \mu\text{m}$ .

The more universal method for evaluating the optimal  $d$  for ensuring independent diffusion domains is a 2-dimensional simulation based on a diffusion domain approach in which each microelectrode is considered as a diffusionally independent 'cell', a square for cubic pack geometries. Using this method it is possible to predict the critical parameters that define steady state behaviour.

Compton and co-workers<sup>5</sup> reported a non-destructive method for estimating individual defective microdisc electrodes in a two-dimensional array, using this simulation technique for cyclic and linear sweep voltammetric response. Experimental responses obtained using the ferrocyanide / ferricyanide couple in aqueous solution agreed within 2.5% between values obtained by comparing with results for the same arrays in which the electroplating of the array with copper from aqueous copper(II) was used as an independent check.

More recently, Amatore<sup>9</sup> and co-workers have extended the application of the quasi-conformal mappings for efficient numerical solution of 2D diffusion at microelectrodes, which allowed for singularities which arise at electrode edges. With this simulation, the normalised dimensionless current  $\Psi$  of a recessed or protruding electrode with respect to the steady-state current of an ideal inlaid microdisc electrode is related by the equation:

$$\Psi = \frac{i_{\text{lim}}}{4 Z n F D C_{\infty} a} \quad \text{Eq. (2)}$$

Where  $i_{lim}$  is the steady-state current of a recessed or protruding microdisc electrodes which is dependent on inclination angles ( $\alpha$ ) and depth ( $L$ ) of the electrodes. The denominator represents the equation for the limiting current of an ideal inlaid electrode. The terms in the denominator are  $n$ , the number of electrons involved in redox reaction,  $F$  and  $D$  the Faraday constant (96484.6 C/mol) and the diffusion coefficient ( $\text{cm}^2 \text{s}^{-1}$ ) respectively,  $a$  the radius of microdisc (cm),  $C_\infty$  the bulk concentration ( $\text{mol cm}^{-3}$ ) and  $Z$ , the number of microdiscs in the array.

In a previous publication<sup>1</sup>, we have shown that the MEAs produced by photolithography, have shallow conical recesses and their voltammetric behaviour is explicable by Amatore's approach.

In this paper, a simple, approach is demonstrated whereby microelectrodes in an MEA maybe flexibly connected to pinpoint a defective group of microelectrode arrays within an extensive array of MEs. The same design concept may be applied to multiple analyte sensing in a single array.

## 4.3. EXPERIMENTAL

---

### 4.3.1. Microfabrication

The fabrication of multi-microelectrode array on silicon substrates was carried out by photolithography in clean room facilities.

#### 4.3.1.1. Pre-oxidation process

HF is used to etch native silicon dioxide ( $\text{SiO}_2$ ) films and contaminants on silicon (Si) wafers. The HF will etch the  $\text{SiO}_2$  without attacking the Si surface.

1. Wash the wafers with HF 10% aqueous solution and deionised water for 10 seconds, using three polypropylene beakers.

NOTE: HF IS EXTREMELY HARMFUL IF IT COMES IN CONTACT WITH ANY PART OF YOUR BODY. FOLLOW ALL STANDARD CLEAN ROOM PRECAUTIONS FOR HANDLING HF.

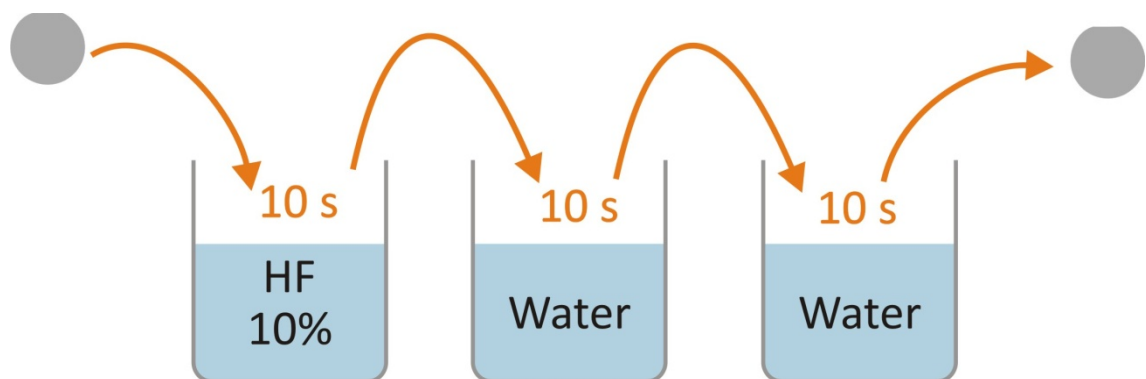


**Figure 1** – Pre-Oxidation Process

#### 4.3.1.2. Oxidation process

The objective of this process is to produce a uniform layer of silicon dioxide ( $\text{SiO}_2$ ) on the wafer.

1. Increase the furnace temperature to 1000°C and set the N<sub>2</sub> flow rate of 2L min<sup>-1</sup>.
2. Put the wafers on boat and insert it into to the mouth of the oxidation furnace.
3. Follow the sequence that is described in the following table, by changing the gas flux and the position of the boat. The oxidation time (stage 4) depends on the desired thickness.

**Table 1** – Procedure for the oxidation furnace.

| Stage    | Position of boat | N <sub>2</sub> flow<br>(L min <sup>-1</sup> ) | O <sub>2</sub> flow<br>(L min <sup>-1</sup> ) | t<br>(min) |
|----------|------------------|---|---|------------|
| 1        | Mouth            | 2.0   | ---   | 10         |
| 2        | Centre           | 2.0   | ---   | 10         |
| 3        | Centre           | ---   | 3.0 dry                                       | 10         |
| <b>4</b> | <b>Centre</b>    | <b>0.3</b>                                    | <b>1.5 wet</b>                                | <b>30</b>  |
| 5        | Centre           | ---   | 3.0 dry                                       | 10         |
| 6        | Centre           | 2.0   | ---   | 10         |

4. When the sequence is finished, remove the boat and decrease the furnace temperature to 620°C and set the N<sub>2</sub> flow rate of 0.6 L min<sup>-1</sup>

#### 4.3.1.3. S-1813 photoresist spin-coating process

This step leaves a uniform coating of photoresist approximately 1.3 microns thick across the wafer.

1. Bake the wafer to dehydrate it for 60s at 90° C and wait 1 min to decrease the temperature of the wafer.
2. Set the wafer on the chuck and turn the vacuum on by pressing the Vacuum button on the spinner control panel.



3. Select program A by using the arrow keys on the spinner. This program will spin at 3700 rpm for 30s.
4. Dispense 1 ml of S-1813 photoresist onto the wafer, and immediately start the spinner with the RUN/STOP button.
5. Remove the sample and place it on the hotplate for 60s at 90°C. This will harden the photoresist for processing.

#### **4.3.1.4. Wafer Exposure Procedure**

The resist is exposed to UV light in order to dissolve (positive) or cure (negative) the photoresist.

1. Turn on the Mask aligner Main Power and the UV lamp and wait 4 minutes.
2. Clamp appropriate mask (mask-side down) in holder.
3. Raise mask and place the wafer in place and turn on vacuum.
4. Rotate table and align sample as desired using X, Y, and Z micrometers.
5. Using the toggle switches and set the exposure time (5 s).
6. Rotate table to expose position.
7. After exposure is complete rotate table and remove the wafer.

#### **4.3.1.5. Develop Procedure of the gold pattern**

In this step the exposed (positive) or unexposed (negative) photoresist is removed to leave the desired mask pattern.

1. Place wafer on a teflon carrier, immerse in AZ-351 (3:1) diluted developer solution, and gently agitate the wafer for 1 min to remove all of the exposed photoresist.
2. Rinse the wafer DI water for 10 s in two different beakers.
3. Dry the wafer with N<sub>2</sub>.
4. Inspect the wafer under the microscope.

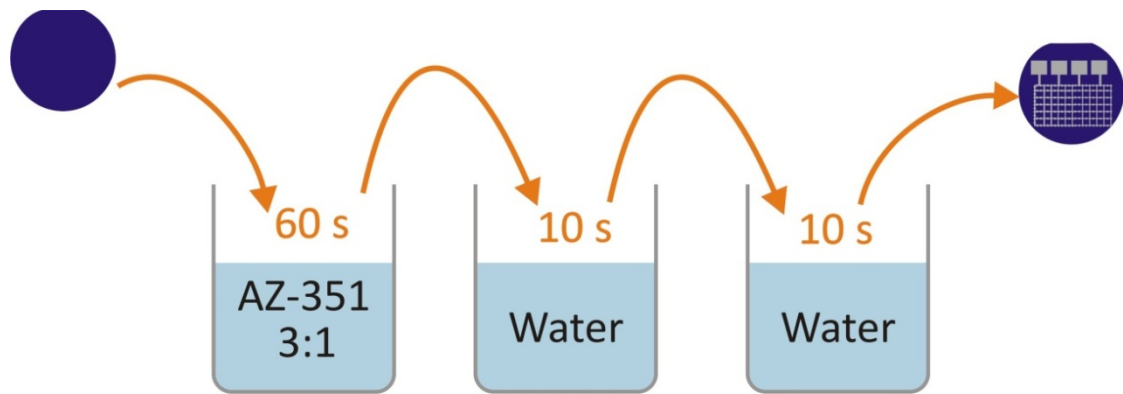


**Figure 2** – *Develop Procedure.*

#### 4.3.1.6. Metal Deposition (Chromium and Gold)

E-beam Evaporator is primarily used to deposit metal on silicon wafers. For these depositions to occur, the wafer and material to be deposited must first be brought to a very low pressure.

Since the instrument is too complex, a technician will do the deposition.

A metallization of 200 Angstrom of Chromium followed by 800 Angstrom of gold is desired.

#### 4.3.1.7. Lift-off Procedure

In this step, the photoresist and the corresponding layer of Cr and Au that is above will be removed to leave the desired gold pattern.

1. Soak the wafer in Acetone for 5 minutes, and apply ultrasonic waves.
2. Rinse the wafer DI water for 30 s in two different beakers.
3. Dry the wafer with N<sub>2</sub>.
4. Inspect the wafer under the microscope.
5. Bake the wafer for 60s at 90° C and wait 1 min to decrease the temperature of the wafer.

#### **4.3.1.8. AZ-4562 photoresist spin-coating process**

This step leaves a uniform coating of photoresist approximately 6 microns thick across the wafer. The procedure is similar than S-1813.

#### **4.3.1.9. Wafer Exposure Procedure**

The resist is exposed to UV light in order to dissolve (positive) or cure (negative) the photoresist.

1. Repeat the procedure 4.3.1.4, but set the exposure time to 30s.

#### **4.3.1.10. Develop procedure of the gold pads and microelectrodes**

In this step the exposed photoresist is removed to leave the desired mask pattern.

1. Repeat the procedure 4.3.1.5.

#### **4.3.1.11. Final procedure**

1. Clean the wafer using Oxygen Plasma.
2. Bake the wafer at 150°C for 30 minutes.

### 4.3.2. Surface analysis

The fabrication and calibration of multi-microelectrode array on silicon substrates was carried out by photolithography in clean room facilities, as described in a previous chapter. A prolonged backing process at 150°C (30 minutes) in the end of the process has changed the angle of inclination  $\alpha$  to 112 degrees.

A Zygo New View 100 White Light Interferometer microscopy (Zygo Co-op., Middlefield, CT, US)<sup>10,11,12,13</sup> was used to measure the device specifications such as microelectrode radius ( $r$ ) and the angle of inclination  $\alpha$  (angle between the electrode surface and the recess walls) and the height of the wall ( $L$ ). White light interferometry is a fast and accurate 3D inspection method and has been widely used as a reliable non-contact profiling system for characterisation of integrated circuits<sup>1</sup> and semiconductor materials<sup>10</sup>, microsystems step heights and discontinuities<sup>11</sup>, biological tissues<sup>12</sup> and rough surfaces<sup>13</sup>.

The electrodes produced using the procedures described previously were conical recessed with 12.5  $\mu\text{m}$  microelectrode radius ( $a$ ) and an angle of inclination  $\alpha$  112° (0.6 rad; Figure 3a and b), The images were obtained using a 40x Mirau objective with a vertical resolution of 0.1nm and maximum lateral resolution of 0.283  $\mu\text{m}$ . A hexagonal geometry was used to optimise packing efficiency. The ratio ( $d/a$ ) of centre-to-centre inter-electrode distance ( $d$ ) to the microelectrode radius ( $a$ ) was 70.

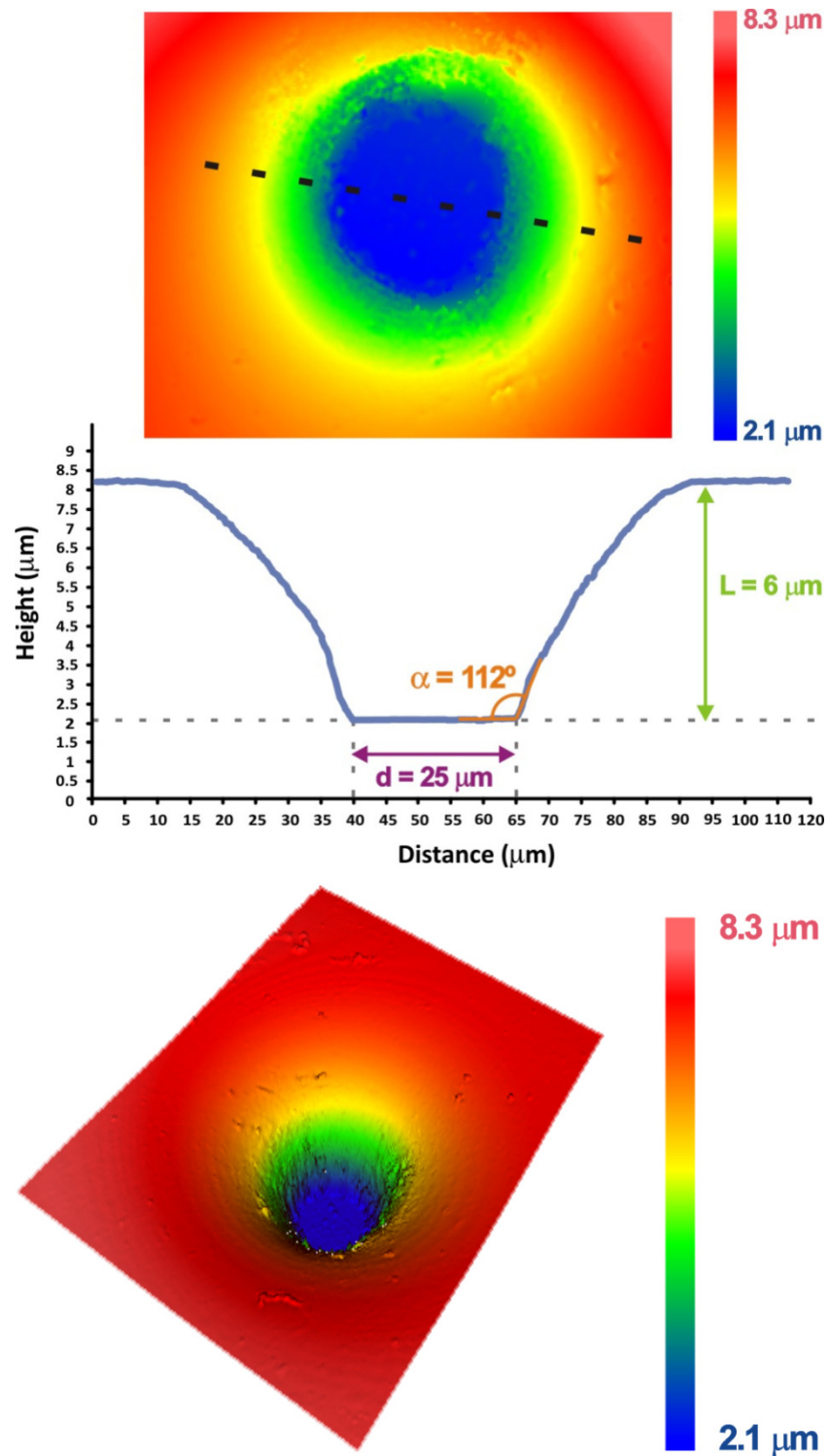


**Figure 3** – A Zygo White light interferometer images of a 12.5  $\mu\text{m}$  radius recessed microelectrode showing the measured angle “ $\alpha$ ”, depth “ $L$ ” and diameter “ $d$ ” with (a) 0.283  $\mu\text{m}$  and (b) 0.565  $\mu\text{m}$  of lateral resolution.

The ME arrays were comprised of “primary” groups microelectrodes with the same nominal defining characteristics, such as, microelectrode radius and inter-space between electrodes. One of the groups contains a known number of defective MEs. To illustrate the principle, 5 primary groups of MEs were selected comprising 30, 100, 150, 200 and 319 MEs. These groups were not connected to each other (Figure 4), but the d/a ratio between the edges of the adjacent groups had the same value. The primary groups could be connected with each other by joining the external wires, maintaining the characteristics.

Thus for example, by combining 100, 150 and 30 MEs of the primary array an array of 280 MEs may be obtained. One of the primary groups nominally comprised of 150 MEs, contained 20 defective MEs to illustrate proof of principle.

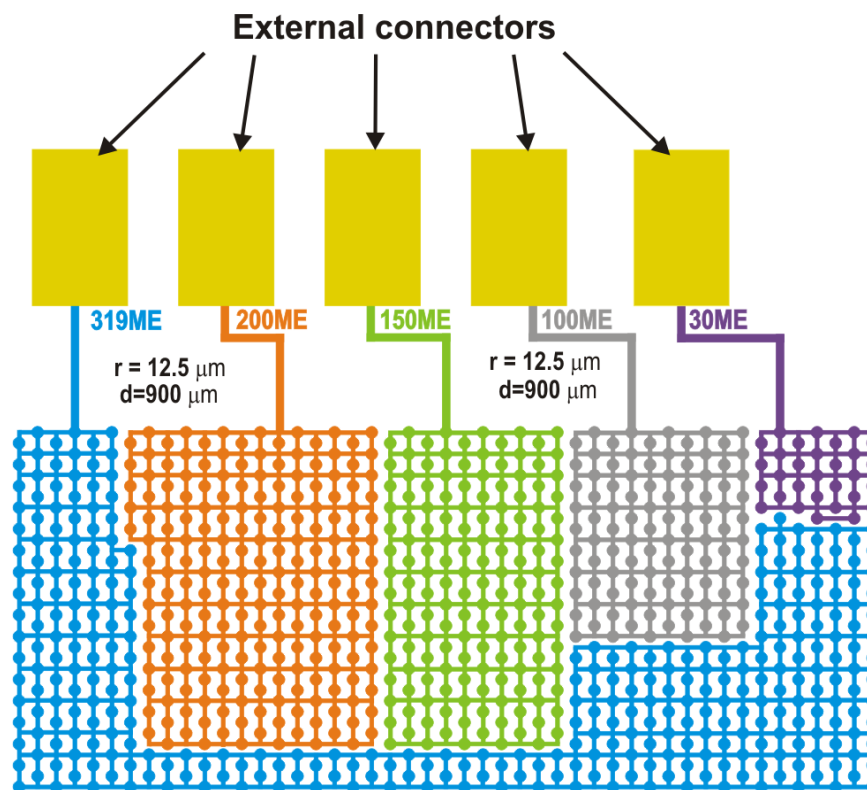


**Figure 4** – Scheme of a ‘grouped’ microelectrode arrays. The microelectrodes are situated in the middle of each circle.

Cyclic voltammetry (CV) in 1M sulphuric acid from -0.2 and 1.6 V (vs. Ag/AgCl/KCl 3.5M) was employed as a measure of the cleanliness of the gold surface. Stripping charges higher than  $1.4 \mu\text{C cm}^{-2}$  were obtained for the microelectrodes. A multichannel potentiostat model VMP (Perkin–Elmer Instruments) was used for electrochemical measurements.

A three electrode cell containing Ag/AgCl (3.5 M KCl), Pt foil ( $A = 1 \text{ cm}^2$ ) and the microelectrode array were employed as reference, auxiliary and working electrodes, respectively. The cell was placed in a Faraday cage to eliminate external interference. All potentials in this work are reported with respect to Ag/AgCl (3.5 M KCl). The measurements were made at 25 K.

Analysis for the gold multi-microelectrode arrays was performed at a scan rate of  $5 - 150 \text{ mV s}^{-1}$  (cyclic voltammetry) and from data acquired by stepping the potential from an initial potential -0.5 V to 0.3 V for 1mM  $\text{Ru}(\text{NH}_3)_6\text{Cl}_3$  (Aldrich,  $D = 7.1 \times 10^{-6} \text{ cm}^2 \text{ s}^{-1}$ ) and 0.1 M  $\text{KNO}_3$  (BDH, background electrolyte), at 20ms intervals (chronoamperometry). Measurements were repeated several times and the results reported in Figure 6 and Table 2 show average values of five measurements.

Atomic force microscopy was used in order to confirm the flatness of the gold substrate produced by electron beam evaporation. The scan was performed in a  $15 \mu\text{m} \times 15 \mu\text{m}$  area and, according to the figures, the gold substrate is flat, having 0.78 nm of average roughness and 1.00 nm of roughness factor.

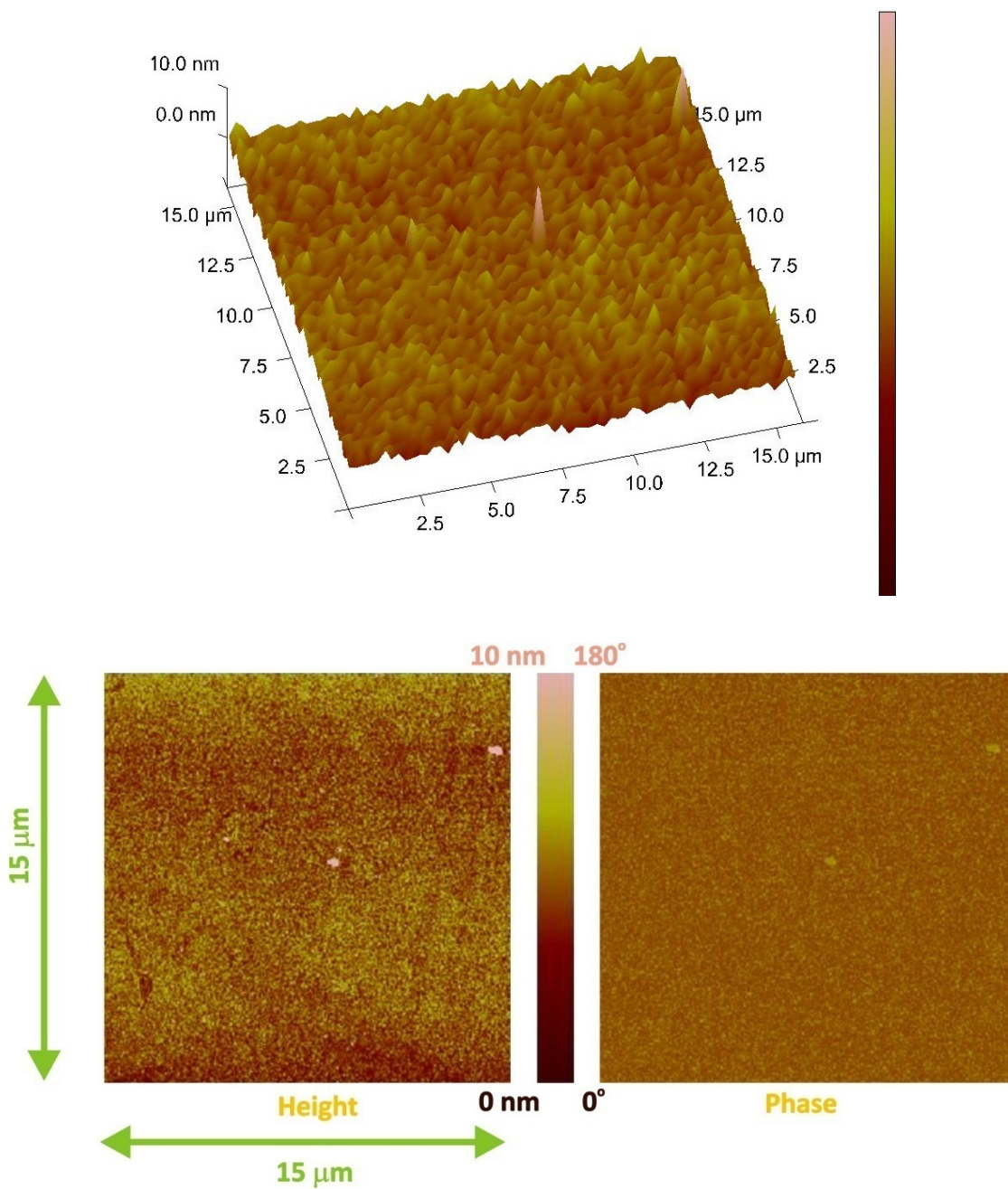


Figure 5 – AFM scan of gold substrate (RMS Roughness: 0.78nm).



## 4.4. RESULTS AND DISCUSSIONS

The MEAs were prepared with a centre-to-centre inter-electrode distance of  $d$  875  $\mu\text{m}$ . This separation is well within the requirements of Eq. (1). For the anodic probe  $[\text{Ru}(\text{NH}_3)_6]^{3+}$  with diffusion constant  $D = 7.1 \times 10^{-6} \text{ cm}^2 \text{ s}^{-1}$ , scan rate  $v = 5 \text{ mV s}^{-1}$  and potential window  $\Delta E = 300 \text{ mV}$ , Eq. (1) requires the interelectrode centre-to-centre separation to be  $d > 584 \mu\text{m}$ ) for avoiding shielding effects caused by diffusional overlap. The  $d$  used in the arrays are therefore well within the requirements.

**Table 2** – Characteristics of MMEA and comparison between experimental and theoretical current obtained for  $\text{Ru}(\text{NH}_3)\text{Cl}_3$  at  $1 \text{ mM}$  in  $0.1 \text{ M KNO}_3$  using CV and CA.

| number<br>MEs | Radius<br>( $\mu\text{m}$ ) | Area<br>( $\text{mm}^2$ ) | $I_{\text{lim}}$<br>inlaid discs<br>( $\mu\text{A}$ ) | $I_{\text{lim}}$<br>Exp (CV)<br>( $\mu\text{A}$ )<br>( $\pm 0.1$ ) | $\psi$ | $I_{\text{lim}}$<br>Exp (CA)<br>( $\mu\text{A}$ )<br>( $\pm 0.1$ ) | $\psi$ |
|---------------|-----------------------------|---------------------------|---|--|--------|--|--------|
| 30            | 12.5                        | 0.0147                    | 0.103   | 0.10   | 0.97   | 0.10   | 0.97   |
| 100           | 12.5                        | 0.0491                    | 0.343   | 0.33   | 0.96   | 0.33   | 0.96   |
| 150           | 12.5                        | 0.0736                    | 0.514   | 0.43   | 0.84   | 0.43   | 0.84   |
| ↓             | ↓                           | ↓                         | ↓   | ↓  | ↓      | ↓  | ↓      |
| 130           | 12.5                        | 0.0638                    | 0.445   | 0.43   | 0.97   | 0.43   | 0.97   |
| 200           | 12.5                        | 0.0982                    | 0.685   | 0.66   | 0.96   | 0.66   | 0.96   |
| 280           | 12.5                        | 0.1374                    | 0.959   | 0.84   | 0.88   | 0.83   | 0.87   |
| ↓             | ↓                           | ↓                         | ↓   | ↓  | ↓      | ↓  | ↓      |
| 260           | 12.5                        | 0.1276                    | 0.891   | 0.84   | 0.95   | 0.83   | 0.94   |
| 319           | 12.5                        | 0.1566                    | 1.093   | 1.06   | 0.97   | 1.05   | 0.96   |
| 519           | 12.5                        | 0.2548                    | 1.778   | 1.72   | 0.97   | 1.70   | 0.96   |

Excellent sigmoidal behaviour within the prescribed voltage window of approximately 300mV<sup>8</sup> is observed for groups of microelectrodes comprising of 30, 100, 150, 100, 200, 280 and 319 MEs.

However for increasing numbers of MEs the sigmoidal shaped is stretched and the voltage window for microelectrode behaviour is enlarged and the steady state current is not fully achieved. The MEA with 519 MEs illustrates this behaviour (Figure 6).

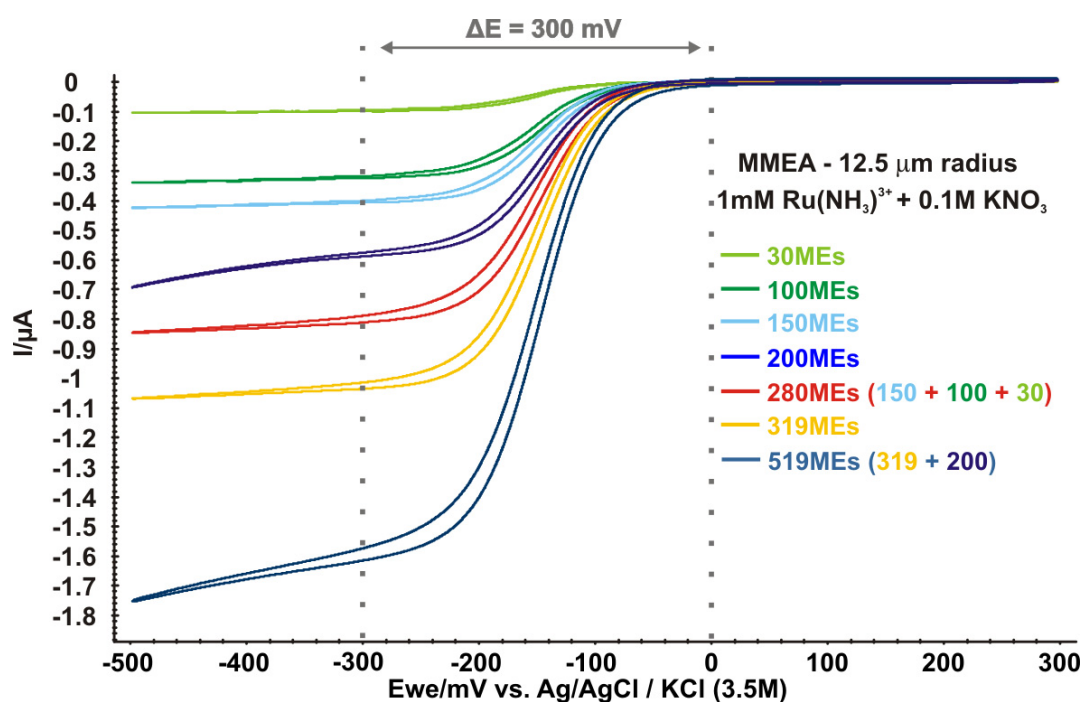


**Figure 6** – Cyclic voltammograms obtained using MMEA at 5 mVs<sup>-1</sup> in the presence of the anodic probe molecule – Ru(NH<sub>3</sub>)Cl<sub>3</sub> at 1mM in 0.1M KNO<sub>3</sub>, showing the voltage window for ME behaviour.

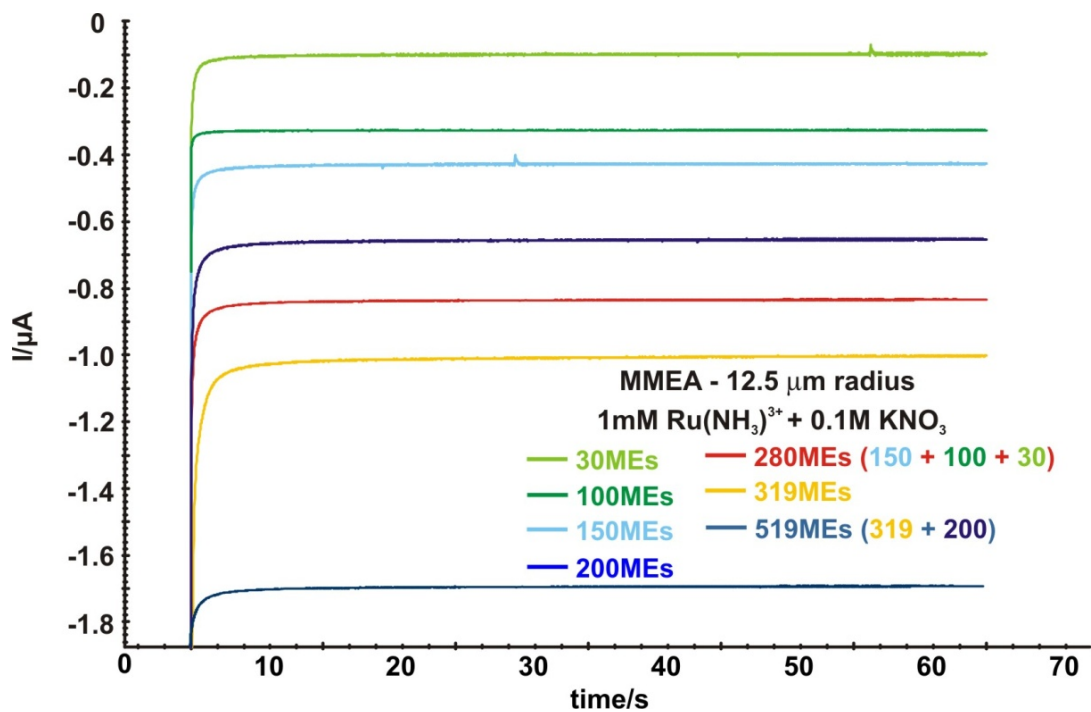


**Figure 7** – Chronoamperograms obtained using MMEA at  $5 \text{ mVs}^{-1}$  in the presence of the anodic probe molecule –  $\text{Ru}(\text{NH}_3)_3\text{Cl}_3$  at 1mM in 0.1M  $\text{KNO}_3$ .

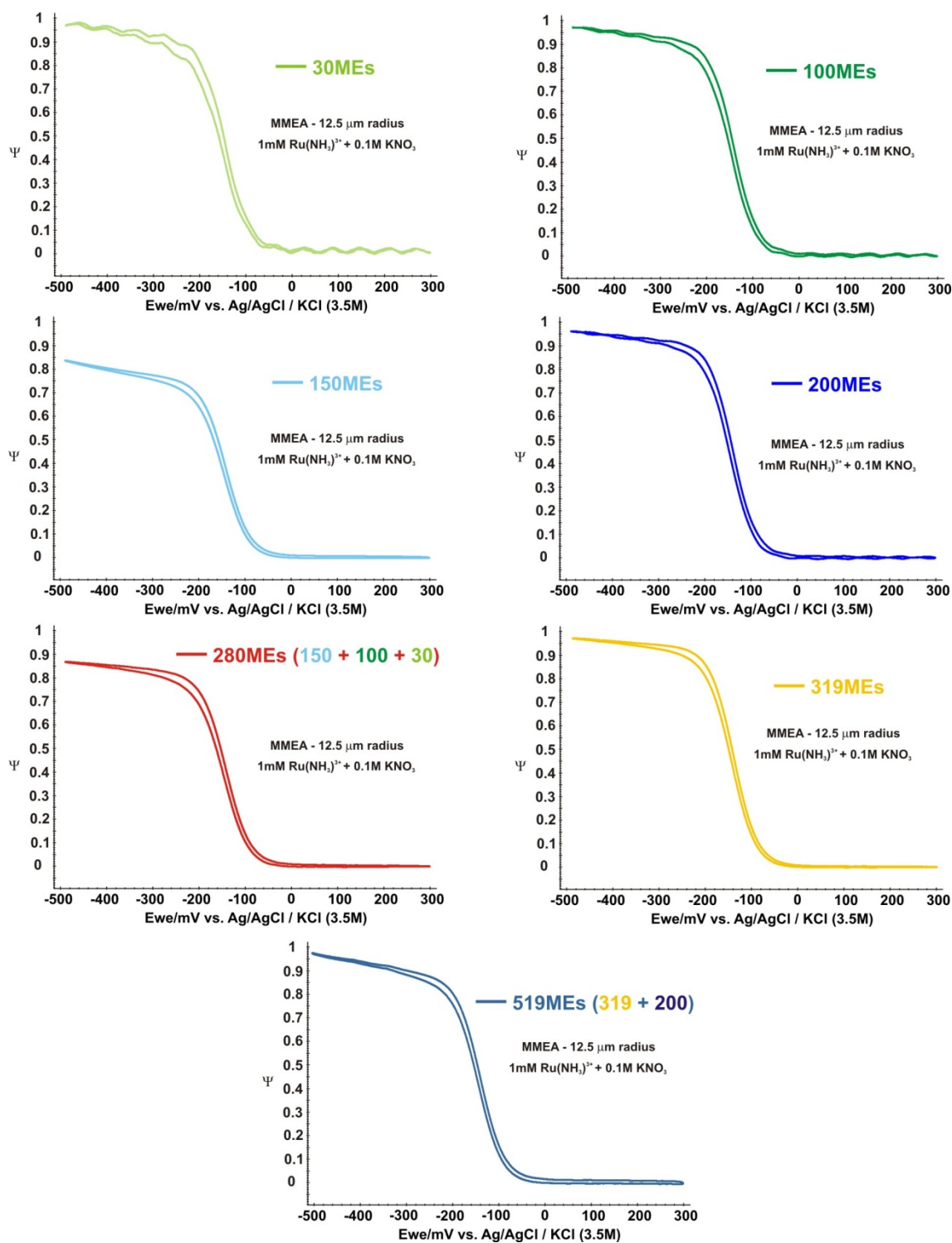


**Figure 8** – Plot of normalised current ( $\Psi$ ) against potential using MMEA at  $5 \text{ mVs}^{-1}$  in the presence of the anodic probe molecule –  $\text{Ru}(\text{NH}_3)_3\text{Cl}_3$  at 1mM in 0.1M  $\text{KNO}_3$ .

The normalised currents ' $\Psi$ ' (Eq. (2)) obtained from CVs and CAs were plotted against the number of electrodes in each group both for the primary groups of MEs (30, 100, 150, 200 and 319 MEs) and the "combined" groups with 260 (130+ 100+30), 280 (150+100+30) and 519 (200+319) MEs (Figure 8).

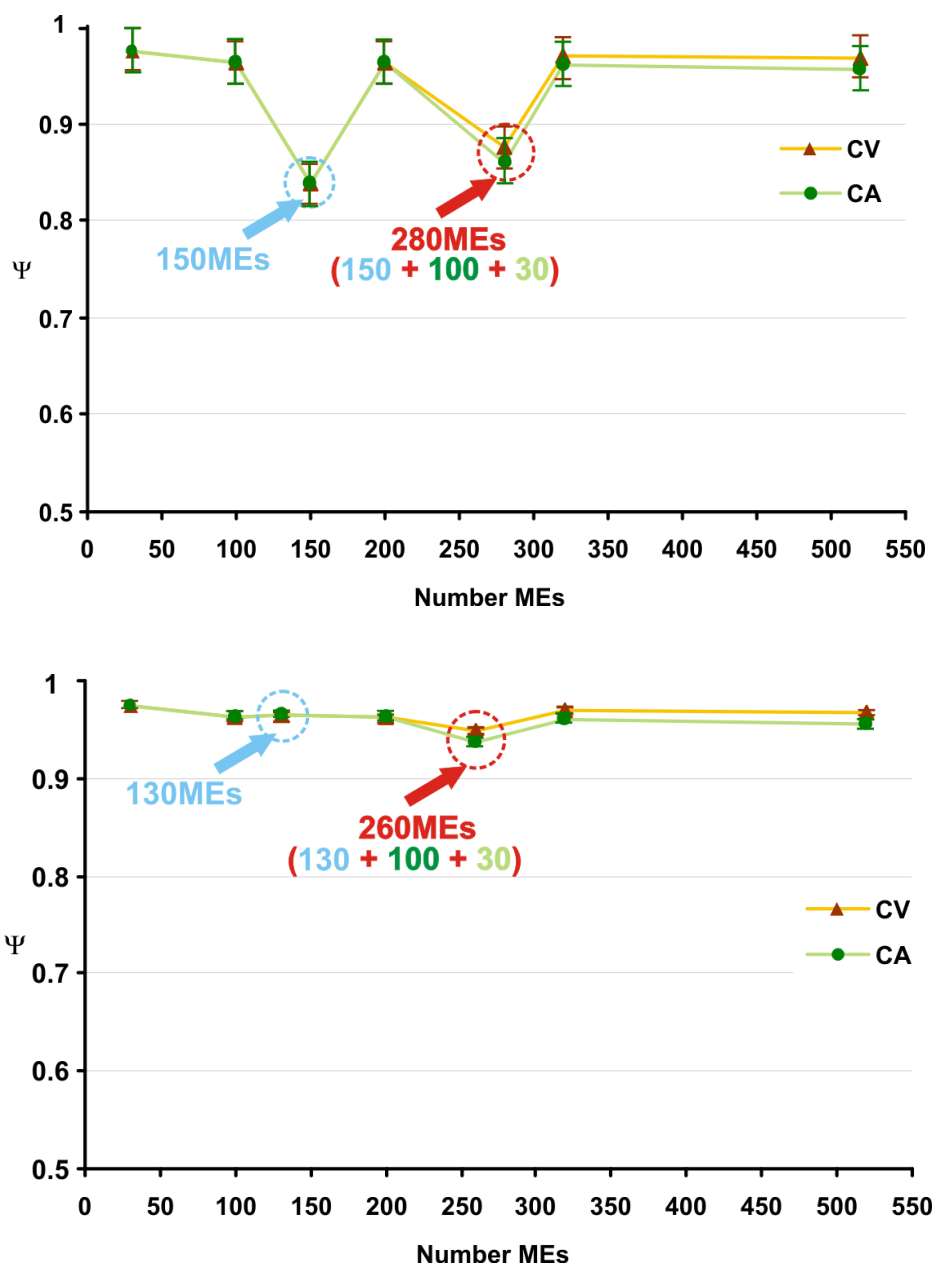


**Figure 9** – Plot of number of microelectrodes against normalised current ( $\Psi$ ) using MMEA at  $5 \text{ mVs}^{-1}$  in the presence of the anodic probe molecule –  $\text{Ru}(\text{NH}_3)\text{Cl}_3$  at  $1\text{mM}$  in  $0.1\text{M KNO}_3$ .

It is immediately obvious that the current response observed for the group of 150 MEs and 280 (150+100+ 30) MEs is lower than the predicted value (Figure 9) by a factor of 16.3% and 12.4% respectively. These values correspond to a deficit of 20 MEs as expected. In contrast the “combined” groups containing 260 and 519 MEs give predicted normalised current values, within experimental error confirming that these groups of arrays do not contain defective MEs. Thus by multiplexing MEA it is immediately obvious if a defective sensor is present. This concept can be extended to calibration of microarrays.

## **4.5. CONCLUSIONS**

---

A new single microelectrode array platform divided into groups of microelectrodes that can be calibrated itself by comparing normalised currents with the numbers of microelectrodes in the groups of arrays was fabricated and characterised successfully.

A potentially useful application of this design, for the construction of single MEA sensor platforms with flexible grouping of MEs is for analysing multianalyte solutions with diverse analyte concentrations. By multiplexing a higher number of MEs the response of an analyte of low concentration in a mixture, may be enhanced to match the response of an analyte of higher concentration.

## 4.6. REFERENCES

---

- 1 – F. A. Aguiar, A. J. Gallant, M. C. Rosamond, A. Rhodes, D. Wood and R. Kataký, *Electrochem. Comm.*, 9 (2007) 879 – 885.
- 2 – C. Amatore, A. Oleinick and I. Svir, *J. Electroanal. Chem.*, 597 (2006) 69 – 76.
- 3 – C. Amatore, A. Oleinick and I. Svir, *J. Electroanal. Chem.*, 597 (2006) 77 – 85.
- 4 – D. Britz, J. Strutwolf, *Electrochimica Acta*, 52 (2006) 33 – 41.
- 5 – O. Ordeig, C. E. Banks, T. J. Davies, J. del Campo, R. Mas, F. X. Mun and R. G. Compton, *Analyst*, 131 (2006) 440 – 445.
- 6 – G. Grancharov, E. Khosravi, D. Wood, A. Turton and R. Kataký, *Analyst*, 130 (2005) 1351 – 1357.
- 7 – H. Montgomery and O. Horwitz, *J. Clin. Invest.*, 29 (1950) 1120 – 1130; K. Štulík, C. Amatore, K. Holub, V. Mareček and W. Kutner, *Pure Appl. Chem.*, 72 (2000) 1483 – 1492; X. Xie, D. Stüben, Z. Berner, J. Albers, R. Hintsche and E. Jantzen, *Sensors and Actuators B*, 97 (2004) 168 – 173; C. Beriet, R. Ferrigno and H.H. Girault, *J. Electroanal. Chem.*, 486 (2000) 56 – 64; B. R. Scharifker, *J. Electroanal. Chem.*, 240 (1988) 61 – 76; T. J. Davies, S. Ward-Jones, C. E. Banks, J. Del Campo, R. Mas, F. X. Munoz and R. G. Compton, *J. Electroanal. Chem.*, 585 (2005) 51 – 62; C. Amatore, J. M. Savéant and D. Tessier, *J. Electroanal. Chem.*, 147 (1983) 39 – 51; A. M. Bond, D. Luscombe



---

and K. B. Oldham, C. G. Zoski, *J. Electroanal. Chem.*, 249 (1988) 1 – 14; R. Ferrigno, P.F. Brevet and H.H. Girault, *Electrochim. Acta*, 42 (1997) 1895 – 1903.

8 – T.J.Davies and R.G.Compton, *J. Electroanal. Chem.*, 585 (2005) 63-62.

9 – C. Amatore, A. Oleinick, I. Svir, *J. Electroanal. Chem.* 597 (2006) 69; C. Amatore, A. Oleinick, I. Svir, *J. Electroanal. Chem.* 597 (2006) 77.

10 – R. T. Blunt, CS mantech conference, 2006, Vancouver, British Columbia, Canada; P. C. Montgomery, In *Near field optics and nanoscopy*; P. C. Montgomery, J. P.Ponpon, M. Sieskind and C. Draman, *Phys. Status Solidi C*, 3 (2003) 1044 – 1050.

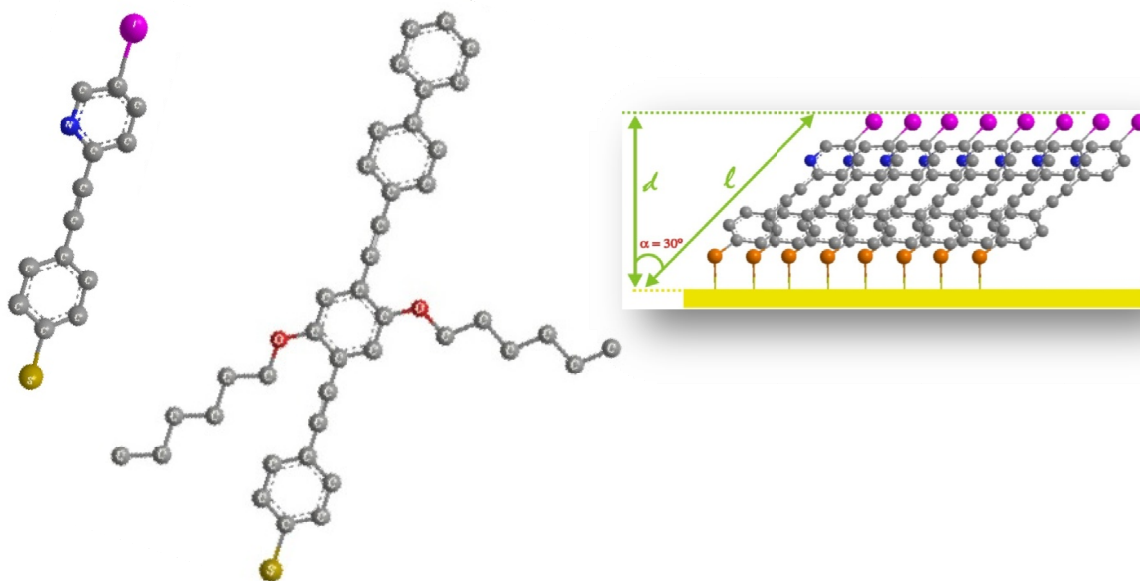
11 – M. B. Sinclair, M. P. de Boer, A. D. Corwin, *Appl. Opt.*, 44 (2005) 7714 – 7721.

12 – Dubois, L. Vabre, A. C. Boccara, E. Beaurepaire, *Appl. Opt.*, 41 (2002) 805 – 812.

13 – E. Pecheva, P. Montgomery, D. Montaner and L. Pramatarova, *Langmuir*, 23 (2007) 3912 – 3918.

## 5. CHARACTERISATION OF SELF-ASSEMBLED MONOLAYERS OF ALKANETHIOLS AND MOLECULAR WIRES ON GOLD USING PEIS AND ELECTROCHEMICAL TECHNIQUES

---



### 5.1. ABSTRACT

---

In this chapter, the charge transfer and self-assembly characteristics of novel molecular wires assembled on flat gold electrodes are evaluated. This class of wires have precisely controlled (ca. 1.5 – 7.5 nm), extended  $\pi$ -conjugation, with extended HOMO and LUMO wavefunctions. While rotations can occur around the C–C single bonds, the molecules cannot isomerise or fold due to their rigid backbone structure. The behaviour of these wires are compared with heptanethiol and dodecanethiol SAMs. Potentiodynamic electrochemical impedance spectroscopy and cyclic voltammetry were used in order to characterise molecular wires.

Assuming that all current is attributed to the electron tunnelling across the monolayer, i.e., the monolayer is pinhole-free, the apparent electron-transfer is expected to decrease exponentially with increasing the thickness of the film, according to the Marcus theory.<sup>1</sup>

It was found that some characteristics of the pinhole-free monolayer change in a potential range (-0.2V to 0.8V vs Ag/AgCl, 3.5MKCl). Although the capacitance maintains constant, the charge-transfer resistance decreases when the potential deviates far from the open potential. Conformations in the structure of the molecules such as side chains lead to a formation of defects that decrease the distance between the electroactive species and the electrode surface and lead to electrode microarrays.

## 5.2. INTRODUCTION

---

The topic of this chapter is the study of a new class of self-assembled monolayers of thiols on gold. The work presented is part of a rapidly growing field of endeavour occupying chemists and physicists from a wide array of backgrounds, and one which was all nonexistent only 20 years ago.

This chapter will focus upon the characterisation of n-alkanethiol SAMs on gold, as both a review of previous accomplishments in the field, and an introduction of two different molecular wires comprised of thiol groups at one end, which were synthesised at the Department of Chemistry and Centre for Molecular and Nanoscale Electronics, Durham University<sup>2</sup>.

Before any of the literature can be discussed, it is important to know the origin and the definition the term "self-assembled monolayer".

A monolayer also called films, thin films or ultra-thin films is made of particles piled up side by side, none of them being on top of the other. Orientation is often part of the qualities matter inside the monolayer acquires.

From the energetic point of view, a self-assembling surfactant molecule can be divided into three distinct parts, as shown in Figure 1. The first part is the head anchoring group that provides the most exothermic process while anchoring on the substrate by the chemisorption. The second part is the alkyl chain and the energy associated with its interchain Van der Waals interaction (exothermic). The third part is the terminal surface group, which determines the surface properties of the SAMs functionalised substrate surface. In the case of simple alkyl chain, the terminal methyl (CH<sub>3</sub>) group provides a hydrophobic surface.

The ordering of alkanethiol is driven by the strong affinity between the head group and the substrates, the lateral Van de Waals interactions between tethered alkyl chains, and the dipole interactions between the polar end groups.

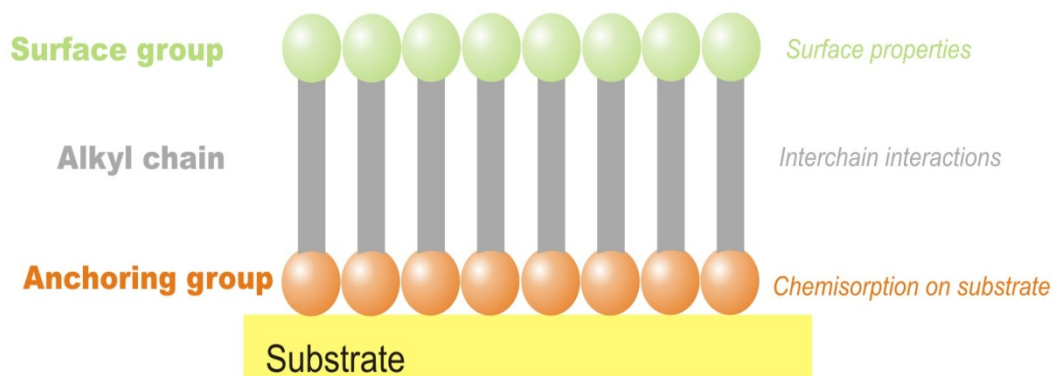


**Figure 1** – A schematic view of the self-assembling surfactant molecule in SAMs.

The first records dates back to the end of 18<sup>th</sup> century, when Benjamin Franklin wrote in his journal his first observation of the effect of oil on water. It was observed that when barrels of oil were thrown on rough sea, waves became smoother, and he reported the volume deposited and the surface covered, the film thickness only a division operation away.



**Figure 2** – Miss Agnes Pockels and Lord Rayleigh.

A century later, Miss Agnes Pockels and Lord Rayleigh (Figure 2) were researching the properties of water surfaces, but she was the first to measure the surface tension properties of water. She developed a rudimentary surface balance in her kitchen sink, which she used to determine water surface contamination as a function of area of the surface for different oils. Because of her lack of credentials, Pockels shared her results with Rayleigh and he accepted to publish her results in the scientific journal *Nature*<sup>3</sup>. This was the beginning of the monolayer odyssey.

The first careful studies of molecular monolayer film were performed by Irving Langmuir and Katherine Blodgett at General Electric during the early part of the 20<sup>th</sup> century<sup>4,5</sup>. In their experiments, monolayers were formed by compressing samples of amphiphilic molecules at the air-water interface (called Langmuir-Blodgett monolayer so far). In consequence of this work, Langmuir was awarded the Nobel Prize in 1932.

Hypothesis on the molecular arrangement were formulated based on macroscopic observations, but only the second half of the 20<sup>th</sup> century, new instruments were rising and the researchers has begun to observe what was really happening at the molecular level.

Self assembly of surfactant molecules on metal surfaces have been reported by Zisman *et al*<sup>6</sup> in 1946. They have discovered that eicosyl alcohol (C<sub>20</sub>H<sub>41</sub>OH) in hexadecane has formed hydrophobic surfaces on platinum, nickel, copper, gold and other metal substrates. The molecular films formed are known as self-assembled monolayers (SAMs).

Self-assembled monolayers are ordered molecular assemblies formed spontaneously by the adsorption of an active surfactant on a solid surface. During the early period, the “potential” of SAMs was not recognised.

In 1983, Nuzzo and Allara <sup>7</sup> published the first paper that deals with the formation of organised self-assembled monolayer, showing that SAMs of Alkanethiolate on gold could be prepared by the adsorption of n-alkyl disulfides from dilute solutions.

Some techniques have been refined to increase sensitivity to permit an easy and facile characterisation molecular level in SAMs. Nowadays, the researchers are being keen to confine desired species in the monolayers in order to give special features, such as, optical, electrical and chemical properties for sensing devices and for study of electron transfer through saturated and unsaturated molecules.

Electron-transfer reactions have been attracted interest for many years. An important contribution to the theory of outer-sphere electron transfer was made by Rudolph Marcus in 1954, called Marcus theory, being devoted in 1992, when he was awarded the Nobel Prize of Chemistry. <sup>8,9</sup>

The most important prediction of the Marcus theory of electron transfer was the observation of the inverted region. Chemical intuition holds that as the driving force of a reaction, in this case the standard free energy ( $\Delta G^0$ ) is increased then the reaction rate should increase. Indeed, Marcus theory predicts that in the “normal” region, where the reorganization energy ( $\lambda$ ) is greater than the absolute value of the standard free energy ( $|\Delta G^0|$ ), electron transfer rate will initially increase reaching the maximum when  $\lambda = |\Delta G^0|$ . Continuing the increase in driving force after this point leads to a decrease in the reaction rate, usually called as the “inverted” region. The reorganization energy ( $\lambda$ ) is the energy required to structurally reorganize the donor and acceptor as well as their solvation spheres upon electron transfer and reflects nuclear configuration displacements from the reactant to the product state.

Especially thiol SAMs on gold substrate have stimulated considerable interest in electrochemistry because of their applications to testing Marcus model of electron-transfer and tunnelling theory<sup>10,11</sup>.

Marcus theory has been applied successfully in the kinetic analysis of electron transfer between gold electrodes and redox species through alkanethiol monolayer. The results included semilogarithmic plots of electron transfer rate constants vs overpotential which exhibited significant curvature, and an “inverted” region.<sup>10,30</sup>

If there are no pinholes at the Au/SAM interface, the current is attributed to the electron tunnelling across the monolayer and it's expected to decrease exponentially with the increase of thickness,

$$i = i_0 \exp(-\beta d) \quad \text{Eq. (1)}$$

Where  $i_0$  is the current measured at a bare electrode,  $\beta$  is the electrode tunnelling coefficient that is potential independent and correlates the rate of electron transfer with the chemical structure and  $d$  is the length of molecule that form the monolayer.

Self-assembling systems are classified by the “pair” of the chemisorbing head group of the organic molecule and the substrate. Many systems have been used to form self-assembled monolayers. Figure 3 shows some molecules that are frequently-used for self-assembled monolayers: n-alkanethiols<sup>12,13,14,15</sup>, alkanedithiol<sup>15</sup>,  $\omega$ -mercaptoalkanol<sup>12</sup>,  $\omega$ -mercaptoalkane carboxylic acid<sup>12,13,16,24,25,35</sup>, oligophenylthiols<sup>17</sup>, dialkyl disulfides<sup>7</sup> and dialkyl sulfides. Substrates used to support self-assembled monolayers include gold, silver, copper, iron, semiconductors such as GaAs(100), InP(100), liquid mercury, and



hydroxylated surfaces such as oxidized silicon or mica. Alkanethiols adsorbed on Au(111) are probably the most common system studied.

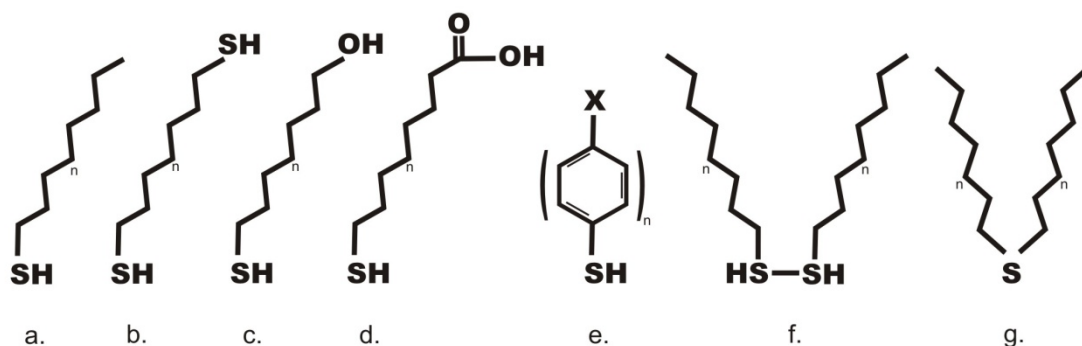


**Figure 3** – Some frequently used molecules for self-assembled monolayers. a) *n*-alkanethiols, b) alkanedithiols, c) mercaptoalkanol, d) mercaptoalkane carboxylic acids, e) Oligophenylthiols, f) dialkyl disulfides, g) dialkyl sulfides

Self-assembled monolayers of thiol derivatives on gold have had considerable attention because of the wide varieties of potential technical applications. A strong thiolate bond between the surfactant molecules and the gold surface drives the self-assembly of these molecules (chemisorption). Once adsorbed, the resulting monolayer is very stable in aqueous and or organic solutions within a large range of electrode potentials.

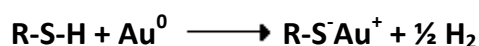
The alkanethiol SAM on gold provide a highly hydrophobicity non-polar surface. The thermodynamic origin of hydrophobic effect is usually attributed to unfavorable free energy of solvation of small non-polar solute molecules, such as, hydrocarbons in water.

This positive free energy of solvation is due to the ordering of water molecules surrounding a hydrocarbon species that results in a decrease of entropy of solvation. This rather significant lowering of entropy of the system dominates

over the favorable energy change associated with the hydrogen bond formation.

The alkanethiol reaction with gold substrate can be described as an oxidative addition of the S-H bond to gold followed by reductive elimination of hydrogen.

18



The combination of hydrogen atoms yields H<sub>2</sub>, which is an exothermic process. The bonding of the thiolate group to the gold surface is strong and the homolytic RS-Au bond strength is ~ 40 Kcal/mol<sup>18</sup>, contributing to the stability of the SAMs.

Several research groups investigated the orientation of alkanethiols at Au substrates. Ulman and co-workers<sup>19</sup> have calculated the free energies of various orientations of long-chain alkanethiols using computer modeling. The lowest free energy of the systems based on van der Waals interactions between adjacent molecules at single crystals of Au was found for a molecular tilt of the carbon backbone of c.a. 30 degrees from normal with a rotation about the chain axis of c.a. 55 degrees.

Electron diffraction and STM measurements reveal that the monolayer forms a ( $\sqrt{3} \times \sqrt{3}\sqrt{3}$ ) R30° overlayer structure with a c(4x2) superlattice on Au(111) as shown in Figure 4<sup>14,20,21,22</sup>.

Frey et al<sup>23</sup> demonstrated that hybridization and, thus, the spatial orientation of the bonding orbital of sulfur is the determining factor for the orientation and density of the alkanethiol monolayer rather than the intramolecular interaction.

The surface order can extend over hundreds of square nanometers, and the symmetry of the sulfur atoms is hexagonal.

The sulfur–sulfur interactions are believed to be minimal (5 Å), because at monolayer assemblies where the head-to-head spacing is greater than the touching Van der Waals distance of the alkyl chains, these tails tilt in such a way as to maximize attractive Van der Waals interactions between molecules and therefore minimize the free energy of the structure<sup>19</sup>.

This tilt angle ( $\alpha$ ) is found to be 30 degrees with respect to the surface normal toward the nearest neighbour direction. The twist angle  $\beta$  (which defines the rotation of the carbon chain backbone about the chain axis with respect to the plane defined by the chain axis and the surface normal) for the long-chain alkanethiol is found to be  $\sim 52$  degrees, which implies that Au–S–C bond angle is nearly 120 degrees, close to the optimum value for the  $sp^2$  hybridized sulfur atoms.<sup>24</sup>

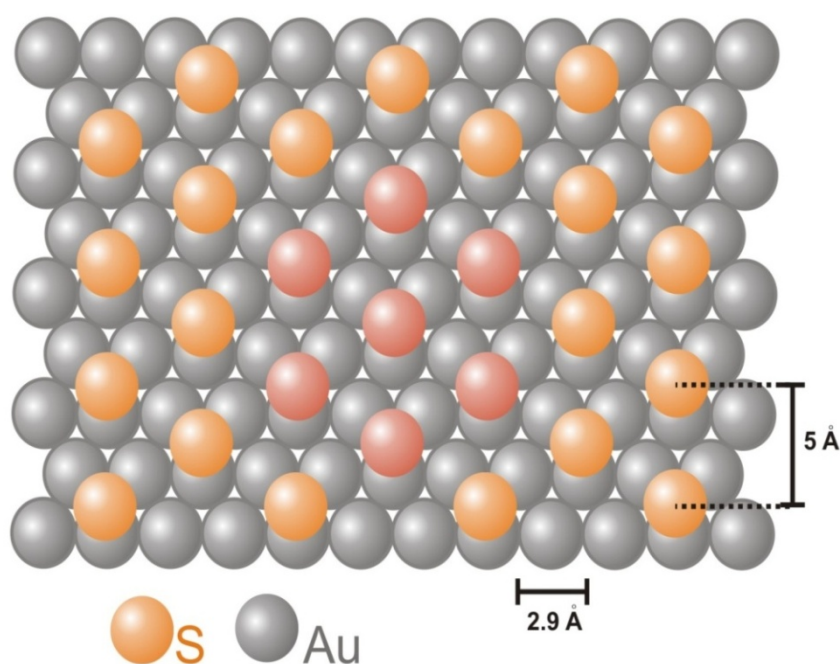


**Figure 4** – Top view of the Structure of SAMs of alkanethiols on Au (111), where the gray circles represent gold atoms and the orange circles represent alkanethiolate adsorbates (the red circles highlight the hexagonal ( $\sqrt{3} \times \sqrt{3}$ )  $R30^\circ$  overlay structure.)

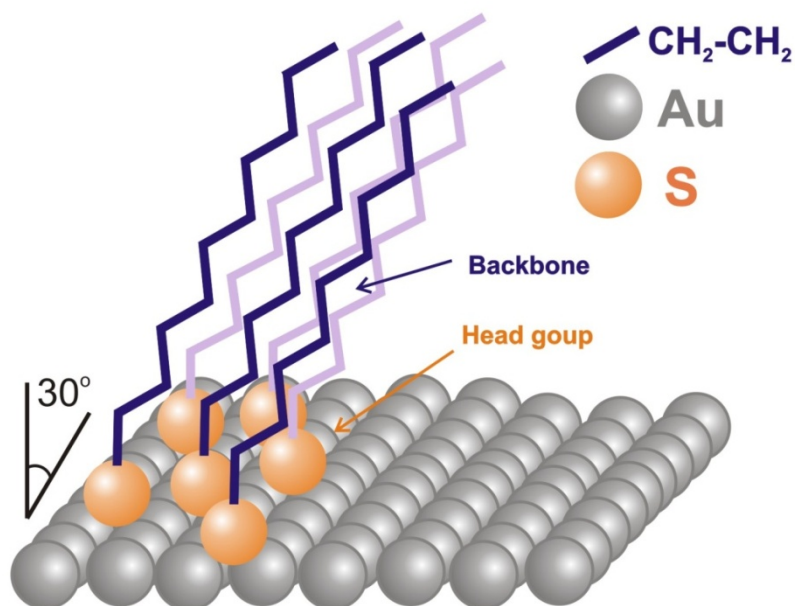


**Figure 5** – Side view of the structure of SAMs of alkanethiols on Au (111), where the adsorbates are packed 5 Å apart with their alkyl chains tilted 30 degrees from the surface normal in a trans-extended conformation.

Since alkanethiol SAMs represent an easy way path to link inorganic, organic and biological materials, they are essential in many of the so-called "bottom-up" methods proposed to build a wide variety of devices and materials. It is important to note that, in a similar way to protein formation, the bottom-up approach could involve different levels of construction. Starting with the primary molecular or atomic building blocks, the next step is their self-assembly into nanometer-sized units forming a secondary structure. These structures then self-organize into larger entities that could have many tens of hundreds of nanometers in at least one direction (tertiary structure). Finally, the quaternary structure involves the architecture of the self-organised system in the actual material or device.<sup>25</sup>

The SAMs have to be so compact that electrochemical processes, such as gold oxidation, will be strongly suppressed<sup>10</sup>. However, it is also well known that alkyl chains affect surface properties. It has been reported that compact and pinhole-free SAMs could be formed with a long hydrocarbon chain ( $n > 9$ ), while for short alkyl chains, defects on the monolayer can be found and also they are not sufficiently hydrophobic to block electron-transfer between electroactive specie in the bulk solution and the electrode surface<sup>26,27,28</sup>.

For CV large potential sweeps are applied to the gold electrode and the resulting current is recorded. However, for EIS only very small sinusoidal potential sweeps with frequencies varying from 100 mHz to 10 kHz are applied to the gold electrode, which makes a less disturbing technique than CV. These two techniques are powerful tools to determine kinetic parameters and the surface coverage with the structural integrity of the monolayer by evaluating the presence of pinholes and defects using redox couple as the probe molecules.<sup>26,27,28,29,30,31</sup>

The role of the medium between a donor and acceptor to control the rate of electron transfer remains a largely unsolved problem of crucial scientific importance. Since contact and manipulating a single molecule is still a challenge, the research was focused on single monolayer films for the first efforts. To immobilize molecules on an electrode, can be achieved by using the self-assembly process. Thiol self-assembled monolayers have been attractive as a model system because they provide a stable and structurally well-defined film with as adjustable thickness and desirable function<sup>32</sup>, and also provide long-range electron transfer that is crucial to know biological systems and to design electronic devices composed of molecular units.

In self-assembled monolayers, the electron transfer from the electrode surface to redox probes can occur either by attaching the electroactive species to the monolayer or by freely diffusing in the electrolyte solution (Figure 6). Therefore, since the monolayer is perfectly organized with no pinhole defects in the structure, the only way for the electron to reach the electrode surface (electron tunnelling - oxidation) or reach the electroactive species (hole tunnelling - reduction) is to tunnel through the chain of the composed molecules of the film.

33

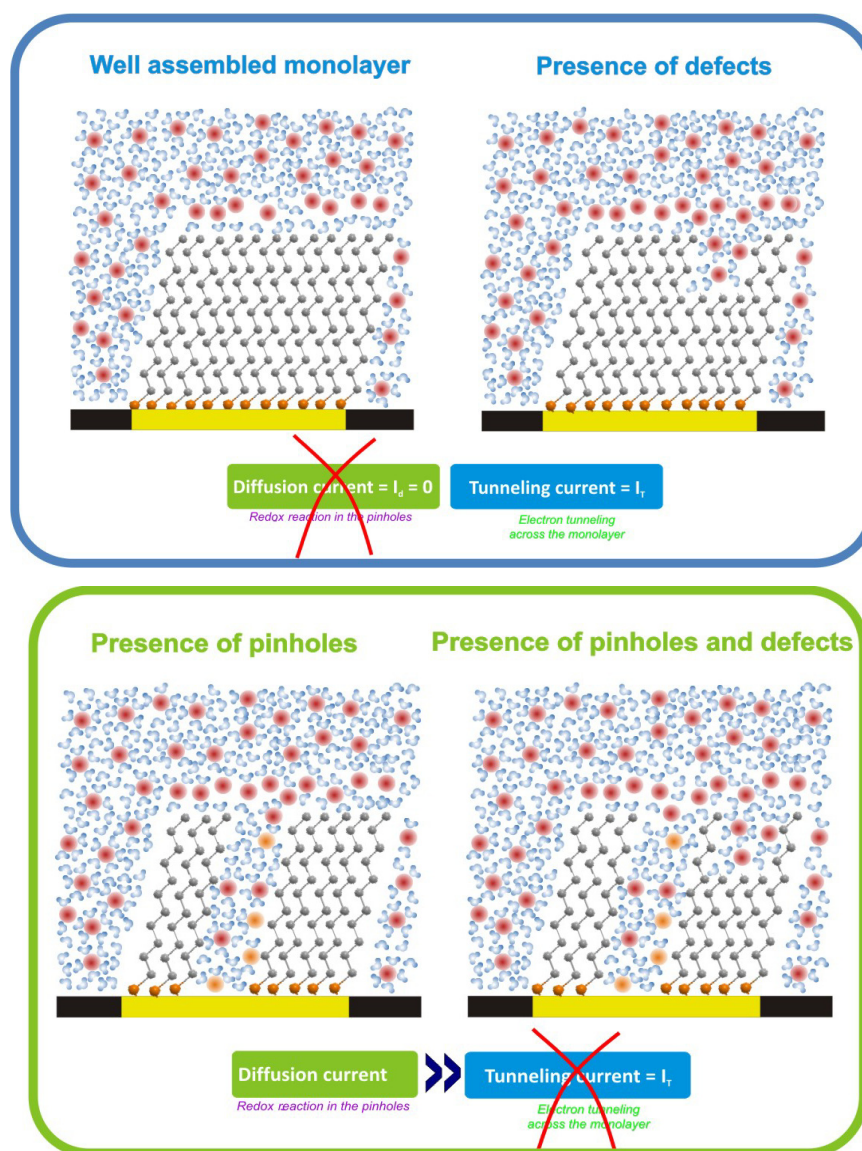


**Figure 6** - Figure illustrating the different types of structures for a monolayer film that self-assembles on gold.

It should be notice that in absence of electroactive species in solution, the electron tunnelling is the dominant mechanism for charge transport, even in presence of pinholes.<sup>34</sup>

The question of the formation of good quality of thiol self-assembled monolayers is still discussed by the researchers. Porter et al<sup>35</sup> showed by cyclic voltammetry that well-prepared long-chain monolayer were free of measurable pinholes defects. In turn, Sabatani and Rubinstein have demonstrated that long-chain monolayer may exhibits behaviour resembling a microelectrode array, i.e. an electrode containing small active sites embedded in an insulating plane.<sup>30</sup>

Although this two different explanations, the authors agreed that the quality and stability of the monolayer on gold are critically dependent on the cleanliness of the gold surface and the mode of preparation.<sup>29</sup>

The purpose is to characterise new functional organic molecular materials and understand the structure and electronic properties of molecular layers.

The RJ12 and CSW564 molecules were synthesised at Durham University, UK (Figure 7). These molecules are rigid as they are comprised of aromatic rings connected with triple bonds. They are fully conjugated molecules and play an important role in electron conduction because  $\pi$ - electrons are delocalized over a distance.<sup>36,37,38</sup>

The first report on this type of molecules was published by Arieh Aviram and Mark A. Ratner<sup>39</sup> in 1974. They constructed a simple electronic device, a rectifier, based on the use of a single organic molecule consisting of a donor  $\pi$ -system and an acceptor  $\pi$ - system, separated by an  $\sigma$ -bonded (methylene) tunnelling bridge.

The simple linear and conjugated structure of these molecules have resulted in the term “molecular wire”. A wire is a basic electronic function that allows the transport of charges from one end to the other.

The n-alkane chains exhibit large energy gaps between HOMO and LUMO. They have usually ca. 5 eV or higher energy gaps, and are relatively insulating materials<sup>40,41,42,43</sup>, whilst the molecular wires have relatively smaller HOMO-LUMO gap and behave like a semiconductor. These molecules have delocalized  $\pi$ -electrons<sup>42,43</sup>. Linear  $\pi$ -conjugated molecules represent the simplest models of molecular level wires.

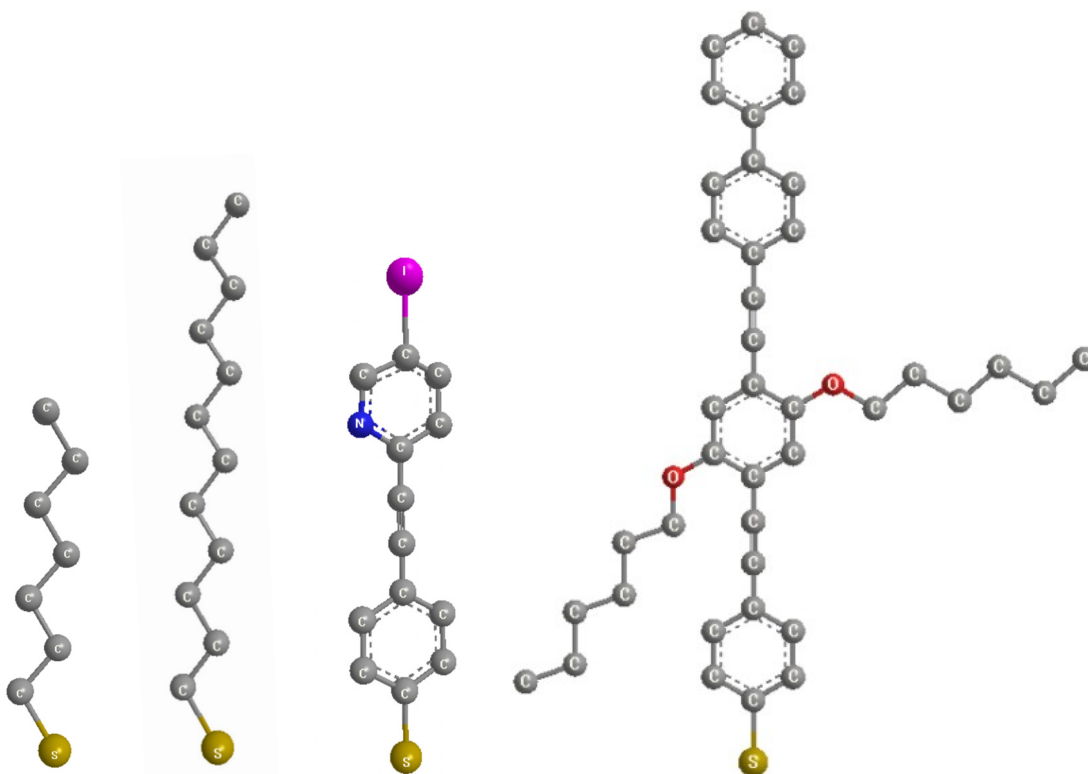


**Figure 7** – Structure of the thiol molecules used in this work (**HPT**- heptanethiol, **DDT**- dodecanethiol, **RJ12** - 3-(4-((5-iodopyridin-2-yl)ethynyl)phenylthiol), **CSW564** - S-4-((4-(biphenyl-4-ylethynyl)-2,5-bis(hexyloxy)phenyl)ethynyl)phenylthiol).



## 5.3. EXPERIMENTAL

---

### 5.3.1. Reagents and chemicals

Potassium ferricyanide, potassium ferrocyanide, potassium nitrate, 1-dodecanethiol and 1-heptanethiol were purchased from Aldrich. Hydrogen peroxide, sulphuric acid were obtained from Acros Organics and Fluka, respectively. Ethanol and THF were provided for the solvent store at Chemistry department in Durham University.

CSW564 and RJ12 molecules (Figure 7) were synthesised at the Department of Chemistry and Centre for Molecular and Nanoscale Electronics, Durham University, UK.

All the aqueous solutions were prepared deionised water supplied by a Sartorius Arium 611 ultrapure water system (conductivity =  $0.055 \mu\text{S cm}^{-1}$ ).

### 5.3.2. Instrumentation

A Potentiostat-Galvanostat Model 283 (Princeton Applied Research) (Figure 8) was used for electrochemical measurements. Electrochemical impedance spectroscopy (EIS) measurements were performed using a Solartron 1260 Impedance/Gain-Phase Analyzer connected with PAR model 283 potentiostat interfaced with a personal computer. Same set-up was applied to perform potentiodynamic EIS, applying DC potential to the system using the potentiostat.

The ZPlot software supplied with the Solartron 1260 was used to collect, plot and interpret the raw impedance data.

A three electrode cell containing Ag/AgCl (3.5M KCl), Pt foil ( $A=1\text{ cm}^2$ ) and either bare gold electrode or SAM electrodes were employed as reference, auxiliary and working electrodes, respectively. The cell was placed in a Faraday cage to eliminate external interference.

All potentials in this work are reported with respect to Ag/AgCl (3.5M KCl). All measurements were carried out at room temperature in solutions purged of oxygen by bubbling with argon for 10 minutes.



**Figure 8** - Potentiostat-Galvanostat Model 283 (Princeton Applied Research)



**Figure 9** - Polycrystalline gold disk electrodes ( $Au(111)$ ) provided from Bioanalytical Systems (area  $0.020\text{ cm}^2$ ) used as working electrode.

### 5.3.3. Substrate preparation

Gold is the most popular substrate for thiol SAMs<sup>44</sup>. Owing to their noble character, gold substrates can be handled in air without oxide surface layer formation and can survive harsh chemical treatments for removal of organic contaminants.

The formation of a monolayer on gold is strongly dependent on the cleanliness and structure of gold prior to modification, since it is well known that gold is a soft metal and is readily contaminated by organic and inorganic species. Therefore, prior to monolayer preparation, the gold substrates need to be well cleaned in order to remove the contaminants on the surface which affect the integrity of the SAMs formation.

Several cleaning procedures have been found in the literature, such as, electrochemical oxidation<sup>45</sup>, immersion into strong oxidizing solutions<sup>46,47,48,49</sup>, polishing and sonicating in organic solution and water<sup>50</sup>, or exposure to reactive oxygen species formed by either U.V. irradiation<sup>51</sup> or Oxygen plasma<sup>52,53</sup>, and a combination between them.<sup>15,26,44,47</sup>

In the work, Polycrystalline gold disk electrodes (Au(111)) provided from Bioanalytical Systems (area 0.020 cm<sup>2</sup>) (Figure 9) were polished for 60 s in a figure-eight pattern on Buhler Microcloth with successively finer grades (15, 3 and 1 μm) of diamond polish slurries and alumina slurry 0.05 μm followed by sonication in ethanol and water for 10 min. Immediately before use, polycrystalline gold electrodes were cleaned by soaking in piranha solution (3:1 (V/V) 98% H<sub>2</sub>SO<sub>4</sub> / 30% H<sub>2</sub>O<sub>2</sub> - Piranha solution reacts violently with organic

materials and should be handled very carefully.) for 20 minutes, rinsed with water and finally dried under N<sub>2</sub>.

Cyclic voltammetry (CV) in 1M sulphuric acid from 0V to 1.5V (vs. Ag/AgCl/KCl 3.5M) was employed as a measure of the cleanliness of the gold surface. Typical CVs recorded in 1M H<sub>2</sub>SO<sub>4</sub> for the Au electrode (data not shown). The shape of the voltammogram and the charge under stripping wave served as metrics for reproducible surface preparation. The gold oxide formation and reduction was clearly visible. Only electrodes with a stripping charge larger than 1.4  $\mu\text{C cm}^{-2}$  were qualified<sup>54</sup>. The procedure was repeated for those electrodes that didn't pass this test until getting the desired stripping charge.

Immediately after the cyclic voltammetry (CV) in 1M sulphuric acid, the electrodes were rinsed copiously with ethanol (alkanethiols) or THF (aromatic thiols), and dried in a direct stream of Nitrogen. After cleaning, alkanethiol self-assembled monolayers have been formed on gold electrode by keeping the substrate in 1mM of thiol solution in Ethanol or THF for 24 hours at room temperature.

The loosely bound thiol molecules were removed from the surface by rinsing successively with ethanol or THF and water.

## 5.4. RESULTS AND DISCUSSION

The electron transfer between  $\text{Fe}(\text{CN})_6^{3-}$  and SAM of alkanethiols and aromatic thiols on a polycrystalline gold surface was investigated using cyclic voltammetry and electrochemical impedance spectroscopy in the present work.

### 5.4.1. Cyclic voltammetry

The blocking properties of the SAM modified gold electrode of the modified electrode were examined by means of cyclic voltammetry in the solution containing 1mM  $[\text{Fe}(\text{CN})_6]^{3-}$  and 0.1M  $\text{KNO}_3$ , at a potential range of -0.2 to 0.6 V. (Figures 10 - 16)

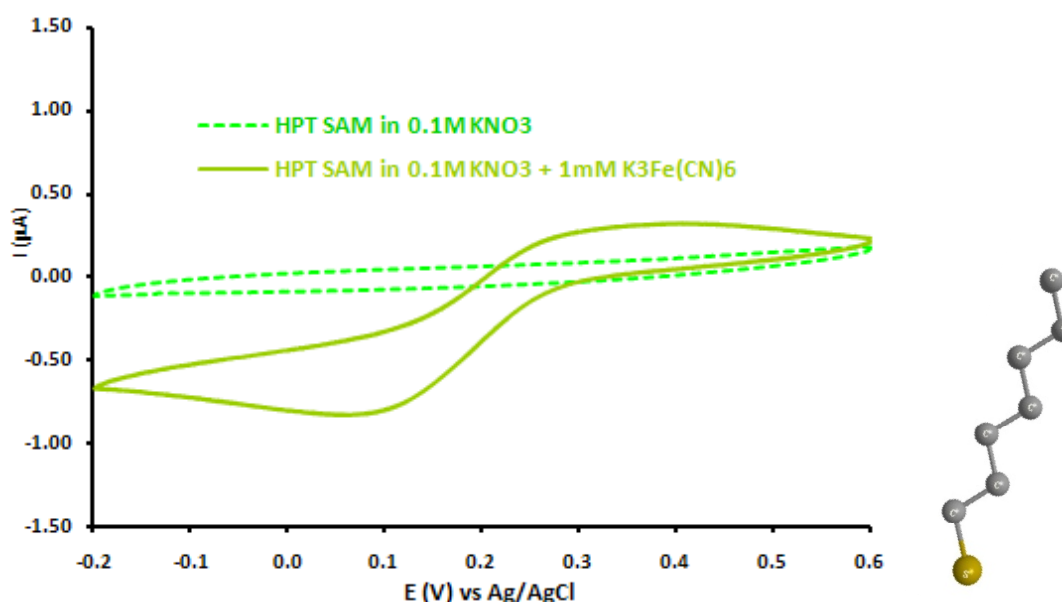


**Figure 10** – CVs obtained for scans from -0.2 to 0.6V in 1mM  $\text{K}_3\text{Fe}(\text{CN})_6$  + 0.1M  $\text{KNO}_3$  and 0.1M  $\text{KNO}_3$  for heptanethiol SAM electrode.

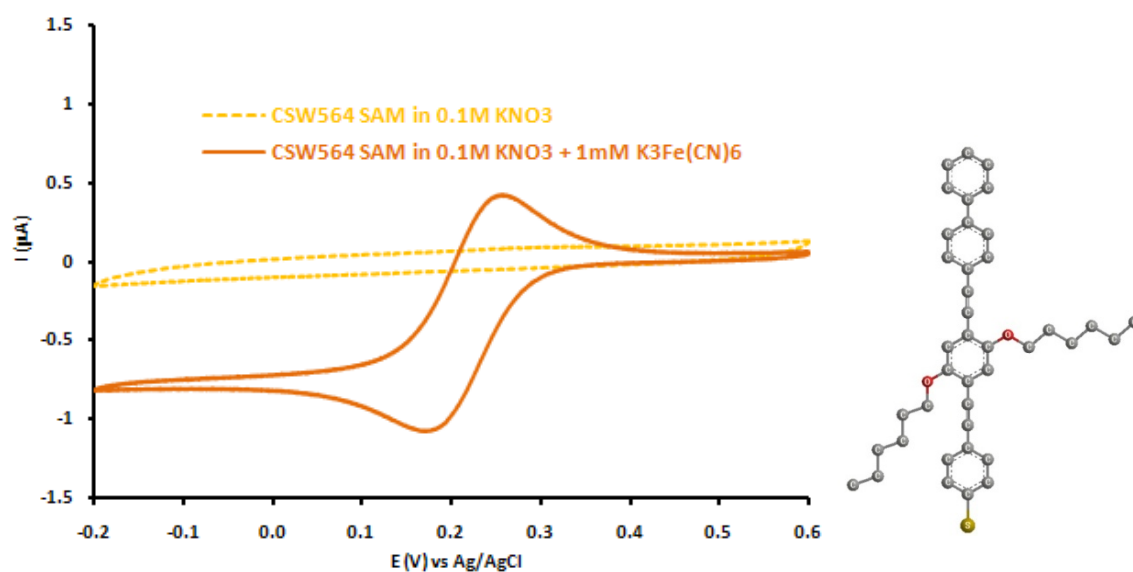


**Figure 11** – CVs obtained for scans from -0.2 to 0.6V in 1mM  $K_3Fe(CN)_6$  + 0.1M  $KNO_3$  and 0.1M  $KNO_3$  for CSW564 SAM electrode.

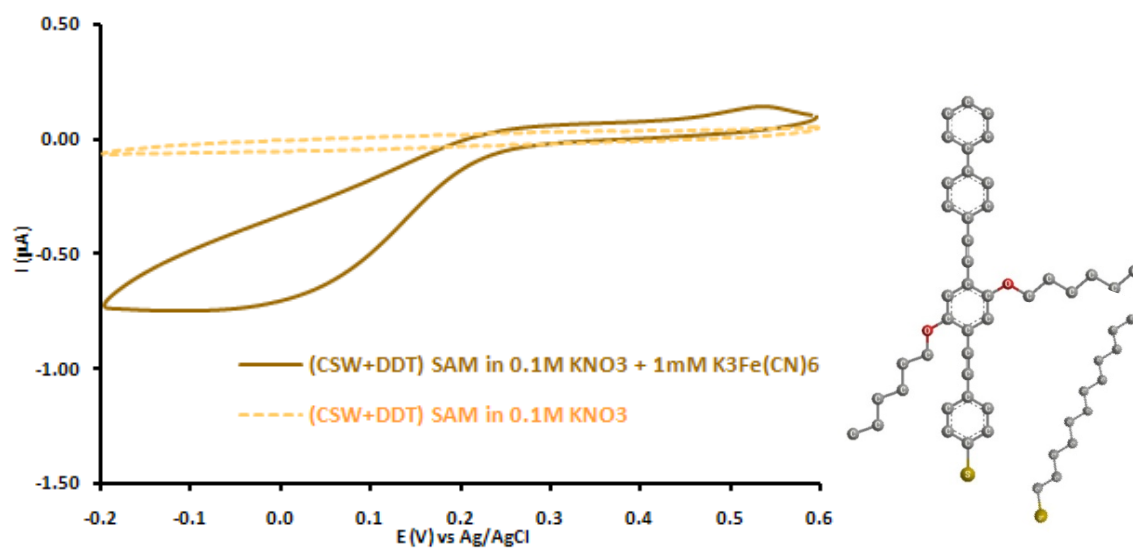


**Figure 12** – CVs obtained for scans from -0.2 to 0.6V in 1mM  $K_3Fe(CN)_6$  + 0.1M  $KNO_3$  and 0.1M  $KNO_3$  for (CSW564+DDT) SAM electrode.

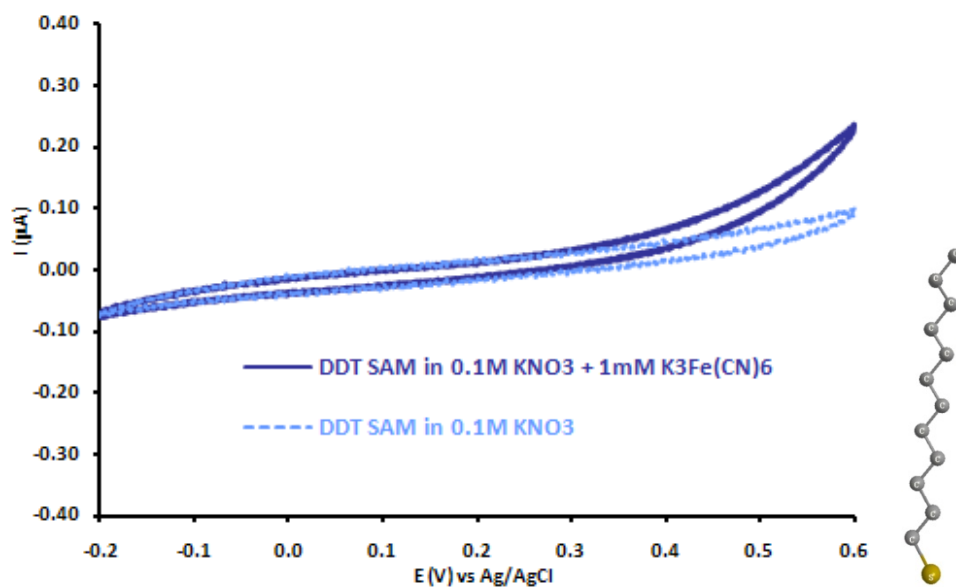


**Figure 13** – CVs obtained for scans from -0.2 to 0.6V in 1mM  $K_3Fe(CN)_6$  + 0.1M  $KNO_3$  and 0.1M  $KNO_3$  for DDT SAM electrode.

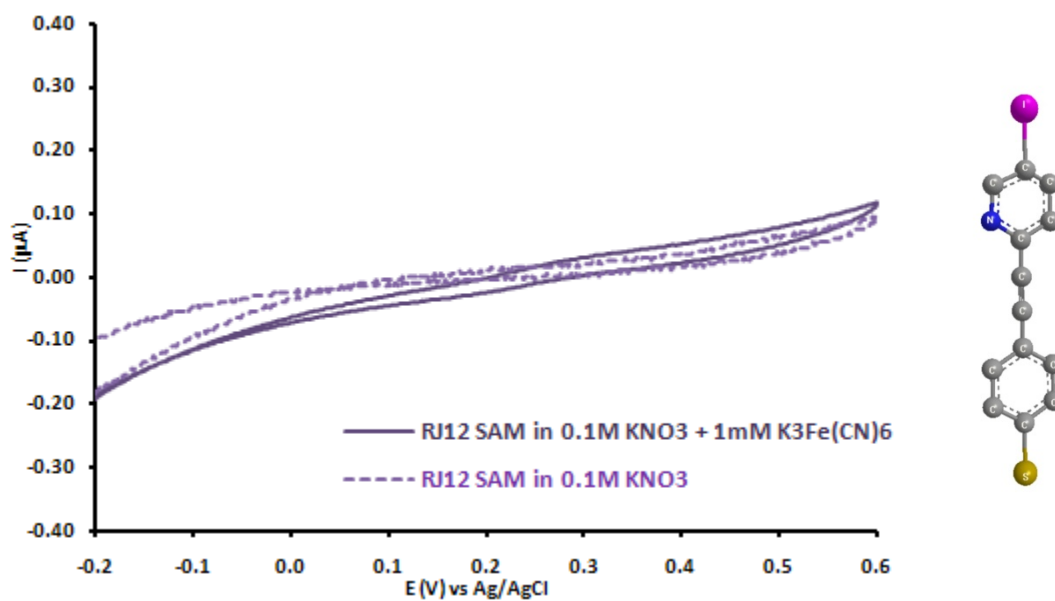


**Figure 14** – CVs obtained for scans from -0.2 to 0.6V in 1mM  $K_3Fe(CN)_6$  + 0.1M  $KNO_3$  and 0.1M  $KNO_3$  for RJ12 SAM electrode.

CV of the HPT monolayer (Figure 10) shows that the redox reaction is not totally suppressed. The CVs also exhibit microelectrode array behaviour, since a sigmoidal rather than peak shaped voltammogram was obtained. This indicates that pinholes formed in the monolayer are very small and widely separated relative to the diffusion layer thickness. In the case of HPT SAM electrodes, the electron transfer can take place by:

- 1) diffusion of electroactive species through the pinholes and access to the electrode surface followed by electron transfer, which facilitates radial diffusion of the redox species in contrast to the linear diffusion, observed in the case of bare gold electrode
- 2) or by tunnelling.

In contrast, the CV of CSW564 SAM electrode shows that the redox reaction is not suppressed, and it still has a peak shape behaving indicative of macroelectrode behaviour (Figure 11). This indicates that radial diffusion of the pinholes formed in the monolayer are closely packed promoting the overlap of diffusion layers. As consequence, peak shaped voltammogram was expected and are similar to those observed at a macroelectrode<sup>55</sup>.

In a cyclic voltammetry experiment, as the redox reaction is driven by the applied potential, the diffusion layer will grow in the region of the electrode surface. In the case of an array of microdisc electrodes separated by insulating material, individual diffusion zones will develop, and continue to grow throughout the experiment, leading to overlap. In this situation, quasi microelectrode regime is observed. Although there is no analytical expression for the peak current in this diffusion regime, numerical simulations can be used to interpret the peak current–scan rate behaviour<sup>56</sup>.



Cyclic voltammetry was performed at different scan rates (figure 15). The behaviour is typical macroelectrode, although the peak current is smaller compared with bare electrode. Approximately 73% of the electrode area is accessible to the electroactive specie (calculated at  $0.1\text{Vs}^{-1}$ ). This indicates that the presence of millions of pinholes and the average distance between them is very low, promoting easily the overlap of diffusion layers. This was expected, since this molecule (CSW564) contains two side chains.

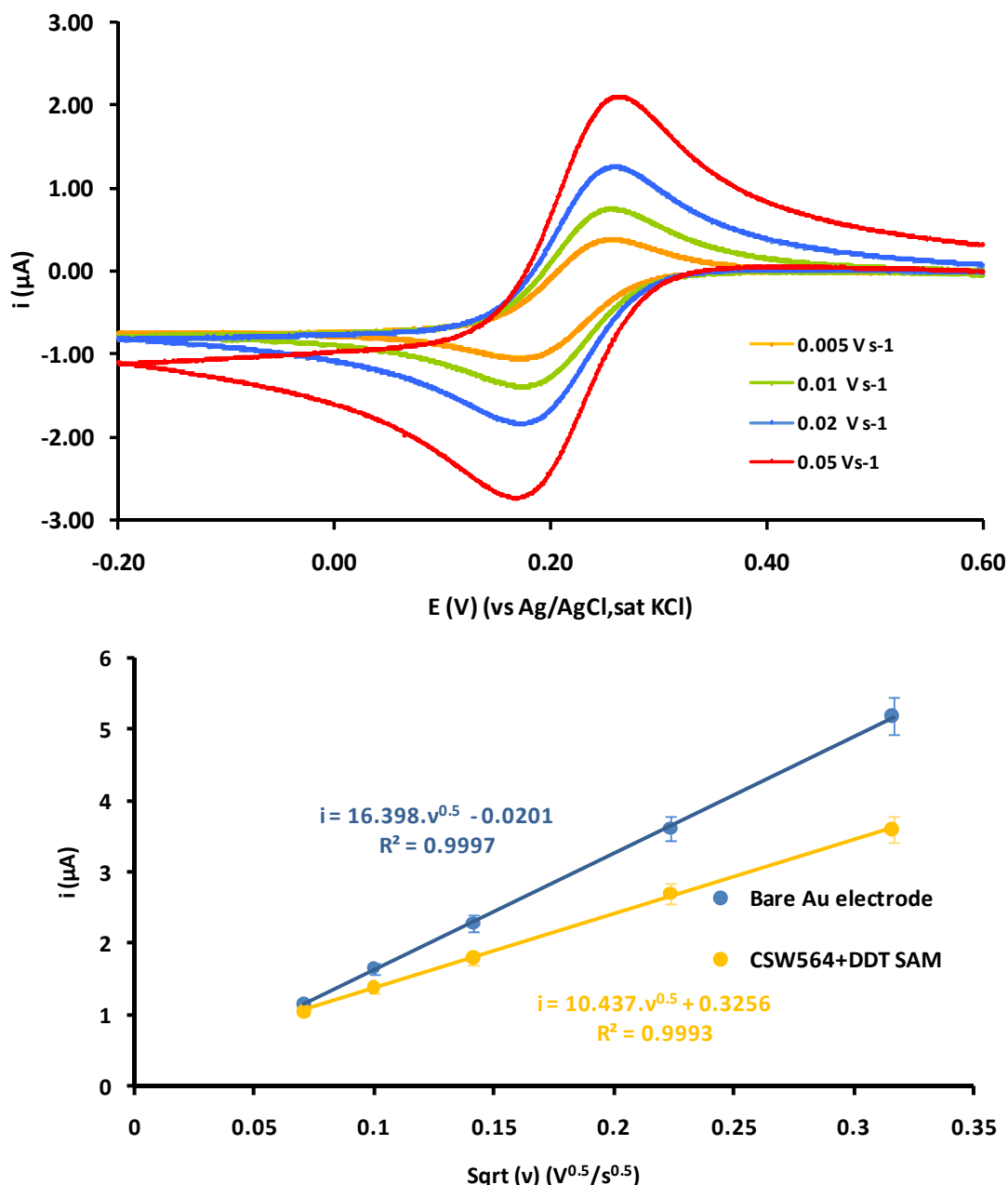


**Figure 15** - CVs obtained for scans from -0.2 to 0.6V in  $1\text{mM } \text{K}_3\text{Fe}(\text{CN})_6 + 0.1\text{M } \text{KNO}_3$  for CSW564 SAM electrode and the peak current dependence to the sqrt of scan rate.

In order to improve the properties of the CSW564 monolayer, the pinholes must be selectively passivated. This was targeted by using a mixed monolayer with equimolar quantities of CSW564 and DDT molecules. The voltammogram (Figure 12) shows that the addition of DDT in MW SAM improves the blocking behaviour, however, a background current is still evident. This can be explained by assuming that the CSW monolayer contains pinholes due to the side chains creating islands. With the mixed monolayer, these islands are partially occupied by DDT molecules, the remaining the pinholes being caused by the side chains.

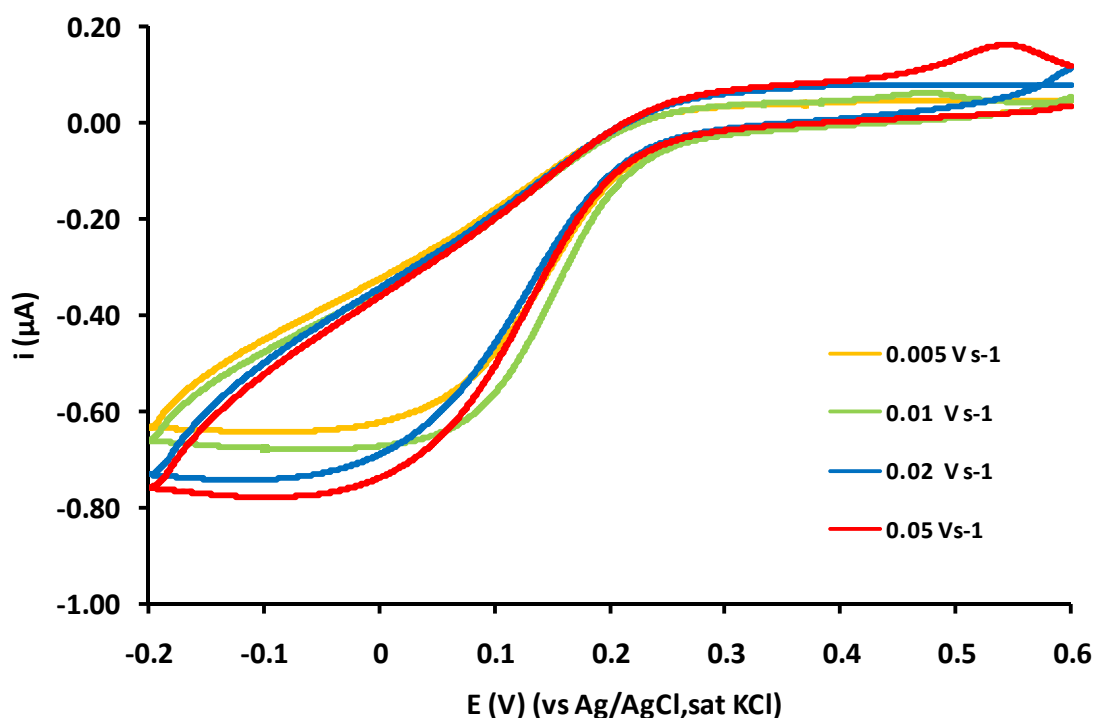


**Figure 16** - CVs obtained for scans from -0.2 to 0.6V in 1mM  $K_3Fe(CN)_6$  + 0.1M  $KNO_3$  for (CSW564+DDT) SAM electrode.

Cyclic voltammograms showed in Figure 16 have demonstrated microelectrode array behaviour without diffusion layer overlap. The limiting current remains constant at different scan rates.

In contrast, the absence of any peak or sigmoidal shape in the CVs of the DDT SAM and RJ12 SAM electrodes (Figure 13 and figure 14, respectively) shows that the redox reaction is inhibited. The observed current has capacitive behaviour, since the current doesn't change with the varying potential. The DDT monolayer exhibits very good blocking to ferricyanide redox reaction, indicating the formation of a very organised and pinhole-free monolayer. This behaviour allows the study of kinetics of electron tunnelling through the SAMs.

The indication of pinhole-free monolayer deduced from cyclic voltammetry experiments does not give information about defects in the film. Flinklea et al <sup>10</sup> have suggested that monolayers may contain defects and collapsed sites, that result in sites at which the redox molecule can approach close to the electrode surface but not come in direct contact with it. They introduced these sites as an explanation to the anomalous low Tafel slopes observed in case of octadecanethiol monolayers that were permanently passivated by electrochemical polymerization of phenol in sulfuric acid, that behave like microelectrode arrays.

## 5.4.2 Electrochemical impedance spectroscopy

Electrochemical impedance spectroscopy is a powerful tool to estimate the structural integrity of the monolayer.

The AC impedance method is based upon a measurement of the response of the electrochemical cell to a small perturbation at the equilibrium potential and monitoring phase shift of the current response, over a range of frequencies.

The impedance measurements were carried out using an ac signal of 10 mV amplitude at a equilibrium potential of the redox couple  $(\text{Fe}(\text{CN})_6^{3-/4-})$  at a wide frequency range of 100KHz to 1Hz. The electrolytic solution contained equal concentrations of both the oxidised and reduced forms of the redox couple, namely, 1mM potassium ferricyanide, 1mM potassium ferrocyanide in 0.1M potassium nitrate. The impedance data were analysed with the software ZView 2 (Scribner Associates, Inc.).

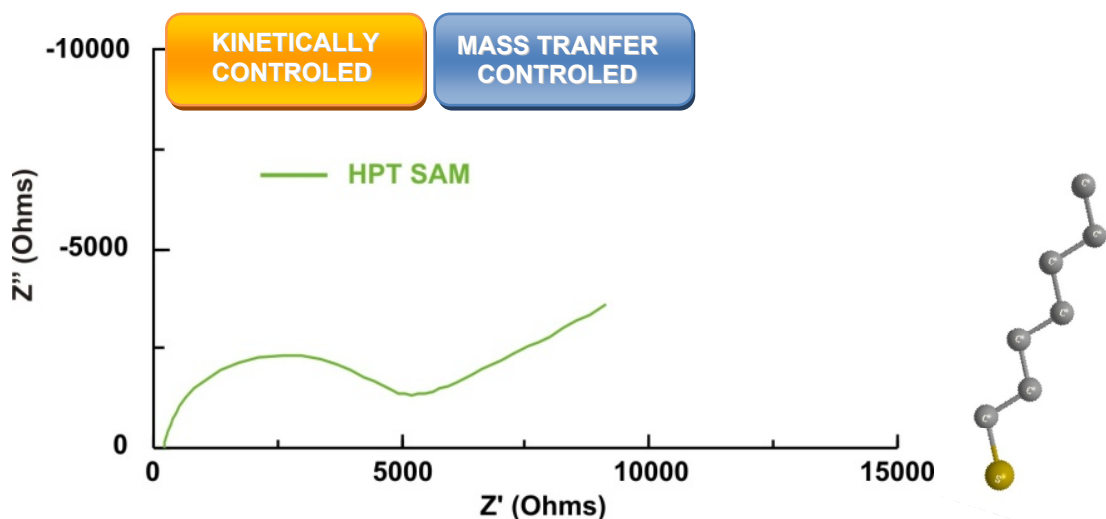


**Figure 17** – Nyquist plot for 1mM  $\text{Fe}(\text{CN})_6^{3-/4-}$  in 0.1M  $\text{KNO}_3$  solution using HPT SAM electrode. Frequency range: 1Hz to 100KHz

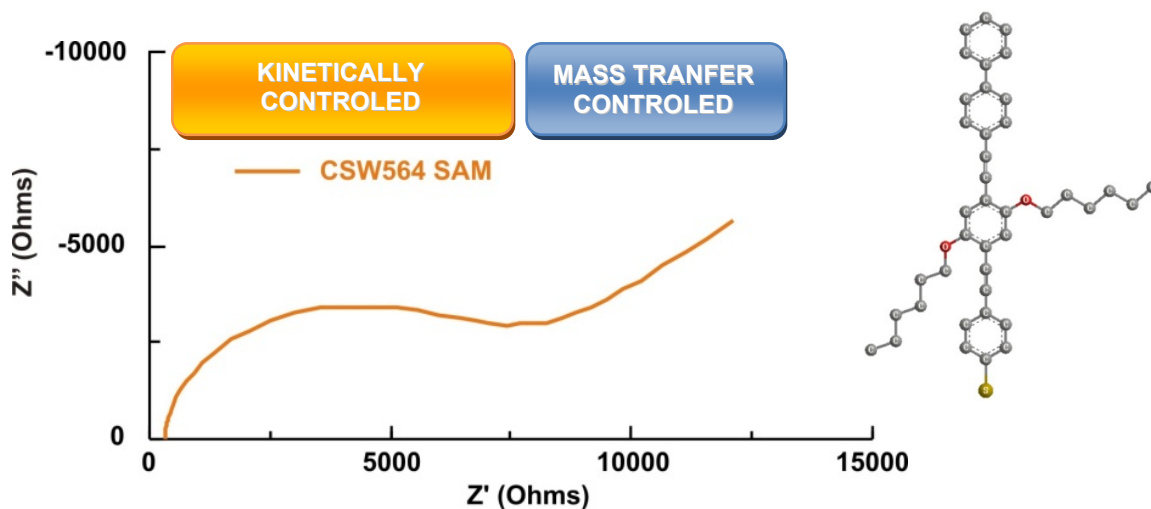


Figure 18 – Nyquist plot for  $1\text{mM Fe(CN)}_6^{3-/4-}$  in  $0.1\text{M KNO}_3$  solution using CSW564 SAM electrode. Frequency range: 1Hz to 100KHz.

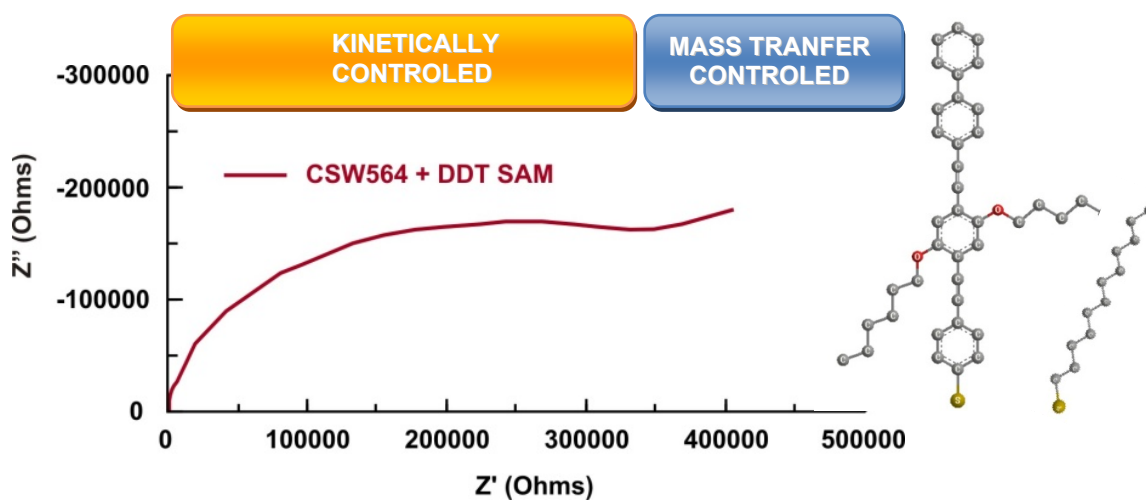
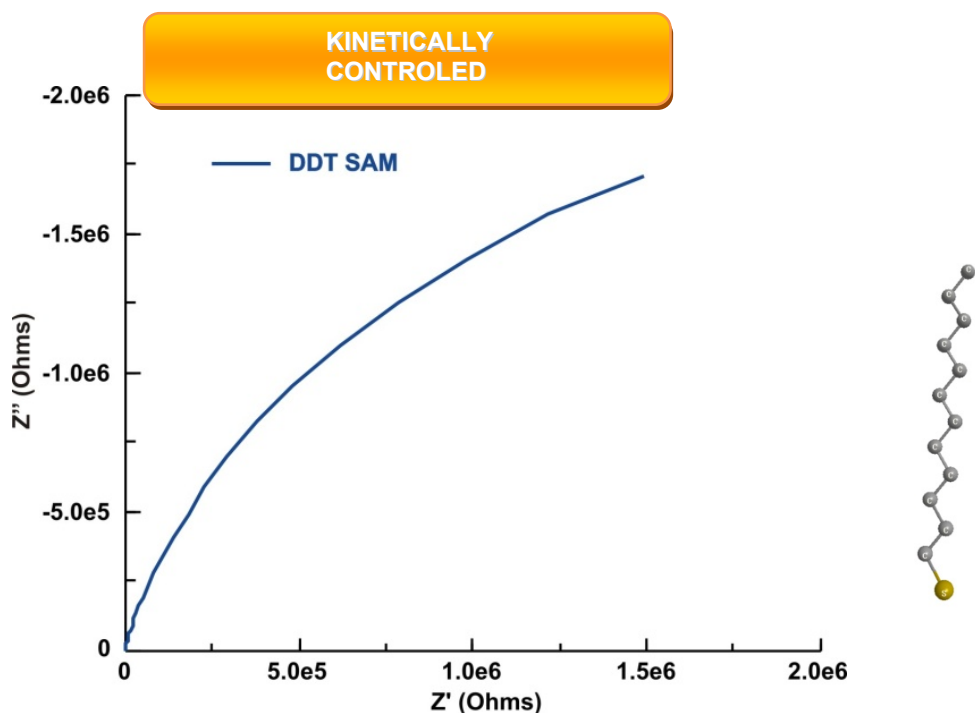
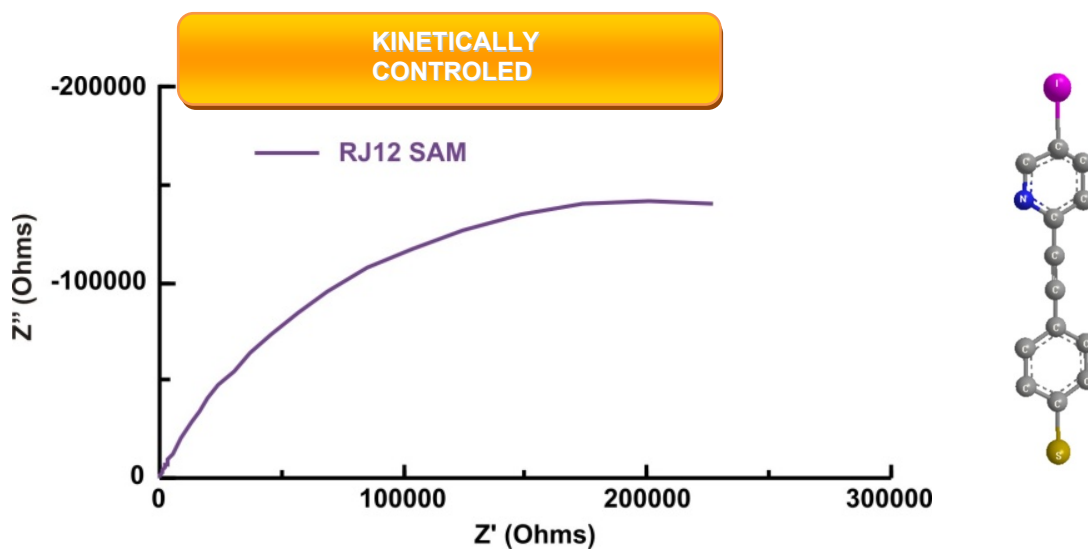


Figure 19 – Nyquist plot for  $1\text{mM Fe(CN)}_6^{3-/4-}$  in  $0.1\text{M KNO}_3$  solution using (CSW564+DDT) SAM electrode. Frequency range: 1Hz to 100KHz



**Figure 20** – Nyquist plot for  $1\text{mM Fe(CN)}_6^{3-/4-}$  in  $0.1\text{M KNO}_3$  solution using DDT SAM electrode. Frequency range: 1Hz to 100KHz



**Figure 21** – Nyquist plot for  $1\text{mM Fe(CN)}_6^{3-/4-}$  in  $0.1\text{M KNO}_3$  solution using RJ12 SAM electrode. Frequency range: 1Hz to 100KHz

The EIS spectrum of HPT SAM (Figure 17) shows a semicircle at high frequency region and a straight line at low frequency region, indicating the facile nature of the redox reaction, and consequently, the poor blocking ability of the monolayer. This response is in accordance with previous one obtained using cyclic voltammetry.

The Nyquist plot for CSW564 SAM (Figure 18) shows similar bare electrode behaviour. A semicircle at high frequency region indicates the redox reaction is kinetically controlled, and a straight line at low frequency region, representing the facile nature of the redox reaction, means that the diffusion is semi-infinite and is mass-transfer controlled. This spectrum is characteristic of poor blocking ability of the monolayer, consistent with CV experiment.

In the case of the mixed-monolayer, the addition of DDT in CSW564 SAM improves the blocking behaviour. The Nyquist spectrum (Figure 19) has the same compartment than DDT SAM. Nevertheless, the charge transfer value is lower compared with the value for DDT. A possible explanation for this observation is the conjugated backbone of the CSW564 molecule, enabling an easy tunnel of electrons and the remaining pinholes in the structure.

Figure 20 and Figure 21 show the Nyquist plots of DDT and RJ12 SAM respectively. It can be seen that these SAMs exhibit a large semi-circle in the entire range of frequencies indicating the complete charge transfer control for the redox reactions and the formation of a very organised and pinhole-free monolayer.

Figure 22 show the Nyquist plots of bare gold electrode. The charge transfer resistance is  $254.80 \text{ Ohm/cm}^2$  and the solution resistance is  $222.10 \text{ Ohm/cm}^2$ . The double-layer capacitance is  $6.56 \text{ }\mu\text{F/cm}^2$ .

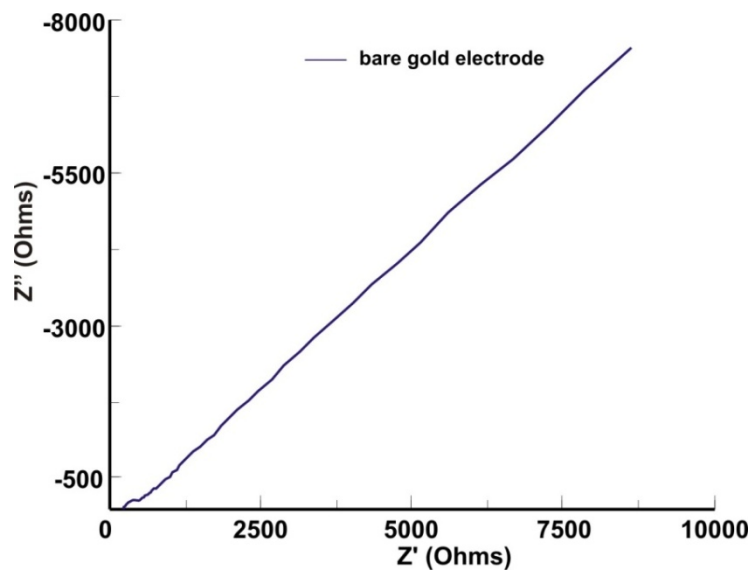


**Figure 22** – Nyquist plot for 1mM  $\text{Fe}(\text{CN})_6^{3-/4-}$  in 0.1M  $\text{KNO}_3$  solution using bare electrode. Frequency range: 1Hz to 100KHz.



## 5.5. ELECTRON TRANSFER KINETICS

---

It has been demonstrated by cyclic voltammetry and electrochemical impedance spectroscopy that we can demonstrate the presence of pinholes on the monolayer straight forward by observing the shape of the plots. However, the existence of defects cannot be proved in this way. The electron transfer kinetics plays an important role in this theme.<sup>11,57</sup>

If there are no pinholes at the Au/SAM interface, the only mechanism for electron transfer is tunneling, i.e. the current is attributed to the electron tunnelling across the monolayer and, according to Marcus<sup>1</sup>, it's expected to decrease exponentially with the increase of thickness,

$$i = i_0 \exp(-\beta d) \quad \text{Eq. (2)}$$

Where,

$i_0$  is the current measured at a bare electrode,

$\beta$  is the electrode tunnelling coefficient that is potential independent and correlates the rate of electron transfer with the chemical structure,

$d$  is the length of molecule that form the monolayer.

When the electrochemical reaction is in equilibrium, It follows that the apparent rate constant is also a function of a length of the molecule that are compose the monolayer:

$$K_{app} = K_0 \exp(-\beta d) \quad \text{Eq. (3)}$$

Where,

$K_0$  is the standard electron transfer rate constant at the bare electrode (1.06E-3 cm/s);

$K_{app}$  is the standard electron transfer rate constant at the film covered electrode.

The standard electron transfer rate  $K_0$  was calculated applying eq. (4), and using  $R_{ct}$  for bare gold electrode.

If the total current is due to electron tunnelling, the theoretical apparent electron-transfer rate for the SAMs can be determined applying Eq. (3), while the experimental electron-transfer rate constant can be obtained by,<sup>57,58</sup>

$$K_{app} = \frac{RT}{F^2 R_{ct} C} \quad \text{Eq. (4)}$$

Where

R is the gas constant (8.314 J K<sup>-1</sup> mol<sup>-1</sup>)

T is the temperature (K)

F is the Faraday constant (96484.6 C mol<sup>-1</sup>)

C is the concentration of the redox couple (mol cm<sup>-3</sup>)

$R_{ct}$  is the charge-transfer resistance per unit geometric area. ( $\Omega$  cm<sup>-2</sup>)

The charge-transfer resistance ( $R_{ct}$ ) for the SAM electrodes were extracted from EIS data by fitting the data applying the following equivalent circuit,

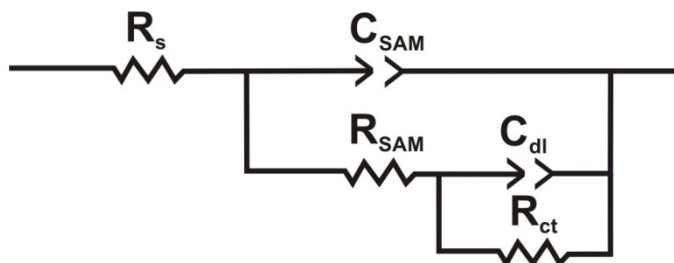


**Figure 23** – Model used for the analysis of EIS data.

The values are described on Table 1.

**Table 1** – Experimental and theoretical rate constants.

|              | th $K_{app}^a$<br>( $cm\ s^{-1}$ ) | $R_{ct}$<br>( $k\Omega$ ) | Exp $K_{app}^b$<br>( $cm\ s^{-1}$ ) |
|--------------|------------------------------------|---------------------------|-------------------------------------|
| HPT          | 3.37E-07                           | 5.142                     | 1.05E-06                            |
| CSW564       | 4.82E-11                           | 6.490                     | 8.34E-07                            |
| CSW564 + DDT | ---                                | 467.8                     | 1.16E-08                            |
| DDT          | 1.07E-09                           | 4326.9                    | 1.25E-09                            |
| RJ12         | 2.38E-08                           | 201.4                     | 2.69E-08                            |

a) From Eq. (3)

b) From Eq. (4)

The  $\beta$  is the decay constant for tunnelling being a parameter sensitively dependent on the electronic coupling of the donor / acceptor across an insulating tunnelling energy barrier. Briefly, this constant is a measure of how much current is lost per unit length of each molecule, which can vary from approximately  $0 \text{ \AA}^{-1}$  (metal) to  $3.5 \text{ \AA}^{-1}$  (close to vacuum).<sup>59,60</sup>

A smaller attenuation factor is expected for aromatic thiols compared to alkanethiols, due to the lower electron transfer energy barrier heights of aromatic chains. This lower value is characteristic of the increase of the energy level of the highest occupied molecular orbital (HOMO) for hole transfer and by the decrease of the energy level of the lowest unoccupied molecular orbital (LUMO) for electron transfer<sup>33</sup>.

The  $\beta$  values used in this work were 1.15 per methylene unit and  $0.67 \text{ \AA}^{-1}$  in the case of alkanethiols and molecular wires, respectively. These values are taken from an experimentally simple method for assembling junctions with nanometer-scale, structured organic films positioned between two metal electrodes.<sup>38</sup>

The molecular lengths were calculated using Chem 3D software developed by Cambridge Scientific Computing with MM2 energy minimization potential function developed by Norman Allinger at Indiana University.<sup>61</sup>

Comparing the electron transfer rate constants, it can be seen that experimental values obtained for HPT and CSW564 SAMs are much larger, approximately one and four orders in magnitude respectively. This result was expected because the presence of pinholes in the film, proved by CV and EIS.

In contrast, there's no significant difference for DDT and RJ12 SAM. The marginal difference may be attributed by negligible defects in the monolayer.

In the case of DDT, if we assume the area occupied by the defects is 1% of the total area, and they cause a 20% decrease of the thickness, the electron transfer rate constant should be  $1.23\text{E-}09 \text{ cm s}^{-1}$ , which is similar to the experimental value. Using this assumption, it can be concluded that DDT and RJ12 SAM were virtually pinhole free and with negligible pinhole defects.

Piao et al <sup>11</sup> have proposed a method to study the fractional coverage of the defects. In the case of pinhole-free monolayer, it was assumed that the apparent rate constant is the sum of the tunnelling currents at defects with different film thickness, following the equation that is derived from Eq. (3):

$$K_{\text{app}} = K_0 \left[ \sigma_0 \exp(-\beta d_0) + \sum_{i=0}^m \sigma_i \exp(-\beta d_i) \right] \quad \text{Eq. (5)}$$

Where,

$\sigma_0$  is the fractional coverage of the well-assembled monolayer.

$d_0$  is the film thickness of well-assembled monolayer.

$\sigma_i$  is the fractional coverage for defects with film thickness  $i$

$d_i$  is the is the film thickness of the defect (Figure 24).

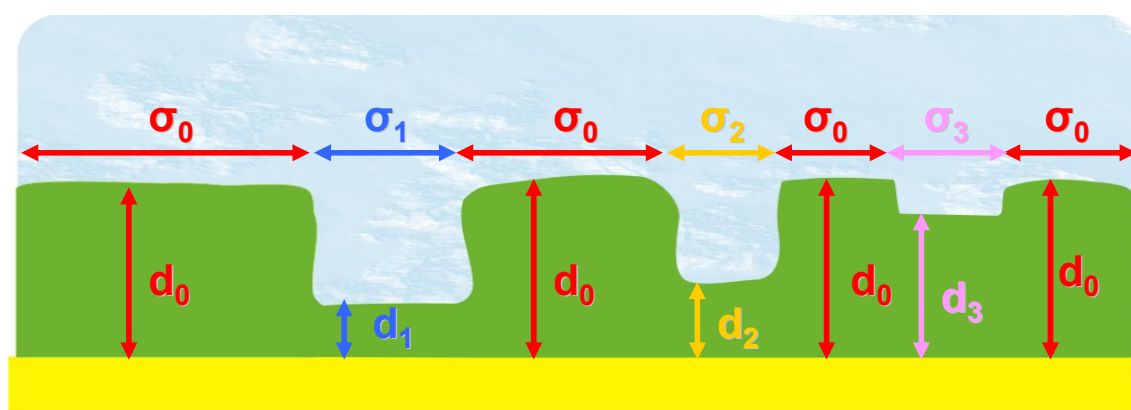


**Figure 24** – Scheme of the SAM with various defects.

However, since it is difficult to calculate the characteristics for each defect, we can use average film thickness of defects ( $d_a$ ) and average fractional coverage of defects ( $\sigma_a$ ). Simplifying the Eq. (5), yields:

$$\sigma_a = \frac{\frac{K_{app}}{K_0} - \exp(-\beta d_0)}{\exp(-\beta d_a) - \exp(-\beta d_0)} \quad \text{Eq. (6)}$$

When  $\sigma_a$  equals 1,  $d_a$  represents the average thickness of the whole monolayer (ATWM) (Figure 25).

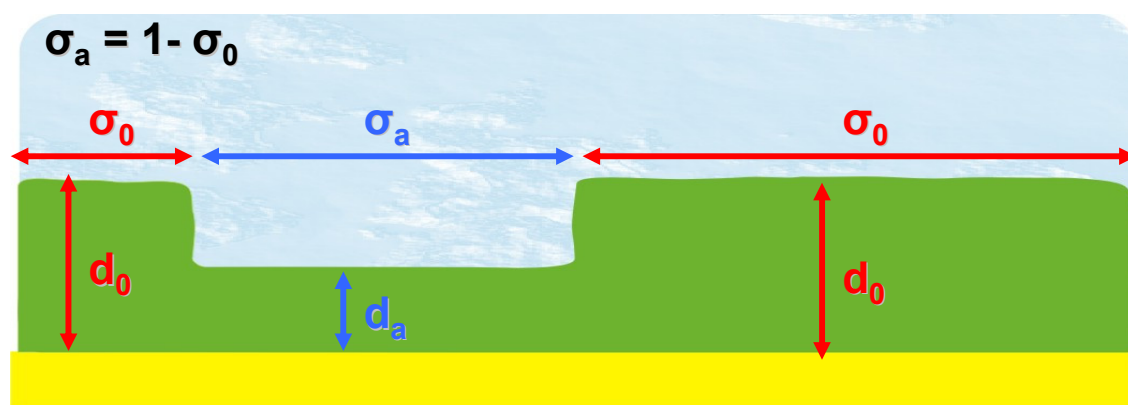


**Figure 25** – Simplification of the defects in the SAM.

This value gives an estimate of the presence of defects in the film. An ATWM value close to  $d_0$ , implies a well-assembled monolayer free of defects.



**Figure 26** – Simplification of the defects in the SAM.

The difference between  $d_0$  and ATWM of DDT and RJ12 SAMs were 0.9 and 0.2 Å, leading the same previous conclusion i.e there are a few negligible defects.

## 5.6. INFLUENCE OF APPLIED POTENTIAL

---

Since DDT and RJ12 SAM were pinhole free and quasi-free of defects, it was found out that the apparent electron-transfer rate constant decreased exponentially with increasing the thickness of the film, according to the Marcus theory.

Electrochemical techniques are widely used in sensors involving self-assembled monolayers, especially with redox molecules bound to the monolayer. Usually, the characteristics of the monolayers are studied under open circuit potential. However, when voltammetry is involved in the biosensor process, the characteristics could vary when the potential change and this is a crucial role in the case of electroactive monolayers and the conditions of pinholes and defects should be studied before the application in any field.

The time scale of electrochemical processes is a key factor in the characterisation of SAMs. For example, high scan rate voltammetry will not give enough time to the conformational changes, whereas a low scan rates, some structural modifications can be found.

Therefore, the influence of applied DC potential over the range of -0.2V to 0.7V (vs Ag/AgCl) on the SAMs was investigated, by superimposing a DC potential on the working electrode and performing EIS at each potential (Figure 27 and Figure 28).

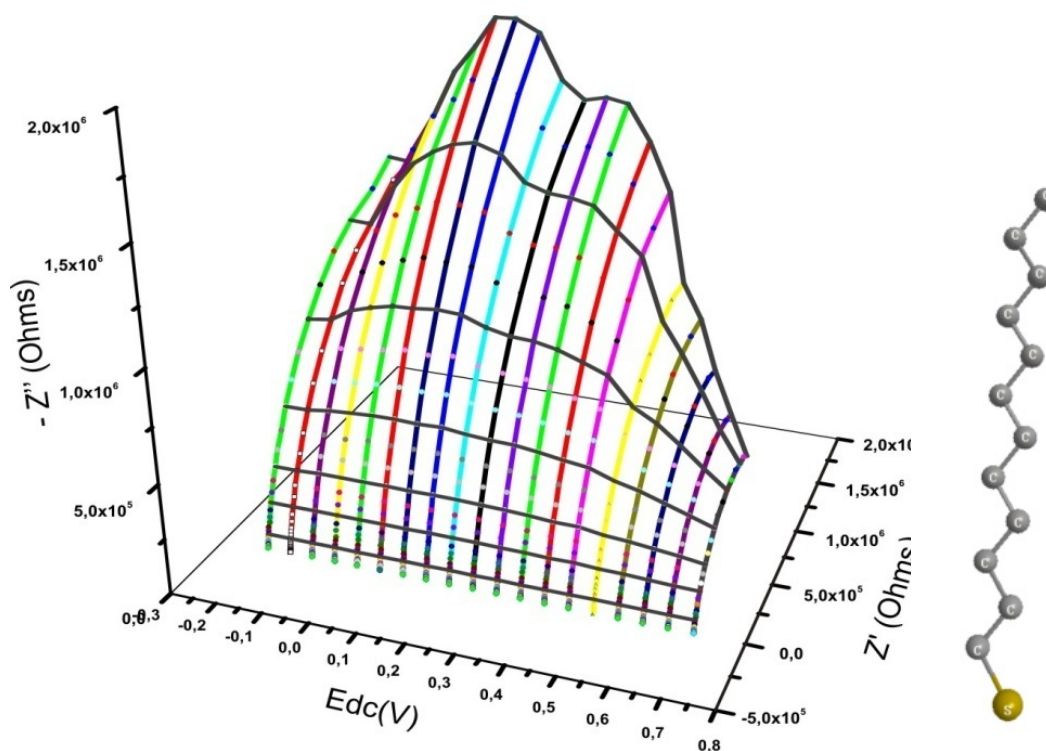


**Figure 27** – Nyquist plots for  $1\text{mM Fe(CN)}_6^{3-/4-}$  in  $0.1\text{M KNO}_3$  solution using DDT SAM electrode. Frequency range:  $1\text{Hz}$  to  $100\text{kHz}$  at different applied potentials.

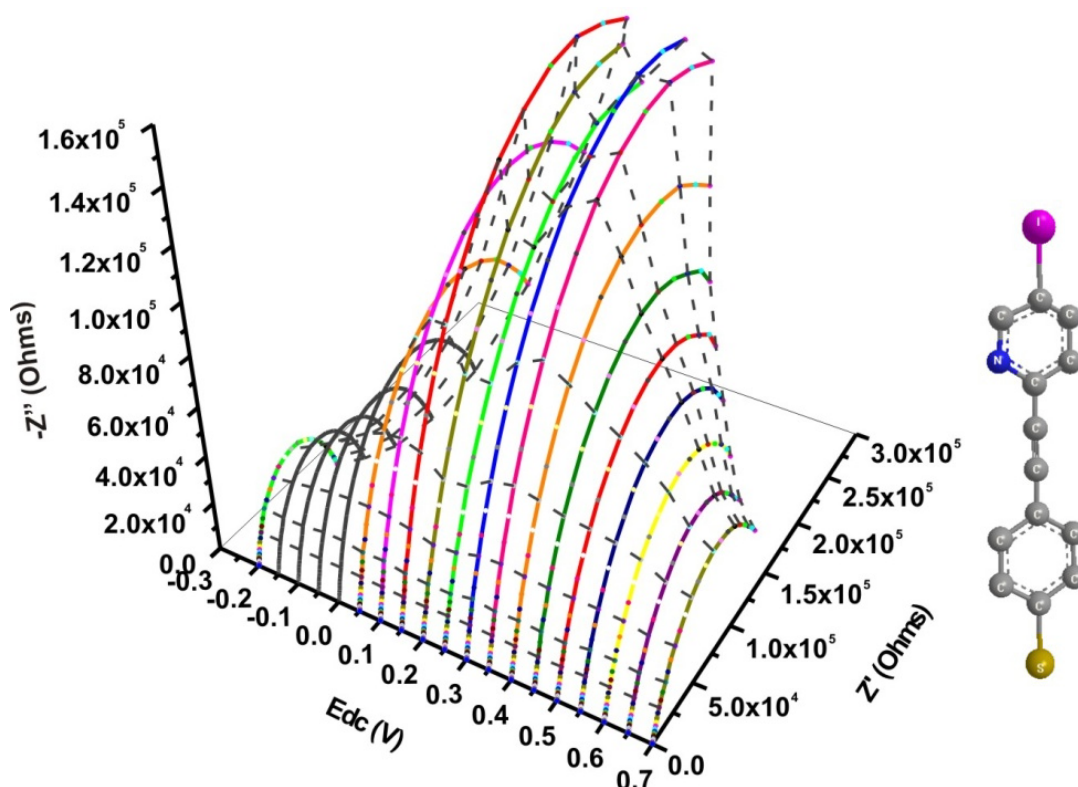


**Figure 28** – Nyquist plots for  $1\text{mM Fe(CN)}_6^{3-/4-}$  in  $0.1\text{M KNO}_3$  solution using RJ12 SAM electrode. Frequency range:  $1\text{Hz}$  to  $100\text{kHz}$  at different applied potentials.



It's clear that EIS response changed at different potentials, and implying that, the characteristics of the monolayer must be modified.

Although the monolayer capacitance of the SAMs remains constant for both SAMs, indicating that this is independent of the potential (Figure 29), the charge-transfer resistance (Figure 30) vary exponentially, according with the following equation,

$$R_{ct} = R_{ct\text{opc}} \exp[-\gamma(E_{app} - E_{opc})] \quad \text{Eq. (7)}$$

Where  $R_{ct}$  is the charge-transfer at the applied potential  $E_{app}$ ,  $R_{ct\text{opc}}$  is the charge-transfer at open circuit potential  $E_{opc}$  and  $\gamma$  is the growth factor (negative overpotentials) or decay factor (positive overpotentials).

When negative overpotentials (relative to the potential of open circuit) were applied, the value increases by a growth factor of  $4.7\text{ V}^{-1}$  (RJ12 SAM) and  $2.9\text{ V}^{-1}$  (DDT SAM) while for positive overpotentials, there's a decrease by a decay factor of  $3.1\text{ V}^{-1}$  (RJ12 SAM) and  $2.5\text{ V}^{-1}$  (DDT SAM), reaching the maximum at the formal potential of the electroactive specie in solution.

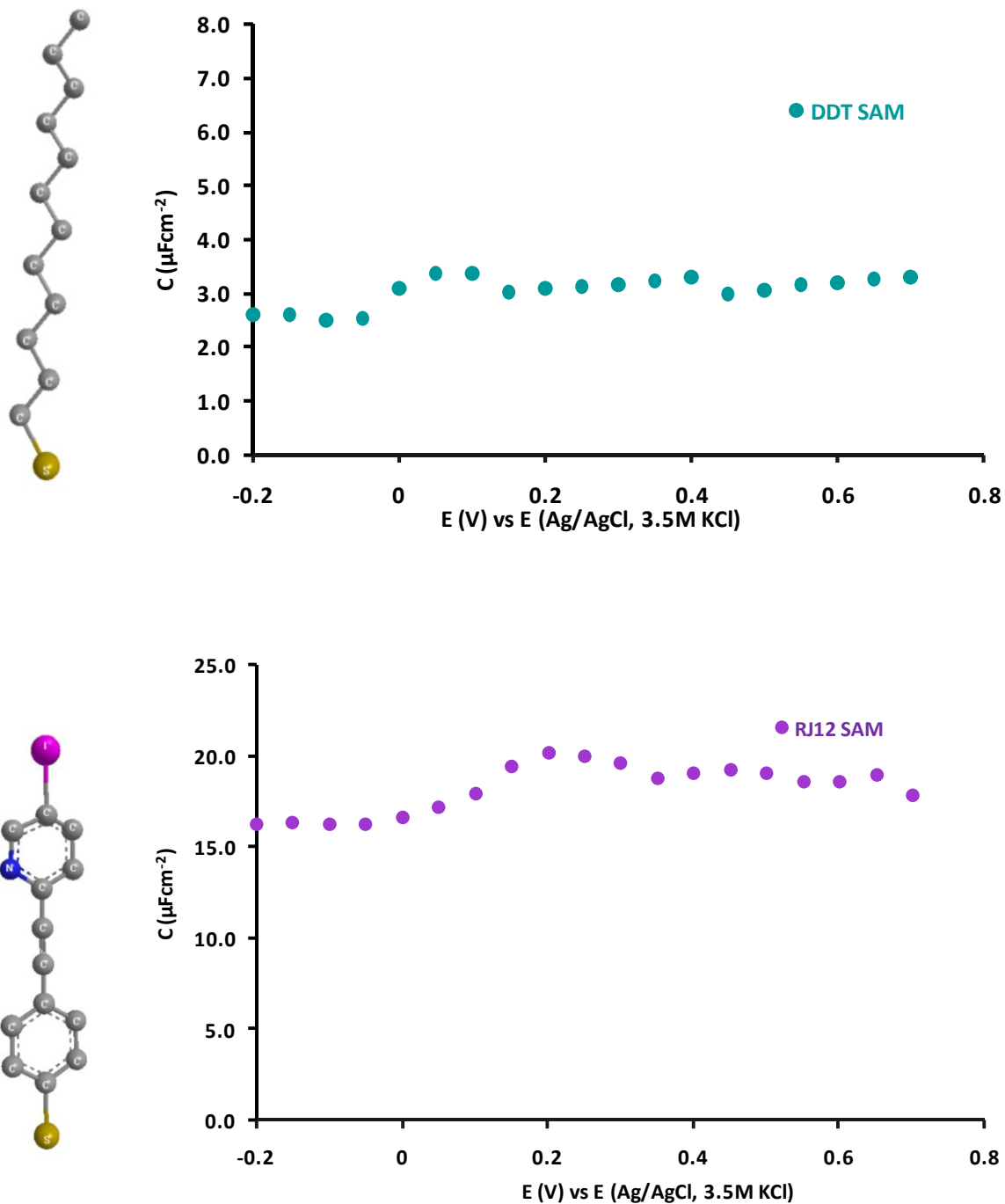


**Figure 29** – Variation of Capacitance of the SAM electrodes over a potential range.

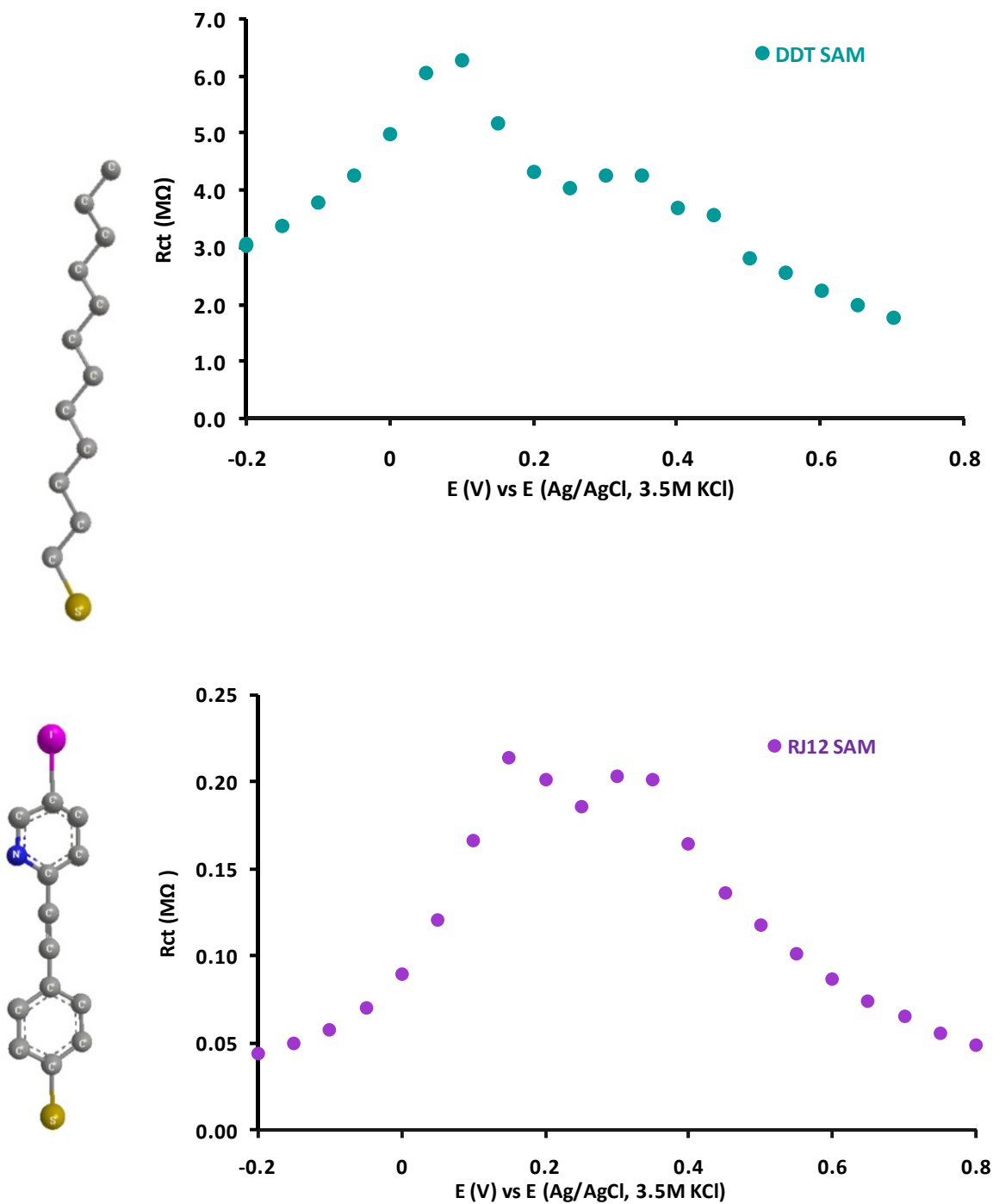


**Figure 30** – Variation of Capacitance of the SAM electrodes over a potential range.

Since the shape of the EIS spectrums maintain typical shape of monolayer free of pinholes, an assumption was made that the difference of the charge transfer resistance was associated with the change of the thickness of the layer due to a change in conformation as reported by previous workers.<sup>62</sup>

ATWM of DDT and RJ12 SAMs at different potentials were determined, and It was noted that the value decreases (relative to  $d_0$ ) when overpotential distance from the open circuit potential. These observation leads to a possible formation of defects that are created due to conformation changes. For DDT SAM, ATWM can achieve a difference of  $1.9\text{\AA}$  from  $d_0$ , whereas for RJ12SAM, ATWM differs at the maximum of  $2.5\text{\AA}$  from  $d_0$ .

## 5.7. CONCLUSIONS

---

In this chapter, the charge transfer and self-assembly characteristics of novel molecular wires assembled on flat gold electrodes are evaluated and the behaviour of these wires are compared with heptanethiol and dodecanethiol SAMs.

HPT and CSW564 SAM electrode have shown that the redox reaction is not suppressed, indicative of presence of pinholes. Voltammetry studies for CSW564 SAM and (CSW564 + DDT) SAM have shown different behaviours, despite the presence of pinholes for both. The CSW564 SAM has presented Nernstian compartment suggesting the presence of millions of small pinholes distributed randomly to the monolayer and their diffusion layers are overlapped responding as macroelectrode. In other hand, (CSW564 + DDT) SAM have presented microelectrode behaviour indicating that each pinhole has acts as a single microelectrode and there is no overlap of the diffusion layers.

The absence of any peak or sigmoidal shape in the CVs and the large semi-circle in the entire range of frequencies for EIS indicating the complete charge transfer control the redox reactions, shows that the redox reaction is inhibited in the DDT and RJ12 SAM, indicating a formation of a very organised and pinhole-free monolayer.

Assuming that all current is attributed to the electron tunnelling across the monolayer, i.e., the monolayer is pinhole-free, the apparent electron-transfer is expected to decrease exponentially with increasing the thickness of the film, according to the Marcus theory.<sup>1</sup>

It was found out that some characteristics of the pinhole-free monolayer change in a potential range. Although the capacitance maintains constant, the

charge-transfer resistance decrease when the potential goes far way from the open potential. Some conformations in the structure of the molecules lead to a formation of defects that decrease the distance between the electroactive species and the electrode surface.

## 5.8. REFERENCES

---

- 1 – R. A. Marcus, N. Sutin, *Biochimica et Biophysica Acta*, 811 (1985) 265 – 322.
- 2 – C. Wang, A. S. Batsanov, M. R. Bryce, *Faraday discussions*, 131 (2006) 221 – 234.
- 3 – S. D. Forester and C. H. Giles, *Chem. Ind.*, (1979) 469 – 474.
- 4 – I. J. Langmuir, *J. Am. Chem. Soc.*, 39 (1917) 1848 – 1906.
- 5 – K. B. Blodgett, *J. Am. Chem. Soc.*, (1935) 1007 – 1022.
- 6 – W. C. Bigelow, D. L. Pickett and W. A. Zisman, *Journal of Colloidal Interface Science*, 1 (1946) 513 – 538.
- 7 – R. G. Nuzzo, D. L. Allara, *J. Am. Chem. Soc.*, 105 (1983) 4481 – 4483.
- 8 – R. A. Marcus, *J. Chem. Phys.*, 24 (1956) 966 – 978.
- 9 – R. A. Marcus, *J. Chem. Phys.*, 43 (1965) 679 – 700.
- 10 – H. O. Finklea, S. Avery, M. Lynch, T. Furtzsch, *Langmuir*, 3 (1987) 409 – 413.
- 11 – P. Diao, M. Guo, D. Jiang, Z. Jia, X. Cui, D. Gu, R. Tong, B. Zhong, *J. Electroanal. Chem.*, 480 (2000) 59 – 63.
- 12 – R. G. Nuzzo, L. H. Dubois, D. L. Allara, *J. Am. Chem. Soc.*, 112 (1990) 558 – 569.

- 
- 13 – R. G. Nuzzo, E. M. Korenic, L. H. Dubois, *J. Phys. Chem.*, 96 (1992) 1355 – 1361.
- 14 – J. Bucher, L. Santesson, K. Kern, *Langmuir*, 10 (1994) 979 – 983.
- 15 – A. Tliti, A. Abdelghani, K. Aguir, M. Gillet, N. Jaffrezic-Renault, *Materials Sci. and Eng. C.*, 27 (2007) 620 – 624.
- 16– R. K. Mendes, R. S. Freire, C. P. Fonseca, S. Neves, *J. Braz. Chem. Soc.*, 15 (2004) 849 – 855.
- 17– C. Lee, Y. Kang, K. Seo, Y. M. Shin, J. H. Kim, S. Choi, J. Kim, H. M. Soh, H. Lee, D. Kim, C. K. Song, *Jap. Journal of Appl. Phys.*, 44 (2005) 530 – 534.
- 18 – A. Ulman, *Chem. Rev.*, 96 (1996) 1533 – 1554.
- 19 – A. Ulman, J. E. Eilers, and N. Tillman, *Langmuir*, 5 (1989) 1147 – 1152.
- 20 – C. A. Widrig, C. A. Alves, E. L. Smith, M. D. Porter, *J. Am. Chem. Soc.*, 113 (1991) 2805 – 2810.
- 21 – C. A. Alves, E. L. Smith, M. D. Porter, *J. Am. Chem. Soc.*, 114 (1992) 1222 – 1227.
- 22 – G. E. Poirier, M. J. Tarlov, *Langmuir*, 10 (1994) 2853 – 2856.
- 23 – S. Frey, V. Stadler, K. Heister, W. Eck, M. Zharnikov, M. Grunze, B. Zeysing, A. Terfort, *Langmuir*, 17 (2001) 2408 – 2415.
- 24 – N. Sandhyarani, T. Pradeep, *Pure appl. Chem.*, 74 (2002) 1593 – 1607.



- 
- 25 – C. Vericat, M. E. Vela, G. A. Benitez, J. A. Martin Gago, X. Torrelles, R. C. Salvarezza, *J. Phys. Condens. Matter*, 18 (2006) 867 – 900.
- 26 – H. Shen, J. E. Mark, C. J. Seliskar, H. B. Mark, W. R. Heineman, *J. Solid. State Electrochem.*, 1 (1997) 148 – 154.
- 27 – M. Yang, Z. Zhang, *Electrochem. Acta*, 49 (2004) 5089 – 5095.
- 28 – C. D. Bain, E. B. Troughton, Y. Tao, J. Evall, G. M. Whitesides, R. G. Nuzzo, *J. Am. Chem. Soc.*, 111 (1989) 321 – 325.
- 29 – E. Sabatani, I. Rubinstein, R. Maoz, J. Sagiv, *J. Electroanal. Chem.*, 219 (1987) 365 – 371.
- 30 – H. O. Finklea, D. A. Snider, J. Fedyk, E. Sabatani, Y. Gafni, I. Rubinstein, *Langmuir*, 9 (1993) 3660 – 3667.
- 31 – Y. F. Xing, S. Li, A. Lau, S. O'Shea, *J. Electroanal. Chem.*, 583 (2005) 124 – 132.
- 32 – H. Hong, W. Park, *Bull. Korean. Chem. Soc.*, 26 (2005) 1885 – 1888.
- 33 – S. Wakamatsu, U. Akiba, M. Fujihira, *Jpn. J. Appl. Phys.*, 41 (2002) 4998 – 5002.
- 34 - C. Gupta, M. A. Shannon, P. J. A. Kenis, *J. Phys. Chem. C*, 113 (2009) 9375 – 9391.
- 35 – M. D. Porter, T. B. Bright, D. L. Allara, C. E. D. Chidsey, *J. Am. Chem. Soc.*, 109 (1987) 3559 – 3568.

- 
- 36 – D. M. Adams, L. Brus, C.E.D. Chidsey, S. Creager, C. Creutz, C. Kagan, P. Kamat, M. Lieberman, S. Lindsay, R. A. Marcus, R. Metzger, M. Beyerle, J. Miller, M. D. Newton, D. R. Rolison, O. Sankey, K. S. Schanze, J. Yardley, X. Zhu, *J. Phys. Chem. B.*, 107 (2003) 6668 – 6697.
- 37– N. K. Chaki, K. Vijayamohanan, *Biosensors & Bioelectronics*, 17 (2002) 1 – 12.
- 38– M. A. Rampi, G. M. Whitesides, *Chemical Physics*, 281 (2002) 373 – 391.
- 39 – A. Aviram and M. Ratner, *Chem. Phys. Lett.*, 29 (1974) 277 – 283.
- 40 – U. Durig, O. Zuger, B. Michel, L. Haussling, H. Ringsdorf, *Physical Review B*, 48 (1993) 1711 – 1717.
- 41 – C. Boulas, J. V. Davidovits, F. Rondelez, D. Vuillaume, *Physical Review B*, 76 (1996) 4797 – 4800.
- 42 – M. A. Reed, C. Zhou, C. J. Muller, T. P. Burgin, J. M. Tour, *Science*, 278 (1997) 252 – 254.
- 43 – L. A. Bumm, J. J. Arnold, M. T. Cygan, T. D. Dunbar, T. P. Burgin, L. Jones, D. L. Allara, J. M. Tour, P. S. Weiss, *Science*, 271 (1996) 1705 – 1707.
- 44 – L. Guo, J. S. Facci, J. G. McLendon, R. Moshert, *Langmuir*, 10 (1994) 4588 – 4593.
- 45 – L. Strong, G. M. Whitesides, *Langmuir*, 4 (1988) 546 – 558.
- 46 – S. D. Evans, R. Sharma, A. Ulman, *Langmuir*, 7 (1991) 156 – 161.
- 47 – H. O. Finklea, D. A. Snider, J. Fedyk, *Langmuir*, 6 (1990) 371 – 376.

---

48 – Y. F. Xing, S. Li, A. Lau, S. O'Shea, *J. Electroanal. Chem.*, 583 (2005) 124 – 132.

49 – Y. Shon, Jr. R. Colorado, C. T. Williams, C. D. Bain, T. R. Lee, *Langmuir*, 16 (2000) 541 – 548.

50 – M. Yang, Z. Zhang, *Electrochimica acta*, 49 (2004) 5089 – 5095.

51 – Y. Zhang, R. H. Terrill, P. W. Bohn, *Chem. Mater*, 11 (1999) 2191 – 2198.

52 – Mahesh G. Samant, Charles A. Brown, Joseph G. Gordon, *Langmuir*, 7 (1991) 437 – 439.

53 – H. Ron, I. Rubinstein, *Langmuir*, 10 (1994) 4566 – 4573.

54 – R.T. Kissinger, W.R. Heineman, *Laboratory Techniques in Electroanalytical Chemistry*, second ed., Marcel Dekker, New York, 1996.

55 – H. J. Lee, C. Beriet, R. Ferrigno, H. H. Girault, *J. Electroanal. Chem.*, 502 (2001) 138 – 145; Trevor J. Davies, Richard G. Compton, *J. Electroanal. Chem.*, 585 (2005) 63 – 82.

56 – I. Streeter, R. G. Compton, *Sensors and Actuators B*, 130 (2008) 620 – 624.

57 – P. Diao, D. Jiang, X. Cui, D. Gu, R. Tong, B. Zhong, *J. Electroanal. Chem.*, 464 (1999) 61 – 67.

58 – E. Sabatani, I. Rubinstein, *J. Phys. Chem.*, 91 (1987) 6663 – 6669.

59 – P. P. Edwards, H. B. Gray, M. T. J. Lodge, R. J. P. Williams, *Angewandte Chemie International Edition*, 47 (2008) 6758 – 6765.

---

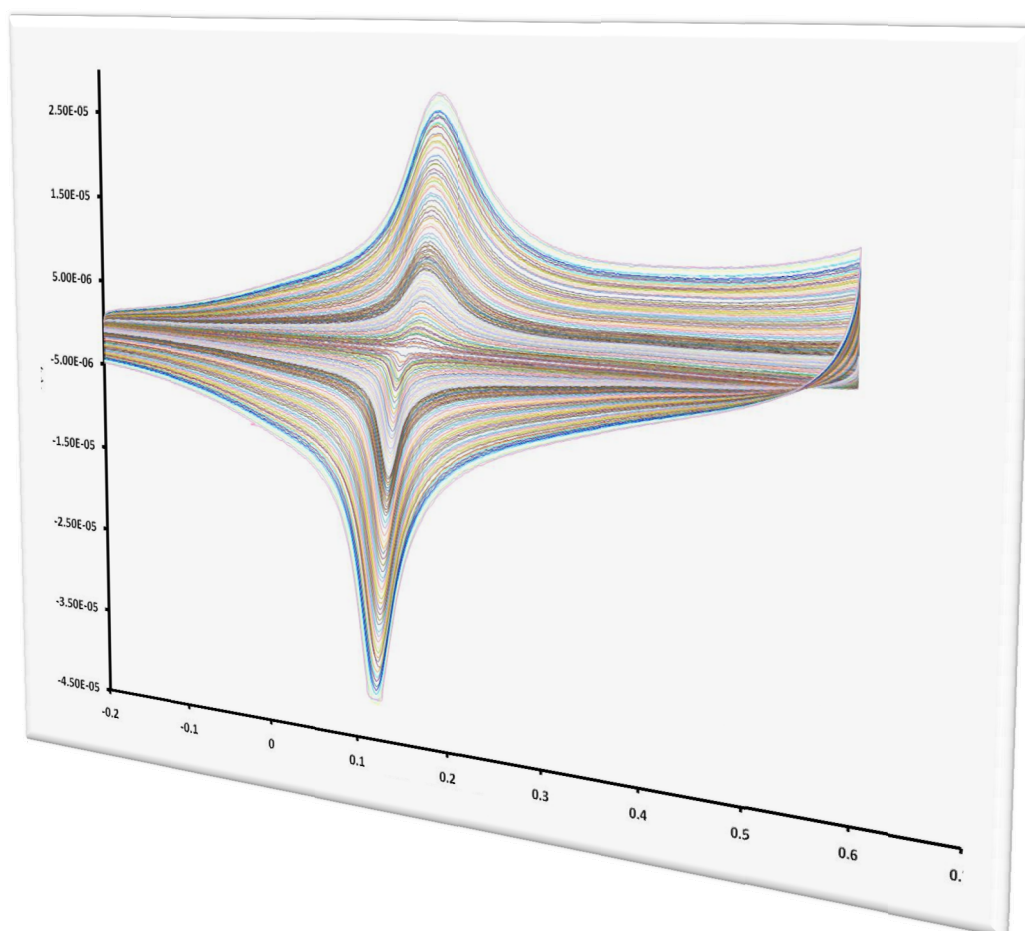
60 – D. K. James, J. M. Tour, *Chem. Mater*, 16 (2004) 4423 – 4435.

61 – K. A. Bunting Lee, *Langmuir*, 6 (1990) 709 – 712.

62 – H. Sahalov, B. O'Brien, K. J. Stebe, K. Hristova, P. C. Searson, *Langmuir*, 23 (2007) 9681 – 9685.

## 6. THE MYSTERY OF THE SHARP PEAKS – ELECTRON TRANSFER OR GOLD CYANISATION?

---



*“Many discoveries have their basis on mistakes committed by the researchers”*

## 6.1. ABSTRACT

---

Sharp peaks using cyclic voltammetry were found with SAM modified gold electrode, platinum electrode and silver silver chloride as working, counter and reference electrode respectively, after have applied +2.0V for 20 s to gold electrode containing thiol self-assembled monolayer accidentally, in equimolar aqueous solution of 1mM ferricyanide / ferrocyanide and 0.1M potassium nitrate.

Cyclic voltammograms of the thiol self-assembled monolayers (DDT and RJ12) showed sharp peaks at formal potential of 0.18V (vs Ag/AgCl, 3.5M KCl), especially the cathodic one. The peak-to-peak separation was very small, indicating that this response may be a typical surface-confined electroactive species. However, the peak height between anodic and cathodic are not equal ( $\frac{i_{pc}}{i_{pa}} \cong 1.7$ ) for both electrodes.

It was conclude that the peaks can be associated with two distinct process: gold cyanisation leading to the formation of  $\text{KAu(CN)}_2$ , and deposition of Prussian Blue in the electrode surface. In both cases, the presence of the self-assembled monolayer is crucial in order to observe the peaks. This is an interesting observation as previous workers reported similar behaviour due to the phase transition of the insoluble AuCN layer (in aqueous solution) to a soluble dicyanoaurate ion at 0.18V in case of gold cyanisation<sup>17</sup>, and the wave redox potential at 0.18 V corresponding to the oxidation/reduction of high spin iron (II) to iron(III) converting Prussian White to Prussian Blue and vice-versa, in case of presence of PB.<sup>12</sup>

FTIR experiments were performed to confirm the presence  $\text{Au(CN)}_2^-$ , and Prussian Blue, due to the presence of a broad band in the region of around  $2127 \text{ cm}^{-1}$  the  $-\text{C} \equiv \text{N}$ : triple bond.

## 6.2. INTRODUCTION

---

During the investigation of the characterisation of self-assembled monolayers of alkanethiols and molecular wires on gold using electrochemical impedance spectroscopy, an accident lead to very interesting results.

A +2.0 V potential against the reference electrode (Ag/AgCl) (instead of the intended +0.2V) was applied while the frequency scan was running, in solution containing  $\text{Fe}(\text{CN})_6^{4-} / \text{Fe}(\text{CN})_6^{3-}$  couple. This resulted in the appearance of very sharp peaks in the cyclic voltammograms.

Experiments were carried out to investigate our results and examine our findings compared to previous reports which are discussed in the section on results and discussions.

Since the experimental procedure is very confused, it is easily comprehended using bullets:

1. Formation of SAM on gold electrode (following procedure explained in the previous chapter);
2. Cyclic voltammetry using SAM electrode, in 1mM  $\text{Fe}(\text{CN})_6^{4-} / \text{Fe}(\text{CN})_6^{3-}$  solution, in order to check the quality of the SAM (no peaks were observed)
3. Application of 2.0V for 20s to the SAM electrode (instead of the intended +0.2V) using electrochemical impedance spectroscopy, in solution containing  $\text{Fe}(\text{CN})_6^{4-} / \text{Fe}(\text{CN})_6^{3-}$  couple. Further experiments were performed using chronoamperometry;
4. Cyclic voltammetry using SAM electrode, in background solution (without electroactive specie), resulting peaks.

Figure 1 gives a picture of this procedure:

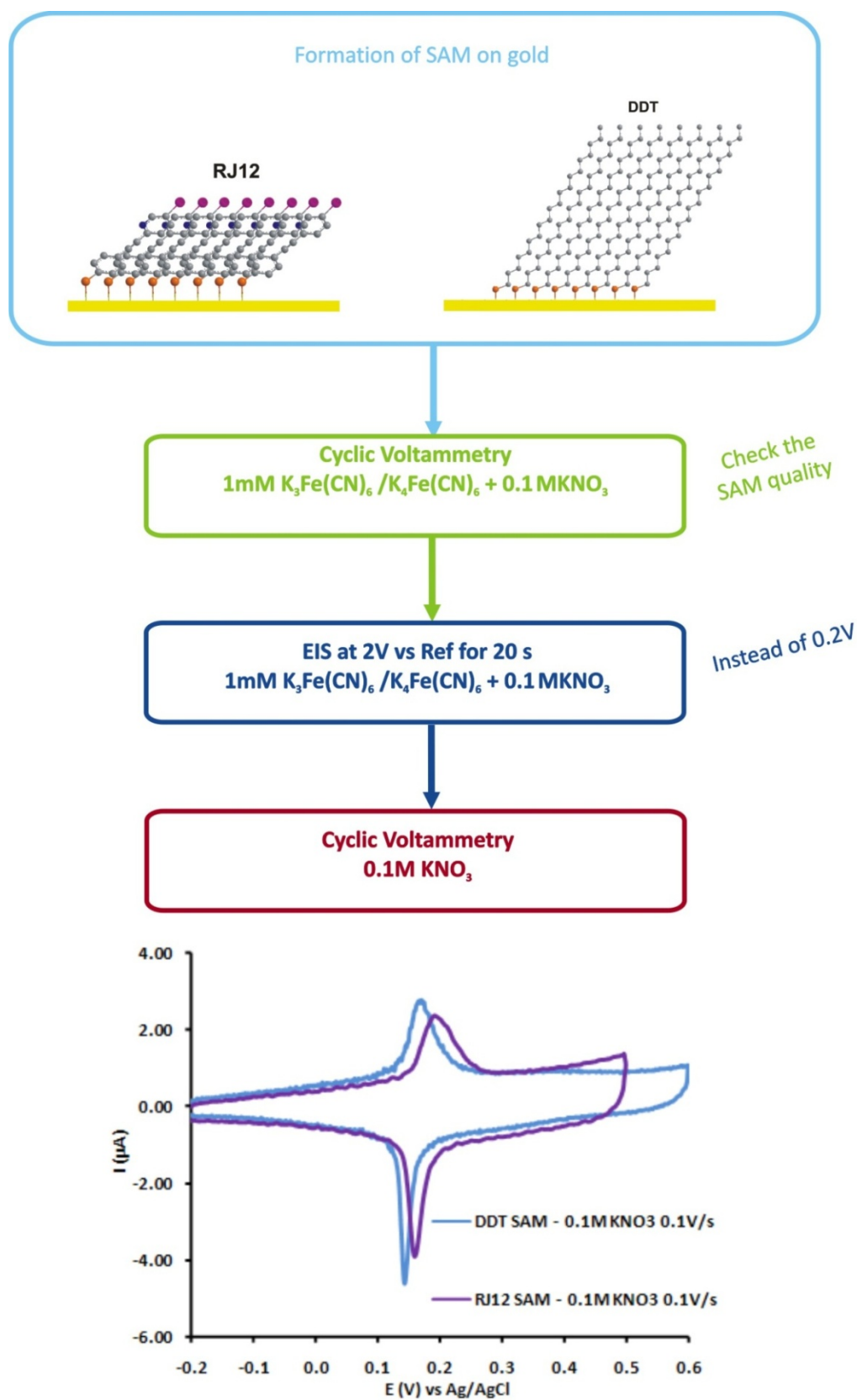


Figure 1 – Explanation of the experimental procedure used in this work.



The influence of scan rate in the peak current was investigated, and the apparent rate constant ( $K_{app}$ ) was evaluated using Laviron's procedure.

The  $i_{pc}/i_{pa}$  ratio is different than unity and the anodic peak is not sharper than the cathodic peak. Also, the apparent rate constant was calculated for both SAMs having similar values. This observation seemed to imply the independence of the electron transfer on the structure of the monolayer, indicating that the redox species are confined in the electrode surface but they are not interact with the molecules that they compose the monolayer, acting as a shield.

Consequently, some experiments were executed in order to find out the cause for these sharp peaks.

The same experiment was carried out without SAM on gold, ie, bare gold electrode, the result have shown that nothing happened, giving a complete flat CV.

A possible consequence of these peaks is gold cyanisation leading to the formation of  $KAu(CN)_2$ , the formation of oxygen created by the applied high potential to the electrode and as consequence, the perturbation in the arrangement of the thiol self-assembled monolayer, contributing to trap the  $KAu(CN)_2$  molecules.<sup>1</sup> Therefore, understanding the process is fundamental.

### 6.2.1. Gold Cyanisation

Cyanisation (also known as the cyanide process or the MacArthur-Forrest process) is a technique for extracting gold from low-grade ore by converting the gold to water soluble aurocyanide metallic complex ion or dicyanoaurate(I) complex (Figure 2).

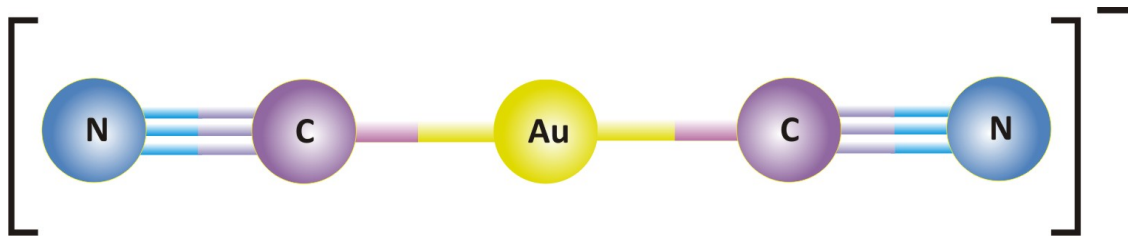


**Figure 2** – Structure of the aurocyanide or dicyanoaurate(I) complex.

The chemical symbol Au for gold derives from the Latin word aurum meaning “shining dawn”. Auroa was the Roman goddess of dawn. From this etymological connection it appears that gold was from early times for humans a symbol of light and beauty, materializing the immortality of the gods. <sup>2</sup>

In gold extraction in ore minerals, the ultimate objective of the metallurgical process is to recover the valuable mineral from the ore gangue minerals in the purest possible form and at the highest possible profitability. Various process designs are available, always following the mother process – gold cyanisation.

An important discovery concerning the treatment of gold ores was made in 1846 by L Elsner <sup>3</sup>, a German chemist, when he demonstrated the solubility of gold in dilute solutions of potassium cyanide as shown in following equation,



John Seward McArthur, a metallurgical chemist in Scotland, realised that Elsner's discovery of the solubility of gold in weak potassium cyanide solution might be of value. The practical use of cyanide for the recovery of gold was thus developed. In 1887 the first cyanisation patent was registered in Great Britain.

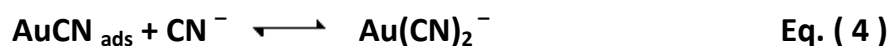
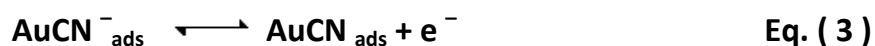
Gold cyanisation has been used as the principle gold extraction technique since the late 19th century, and since their invention, its chemistry and leaching kinetics have been the subjects of considerable investigation and several theories have been proposed to explain the reaction mechanism, but, this method has been the most popular for recovering gold from the ores and cyanide is still the most important commercial lixiviant in today's gold operations throughout the world, because of its relatively low cost and great effectiveness for gold dissolution, despite some concerns over the toxicity of cyanide (Cyanide is poisonous because it reacts with haemoglobin, reducing the oxygen-carrying capacity of blood).

New environmental friendly processes are in study, and the goal is to find a method which uses microorganisms for the recovery of precious metals from metal-containing processes and streams. This technology is targeted at using naturally-occurring, sulfate-reducing bacteria for the recovery of gold and silver from ores.<sup>4</sup>

The exceptional success of this method, still in nowadays, although several noncyanide lixivants were suggested and tested<sup>5</sup>, is the fact of high selectivity and the simplicity of the process, such as, the high stability of dicyanoaurate ion

comparing with other metal-cyanide complexes, and the high solubility of gold-cyanide complex in aqueous solutions.

The dissolution of gold in cyanide solutions exhibits wide variation. The most important studies were made by Kirk et al <sup>6</sup> using coulometry, and they have proposed the following reactions sequence:



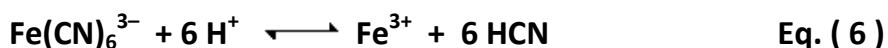
Various variables affecting gold cyanisation, such as dissolved oxygen concentration, free cyanide concentration, temperature, pH and particle size, have been studied.

Some investigators on the leaching of gold in aerated cyanide solution have shown that both cyanide and dissolved oxygen concentration play important roles. <sup>7</sup> The availability and reactivity of oxygen is believed to be the critical factor in the traditional gold cyanisation process, however, various researchers have shown that the presence of another oxidants (with oxygen) improve the efficiency of gold cyanisation, such as, Ferricyanide, due to their high solubility in cyanide solution they are very stable over a wide range of pH. <sup>8</sup>

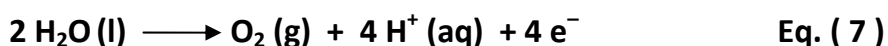
The dissolution of gold in ferricyanide – cyanide solution can be expressed as following,



Ferrocyanide and ferricyanide complexes are very stable and they are unable to dissociate to release free ions  $\text{CN}^-$  in solution ( $\log k=38.3$ )<sup>9</sup>. However, it has been established that the ferricyanide complex can be dissociated in acidic solution, releasing a limited concentration of free ferric ions and free cyanide ions, according to the following equation,<sup>15,20,21,22</sup>



In this case, the solution is not acid enough to promote the dissociation. However, there is formation of  $\text{H}^+$  ions in the oxygen evolution region (1.8 V), when +2.0V is applied to the cell. The water oxidation reaction occurs in the solution near to the electrode surface becoming acid (only on the electrode surface area), according with the water electrolysis,



The oxygen reacts in the gold cyanisation mechanism. Therefore, with cyanide ions and oxygen in solution which are in contact with gold substrate, there are all the ingredients of the gold cyanisation recipe, and gold should spontaneously reacts to form gold cyanide complex – dicyanoaurate.

However, the dissociation of ferricyanide ensures free iron (III) ions essential for the formation of a layer of Prussian Blue (ferric ferrocyanide) on the gold surface. It is pertinent to give a brief introduction to Prussian Blue chemistry.

### 6.2.2. Deposition of Prussian Blue (PB)

Prussian Blue (PB) has the structure  $KFe_4^{(III)}[Fe^{(II)}(CN)_6]_3$  consisting of alternating  $Fe^{3+}$  and  $Fe^{(II)}(CN)_6^{4-}$  located on a face centred cubic lattice. The  $Fe^{3+}$  ions (high spin) are surrounded by an octahedral arrangement of nitrogen atoms and the  $Fe^{2+}$  (low spin) by carbon atoms.

The history of Prussian Blue is long, dating back to the beginning of the 18<sup>th</sup> century, when was discovered the potential applications as a blue pigment. Since the discovery, a bunch of scientists have focused their studies on this compound due to its attractive electrochromic property<sup>10</sup>, easy preparation and low cost, but due to the excellent electrocatalytic properties, PB is widely used as an electron transfer mediator in the amperometric sensors, also called as “artificial peroxidase” caused by the analogy to peroxidase that is responsible in nature for reduction hydrogen peroxide.<sup>11,12</sup>

In 1978, Vernon D. Neff<sup>13</sup> has reported that PB can form electroactive films after electrochemical deposition on the surfaces of the electrodes, opening at that time, a new area of investigation.

Traditional methods for the deposition of PB in conductive substrates require the simultaneous presence of free metallic ions and the corresponding metal-cyanide ions in solution<sup>10,11,12</sup>. Nevertheless, Deng et al<sup>14</sup> reported the electrochemical preparation of PB film modified electrodes from an acidic solution of ferricyanide without free metallic ions.

As it was discussed above, the authors mentioned that the dissociation of ferricyanide must be the main source of iron (III) ions. This procedure provides a densely packed ultrathin film of PB.<sup>15</sup>

## 6.3. EXPERIMENTAL

---

### 6.3.1. Reagents and chemicals

Potassium ferricyanide, potassium ferrocyanide, potassium nitrate and 1-dodecanethiol were purchased from Aldrich. THF were provided for the solvent store at Chemistry department in Durham University.

RJ12 molecules were synthesised at the Department of Chemistry and Centre for Molecular and Nanoscale Electronics, Durham University, UK.

All the aqueous solutions were prepared deionised water supplied by a Sartorius Arium 611 ultrapure water system (conductivity =  $0.055 \mu\text{S cm}^{-1}$ ).

### 6.3.2. Instrumentation

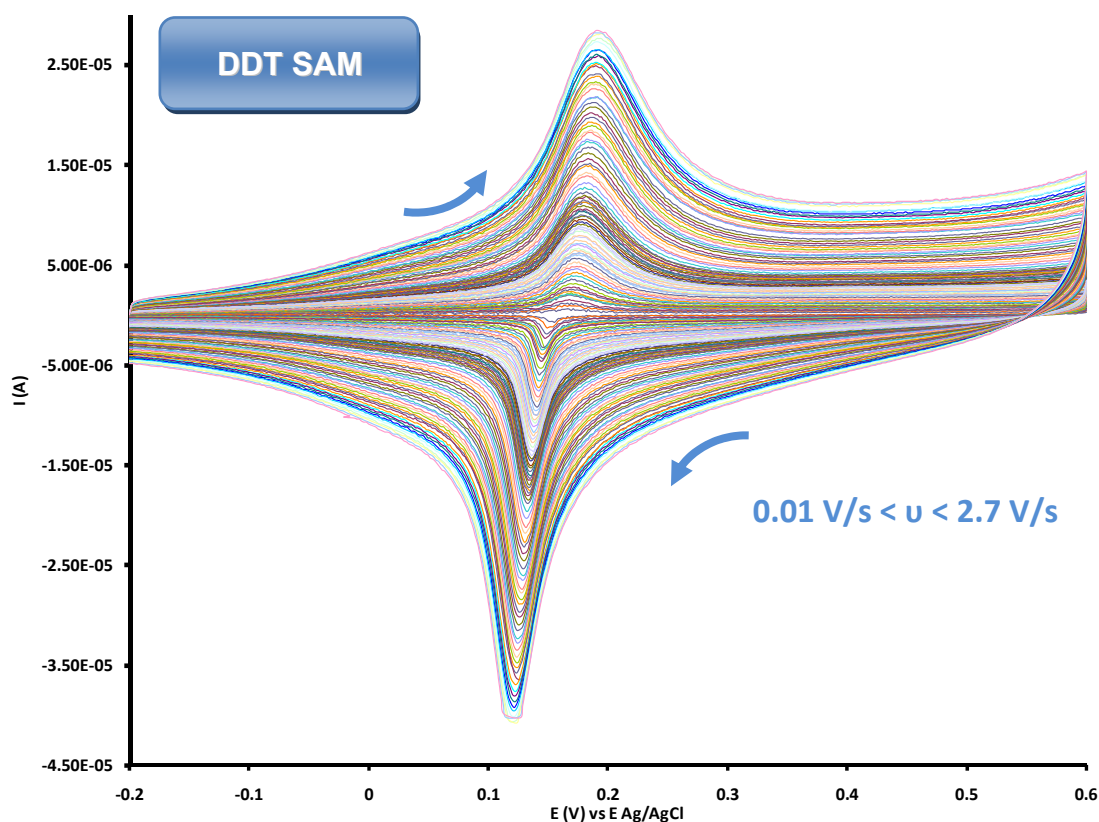
Electrochemical experiments were performed using a Potentiostat-Galvanostat Model 283 (Princeton Applied Research). Ag/AgCl (3.5M KCl) was used as reference electrode, Platinum foil ( $A=1 \text{ cm}^2$ ) was used as auxiliary electrode and the working electrode was bare gold electrode or Dodecanethiol self-assembled monolayer on gold electrode. The cell was placed in a Faraday cage to eliminate external interference. All electrode potentials are reported with respect to Ag/AgCl (3.5M KCl).

FTIR experiments were carried out using a Thermo Nicolet Nexus™ FTIR spectrophotometer controlled by OMNIC software Version 5.1.. Infrared spectroscopy is an excellent tool to explore the bonding of the molecular structure adsorbed on the electrode surface.

## 6.4. RESULTS AND DISCUSSIONS

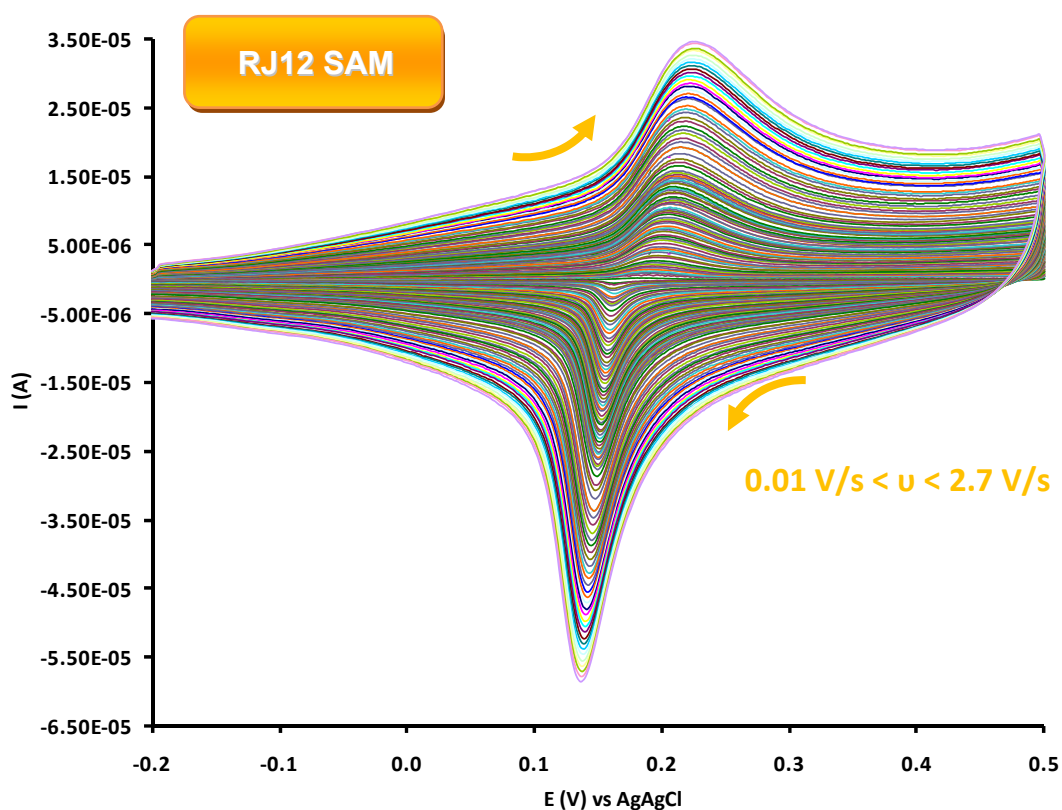
### 6.4.1. Cyclic voltammetry

Figure 3 and Figure 4 show Cyclic voltammograms obtained at DDT SAM and RJ12 SAM on gold electrodes in 0.1 M  $\text{KNO}_3$  solution, performed after the application of +2V in 1mM Ferri-ferrocyanide + 0.1 M  $\text{KNO}_3$  for 20 seconds. Scan rates are between  $0.01 \text{ Vs}^{-1}$  and  $2.7 \text{ Vs}^{-1}$ .



**Figure 3** – Cyclic voltammograms of DDT SAM on gold in 0.1 M  $\text{KNO}_3$ . Scan rate:  $0.01$  to  $2.7 \text{ Vs}^{-1}$ .





**Figure 4** – Cyclic voltammograms of RJ12 SAM on gold in 0.1 M  $\text{KNO}_3$ . Scan rate: 0.01 to 2.7  $\text{Vs}^{-1}$ .

Several cyclic voltammograms at different scan rates were carried out and then the peak current and the associated charge calculated (Figure 3 and Figure 4).

As expected for the voltammetric behaviour of the surface-confined redox molecule, reversible redox peaks produce very small peak-to-peak separation ( $\Delta E_p$ ). These values are 13mV for DDT SAM and 17mV for RJ12 SAM, at 50  $\text{mVs}^{-1}$ ). However, the ratios of peak current are different than the unity, having respectively, 1.6 and 1.7 for DDT and RJ12 SAM electrode

The influence of scan rate is also investigated and the redox currents of SAM monolayers linearly increase with scan rate, representing a typical electron transfer surface process<sup>16</sup> (Figure 5, figure 6, figure 7, and figure 8).

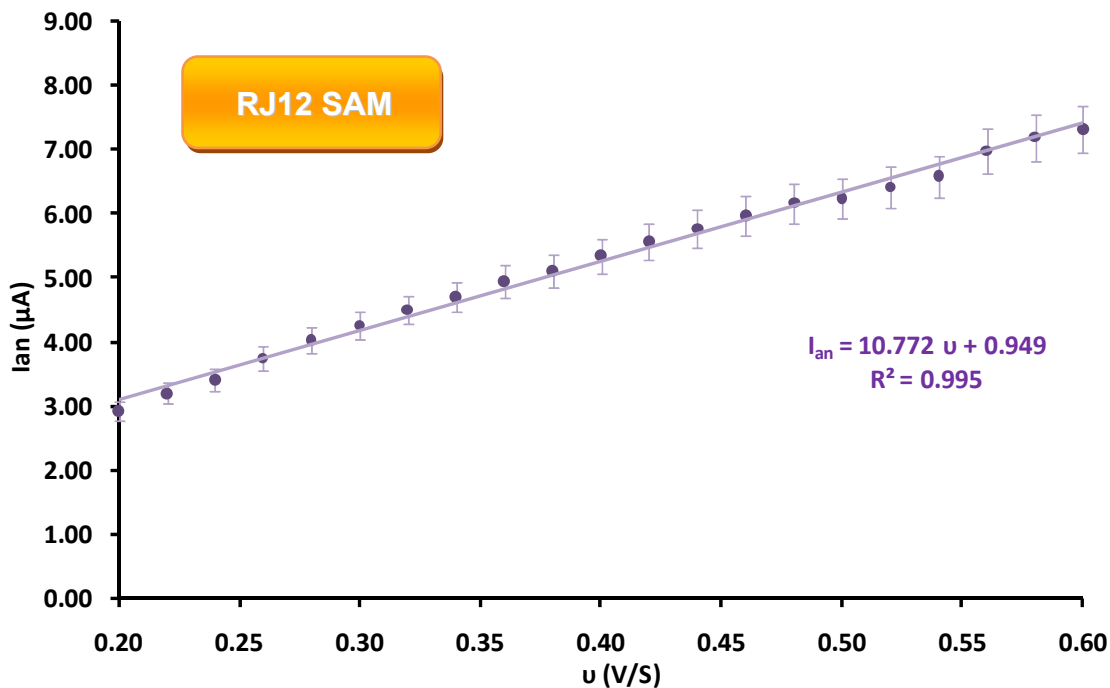


Figure 5 – Scan rate dependence of the anodic peak current in cyclic voltammetry for RJ12 SAM electrode in 0.1M  $KNO_3$  solution.

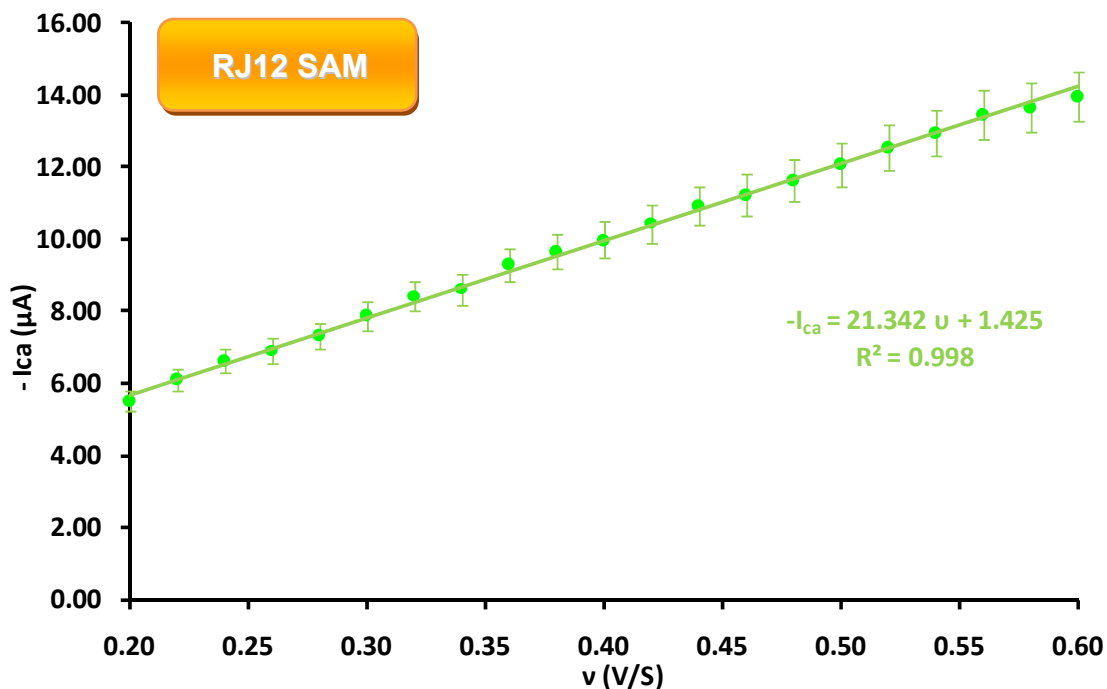


Figure 6 – Scan rate dependence of the cathodic peak current in cyclic voltammetry for RJ12 SAM electrode in 0.1M  $KNO_3$  solution.

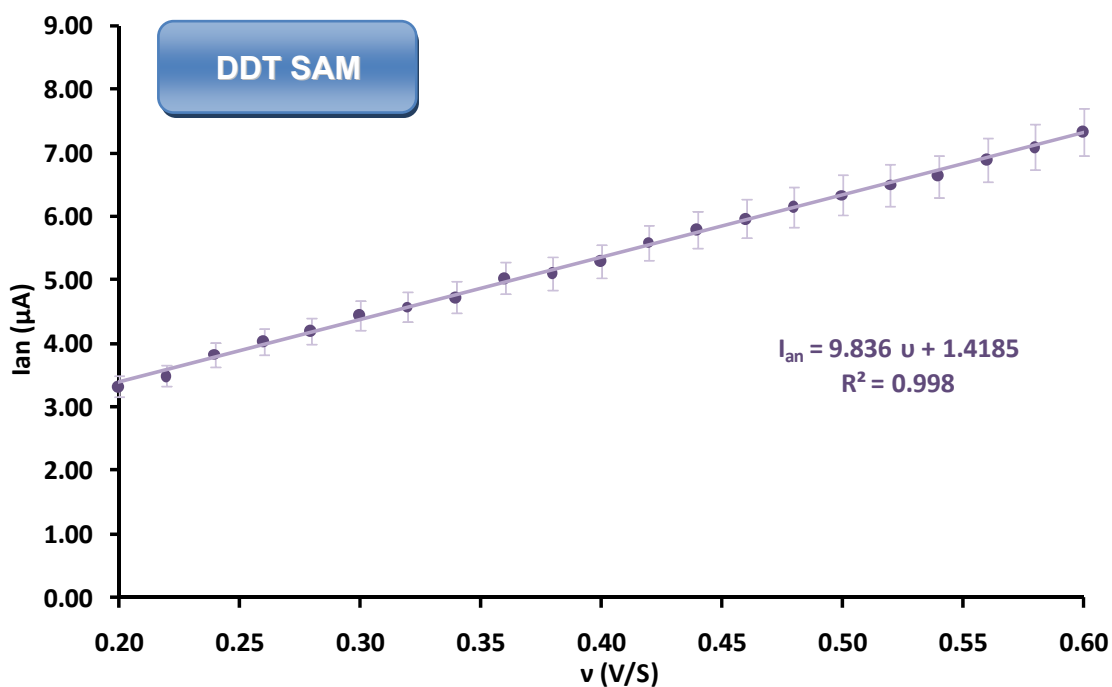


Figure 7 – Scan rate dependence of the anodic peak current in cyclic voltammetry for DDT SAM electrode in 0.1M  $\text{KNO}_3$  solution.

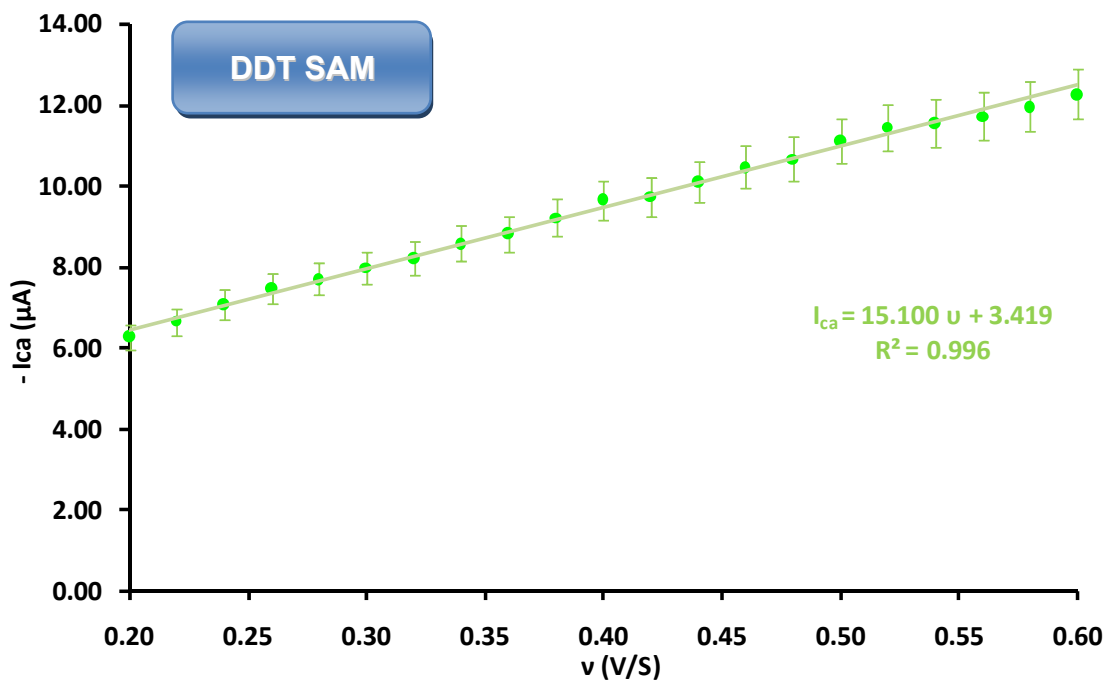


Figure 8 – Scan rate dependence of the cathodic peak current in cyclic voltammetry for RJ12 SAM electrode in 0.1M  $\text{KNO}_3$  solution.

The literature review has evidenced two possible causes for the appearance of sharp peaks in CVs using only potassium nitrate in solution – gold cyanisation or Prussian Blue redox reaction.

Kingo Itaya et al <sup>17</sup> have reported an electrochemical scanning tunnelling microscopy and ultrahigh-vacuum investigation of gold cyanide adlayers on Au(111) formed in aqueous solution in order to characterise the adsorption process of  $\text{Au}(\text{CN})_2^-$  (dicyanoaurate).

The electrochemical deposition of gold is usually performed in  $\text{KAu}(\text{CN})_2$  solutions. They carried out cyclic voltammetry experiments on gold electrode in the presence and absence of 1mM  $\text{KAu}(\text{CN})_2$ .

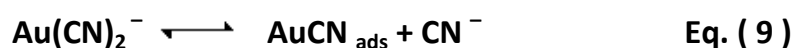
Reversible couple of peaks were found in the cyclic voltammograms at -0.61 V, which was due to the redox reaction of the couple  $\text{Au}(0) / \text{Au}(\text{I})$ , according with the following equation,



This redox system has Nernstian behaviour, resulting in two peaks of equal height and the peak current is proportional to the square root of scan rate.

A set of sharp peaks have appeared on gold electrode at + 0.18 V (vs Ag/AgCl, 3.5M KCl) in the presence of potassium dicyanoaurate, having small peak separation and the peak current increase linearly with the potential sweep rate.

Scanning tunnelling microscopy experiments have confirmed that these sharp peaks are due to the phase transition of the insoluble AuCN layer (in aqueous solution) to a soluble dicyanoaurate ion, according with the equation,



Although similar peaks were found in our system, it should be noted that the concentration of  $\text{KAu}(\text{CN})_2$  was very low, because this compound was obtained by the gold cyanisation process itself.

Since the larger gold area the higher peak current for gold cyanisation, then, performing the same experience using bare gold electrode would be desirable.

Consequently, same experiment was carried out without SAM on gold, ie, bare gold electrode, and the result have shown that nothing happened, giving a complete flat CV. Obviously, this behaviour was expected since had this phenomenon been valid, it should have been observed at long time ago by other researchers and it has not been reported. However, Kingo Itaya et al <sup>17</sup> have mentioned that these sharp peaks are observable at single – crystal Au(111) surface, but not on polycrystalline gold electrodes. They observed different adlattices in the structure of the single-crystal gold in the positive and negative potential regions in respect to the phase transition peaks. In our experiments very similar redox peaks are observed which leads us to believe that in polycrystalline Au(111) modified with monolayers, the available vacancies left by any desorbed thiol molecules may act in a similar manner to single - crystal Au(111).

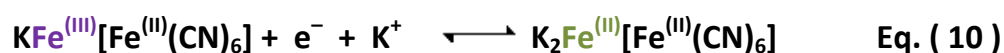
Robin L. McCarley and Allen J. Bard have reported the formation and subsequent annealing of monolayer pits on Au(111) using scanning tunneling microscopy (STM) in presence of cyanide in solution. <sup>18</sup> The cyanide etches the metal surface creating triangular etch pits, reflecting the bulk geometry of the Au(111) face-centered cubic crystal. Once the pits are formed, there is an annealing mechanism resulted by self-diffusion of gold atoms, according to the mobile adatom mechanism, collapsing the pits. <sup>18</sup>

The concentration of Potassium dicyanoaurate formed during gold cyanisation is extremely low, and this compound is highly soluble in aqueous solution, therefore, although gold cyanisation may occur in bare gold electrodes, the concentration is too low and any molecule is able to diffuse away from the electrode surface. However, it is possible that in the presence of a self-assembled monolayer the molecules are retained close to the electrode surface.

### 6.4.2. Formation of Prussian Blue layer

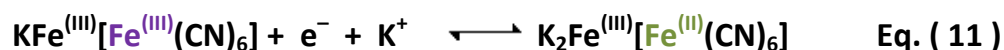
The possible formation of Prussian Blue on the electrode surface led to further literature survey and investigations.

Cyclic voltammogram of Prussian blue modified electrode exhibits two redox waves peaked at 0.18 V and 0.85 V caused by the following reversible reactions,



Prussian Blue

Prussian White



Prussian Blue

Prussian Green

The peak corresponding to 0.18 V wave redox potential corresponds to the oxidation/reduction of high spin iron (II) to iron(III) converting Prussian White to Prussian Blue and vice-versa, while the pair centred at 0.85 V refers to the oxidation/reduction of Prussian Blue to Prussian Green and vice-versa, occurred in the low spin iron.

These reactions are accompanied by mass changes due to the transfer of  $K^+$  cations into/out of the PB film to preserve the electroneutrality of the system.

The Prussian Blue/Prussian White redox couple with potassium as counter cation has specific characteristics. The corresponding peaks are sharp, specially the cathodic one <sup>11</sup>, and the peak height differs from the anodic to the cathodic. A linear relationship of the peaks of PB as a function of the potential sweep rate is observed, indicating that electrochemical reaction is a surface-controlled process. <sup>15,17,19,20</sup>

The quality of the electrodes modified by Prussian Blue layer can be judged by the sharpness of the peaks in cyclic voltammograms. To achieve a regular structure, the pH should be taking into account, since the stability of PB is only satisfactory in acidic aqueous solutions, while at alkaline or neutral pH decomposition occurs. This is the comportment in the case of bare gold electrode. However, there are some studies indicating that the presence of SAM can increase the greatly the stability of PB film.

J. Kwak et al have reported the characterisation of PB film deposited on nano structures of gold that are attached to thiol self-assembled monolayer and a dendrimer. <sup>21</sup> They have studied the effect of pH on the electrochemical behaviour of PB films at different electrodes. In the case of Au/PB modified electrode, the stability was compromised at  $pH > 6.8$ . However for Au/SAM/PB and Au/SAM/Nano-Au/PB modified electrodes, the stability further increases to

9.55, concluding that thiol SAMs on gold electrodes can enhance greatly the consistence of PB film, even at alkaline media.

Certainly, the flat CV observed using bare gold electrode is expected, since the solution is neutral.

The cyclic voltammograms observed for DDT and RJ12 SAM, suggesting the formation of Prussian Blue in the vacancies liberated by the removal of the thiol molecules.<sup>22</sup> The monolayer protects the PB film, acting like a shield, due to the rearrangement of the thiol molecules after the perturbation. Furthermore the microenvironment at the SAM modified electrodes probably provides local pH environment conducive to the formation of PB

The formation of this film using the dissociation of ferricyanide as the source of free iron ions gives an ultrathin film with thickness in nanometer range. This is the reason why it is not possible to see the change of colour by naked eye.<sup>23</sup>

Calculation of the electron transfer kinetics, the number of exchanged electrons and the surface coverage of PB in the SAM electrodes at 0.18V were fully characterised.

### ***6.4.3. Electron transfer kinetics***

The study of electron transfer was performed in order to calculate the concentration of confined electroactive species in dodecanethiol and RJ12 self-assembled monolayer on gold electrode.

The apparent rate constant ( $k_{app}$ ) for the process was extracted using Laviron's procedure<sup>16</sup>. Figure 9 and Figure 10 show typical redox peak splitting by  $E_{pc}$  and  $E_{pa}$  overpotentials observed for DDT and RJ12 SAMs on gold electrode as a function of logarithm of the scan rate ( $Vs^{-1}$ ). Using this procedure, the kinetic



parameters such as  $k_{app}$  and symmetry factor ( $\alpha$ ) may be obtained in a straightforward manner from eqs (12) and (13),

$$E_{pc} = E_c^{0'} - \frac{RT}{\alpha nF} \ln \left[ \frac{\alpha nF v_c}{RT k_{app}} \right] \quad \text{Eq. (12)}$$

$$E_{pa} = E_a^{0'} - \frac{RT}{(1-\alpha)nF} \ln \left[ \frac{(1-\alpha)nF v_a}{RT k_{app}} \right] \quad \text{Eq. (13)}$$

Where  $n$  is the number of electrons,  $F$  is the faraday constant,  $R$  and  $T$  is the gas constant and the temperature respectively.  $v_a$  and  $v_c$  are the critical scan rates obtained by extrapolating the linear portion of the straight line fits to the anodic and cathodic data to the logarithm of scan rate axis.

The slopes of the linear portion of the overpotential  $\eta$  vs  $\log(v)$  curve are  $\frac{RT}{\alpha nF}$  for the cathodic branch and  $\frac{RT}{(1-\alpha)nF}$  for the anodic branch.

The values of the transfer coefficient  $\alpha$ , were obtained from the values of each slope and substituted back in eqs 14 and 15 to solve for  $k_{app}$ .

$$\frac{n\alpha}{(1-\alpha)n} = \frac{v_a}{v_c} \quad \text{Eq. (14)}$$

$$k_{app} = \frac{\alpha nF v_c}{RT} = \frac{(1-\alpha)nF v_a}{RT} \quad \text{Eq. (15)}$$

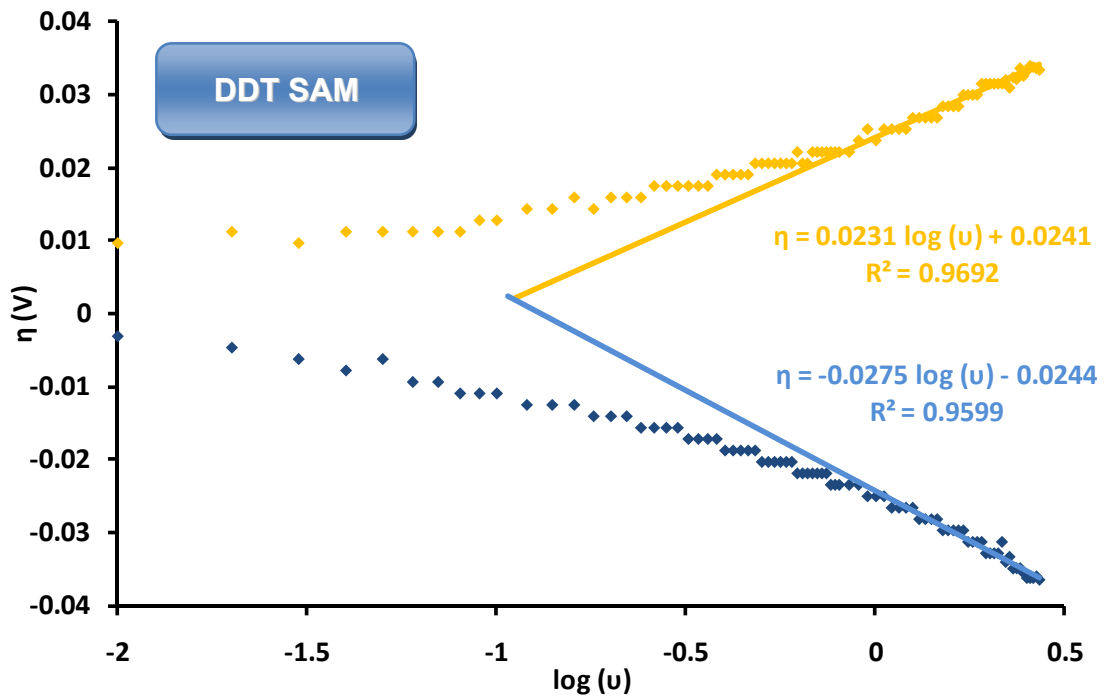


Figure 9 – Plot of overpotential vs.  $\log v$  for DDT SAM on gold (in 0.1M  $KNO_3$ ).

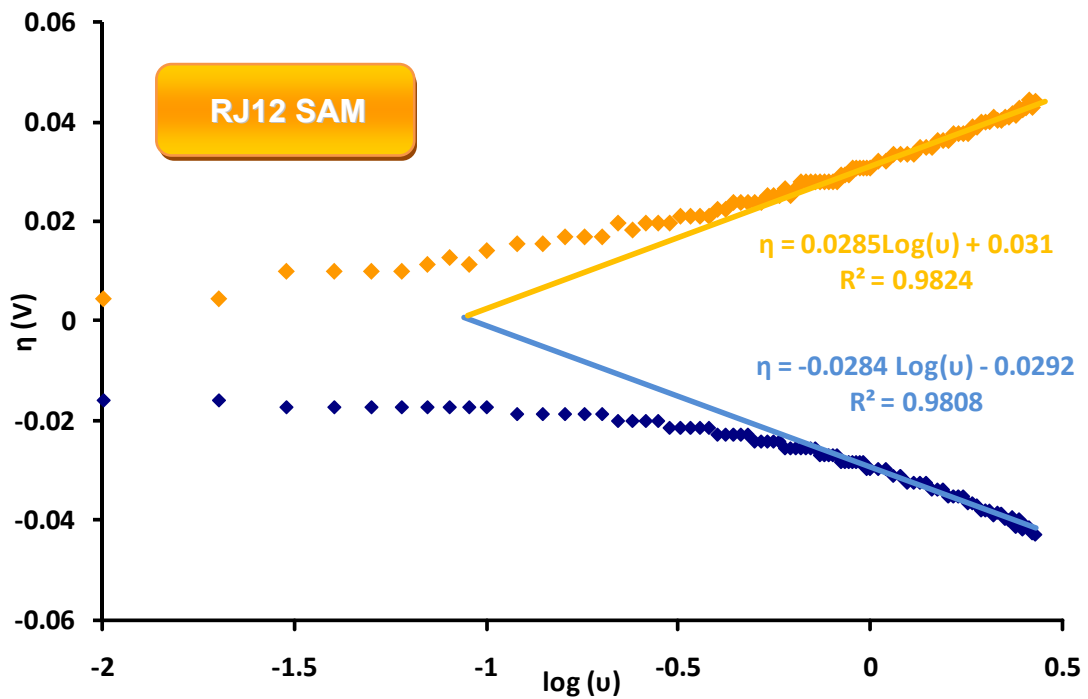


Figure 10 – Plot of overpotential vs.  $\log v$  for RJ12 SAM on gold (in 0.1M  $KNO_3$ ).

Although gold cyanisation may happen at same potential, their corresponding charge value should be negligible.

The values of apparent electron transfer rate constant calculated in this manner were  $19.60 \pm 2.00 \text{ s}^{-1}$  (RJ12 SAM) and  $19.47 \pm 1.95 \text{ s}^{-1}$  (DDT SAM) and suggest a very fast electron transfer rate.

These results have proved that the molecular constitution of the monolayer does not interfere with the electron transfer process, since DDT and RJ12 have distinct characteristics such as structure (saturated vs unsaturated) and the length of the surfactants.

This observation seems to imply the independence of the electron transfer on the structure of the monolayer, indicating that the redox species are confined near the electrode surface but their redox mechanism is not influenced by the molecules that comprise the monolayer.

The electron transfer coefficient,  $\alpha$ , is calculated to be  $0.51 \pm 0.05$  for both SAM electrodes. Given  $0.3 < \alpha < 0.7$  in general, it could be concluded that  $n = 1$  and  $\alpha = 0.51 \pm 0.05$ . So the redox reaction is a single electron transfer process.

The surface coverage of PB ( $\Gamma$ ) also was estimated from integration of the reduction peak of the CVs according to faraday's law:

$$\Gamma = \frac{Q}{nFA} \quad \text{Eq. (16)}$$

where  $Q$  is the charge involved in the reaction obtained by integrating the cathodic peak,  $n$  the number of electron transferred,  $F$  Faraday constant, and  $A$  the electrode area.

Using this equation, the value of the surface coverage was evaluated as  $14.5 \pm 1.3 \text{ nmol/cm}^2$  and  $24.4 \pm 1.2 \text{ nmol/cm}^2$  for RJ12 SAM and DDT SAM electrode respectively, by the involvement of one electron in the process.

These results are in accordance with the structure of the monolayers. RJ12 molecule is constituted by aromatic rings connected with triple bonds. Therefore, they are very rigid compared to dodecanethiol. However, it should be noted that the application of such a high potential (2V) is likely to lead to some conformational changes in the structure. This effect will be more apparent with the less rigid dodecanethiol monolayer.

Therefore, the dodecanethiol monolayer is likely to be more efficient in trapping PB close to the electrode surface, preventing the molecules from diffusing away from the surface compared to RJ12 one. That's why the surface coverage is nearly double for the alkanethiol.

#### ***6.4.4. Characterisation of the electrode surface by FTIR***

Fourier Transform Infrared (FTIR) spectroscopy studies on the DDT SAM gold electrode and bare gold electrode were performed in order to confirm the cyanisation of the Au electrode, based on the IR absorption by the  $-C \equiv N$ : triple bond and the CS bond ( $H_2C - S -$ ).

The vibrational spectra of cyano complexes have been studied extensively. They can be identified easily by a small band in the  $2200 - 2000 \text{ cm}^{-1}$  region, because of the stretching mode of triple cyanide bond.<sup>24</sup> The stretching band of free cyanide is  $2080 \text{ cm}^{-1}$  (aqueous solution), but when is coordinated to a metal ( $M - CN$ ), this value shift to higher frequencies.

The stretching frequency of CN in the dicyanoaurate compound ( $Au - CN$ ) is at  $2110 - 2150 \text{ cm}^{-1}$  region.<sup>25</sup>

Prussian Blue has a characteristic absorption band at  $2090 - 2110$  band corresponding to the vibrational mode energy of cyanide.<sup>21, 26</sup>

Figure 11 shows a FTIR spectrum at bare gold electrode and DDT SAM on gold electrode after applying CA at 2V for 20s. The large broad band between 2800 and 3100  $\text{cm}^{-1}$  proves the presence of thiol monolayer. This vibration is due to C–H and S–C stretching vibrations of the molecule that form the monolayer.<sup>27</sup>

The broad band around 2127  $\text{cm}^{-1}$  is due to the stretching vibration mode of CN, but bonded with different metals, covering the regions of Dicyanoaurate and Prussian Blue. The spectra using bare gold electrode indicates the absence of any cyanide compound in the surface giving 0% absorbance, as it is show in figure 11 (inset).

This band might be broader due to the presence of both compounds in the electrode surface.

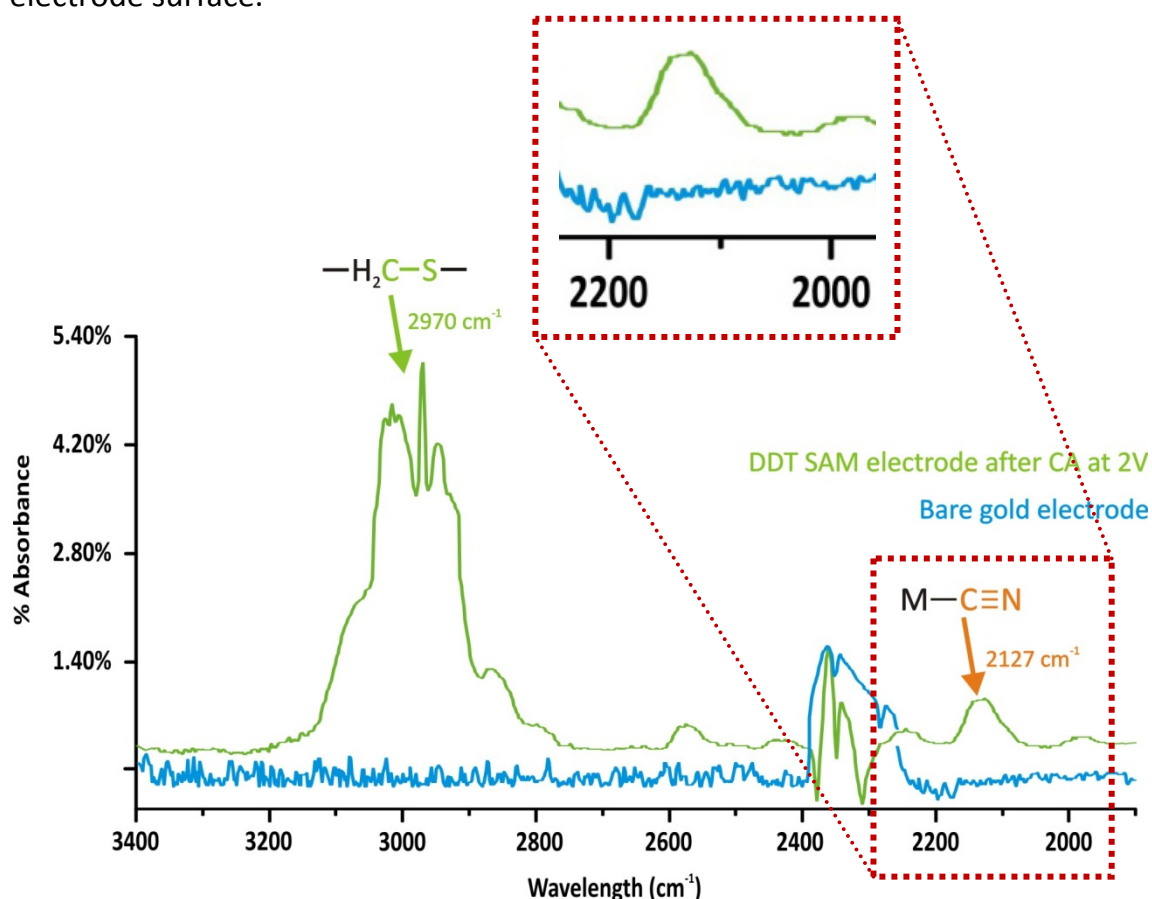


**Figure 11** – FTIR spectra at bare gold electrode and DDT SAM on gold electrode after CA at 2V.

### 6.4.5. Influence of the applied potential

The influence of the potential in the structure of the monolayers has been performed. Although these systems are different compared with last chapter since there are peaks in the cyclic voltammograms involving gold cyanisation and formation of PB, it is still possible to observe the integrity of the monolayer.

Figure 12 and Figure 13 show Nyquist plots in 0.1M  $\text{KNO}_3$  solution using DDT and RJ12 SAM modified electrodes carried out after the application of 2V for 20s.

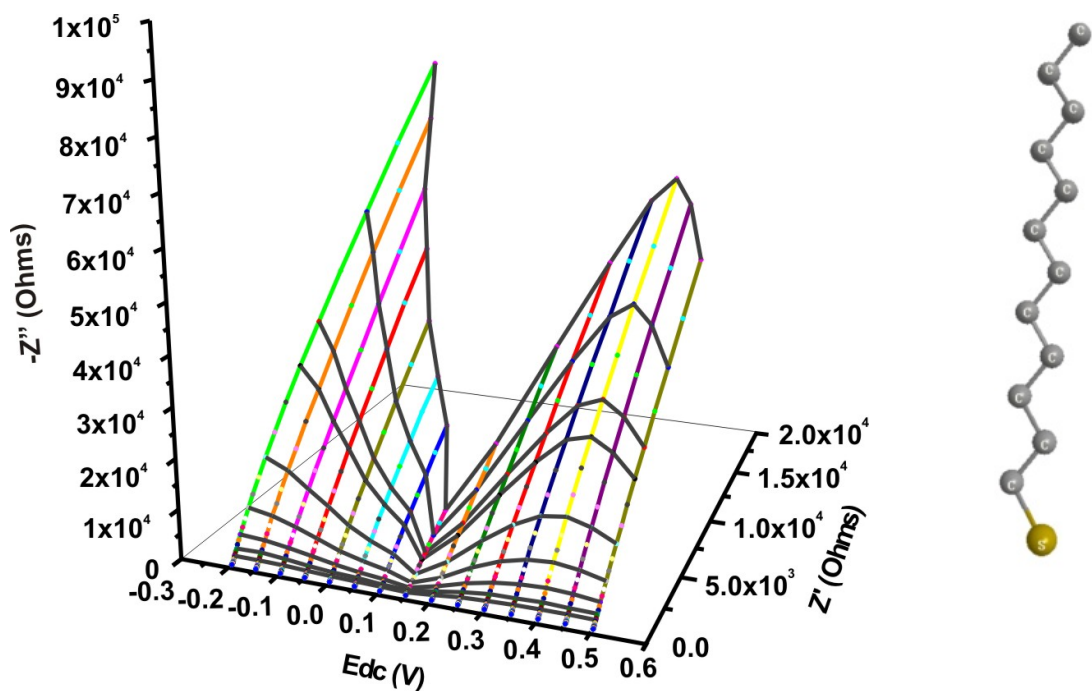


**Figure 12** – Nyquist plots in 0.1M  $\text{KNO}_3$  solution using DDT SAM modified electrode. Frequency range: 1Hz to 100KHz at different applied potentials.

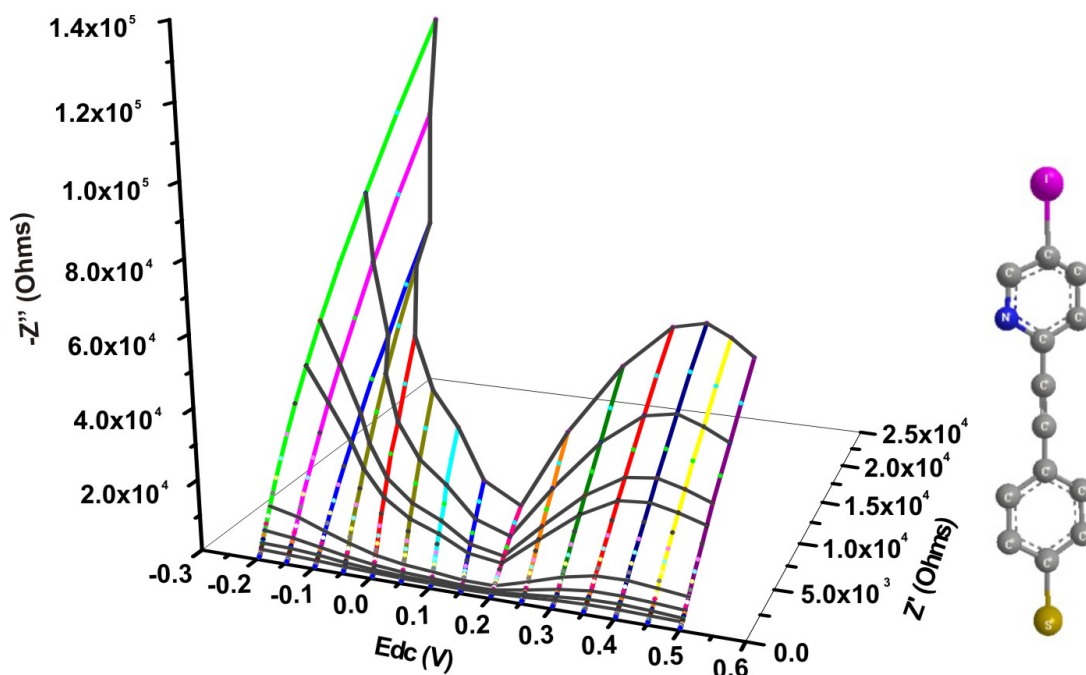


**Figure 13** – Nyquist plots in 0.1M  $KNO_3$  solution using RJ12 SAM modified electrode. Frequency range: 1Hz to 100KHz at different applied potentials.

The value of charge-transfer resistances were not calculated due to the complex equivalent circuit that this system represents. However, a simple observation to Nyquist plots provides valuable qualitative information, revealing particular characteristics of the chemical system. Briefly, the 3D impedance spectra have a V shape and the lower value of impedance is situated at 0.18V.

The study of the variation of the space charge capacitance in a potential range was performed. The idea was imported from a typical analysis widely used in semi-conductor characterisation based in EIS, called as Mott-Schottky plot.  
28,29,30,31

Acquisition of Mott-Schottky plots provides values of doping density and the flatband potential. A negative slope suggests a n-type and a positive slope suggests a p-type semiconductor.<sup>30,31</sup> The space charge capacitance is calculated from the imaginary component of the impedance ( $Z''$ ) using the relationship,

$$\frac{1}{C^2} = 2\pi f Z'' \quad \text{Eq. (17)}$$

Where  $f$  is the frequency and  $Z''$  is the imaginary component of the impedance.

In a pinhole free gold-insulating monolayer-electrolyte interface, when the bulk electrolyte does not contain redox ions, the response is mainly capacitive. In presence of redox active ions charge transport is expected to occur via leakage currents and at any pinhole defects. In a conjugated system the rate limiting step will be the charge transport through the conjugated structure and should be faster than that in an insulating layer. However, following the same analogy for semi-conductors, the imaginary impedance measured at sufficiently high frequencies excludes the contribution of the current produced by electron transfer process. Thus, in the presence of pinhole-free monolayer, Mott-Schottly plot has a trend line of slope nearly zero, acting as a capacitor. Figure 14 shows this behaviour, and the RJ12 trend line is lower than DDT, which is expected.

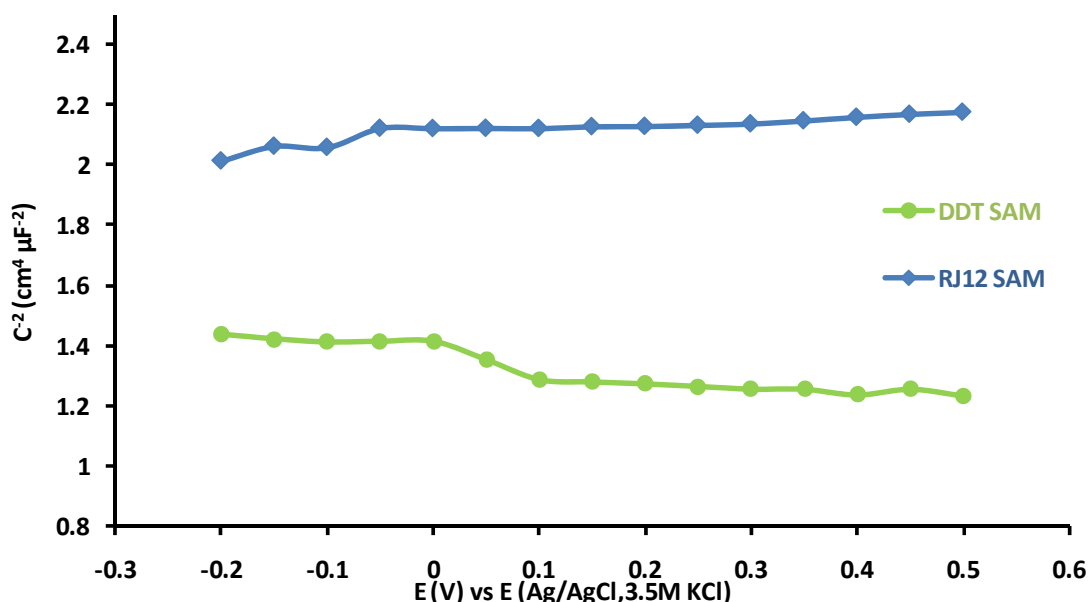


**Figure 14**– Mott-Schottky plots using pinhole free DDT and RJ12 SAM in 1mM  $\text{Fe}(\text{CN})_6^{3-/4-}$  and 0.1M  $\text{KNO}_3$  solution. Frequency: 100 KHz.



Figure 15 shows Mott-Schottky plot for the DDT and RJ12 SAM after the application of 2V for 20 s. Since we have PB and  $\text{Au}(\text{CN})_2^-$  within the monolayer, the behaviour should be different comparing with pinhole free monolayer. In this system, the current that is produced is mainly due to the electron transfer process of PB and  $\text{Au}(\text{CN})_2^-$  that is confined in the electrode surface, but and as it was mentioned before, the imaginary impedance measured at sufficiently high frequencies excludes the contribution of the current produced by electron transfer process, implying that the Mott-Schottky analysis should be similar comparing with pinhole free monolayer. However, the modified films acquire a Gaussian wave shape. Since the use of high frequency suppresses all leakage current, the wave may be linked to phase transition of  $\text{Au}(\text{CN})_2^-$ , which is evidence that both processes may occur.

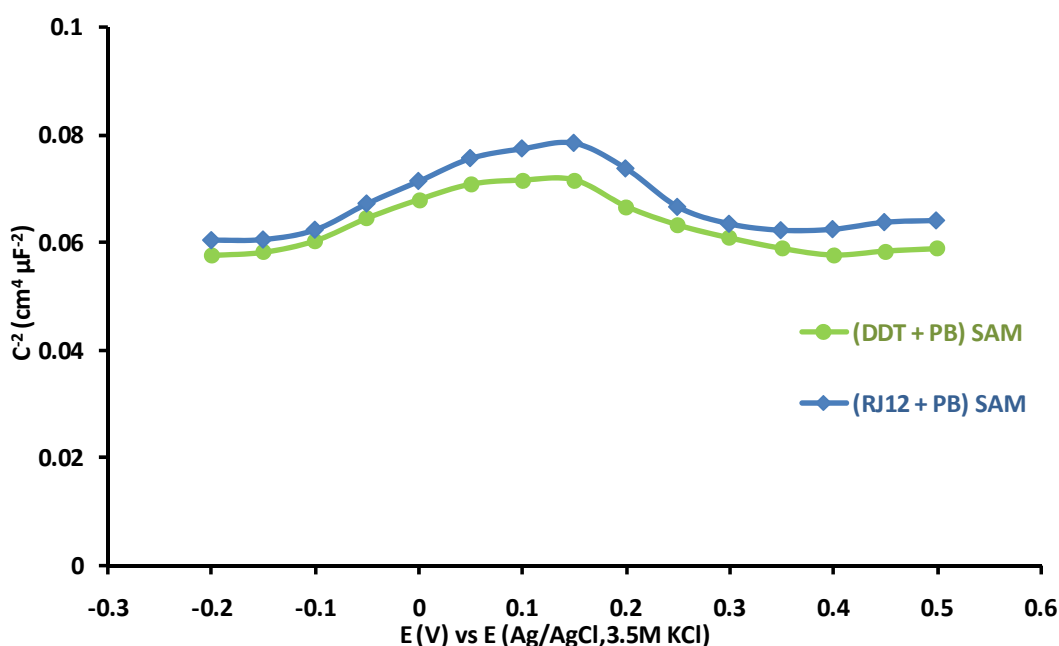


**Figure 15**– Mott-Schottky plots using DDT and RJ12 SAM after CA at 2V in 0.1M  $\text{KNO}_3$  solution. Frequency: 100 KHz.

## 6.5. CONCLUSIONS

---

The investigation has evidenced two possible causes for the appearance of sharp peaks in CVs using only potassium nitrate in solution, after application of 2V to SAM gold electrodes at solution of 1mM Ferricyanide / Ferrocyanide and 0.1M KNO<sub>3</sub> – gold cyanisation or Prussian Blue redox reaction.

These peaks at 0.18V are due to the phase transition of the insoluble AuCN layer (in aqueous solution) to a soluble dicyanoaurate ion, and due to the electron transfer of high spin iron (II) to iron(III) converting Prussian White to Prussian Blue.

The current involve on gold cyanisation process should be negligible. So, these peaks are masked by the electron transfer of Prussian Blue.

FTIR experiments have confirmed the presence Au(CN)<sub>2</sub><sup>-</sup>, and Prussian Blue, due to the presence of a broad band in the region of around 2127 cm<sup>-1</sup> the CN triple bond and Mott-Schottky plots have shown an evidence that gold cyanisation may occur.

In conclusion, the mystery was unveiled and the answer for the question that is on title is: there is electron transfer and gold cyanisation.

## 6.6. REFERENCES

---

- 1 – H. Tan, D. Feng, J.S.J. Van Deventer, G. C. Lukey, *Hydrometallurgy*, 84 (2006) 14-17.
- 2 – Morteani, G., in Schmidbaur, H., *Gold, Progress in Chemistry, Biochemistry and Technology*, Wiley & Sons, Chichester, p.40, 1999;
- 3 – L. Elsner, Über das verhalten verschiedener metalle in einer wässrigen lösung von zyankalium, *J. Prakt. Chem.*, 37 (1846) 441 – 446.
- 4 – R. M. Hunter, F. M. Stewart, Tamara Darsow, Method and apparatus for extracting precious metals from their ores and the product thereof, *U.S. Patent No. 5672194*, issued 30-09-97
- 5 – Hiskey, J.B. and Atluri, V.P., Dissolution chemistry of gold and silver in different lixivants, *Mineral Processing and Extractive Metallurgy Review*, 4 (1988) 95 – 132;
- 6 - D.W. Kirk, F. R. Foulkes, W. F. Graydon, A study of anodic dissolution of gold in aqueous alkaline cyanide, *J. Electrochem. Soc.*, 125 (1978) 1436-1443;
- 7 – F. Xie, D. Dreisinger, J. Lu, *Minerals Engineering*, 21 (2008) 1109 – 1114;
- 8 – Guy Deschênes, Marlaine Rousseau, Jean Tardif and P. J. H. Preud'homme, *Hydrometallurgy*, 50 (1998) 205 – 221.
- 9 – M. J. Nicol et al., The chemistry of the extraction of gold in the extractive metallurgy of Gold, *Ed. Stanley*, pp. 83, 1987;

- 
- 10 – P. J. Kulesza, K. Miecznikowski, M. Chojak, M. A. Malik, S. Zamponi, R. Marassi, *Electrochem Acta*, 46 (2001) 4371 – 4378;
- 11 – A. A. Karyakin, E. E. Karyakina, *Russian Chem. Bull.*, 50 (2001) 1811 – 1817;
- 12 – A. A. Karyakin, E. E. Karyakina, Lo Gorton, *Talanta*, 43 (1996) 1597 – 1606;
- 13 – V. D. Neff, *J. Electrochem. Soc.*, 128 (1978) 886 – 887;
- 14 – R. Yang, Z. Quian, J. Deng, *J. Electrochem. Soc.*, 145 (1998) 2231 – 2236;
- 15 – D. Zhang, K. Wang, D. Sun, X. Xia, H. Chen, *J. Solid State Electrochem.*, 7 (2003) 561 – 566;
- 16 – E. Laviron, *J. Electroanal. Chem.*, 101 (1979) 19 – 28;
- 17 – T. Sawaguchi, T. Yamada, Y. Okinaka, K. Itaya, *J. Phys. Chem.* 99 (1995) 14149 – 14155;
- 18 – R. L. McCarley, A. J. Bard, *J. Phys. Chem.*, 96 (1992) 7410 – 7416;
- 19 – D. Zhang, K. Wang, D. Sun, X. Xia, H. Chen, *Chem. Mater*, 15 (2003) 4163 – 4165;
- 20 – D. Zhang, K. Zhang, Y. Yao, X. Xia, H. Chen, *Langmuir*, 20 (2004) 7303 – 7307;
- 21 – C. Yang, C. Wang, J. Wu, X. Xia, *Electrochimica Acta*, 51 (2006) 4019 – 4023;
- 22 – N. Li, J. Park, K. Park, S. Kwon, H. Shin, J. Kwak, *Biosensors and Bioelectronics*, 23 (2008) 1519 – 1526;
- 23 – C. Yang, C. Wang, J. Wu, X. Xia, *Electrochimica Acta*, 51 (2006) 4019 – 4023;

- 
- 24 – kazuo Nakamoto, *Infrared and Raman spectra of inorganic and coordination compounds*, 6<sup>th</sup> edition, Wiley-Interscience, 2009, pp.112;
- 25 – A.S. Ibrado, D.W. Fuerstenau, *Minerals Engineering*, 8 (1995) 441 – 458;
- 26 – C. Korzeniewski, M. W. Severson, P. P. Schmidt, S. Pons, M. Fleischmann, *J. Phys. Chem.*, 91 (1987) 5568 – 5573;
- 27 – R. C. Nuzzo, B. R. Zegarski, E. M. Koreniqt, L. H. Dubois, *J. Phys. Chem.*, 96 (1992) 1335 – 1361;
- 28 – A. S. Bondarenko, G. A. Ragoisha, *J. Solid State Electrochem.*, 9 (2005) 845 – 849.
- 29 – Eung-Jo Lee, Su-Il Pyun, *J. of App. Electrochem.*, 22 (1992) 156 – 160;
- 30 – E. M. García-Frutosa, E. Gutierrez-Pueblaa, M. A. Mongea, R. Ramíreza, P. de Andrésa, A. de Andrésa, R. Ramírezb, B. Gómez-Lor, *Organic Electronics*, 10 (2009) 643 – 652.
- 31 – C. Gupta, M. A. Shannon, P. J. A. Kenis , *J. Phys. Chem. C*, 113 (2009) 9375 – 9391.

## 7. CONCLUSION AND FUTURE WORK

---

The objective of the research presented in this thesis was the characterisation of electrode microarrays and conventional electrodes modified with molecular wires as platforms for biosensors.

Fabrication of microelectrode arrays of gold using photolithography was achieved. Although most of the researchers accepted the inlaid geometry as the result using photolithographic technique, the surface analysis techniques lead us to believe that the geometry of microelectrodes produced as standard with the photolithography protocol is conical recessed. This is clearly evident from the SKN scans which show a decrease in CPD values with increasing depth.

Microarrays are used for high-throughput measurements using various signal transduction techniques. Ideally each sensor in a microarray platform should perform optimally to ensure an error free response. In this thesis, a simple method for designing a microelectrode array platform (MEA) is described, allowing a 'defective' cluster of sensing arrays to be easily identified. It is possible to extend this concept for multiple analyses on a single chip. This work provides solid basis for future studies in this field, showing valuable information about fabrication of microelectrode arrays patterning in different designs on silicon wafers by photolithography in order to promote multi-analyte sensing in a single microarray platform.

The study of formation and characterisation of thiol-based self-assembled monolayers on conventional-sized gold electrodes have been performed. The charge transfer and self-assembly characteristics of novel molecular wires (fully conjugated molecules) which were synthesised at the Department of Chemistry

---

were evaluated. This work will be very useful since it gives valuable information about the perfect conditions for deposition of thiol molecules on gold and its characterisation using electrochemistry. The electron transfer has also been studied in detail. The behaviour of these wires is compared with heptanethiol and dodecanethiol SAMs. Voltammetric studies for CSW564 SAM, HPT SAM and (CSW564 + DDT) SAM on gold electrodes have demonstrated the presence of pinholes in the monolayer. CSW564 SAM has presented Nernstian behaviour suggesting the presence of millions of small pinholes distributed randomly to the monolayer and their diffusion layers are overlapped responding as macroelectrode. HPT SAM and (CSW564 + DDT) SAM have presented microelectrode behaviour indicating that each pinhole acts as a single microelectrode and there is no overlap of the diffusion layers.

In other hand, DDT SAM and RJ12 SAM were free of pinholes due to the absence of any peak or sigmoidal shape in the CVs. Large semi-circle in the entire range of frequencies for EIS indicated the complete charge transfer control the redox reactions, shows that the redox reaction is inhibited in the DDT and RJ12 SAM, indicating a formation of a very organised and pinhole-free monolayer. The influence of applied potential to the stability of the monolayer was studied. It was proved that although the capacitance maintains constant, the charge-transfer resistance decrease when the potential goes far way from the open potential. Some conformations in the structure of the molecules lead to a formation of defects that decrease the distance between the electroactive species and the electrode surface.

Finally, the investigation has evidenced two possible causes for the appearance of sharp peaks in CVs using only potassium nitrate in solution, after application of 2V to SAM gold electrodes at solution of 1mM Ferricyanide / Ferrocyanide and 0.1M  $\text{KNO}_3$  – gold cyanisation or Prussian Blue redox reaction.

These peaks at 0.18V are due to the phase transition of the insoluble AuCN layer (in aqueous solution) to a soluble dicyanoaurate ion, and due to the electron transfer of high spin iron (II) to iron(III) converting Prussian White to Prussian Blue. FTIR experiments have confirmed the presence  $\text{Au}(\text{CN})_2^-$ , and Prussian Blue, due to the presence of a broad band in the region of around  $2127\text{ cm}^{-1}$  the CN triple bond and Mott-Schottky plots have shown an evidence that gold cyanisation may occur.

Future avenues of research include the application of self-assembled monolayer of molecular wires in microelectrode arrays for multiple analyses on a single chip. First, there will be a need of modification the molecular wire in order to acquire specificity to one analyte. Further investigation about gold cyanisation and formation of Prussian Blue needs to be performed, that can be useful in the future using Prussian Blue as electron shutter in sensor analysis.